

Novel Approaches to Manufacturing Membranes with Controlled Selectivity

A dissertation submitted by

Ilin Sadeghi

in partial fulfillment of the requirements for the degree of

Doctor of Philosophy

in

Chemical & Biological Engineering

Tufts University

May 2018

Advisor: Ayse Asatekin

Copyright (2018) by Ilin Sadeghi

ABSTRACT

Membrane separation processes are energy-efficient, green and easy to implement. They are used in a wide array of applications from waste water treatment to pharmaceuticals to food industries. However, these established applications are mostly constrained to separations based on a size sieving mechanism. Moreover, there are only a handful of membrane chemistries on the market, further limiting their applications. In this dissertation, these two problems are addressed by utilizing new approaches.

First, chemoselective membranes are fabricated by self-assembly of random copolymer micelles, a simple and scalable method. This copolymer self-assembles during coating to form a structure with interconnected 1-2 nm nanochannels, lined with functional groups. The nanoconfinement along with chemical functionality leads to high separation efficiency of small organic molecules. In addition, the high porosity of the membrane selective layer leads to high permeability. Initially, this approach was used to prepare membranes to separate a mixture of two solute with similar size, but different charge in both diffusion and pressure-driven filtration experiments. The membranes exhibited unprecedented charge-based selectivity for small molecules that was further enhanced in competitive experiments. This effect is similar to that observed in biological pores such as ion channels, implying novel selective transport mechanisms.

Next, these membranes were modified to address a more complex separation of small molecules based on their aromaticity. A simple and straightforward

conjugation chemistry was used to convert the carboxylate groups in the pores to aromatic groups. The permeation selectivity of these membranes for separation of two steroid hormones of similar size and charge was examined. Selectivity was linked with the interactions of these solutes with functional groups on the membrane surface, measured using quartz crystal microbalance with dissipation (QCM-D), which provides a significant insight into separation mechanism. The functionalized membrane showed exceptionally high selectivity for the aromatic solute in competitive diffusion experiments. This, in combination with additional results, imply a hopping transport mechanism.

In another direction, a novel method to fabricate of membranes with a wide range of monomer chemistries in a simple and scalable manner, interfacially initiated free radical polymerization (IIFRP), is presented. We developed this method and exploited the applicability of this method for fabrication of ultrathin hydrogel selective layers and its application for protein purification. Membrane performance can be tuned by experimental parameters such as UV irradiation time, monomer concentration, and the addition of porogen or functional comonomers. The results illustrate successful fabrication of uniform, defect-free and ultrathin hydrogel layers whose dry thickness varies by UV irradiation time. The hydrogel membranes are efficient and stable with excellent antifouling properties, and suitable for protein purification.

Overall, the results presented in this dissertation illustrate simple, robust and scalable approaches for fabrication of selective membranes for various targeted separations. Both methods can have a broad impact in various areas from

pharmaceuticals, drug delivery, sensors, barrier materials to water filtration or gas purification.

ACKNOWLEDGEMENTS

The successful completion of my doctorate studies would have not been possible without the support of several remarkable individuals. One person's influence, however, stand significantly taller than anyone else and that person is my advisor, Prof. Ayse Asatekin. I greatly appreciate her invaluable guidance, continuous support and encouragements throughout my PhD. She has given me so many wonderful opportunities by opening up new doors and keeping me motivated all along. She gave me the freedom to explore various research directions and was supportive throughout the whole journey even over months of failed experiments! She has provided me with the strongest research tools and that is the confidence and independence of exploring new directions. Moreover, her joy and enthusiasm for polymer science, especially during the two courses, I have taken with her, was extremely inspirational and opened my eyes to a world of possibilities and made me realize that I am only a beginner in this exciting field. I would also like to thank her for her friendship, understanding and for making my PhD journey such a fun and joyful experience. Ayse, working in your lab was such a great privilege, you showed me what it means to be a great mentor and you will remain a role model for me as a scientist and as an individual.

I would like to express my profound gratitude to the members of my doctoral committee starting with Prof. Hyunmin Yi, whom I had the pleasure of working closely on two fascinating projects since very beginning of this journey. His invaluable insights, endless passion and involvement in all the projects made me so

motivated and encouraged throughout my research. He has been extremely supportive and available whenever I needed discussions and logical support. Furthermore, his willingness to walk me through the craft of putting words together more potently for scientific writings just made the challenge of honing and polishing my sentences so enjoyable. His constant enthusiasm and excitement and his belief in me has fueled me throughout my PhD. His unique attributes as a mentor will always be an example for me in the future. I would like to extend my appreciation to the rest of my PhD committee members Prof. William Philip and Prof. Iryna Zenyuk for their valuable inputs, and for all their questions which incited me to widen my research from various perspectives.

A special acknowledgement goes to Prof. Peggy Cebe, in physics department, whom I had the opportunity to work in a collaborative project and several instructive interactions during joint group meetings. Her profound knowledge and meticulous approach to research with such attentions to all the details and technical depth has had a huge influence on me.

I would like to express my gratitude to Prof. David Kaplan, in biomedical engineering department, for generous access to his lab instruments especially QCM, which became my favorite toy at the end! Also, I would like to thank professor Qiaobing Xu for access to DLS, which I extensively used during my PhD. I am also greatly indebted to Dr. David Wilbur in chemistry department, for his helpful discussion, technical assistance and great training for almost all the analytical instruments that I used at Tufts! I also would like to thank Dr. Martin Hunter in biomedical engineering department for his informative discussion, great

trainings on all the spectroscopy facilities and his wonderful characterization laboratory course.

Studying at Tufts University has been a great pleasure of my life. The friendly environment and close academic relationship between students and faculty made it feel like my academic home. It was amazing to have family close by so far away from home. I would like to further thank all the faculty in chemical and biological engineering department at Tufts University as well as the nice and friendly staff. I also want to thank my colleagues, Papatya Kaner, Nelaka Govinna and Eric Liu and my undergraduate assistant, Jacob Kronenberg.

I would like to thank Tufts University, National Science Foundation (NSF) for Grant Nos. CBET-1553661 and CBET-1703549. Tufts University's Tufts Collaborates Seed Grant Program, and Tufts Institute of the Environment (TIE) Research Fellowship for supporting this research.

Last but not the least, I would like to express my deepest gratitude to my family: my parents, my sister and brothers for all their love and encouragement. Most of all, I want to thank my loving, encouraging and supportive better half, Mahdi, who has shared all the ups and downs of this wonderful journey with me, even across the oceans! THANK YOU!

Alin Sadeghi

Tufts university

April 2018

LIST OF PUBLICATIONS

Research Papers

1. Sadeghi, I., Govinna, N., Cebe, P., Asatekin, A., “*Superoleophilic and Robust Nanofibrous Membranes for Ultrafast Gravity-driven Oil/Water Separation Based on Surface Segregating Copolymer*”, Close to submission.

2. Sadeghi, I. Liu, E., Yi, H., Asatekin, A., “*Controlled Fabrication of Catalytically Active Ultrathin Hydrogel Selective Layers Containing Viral Templated Palladium Nanoparticles via Interfacially Initiated Free Radical Polymerization*”, Close to submission.

3. Sadeghi, I., Asatekin, A., “*Chemoselective Nanoporous Membranes for Aromaticity-Based Separation of Sub-nanometer Molecules*”, Close to submission.

4. Holding, S., Sadeghi, I., White, T., Murray, A., Asatekin, A., Lantagne, D., “*Acceptability, Effectiveness, and Fouling of Household Membrane Filters Distributed in South Sudan*”, Journal of Water, Sanitation and Hygiene for Development, Submitted to Journal of Water Sanitation and Hygiene for Development.

5. Sadeghi, I., Yi, H., Ayse, A., “*A Method for Manufacturing Membranes with Ultrathin Hydrogel Selective Layers for Protein Purification: Interfacially Initiated Free Radical Polymerization (IIFRP)*”, Chemistry of Materials, 30, 4, (2018), 1265-1276.

6. Sadeghi, I., Kronenberg, J., Asatekin, A., “*Selective Transport through Membranes with Charged Nanochannels Formed by Scalable Self-Assembly of Random Copolymer Micelles*”, ACS Nano, 12, 1, (2017), 95-108; ***selected to be featured in ACS Editors' Choice.***

- Featured in R&D magazine, Feb., 2018;

- Featured in Chemical Engineering magazine, Mar., 2018.

7. **Sadeghi, I.**, Asatekin, A., “*Spontaneous Self-Assembly and Micellization of Random Copolymers in Organic Solvents*”, *Macromolecular Chemistry and Physics*, 218, 20, (2017).

Review Papers

1. **Sadeghi, I.**, Asatekin, A., “*Chemoselective Membranes for Separation of Small Molecules*”, in preparation.

2. Kaner, P., Bengani, P., **Sadeghi, I.**, Asatekin, A., “*Responsive filtration membranes by polymer self-assembly*”, *Technology*, (2016), 1-12.

TABLE OF CONTENTS

1 INTRODUCTION.....	1
1.1. Chemical Selectivity	2
1.1.1. Challenge: Separation of Small Molecules by Chemical Structure	2
1.1.2. Inspiration and Selectivity Mechanism: Biological Pores.....	3
1.1.3. Transport Modulation by Chemically Functional Nanostructures	5
1.1.4. Approaches for Fabrication of Chemoselective Membranes	6
1.1.4.1. Top-down approaches.....	6
1.1.4.2. Bottom-up approaches	10
1.1.4.2.1. Self-assembly of organic materials	10
1.1.4.2.2. Copolymer self-assembly.....	12
1.2. Fabrication of Ultrathin Selective Layers	15
1.2.1. Commercial Thin Film Composite Membranes	15
1.2.2. Hydrogels.....	17
1.2.3. Existing Methods for Fabrication of Hydrogel Layers.....	17
1.2.3.1. Membrane selective layers by coating.....	18
1.2.3.2. Membrane selective layers by grafting	18
1.3. Dissertation Outline.....	19
2 SELECTIVE TRANSPORT THROUGH MEMBRANES WITH CHARGED NANOCHANNELS FORMED BY SELF-ASSEMBLY OF RANDOM COPOLYMER MICELLES.....	21
2.1. Introduction	21
2.2. Materials and Methods.....	26
2.2.1. Materials	26
2.2.2. Polymer Synthesis and Characterization	27
2.2.3. Characterization of micelles	28
2.2.4. Membrane Fabrication and Characterization	30
2.2.5. Characterization of Membrane Performance.....	31
2.3. Results and Discussion.....	34
2.3.1. Copolymer Synthesis and Characterization.....	34

2.3.2. Micelle Formation	37
2.3.2.1. Micelles in methanol.....	38
2.3.2.2. Micelles in THF	41
2.3.2.3. Micelles morphology in a thin film	43
2.3.2.4. Interaction of dissolved metal ions with micelles.....	44
2.3.3. Formation of packed micelle arrays	51
2.3.4. Membrane Formation and Morphology	54
2.3.5. Membrane Performance	60
2.3.5.1. Effect of copolymer composition on membrane permeability	61
2.3.5.2. Effect of pH on membrane permeance	62
2.3.5.3. Diffusion experiments: charge-based selectivity between organic solutes	63
2.3.5.3.1. Single-solute diffusion experiments.....	63
2.3.5.3.2. Competitive diffusion experiments	70
2.3.5.4. Rejection of organic solutes in filtration experiments	72
2.3.5.4.1. Single-solute filtration experiments	72
2.3.5.4.2. Separation of two-solute mixtures based on solute charge	74
2.3.5.5. Effect of Ionic Strength on Organic Solute Rejection	75
2.3.5.6. Salt rejection and rejection mechanism	78
2.4. Conclusions	81
3 CHEMOSELECTIVE NANOPOROUS MEMBRANES FOR AROMATICITY-BASED SEPARATION OF SMALL MOLECULES	83
3.1. Introduction	83
3.2. Materials and Methods	88
3.2.1. Materials	88
3.2.3. Membrane Fabrication and Characterization	90
3.2.4. Membrane Functionalization.....	90
3.2.5. Characterization of Membrane Performance.....	91
3.2.5.1. Filtration experiments	91
3.2.5.2. Diffusion experiments.....	92
3.2.6. Quartz Crystal Microbalance with Dissipation (QCM-D) Studies.....	93

3.2.6.1. Preparation and coating of the quartz crystal sensor	93
3.2.6.2. Measuring coating layer thickness	94
3.2.6.2. Adsorption/Desorption of solute on the selective layer	95
3.3. Results and Discussion.....	95
3.3.1. Copolymer Synthesis and Unfunctionalized Membrane Formation	95
3.3.3. Selection of Surface Functionality and Membrane Functionalization .	96
3.3.4. Solute/Pore Wall Interactions that Control Permeation	103
3.3.5. Membrane Permeance	105
3.3.5.1. Water permeance: pressure-driven filtration	105
3.3.5.2. Permeation of Aromatic and Non-Aromatic Organic Molecules	107
3.3.5.2.1. Single-solute diffusion experiments.....	107
3.3.5.2.1. Competitive diffusion experiments	110
3.4. Conclusions	114
4 A NOVEL METHOD FOR FABRICATION OF ULTRATHIN SELECTIVE LAYERS: INTERFACIALLY INITIATED FREE RADICAL POLYMERIZATION (IIFRP)	116
4.1. Introduction	116
4.2. Materials and Methods	121
4.2.1. Materials	121
4.2.2. Fabrication of Ultrathin Hydrogel Layer.....	122
4.2.3. Membrane Characterization	122
4.2.4. Membrane Performance.	123
4.3. Results and Discussion.....	125
4.3.1. Hydrogel Layer Morphology.....	125
4.3.2. Chemical Structure of the Hydrogel Layer.....	130
4.3.3. Membrane Permeation Properties	133
4.3.4. Membrane Selectivity and Protein Rejection	137
4.3.5. Effect of Drying on Membrane Performance	139
4.3.6. Effect of Monomer Solution Composition on Membrane Selectivity and Permeance	140
4.3.7. Fouling Resistance.....	147
4.4. Conclusions	149

5 CONCLUSIONS AND FUTURE PROSPECTS.....	152
APPENDICES	161
A1 SELECTIVE TRANSPORT THROUGH MEMBRANES WITH CHARGED NANOCHANNELS FORMED BY SELF-ASSEMBLY OF RANDOM COPOLYMER MICELLES.....	161
A1.1. Documentation of Hydrogen Bonding in Methanol Using FTIR Spectroscopy	161
A1.2. Effect of Metal Ions on Micelle Size Quantified by DLS	162
A1.3. Characterization of Complexation Geometries Using UV-vis and FTIR Spectroscopy	163
A1.4. Effect of Solvent Evaporation Time on Membrane Morphology	165
A1.5 Effect of Support Membrane Surface Morphology.....	165
A1.6. Determination of the Micelle Size Distribution from FESEM Images ..	167
A1.7. Membrane Pore Size Estimation	169
A2 CHEMOSELECTIVE NANOPOROUS MEMBRANES FOR AROMATICITY-BASED SEPARATION OF SMALL MOLECULES	172
A2.1. Selective layer thickness measurement with QCM-D.....	172
A2.2. Adsorption/Desorption of Hormones on the Selective Layer	173
REFERENCES.....	177

LIST OF FIGURES

Figure 1. 1. Structures and operating mechanism of three biological pores: (a) A bacterial porin trimer showing three pores $\sim 7\text{-}11 \text{ \AA}$ in size, (b) Maltoporin monomer bound to maltotriose (black), showing the interaction between the sugar molecule and pore walls. Reproduced with permission from ¹⁶. Copyright © 1998, Academic Press. (c) A model of operation for the nuclear pore complex, regulated by binding and unbinding interactions between phenylalanine-glycine domains and the carrier proteins. Reprinted with permission from ¹⁷. Copyright © 2007, American Association for the Advancement of Science. 5

Figure 1. 2. Effect of solute-wall interaction on transport features. 6

Figure 1. 3. Top-down approaches for fabrication of chemoselective membranes; (a) Electroless plating to form gold nanotube membrane and their functionalization with self-assembled thiol monolayers; reprinted with permission from²⁶. Crown copyright © 2008 Published by Elsevier B.V. (b) Chemical modification of porous anodic alumina membrane by atomic layer deposition of silica, subsequent hydroxylation step by water plasma and functionalization by fluorinated silane; reprinted with permission from³⁵. Crown copyright © 2009 Published by Elsevier B.V. (c) Polymer self-assembly within a track-etched polycarbonate membrane, PCTE, by functionalizing the membrane with a PVP layer, followed by immersion in SnCl_2 and filtration of an anionic polymer; reprinted with permission from³⁸. Copyright © 2008, Springer Nature and (d) Initiated chemical vapor deposition approach to narrow down pores of a PCTE membrane; reproduced in part (with modification) with permission from³⁹. Copyright © 2017, Springer Nature. 9

Figure 1. 4. Self-assembly approaches for fabrication of chemoselective membranes; (a) A glass filter, hybrid membrane consisting of nanoparticle-dendrimer composites, reprinted with permission from⁴⁰. Copyright © 2012, John Wiley and Sons. (b) Formation of a TFC membrane using an imidazolium-based LLC monomer, reproduced with permission from⁵⁴. Copyright © 2012, American Chemical Society. (c) Directed co-assembly of cyclic peptide and a block copolymer, reproduced with permission from⁴⁹. Copyright © 2011, American Chemical Society, and (d) Self-assembly of crown ether amphiphiles into columnar structure and formation of oriented matrix-fixed supramolecular channel, reproduced with permission form⁵⁵. Copyright © 2000, John Wiley and Sons..... 12

Figure 1. 5. Examples of phase-separated morphologies in A–B type diblock copolymers. Various morphologies are observed as the fraction of the A block (f_A) increases, such as spherical (S), cylindrical (C), gyroidal (G) and lamellar (L), reprinted with permission from⁵⁶. Copyright © 2009, Springer Nature. 14

- Figure 2. 1. ^1H NMR spectrum of CP40 deuterated DMSO showing the characteristic peaks and corresponding protons. a, and d peaks are used to calculate copolymer composition. Reprinted with permission from¹⁷¹. Copyright © 2017, John Wiley and Sons..... 36
- Figure 2. 2. TEM micrographs of supramolecular structures formed by P(TFEMA-*r*-MAA) prepared with 0.3 wt% copolymer in solution. (a, b) Micelles and vesicles formed in methanol; (c, d) Reverse micelles in THF, exhibiting the onset of morphological transition from sphere to rods; (e, f) Micelles and vesicles formed in methanol in the presence of $\text{Cu}(\text{OAc})_2$ in polymer solution. All samples were stained by immersion in 0.5 wt% of $\text{Cu}(\text{OAc})_2$ in water after preparation to identify carboxylic acid groups. Reprinted with permission from¹⁷¹. Copyright © 2017, John Wiley and Sons..... 40
- Figure 2. 3. DLS micelle size distribution for CP40 and CP50 in (a) Methanol, and (b) THF. Reprinted in part with permission from¹⁷¹. Copyright © 2017, John Wiley and Sons..... 40
- Figure 2. 4. Determination of CMC by DLS in (a) Methanol and (b) THF. Reprinted with permission from¹⁷¹. Copyright © 2017, John Wiley and Sons..... 43
- Figure 2. 5. Micelles cast from copolymer solution of (a) 0.3 wt% in methanol, (b) 0.1 wt% in methanol, and (c) 0.3 wt% in THF on mica. Reprinted with permission from¹⁷¹. Copyright © 2017, John Wiley and Sons..... 44
- Figure 2. 6. DLS micelle size distribution for 0.5 w% micellar solutions in methanol (a) with Na^+ added in methanol, $r=20$, and (b) with Cu^{2+} added, $r=20$; r is defined as the molar ratio of MAA groups to metal ions in solution. Reprinted with permission from¹⁷¹. Copyright © 2017, John Wiley and Sons..... 46
- Figure 2. 7. FTIR spectra for the copolymer and its solutions in methanol with the addition of different metal ions at increasing concentrations. Reprinted with permission from¹⁷¹. Copyright © 2017, John Wiley and Sons..... 47
- Figure 2. 8. UV-visible spectra showing the complexation of carboxylate with Cu^{2+} ions; $\text{Cu}(\text{OAc})_2$ in methanol is shown by dotted line, dash line corresponds to the copolymer solution with $\text{Cu}(\text{OAc})_2$ in methanol at $r=50$, and solid line shows the copolymer solution with $\text{Cu}(\text{OAc})_2$ at $r=20$. Reprinted with permission from¹⁷¹. Copyright © 2017, John Wiley and Sons..... 50
- Figure 2. 9. TEM images of the P(TFEMA-*r*-MAA) micelle assemblies cast from a solution in methanol by immersion into water after (a) No evaporation time (b) 10 s evaporation and (c) 20 s evaporation. The insets in (a) and (b) show higher magnification images (scale bar: 100 nm) of the smaller ~ 20 nm micelles, in isolation or in clusters. Large vesicles and small isolated micelles cluster form packed

assemblies upon solvent evaporation. Reprinted from ¹⁷⁰ . Copyright © 2017 American Chemical Society.	53
Figure 2. 10. SEM micrographs of (a) PAN 400 support membrane surface morphology, (b) CP40 membrane surface morphology, (c) CP50 membrane surface morphology, (d,g) PAN 400 cross section, (e, h) CP40 cross section, (f, i) CP50 cross section. Both CP40 and CP50 coated membranes exhibit packed arrays of micelles, interstices between which act as permeation pathways. Reprinted from ¹⁷⁰ . Copyright © 2017 American Chemical Society.	56
Figure 2. 11. (a) AFM height image of CP40 membrane (10 μm× 10 μm with z-range of 200 nm), showing spherical micelles packed in a hexagonal close packed (HCP) array with few irregular polygons (b) 2D FFT pattern corresponding to AFM height image (c) FFT analysis; dash markings correspond to $(q/q^*)^2 = 1, 3, 3.7$ showing almost 2D HCP structure. Reprinted from ¹⁷⁰ . Copyright © 2017 American Chemical Society.	58
Figure 2. 12. Effect of pH on permeance of CP40 coated membrane, pH was adjusted by HCl or NaOH. Reprinted from ¹⁷⁰ . Copyright © 2017 American Chemical Society.	63
Figure 2. 13. Structure and solubility parameters of organic molecules; molecule size is calculated using Molecular Modeling Pro. Reprinted from ¹⁷⁰ . Copyright © 2017 American Chemical Society.	65
Figure 2. 14. Diffusion of organic molecules through support membrane in (a) Single-solute, and (b) Competitive diffusion experiment. Reprinted from ¹⁷⁰ . Copyright © 2017 American Chemical Society.....	67
Figure 2. 15. The permeation of organic molecules through (a,c) CP40- and (b,d) CP50-coated membranes in (a,b) Single-solute and (c,d) Competitive diffusion experiments for a mixture of negative and neutral solutes. Selectivity between neutral RIB and anionic AB45 is enhanced in competitive diffusion experiments, as the permeation rate of AB45 through both CP40- and CP50-coated membranes is shifted below the detection limit. N is defined as the total number of moles of solute transferred divided by feed concentration. Reprinted from ¹⁷⁰ . Copyright © 2017 American Chemical Society.	68
Figure 2.16. Rejections of organic molecules by the (a) CP40, and (b) CP50 coated membranes. Negatively charged solutes (from left to right: MO, AB45, CAL, BBR) are rejected by >85%, whereas low rejections are observed for neutral (from left to right: RIB, RTH, B12) and cationic solutes (from left to right: BB3, Rho6G) of similar size. Reprinted from ¹⁷⁰ . Copyright © 2017 American Chemical Society.....	74
Figure 2.17. Separation of mixture of negative and neutral molecules (a) RIB and AB45 for CP40, (b) BBR and Vitamin B12 for CP40, (c) RIB and AB45 for CP50, (d) BBR and Vitamin B12 for CP50. Reprinted from ¹⁷⁰ . Copyright © 2017 American Chemical Society.	75

- Figure 2.18. Effect of ionic strength on dye rejection of the CP40 membrane, consistent with selectivity driven by electrostatic interactions. Reprinted from¹⁷⁰. Copyright © 2017 American Chemical Society..... 77
- Figure 2. 19. Rejection of four salts at different concentrations by the CP40 coated membrane. Bars denote experimental data, and filled symbols show values calculated by fitting the Donnan model using a single parameter, C_{mx} , obtained 3.65 mM. Reprinted from¹⁷⁰. Copyright © 2017 American Chemical Society. 79
- Figure 3. 1. FTIR spectra of (a) membrane before and after EDC/NHS activation; (b) deconvolution of the carbonyl stretching region of the activated membrane; NHS-ester and anhydride intermediates were formed..... 101
- Figure 3. 2. (a) Infrared spectra of unfunctionalized and functionalized membranes. Formation of new amide bonds upon functionalization confirms covalent attachment of amino compounds. SEM micrographs of (b) Membrane cross section, and (c) Membrane surface; showing the packed micelle structure is intact upon membrane functionalization. 102
- Figure 3. 3. Frequency shift upon injection of hormones for unfunctionalized and functionalized films. 105
- Figure 3. 4. Diffusion of steroid hormones through support membrane (PAN400) in (a) Single-solute, and (b) Competitive diffusion experiment. 108
- Figure 3.5. Permeation of steroid hormones through (a,e) Unfunctionalized and (b,f) TYR-functionalized and (c,g) ACP-functionalized membrane in (a-c) single-solute and (e-g) Competitive diffusion experiments. Permeation flux and selectivity in (d) Single-solute, and (h) Flux in competitive diffusion experiments. All experiments demonstrate aromaticity-driven selectivity. The selectivity pattern is switched in competitive experiments. 113
- Figure 4. 1. Membrane prepared using single phase aqueous solution containing 40 v/v% PEGDA and 1 wt% water-soluble PI (Irgacure 2959) showing formation of a very thick and non-uniform hydrogel layer on the PS support. Reproduced with permission from³³³. Copyright © 2018, American Chemical Society..... 126
- Figure 4. 2. Morphology of (a) Support membrane, PS, (b) Higher magnification of PS support, (c) Hydrogel layer at 5 min UV exposure time (d) Higher magnification of hydrogel at 5 min UV exposure time, (e) Hydrogel layer after 10 min UV exposure time, (f) Hydrogel layer at 10 min UV exposure time at higher magnification. Continuous and uniform hydrogel layers are formed on the support membrane upon exposure to UV at varying times. Longer UV exposure time leads to formation of a

thicker layer. Reproduced with permission from ³³³ . Copyright © 2018, American Chemical Society.	127
Figure 4. 3. Photograph of a smooth hydrogel (5 v/v% PEGDA-5 min UV exposure) transferred to a wire lasso. Reproduced with permission from ³³³ . Copyright © 2018, American Chemical Society.	129
Figure 4. 4. FESEM image of a membrane formed with 20 min UV exposure time, with a thicker hydrogel layer. Reproduced with permission from ³³³ . Copyright © 2018, American Chemical Society.	130
Figure 4. 5. (a) Chemical structure of PEGDA and PS, (b) ATR-FTIR spectra of PS support membrane (bottom) and coated with an ultra-thin hydrogel layer (top) with 5 min UV exposure. Absorption bands corresponding to CH (blue) and ester (pink) groups are marked to demonstrate the formation of a cross-linked PEGDA hydrogel selective layer in the PS support. Reproduced with permission from ³³³ . Copyright © 2018, American Chemical Society.	132
Figure 4. 6. Effect of transmembrane difference on flux for hydrogel membrane prepared with monomer solution containing 5 v/v% PEGDA, 2.5 v/v% PEG200. Reproduced with permission from ³³³ . Copyright © 2018, American Chemical Society.	133
Figure 4. 7. Effect of UV exposure time on membrane permeance; all membranes are prepared with monomer solution containing 5% PEGDA and 2.5% PEG200. Significant difference between the permeance of the support membrane and hydrogel-coated membranes indicates the formation of the hydrogel layer, with permeances depending on UV exposure time. Reproduced with permission from ³³³ . Copyright © 2018, American Chemical Society.....	135
Figure 4. 8. Rejection properties of hydrogel-coated membranes. The PS support membrane shows limited rejection for all three proteins, whereas cross-linked PEGDA coated membranes prepared by IIFRP reject Cytochrome C and BSA by >90%, indicating a MWCO around 8-10 kDa. Reproduced with permission from ³³³ . Copyright © 2018, American Chemical Society.	138
Figure 4. 9. Effect of PEGDA concentration on membrane permeance. Error bars indicate the range of permeances obtained for a minimum of three samples.....	141
Figure 4. 10. Membrane prepared with monomer solution containing 10 v/v% PEGDA and 5 min UV exposure time; a thicker layer is formed compared to monomer solution with 5 v/v% PEGDA at same UV exposure time. Reproduced with permission from ³³³ . Copyright © 2018, American Chemical Society.	142
Figure 4. 11. Long-term fouling resistance of hydrogel-coated membrane upon exposure to a model protein (BSA) solution. Tests performed in a cross-flow set up at a TMP of 40 psi; flux is normalized by average initial water flux. Hydrogel-coated is	

extremely fouling resistant suitable for protein purification. Reproduced with permission from ³³³ . Copyright © 2018, American Chemical Society.	149
Figure A1. 1. FTIR spectra of the copolymer solution in methanol and solid copolymer powder. Yellow highlighted regions correspond to hydrogen bonding between copolymer and methanol.....	162
Figure A1. 2. UV-visible spectra of the copolymer solution with CuCl ₂	164
Figure A1. 3. FTIR spectra of copolymer solution in methanol in presence of CuCl ₂ and CaCl ₂	164
Figure A1. 4. Effect of solvent evaporation time on selective layer structure of CP50-coated membrane (a) 20 s and (b) 120 s evaporation time.....	165
Figure A1. 5. Surface morphology of (a) PVDF 400R (MWCO: 250K), (b) PAN 400 (MWCO: 200K), (c,e) cross-section of PVDF 400R support membrane, (d,f) Cross-section of PVDF 400R membrane coated with CP40 polymer. No coating is visible when PVDF 400R was used as the support membrane.....	166
Figure A1. 6. 1. Micelle size distributions for (a) CP40 and (b) CP50 membranes; calculated using Image J software.	167
Figure A1. 7. HCP structure and pore geometry.....	169
Figure A1. 8. Lattice parameters for HCP structure.	171
Figure A2. 1. Representative vibration frequency of the bare sensor (open symbols), and coated sensor (solid symbols) at n=3. The change in frequency is directly correlated with the mass of selective layer.	173
Figure A2. 2. Frequency shift vs. time upon injection of hormones for unfunctionalized and (A) TYR-Functionalized, (B) ACP-Functionalized membranes at n = 3. The change in frequency for PREG and ESTR is shown with blue and pink arrows, respectively for both functionalized membranes.	176
Scheme 2. 1. Formation mechanism of the membrane selective layer featuring charged nanochannels. Reprinted from ¹⁷⁰ . Copyright © 2017 American Chemical Society..	26
Scheme 2. 2. Synthesis scheme for P(TFEMA- <i>r</i> -MAA). Reprinted with permission from ¹⁷¹ . Copyright © 2017, John Wiley and Sons.	34

Scheme 2. 3. The effect of metal ions on micelle size and morphology; (a) Micelle morphology in MeOH, (b) in presence of Na(OAc), (c) Formation of micelle clusters in presence of Cu(OAc)₂, (d) Transition from micelle to vesicle by addition of Cu(OAc)₂, and (e) Inter-micellar bridging by Cu²⁺. Reprinted with permission from¹⁷¹. Copyright © 2017, John Wiley and Sons..... 46

Scheme 3. 1. (a) Polymer chemistry, (b) Membrane structure, (c) Membrane nanopores lined with COOH groups (unfunctionalized membrane); and (d) Functionalized membrane selectivity mechanism in a competitive diffusion experiment. 87

Scheme 4. 1. Schematic showing fabrication of membranes with ultra-thin hydrogel selective layers by interfacially initiated free radical polymerization (IIFRP).* Reproduced with permission from³³³. Copyright © 2018, American Chemical Society. 120

LIST OF TABLES

Table 2. 1. Compositions, molecular weights, water uptake values of synthesized copolymers, membrane pore size, membrane pore density, membrane permeance, selective layer permeability and water contact angle values. Reprinted from ¹⁷⁰ . Copyright © 2017 American Chemical Society.	35
Table 2.2. Solute transfer rates and separation coefficients (α) for PAN400, CP40 and CP50 membranes in single-solute and competitive diffusion experiments. Reprinted from ¹⁷⁰ . Copyright © 2017 American Chemical Society.	66
Table 2. 3. Static adsorption experiments for support membrane, CP40 and CP50. Reprinted from ¹⁷⁰ . Copyright © 2017 American Chemical Society.	70
Table 3. 1. Structure, size and van Krevelen solubility parameters of organic molecules used in this study.	98
Table 4. 1. Effect of comonomer/porogens as additives in monomer solution on hydrogel-coated membranes' permeance and rejection properties. Reproduced with permission from ³³³ . Copyright © 2018, American Chemical Society.	144
Table 5. 1. Comparison of the work described here with other membranes for charge-based separation of small organic molecules reported in literature.	154
Table 5. 2. Comparison of our approach with alternative TFC membrane preparation techniques.	158
Table A1. 1. Effective hydrodynamic diameters measured in P(TFEMA- <i>r</i> -MAA) solutions in methanol in the presence of different metal salts.	163

1 INTRODUCTION

Overview

Membrane separations are green, energy efficient and easy to implement in comparison to other separation processes such as distillation, extraction and chromatography. They are used in a wide array of applications, from water treatment,¹⁻³ gas separation⁴ to the purification of biopharmaceuticals⁵ to the food industry.⁶ Despite wide range of applications, there still remain two main challenges toward broadening membrane applications and replacing the more energy-intensive separation processes. First, the applicability of membranes is often limited to removal of all solutes above a given size from a feed stream (i.e. size-based separation). While there are number of methods to impart chemical selectivity to membranes, their complex and time-consuming fabrication procedure as well as low permeation prevents them from commercialization. In this dissertation, these challenges are addressed by developing highly selective and permeable membranes in a simple and scalable manner using polymer self-assembly.

Second, despite the diversity in membrane applications, membranes today are made of only a handful of polymer chemistries (e.g. thin film polyamide, PA) due to limited scalable and simple fabrication methods. Most thin film composite (TFC) membranes on the market feature interfacially-polymerized (IP) cross-linked polyamide selective layers.⁷⁻⁸ This method creates a very thin selective layer using a simple, scalable roll-to-roll process, resulting in high flux, but is limited to a

narrow range of polymer chemistries. Furthermore, IP also generates a highly cross-linked and dense layer that limits the application of this method to desalination and reverse osmosis (RO). In this dissertation, these challenges are overcome by developing a novel method that enables fabrication of ultrathin selective layers from a wide range of monomer chemistries in a simple and reliable manner. It also provides an easy approach for incorporation of different nanomaterials within the selective layer, enabling fabrication of multifunctional selective layers.

Developing membranes possessing new features (e.g. chemical selectivity, catalytic activity, etc.) can have a great impact in broadening the scope where membranes are utilized. This introductory chapter describes the fabrication methods that have been utilized for fabrication of chemoselective membranes. It also explains the methods that have been exploited to make ultra-thin layer with a focus on hydrogel layers. Lastly, an outline of this dissertation is provided at the end of this chapter.

1.1. Chemical Selectivity

1.1.1. Challenge: Separation of Small Molecules by Chemical Structure

Separation processes account for 45% of energy used by chemical and petroleum industries.⁹ Separation of small molecules is especially energy-intensive, often conducted by distillation, extraction or chromatography.¹⁰ In contrast, membrane filtration is energy efficient, simple, and requires no additional chemicals.¹¹ However, membranes today can only separate solutes based on their size. Membranes capable of more challenging separations, with selectivity

controlled not only by size but also chemical features, could significantly expand the applications where membrane technology is used. These separations are not feasible using current membrane technologies that rely solely on either morphology (i.e. pore size) or the chemistry of a thin homogeneous polymer layer (e.g. cross-linked polyamide selective layers of RO and NF membranes, gas separation membranes). Thus, there is an urgent need for membranes that can separate small organic molecules that are of similar size but have different chemical structures – a task that current filtration membranes cannot achieve. The development of such membranes would be a transformative step that can potentially replace energy-intensive separation processes with membrane systems, making the overall processes more sustainable and energy-efficient. Such membranes could potentially replace more energy-intensive unit operations such as distillation, extraction and chromatography, significantly improving the environmental profile of chemical processing.

1.1.2. Inspiration and Selectivity Mechanism: Biological Pores

For devising such new membranes, it is important to view membrane as more than a passive filter and gain a better understanding of structure-property relationships regarding how polymer chemistry and nanostructure affect membrane-solute interactions and subsequently its separation performance especially when the nanostructure size is comparable with solute size.¹²

Commercial separation membranes operate either based on a sieving mechanism, or on a solution-diffusion mechanism where the solubility and

diffusivity in the membrane selective layer controls permeation.¹³ The first treats the membrane material as an inert structure. The latter relies on bulk properties (solubility and diffusivity) for separation.

In contrast, nature uses nanostructure and chemical functionality synergistically to modulate transport of specific molecules or ions into and out of the cell with great efficiency and selectivity. Biological pores feature a constricted pore comparable in diameter to the target compound, and functional groups lining the pore that interact with the target, Figure 1.1.¹⁴⁻¹⁶ The nanostructure constricts flow and confines all components passing through, forcing them to interact with the chemically functional walls. The solute that interacts favorably and reversibly with the nanochannels is preferentially partitioned into the nanopores, which prevents the entry of other solutes. In fact, nature utilizes nanoconfinement and chemical functionality, which bring about superior selectivity and permeability for the target solute. The mechanism is valid only if the interactions are reversible; otherwise solutes are stuck in a channel and prevent permeation through it. Models propose a hopping mechanism through the pore, emphasizing the need for reversible interaction.¹² This mechanism suggests that fabrication of membranes with exceptional selectivity and permeability may be possible by engineering nanostructure and functionality, leading to facilitated transport of specific solutes.

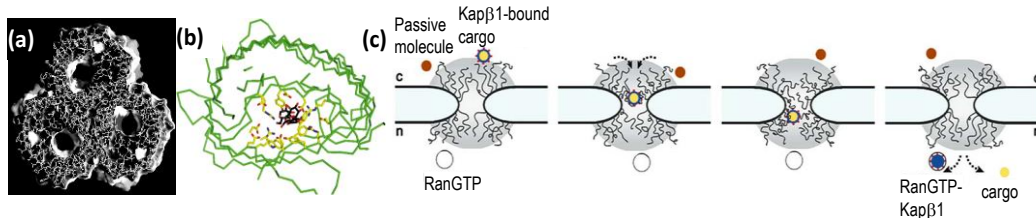


Figure 1. 1. Structures and operating mechanism of three biological pores: (a) A bacterial porin trimer showing three pores $\sim 7\text{-}11 \text{ \AA}$ in size, (b) Maltoporin monomer bound to maltotriose (black), showing the interaction between the sugar molecule and pore walls. Reproduced with permission from ¹⁶. Copyright © 1998, Academic Press. (c) A model of operation for the nuclear pore complex, regulated by binding and unbinding interactions between phenylalanine-glycine domains and the carrier proteins. Reprinted with permission from ¹⁷. Copyright © 2007, American Association for the Advancement of Science.

1.1.3. Transport Modulation by Chemically Functional Nanostructures

Solute-polymer interactions have crucial effects in membrane separations. If a sieving style separation is desired, polymer-solute interactions need to be avoided, because they cause fouling (Figure 1.2).¹⁸⁻¹⁹ Strong interactions are desired for chromatography and adsorption, but this also means solutes are simply adsorbed on channel walls and do not permeate.²⁰ Improved transport can potentially be achieved in the intermediate range, where solutes associate and dissociate repeatedly with the functional groups in the channel.¹² However, if polymer-solute interactions are selective and reversible, and if the pore size is only slightly larger than the solute size, facilitated transport can potentially be achieved.^{12, 14} The solute that reversibly interacts with the nanochannels is preferentially partitioned into the nanopore, which prevents the entry of other solutes. Then, it moves from interacting site to interacting site.¹² This leads to exceptional selectivity. Selectivity decreases as pore size increases. The mechanism is valid only if the interactions are reversible; otherwise solutes are stuck in a channel and prevent permeation through

it.¹² This means that using engineered nanostructure and functionality, we can make membranes with exceptional selectivity. The challenge is to achieve such structures using scalable manufacturing methods.

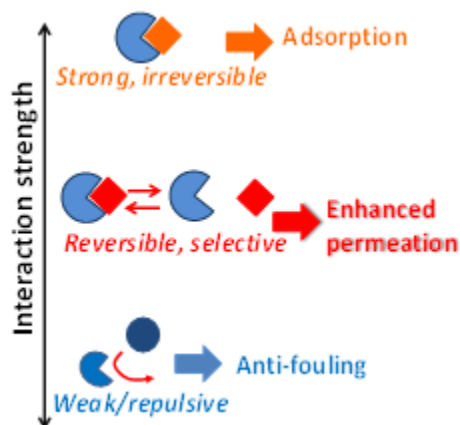


Figure 1. 2. Effect of solute-wall interaction on transport features.

1.1.4. Approaches for Fabrication of Chemoselective Membranes

1.1.4.1. Top-down approaches

Attempts have been made to mimic these biological channels and incorporate chemical functionality into artificial nanochannels by generating functionalized nanopores and documenting differences in the transport rate of solutes of similar size but differing chemical features. To date, most attempts to create functionalized nanochannels have focused on narrowing and modifying the pores of track-etched (TE) or anodized alumina membranes, which feature cylindrical through-pores down to 20 nm in diameter. The pioneering work by Martin and coworkers, which includes the electroless deposition of gold onto pore walls, is one of the most reliable methods currently available to tune the pore size and membrane pore chemistry. In this approach, after narrowing down the pores to a desired pore size

by electroless deposition of gold, the membrane is treated with thiols carrying the desired functionality to form self-assembled monolayer (SAM) within the membranes' pores. Gold nanotube membranes have been used for small molecule separation based on size, charge, hydrophobicity, and chirality.²¹⁻²⁸ They also have been examined for protein and DNA separations and sensing applications.²⁹⁻³²

Commercial and widespread application of gold nanotube membranes is however limited because of their complex and lengthy (>24 h) manufacturing method. The process involves using toxic chemicals and heavy metal salts such as AgNO_3 , SnCl_2 , and $\text{Na}_3\text{Au}(\text{SO}_3)_2$. More importantly, although this method provides precise pore size control, functionalization of these membranes is further challenged because of very slow formation of SAM within the nanopores. Moreover, the thiol functionalization of the gold surface inside the nanopores has often founds to be incomplete.³³ Furthermore, the electrical double layer formation due to presence of metal further complicates the prediction of separations.³³⁻³⁴

Another method for narrowing down the pores uses atomic layer deposition (ALD) within anodized aluminum oxide membrane (AAO) with SiO_2 , followed by silane treatment to functionalize the pores.³⁵⁻³⁶ This method requires temperatures over 200 °C for deposition. In this elevated temperature, most polymeric membranes undergo structural and morphological deformation, which makes them unusable for this method. Inorganic membranes, on the other hand, are quite fragile. This limits their applicability. Also, the diffusion selectivities reported for these membranes are not very high (~5.5).

Chemical vapor deposition (CVD) is another method in which monomers and initiator enters a chamber held under low vacuum as vapors. The substrate to be coated is placed on a chilled stage. The initiator is decomposed by interaction with a hot filament and reacts with the monomer adsorbed on the surface. Even though high diffusion selectivity is reported for membranes prepared with this method for hydrophobicity based separation,³⁷ CVD also has a number of disadvantages. It is still a long procedure. Furthermore, functionalization is limited to only volatile monomers. In addition, it requires cooling, heating (>150 °C) as well as a vacuum system which may make it difficult for scalable, roll-to-roll processing.

A simpler alternative for the functionalization of track-etched polycarbonate membranes exploits vacuum filtration of a polymer that self-assembles within membrane pores and narrows them down to a final pore size of 6-9 nm. Polymer binds to the pore walls through ionic interactions.³⁸ Polymers bearing different functionalities (charge density, size, and hydrophobicity) lead to different effective pore sizes and selectivities. While the method is simple, tunability of the pore size is not easy. The polymer structure determines the final pore size. Moreover, the range of functionalities that can be obtained is also limited. More importantly, the pore size is still too large for separation of small molecules leading to charge-based selectivity of up to about 3.

All these top-down approaches share one main disadvantage: they all have a very low porosity (<1% versus 70-90% for typical membranes). The porosity is further reduced during the coating process, yielding very low fluxes. This significantly limits their use in membrane separation applications at large-scale.

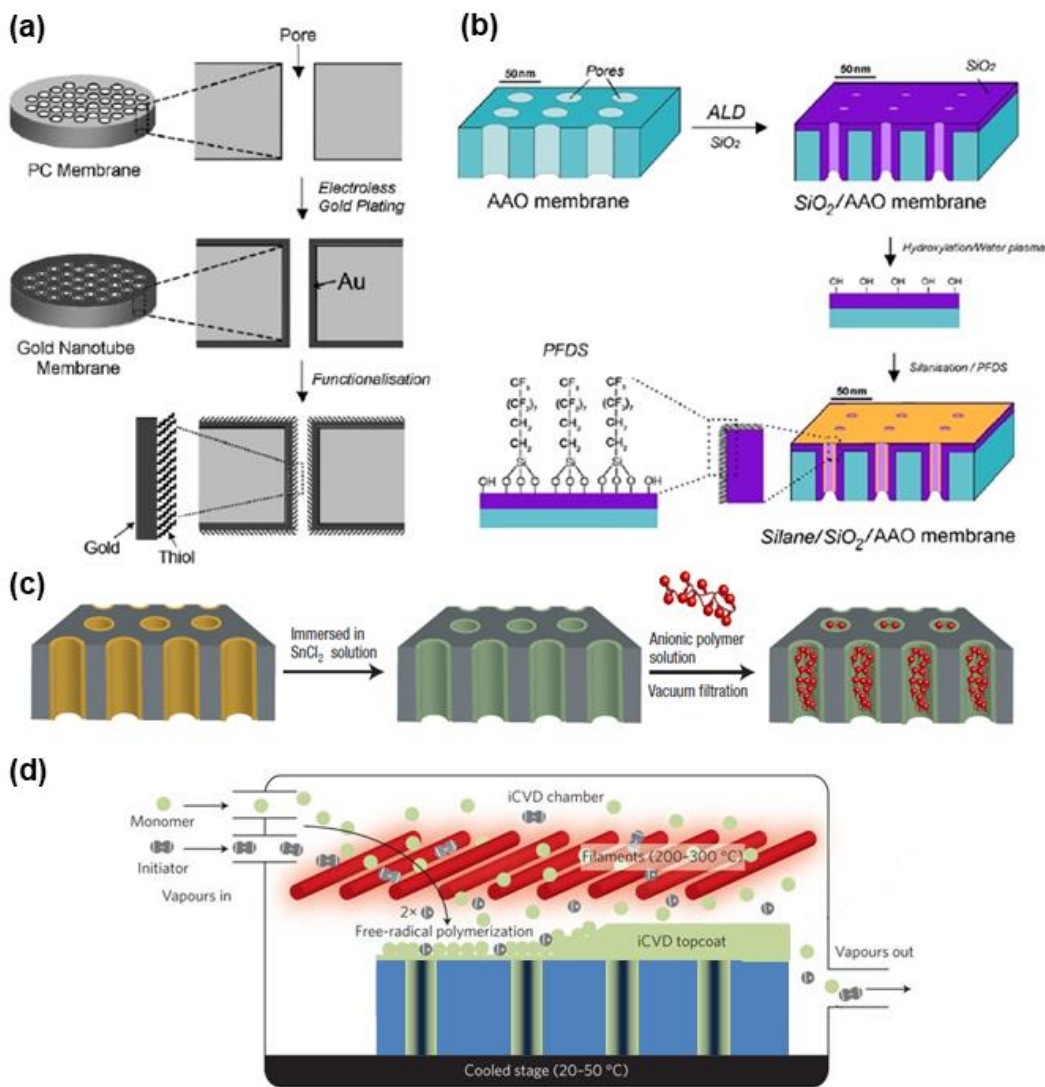


Figure 1. 3. Top-down approaches for fabrication of chemoselective membranes; (a) Electroless plating to form gold nanotube membrane and their functionalization with self-assembled thiol monolayers; reprinted with permission from²⁶. Crown copyright © 2008 Published by Elsevier B.V. (b) Chemical modification of porous anodic alumina membrane by atomic layer deposition of silica, subsequent hydroxylation step by water plasma and functionalization by fluorinated silane; reprinted with permission from³⁵. Crown copyright © 2009 Published by Elsevier B.V. (c) Polymer self-assembly within a track-etched polycarbonate membrane, PCTE, by functionalizing the membrane with a PVP layer, followed by immersion in SnCl₂ and filtration of an anionic polymer; reprinted with permission from³⁸. Copyright © 2008, Springer Nature and (d) Initiated chemical vapor deposition approach to narrow down pores of a PCTE membrane; reproduced in part (with modification) with permission from³⁹. Copyright © 2017, Springer Nature.

1.1.4.2. Bottom-up approaches

1.1.4.2.1. Self-assembly of organic materials

Bottom-up approaches to generating functional nanopores by self-assembly are simpler, more scalable and can offer a higher pore density and thus higher permeability. For example, composite membranes can be fabricated by immersing an amine-functionalized glass support membrane in a solution of gold nanoparticle, polyamidoamine dendrimers (PAMAM-Den) and carbon disulfide. This leads to the precipitation and cross-linking of the dendrimers and nanoparticles on the membrane surface. These dendrimer-nanoparticle (Den-NP) composite membranes provide permeation pathways in between the gold particles. Membrane pore size can be tuned by using different dendrimer generations (as low as 7 nm). Membrane functionality can be tailored with post-functionalization.⁴⁰ This approach is shown to be effective in charge-based separation of both small organic molecules and proteins, but due to the relatively large pore size, small molecule selectivities were significantly lower (separation factor of 4.2 for a pair of an anionic vs. cationic small molecule dyes versus 8.6 for a pair of proteins of opposite charges). Furthermore, all data reported on these membranes rely on diffusion experiments. Pressure-driven filtration performance of these membranes is not reported.

To reach smaller size scales, self-assembly of organic materials has been explored. For example, cross-linkable lyotropic liquid crystals (LLCs) have been used to form ordered hydrophilic phases that act as nanopores. This approach requires custom-synthesized surfactants and precise manufacturing conditions, but

recent progress has shown it can be applied in a roll-to-roll system to form composite membranes.⁴¹ This approach has been specifically studied for water desalination⁴²⁻⁴⁵ and chemical agent protection.⁴⁶ While the structure has the potential to be functionalized for other features, this has not yet been studied.

Another approach to membranes with small molecule selectivity involves the custom synthesis of cyclic peptides that form hydrogen-bonded nanotubules. These nanotubes, however, need to be embedded in a lipid membrane⁴⁷⁻⁴⁸ or a block copolymer (BCP) whose pores are aligned perpendicular to the film surface.⁴⁹ Self-assembly of crown ether amphiphiles into long, cylindrical channels have also been utilized to create small pores. Aligned carbon nanotubes have also been studied in similar contexts.⁵⁰⁻⁵³

In each of these cases, forming large scale membranes is difficult. These systems require custom synthesis of reagents (polymerizable amphiphiles or peptide rings) and are difficult to process into thin films with large area and proper alignment. Furthermore, there are limited options for functionalizing the nanopores due to limited stability and poor accessibility of functional groups during post-modifications. This means most of these systems are limited in type of separation they can perform.

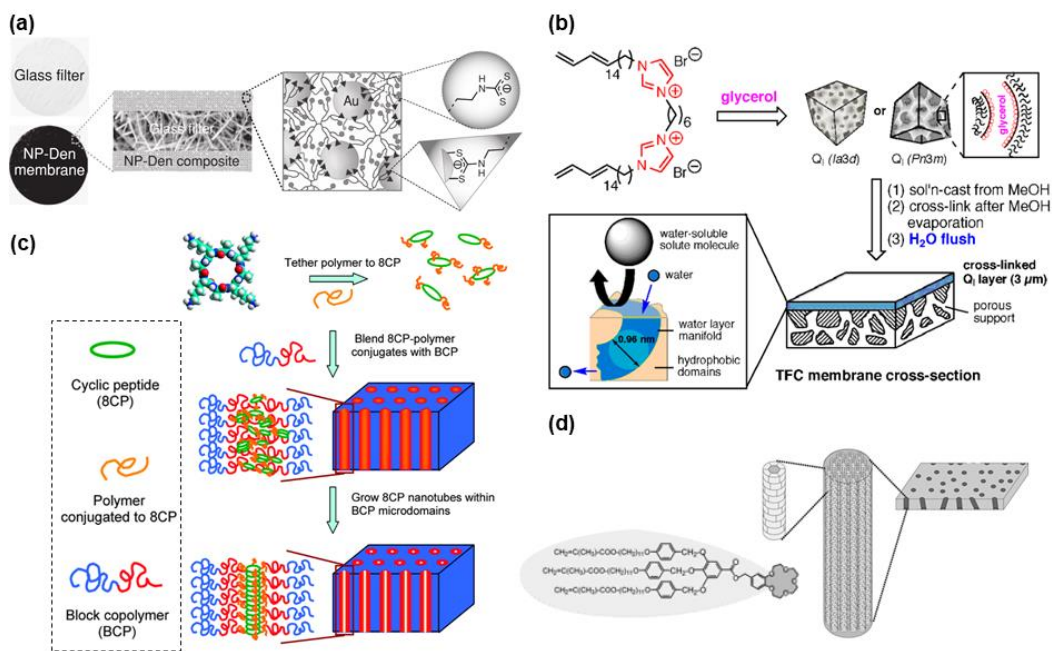


Figure 1. 4. Self-assembly approaches for fabrication of chemoselective membranes; (a) A glass filter, hybrid membrane consisting of nanoparticle-dendrimer composites, reprinted with permission from⁴⁰. Copyright © 2012, John Wiley and Sons. (b) Formation of a TFC membrane using an imidazolium-based LLC monomer, reproduced with permission from⁵⁴. Copyright © 2012, American Chemical Society. (c) Directed co-assembly of cyclic peptide and a block copolymer, reproduced with permission from⁴⁹. Copyright © 2011, American Chemical Society, and (d) Self-assembly of crown ether amphiphiles into columnar structure and formation of oriented matrix-fixed supramolecular channel, reproduced with permission from⁵⁵. Copyright © 2000, John Wiley and Sons.

1.1.4.2.2. Copolymer self-assembly

The self-assembly of copolymers, as opposed to surfactants, peptides or dendrimers, is a promising approach due to the well-understood synthesis and assembly methods for these materials. Polymer self-assembly, where polymer chemistry and physics drive the spontaneous formation of nanoscale structures, is an especially promising tool that has the potential not only to generate better membranes but also to do this in a scalable manner that can impact the industry. Polymers with different compositions are generally immiscible, so mixing two or

more together results in macroscopic phase separation. If segments of different polymers are covalently bonded, this propensity to phase separate results in microphase separation⁵⁶⁻⁵⁸ with the dimensions of each domain comparable to the size of the polymer segment (1-100 nm). Microphase separation can form an array of nanostructures, including lamellae, cylinders, spheres, and bicontinuous structures.⁵⁷⁻⁵⁸ For example, block copolymers (BCPs) can form nanostructures between 3-100 nm in size⁵⁸ and highly ordered structures can be achieved by controlling polymer structure and processing conditions, Figure 1.5.⁵⁷⁻⁵⁸ Formation of nanostructure and transport modulation in BCPs has been previously studied.⁵⁹⁻⁶⁰ While most studies have focused on controlling pore size and the responsive properties of the membranes, this approach has also been utilized to improve the selectivity of membranes between proteins of similar size based on their charge.⁶¹ But BCP self-assembly is limited to size scales useful for separating macromolecules and particles. Domain sizes are typically between 10-100 nm due to structural feature of the blocks. To our knowledge, 3 nm is the smallest microphase separated domain size to date, too large in comparison with small molecules.^{49, 59-60, 62}

One of the most significant potential applications of membranes focuses on separating small molecules. There are few researchers attempting to separate small molecules (<2000 Da) using membranes with self-assembled polymers, because generating nanostructures at this size scale is challenging. Graft (or comb-shaped) and random copolymers, on the other hand, can create bicontinuous microphase separated structures as small as 1 nm in diameter.⁶³⁻⁷⁶ Thus, these copolymer

architectures are especially promising for preparing membranes that can potentially separate small molecules by chemical features.

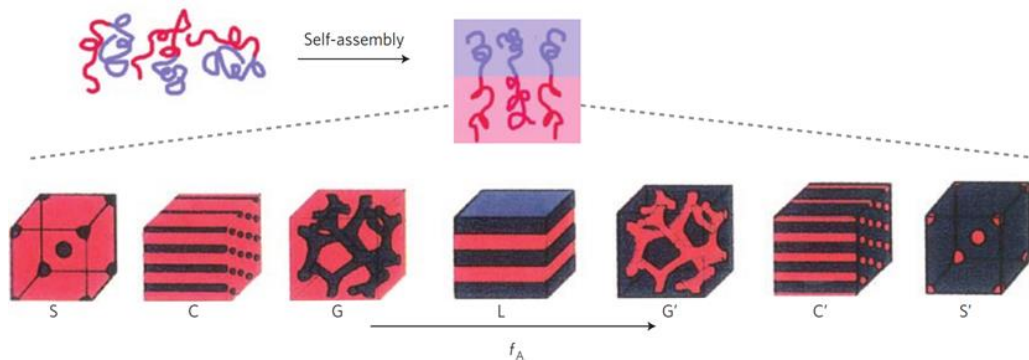


Figure 1. 5. Examples of phase-separated morphologies in A–B type diblock copolymers. Various morphologies are observed as the fraction of the A block (f_A) increases, such as spherical (S), cylindrical (C), gyroidal (G) and lamellar (L), reprinted with permission from⁵⁶. Copyright © 2009, Springer Nature.

Membranes that take advantage of this microphase separation behavior to form effective “nanopores” have been prepared by coating the copolymer onto a porous support to form a thin film. Nanochannels with size of ~ 1 nm are formed by self-assembly through microphase separation. The structure has a high nanopore density, leading to high permeability without sacrificing selectivity. To date, these systems have mostly been investigated as size-selective membranes for aqueous filtration, with side-chains treated as inert pore-formers and solutes characterized by their molecular volume.⁷⁷ An example of such a copolymer is a graft copolymer with a poly(acrylonitrile) (PAN) backbone and poly(ethylene oxide) (PEO) side-chains, PAN-*g*-PEO. This copolymer forms a bicontinuous microphase separated structure with permeation occurring through the interconnected PEO phases, acting as effective pores ~ 1 nm in diameter.⁶⁶ A recent study by Phillip and coworkers utilized a terpolymer that includes by addition of epoxide groups to PAN-*g*-PEO to

prepare such membranes with multiple functionalities.⁷⁸ These moieties in the terpolymer lined the pore walls upon microphase separation. Both positively charged and negatively charged moieties can be introduced through a post-modification process. These membranes match predictions from the Donnan exclusion theory and imply that these materials can exhibit charge-based selectivity.

This indicates that polymer microphase separation can be used to impart small molecule selectivity based on chemical features such as charge. But the small number of these studies, complete lack of models, and limited range of approaches to create functional nanostructures using scalable manufacturing methods shows that this avenue is worth investigating. In this dissertation, this knowledge gap is addressed by demonstrating an alternative approach to creating functional nanostructures, studying membranes selectivities in diffusion and filtration experiments, examining solute-pore walls interactions, linking performance with fundamental models of interaction (e.g. Donnan exclusion, binding-unbinding equilibria), and exploring multiple modes of chemical selectivity.

1.2. Fabrication of Ultrathin Selective Layers

1.2.1. Commercial Thin Film Composite Membranes

The most important step in the commercial and industrial success of membranes was the development of methods to make membranes that feature a very thin, dense selective layer supported by a thicker, highly porous support layer that confers mechanical integrity. The development of such membranes from

cellulose acetate by Loeb and Sourirajan⁷⁹ transformed membrane separation and made reverse osmosis (RO) practical at an industrial scale. Another breakthrough was the invention of interfacially polymerized (IP) TFC membranes for RO with only a <0.1 μm thick polyamide selective layer by Cadotte.⁸⁰ The thinness of this layer enables high flux through the membrane, better energy efficiency, and lower operating costs.

Since then, both processes have been extensively optimized, improving flux and energy efficiency. Yet progress in introducing new membrane materials has been limited. Today, essentially all commercial TFC membranes utilize IP cross-linked polyamide selective layers formed by interfacial step growth polymerization of an amine monomer and an acyl chloride monomer.^{7-8, 81-84} Some researchers have prepared membrane selective layers by other step growth polymerization schemes, such as the IP of carboxymethyl cellulose and poly(vinyl alcohol) (PVA) in water with a diisocyanate in an organic phase.⁸⁵ However, IP methods are limited to polymers formed by step growth polymerization. At least one monomer needs to be oil-soluble, which prevents the manufacture of inherently hydrophilic selective layers. The hydrophobicity of the resultant selective layer leads to fouling. Furthermore, these selective layers have very small effective pore sizes, limiting their use to nanofiltration (NF) and RO. Developing new fabrication methods that enable formation of thin selective layers with various chemistries and tunable pore size in a simple and scalable manner can have a great impact in many industries.

1.2.2. Hydrogels

Literature shows many other selective layer chemistries can be designed for membrane applications to achieve tunable selectivity, functionalized pores, responsive materials, and/or fouling resistance. Researchers have used hydrogels,⁸⁶⁻⁸⁷ amphiphilic copolymers,^{63, 65, 88-92} and polymerizable lyophilic liquid crystals^{44, 54, 93} as membrane selective layers. Among these, hydrogel selective layers are especially promising as highly effective selective layers that are inherently fouling resistant. Selectivity is controlled by the mesh size of the cross-linked polymer with the effective pore size typically in the ultrafiltration (UF) range, 1-5 nm.⁸⁷ Hydrogel coatings are also used to prevent fouling.⁹⁴ PEG hydrogel membranes are also very promising for gas separations, specifically for natural gas upgrading.⁹⁵⁻⁹⁸ Hydrogel selective layers are very versatile, tunable, and functionalizable.⁹⁹ Selectivity can be modulated by the addition of functional groups such as charged units that impart charge-based selectivity through Donnan exclusion. Responsive properties can be imparted by proper selection of monomers. Hydrogels are particularly suitable for the incorporation of nanomaterials that add new functionalities. Therefore, better methods for readily creating thin hydrogel selective layers are needed.

1.2.3. Existing Methods for Fabrication of Hydrogel Layers

Applying hydrogels as ultrathin layers can, however, be challenging. Many researchers focus their studies on thick (10s of μm) layers that have low flux, with the premise of future improvement.¹⁰⁰ Others create TFC membranes by one of two

methods: coating^{99, 101} or grafting.^{99, 102} In each case, there are significant challenges to overcome.

1.2.3.1. Membrane selective layers by coating

Several researchers have formed hydrogel coatings on porous and TFC membranes for the purpose of preventing fouling.^{18, 99} Most studies in this field focus on cross-linked PVA⁸⁶ and PEG-based hydrogels,¹⁰³⁻¹⁰⁴ though selective layers that include charged¹⁰³ and/or zwitterionic¹⁰⁵ monomers have also been reported. To create a hydrogel coating using this method, a monomer or pre-polymer solution is spread on the membrane (e.g. by doctor blading), and then cross-linked, e.g. by UV exposure in the presence of a photoinitiator.^{86, 92, 94, 103-106} This approach requires a high viscosity monomer/pre-polymer solution and specific wetting properties to achieve a good coating that remains on top of the membrane. This makes various coating formulations unusable. The viscosity can be increased with additives, but this can simultaneously change the coating properties such as pore size.^{94, 103-104} Achieving thin (<0.5 μm) defect-free coatings using this method is also very difficult in large scale manufacturing. Spin-coating can form thinner layers but is not scalable to a roll-to-roll process.^{86, 92}

1.2.3.2. Membrane selective layers by grafting

Grafting from membrane surfaces is a popular membrane surface modification method.^{18, 99} This approach relies on creating groups that initiate polymer growth on the membrane surface by various methods including plasma treatment,¹⁰⁷⁻¹⁰⁹ UV irradiation,¹¹⁰⁻¹¹⁹ or attaching initiating groups on the surface

for atom transfer radical polymerization (ATRP)¹²⁰⁻¹²¹ or photo-polymerization.¹²²⁻¹²³ The membrane is then exposed to the monomer to grow polymer chains. Typically, this approach creates a polymer brush lining the membrane pores and surface rather than a continuous selective layer,^{102, 124} but there are some studies on forming continuous cross-linked and hydrogel layers on membranes by adding poly-functional monomers.¹¹⁵⁻¹¹⁹ To form a selective layer using this method, the pore diameter has to be spanned by growing polymer chains from a limited number of initiating sites on pores followed by cross-linking. This can require long reaction times and is prone to defects due to pore size polydispersity in the support membrane. Grafting-from approaches are also not typically amenable to incorporating functional nanomaterials into the selective layer to create multi-functional membranes. Thus, development of a new method that enables fabrication of ultrathin hydrogel selective layers is highly desired.

1.3. Dissertation Outline

The objectives of this dissertation are: (i) to create functional nanostructures, studying its selectivity and structure-property relationship, (ii) exploring the feasibility of introducing new functionalities to the nanostructure for targeted separation, and (iii) development of a novel method for fabrication of ultrathin selective layers. The Dissertation is organized as follows:

Chapter 2 describes random copolymer self-assembly and the formation of micelles in organic solvents which will then be utilized for fabrication of charged nanochannels membrane selective layers. The nanostructure as well as separation

mechanism has been characterized in detail. The work presented in this chapter illustrates that random copolymer self-assembly can be utilized for fabrication of membranes with functional pores and size of 1-3 nm in a simple and scalable manner, leading to membranes with high selectivity and permeability.

Chapter 3 exploits the versatility of this method to introduce new functionality, aromaticity-based separation, to the membranes described in Chapter 2. The solute and pore wall interaction mechanisms, membrane selectivity and permeation properties are studied thoroughly. This chapter illustrates the exceptionally high selectivity of these membranes for separation of small molecules based on their aromaticity.

Chapter 4 presents a new method, interfacially initiated free radical polymerization (IIFRP), for the fabrication of membranes with ultrathin hydrogel selective layers. The effect of experimental parameters such as UV exposure time and monomer concentration were studied. Also, different porogens were utilized to tune the hydrogel membrane selectivity. The fouling properties of these membranes were further investigated upon long term exposure to a model protein solution. The work in this chapter reveals that IIFRP is a simple, reproducible, tunable and scalable method for fabrication of uniform, defect-free, ultrathin hydrogel selective layer for protein purification.

Chapter 5 summarizes the findings of this dissertation and describe future directions that can lead to further improvement of either of these projects, as well as opening up new research directions.

2 SELECTIVE TRANSPORT THROUGH MEMBRANES WITH CHARGED NANOCHANNELS FORMED BY SELF- ASSEMBLY OF RANDOM COPOLYMER MICELLES¹²

2.1. Introduction

Today, most membrane-based separations rely on differences in solute size relative to membrane pore size. Membranes that combine this size-based selectivity with a capability to differentiate between solutes that feature different functional groups can enable us to design membranes for custom applications and expand their use in chemical and pharmaceutical manufacturing. Such “chemo-selective” membranes also have potential applications in chemical/biosensing,¹²⁵⁻¹²⁸ DNA detection and analysis,¹²⁹⁻¹³³ nanofluidics,¹³⁴⁻¹³⁵ and drug delivery.¹³⁶

Biological pores such as porins, proton channels and ion channels display this chemical selectivity exquisitely.¹⁴ For example, ion channels present in the cell membrane are indispensable in controlling electrical signaling in nerves, muscles

¹ Reproduced in part with permission from reference 170. Copyright © 2017 American Chemical Society.

² Reproduced in part with permission from reference 169. Copyright © 2017, John Wiley and Sons.

and thus maintaining cell balance through highly permeable and selective transportation of ions. These structures have two distinctive features in common: hydrophobic pores only slightly larger than the target they transport (e.g., ~1 nm for ion channels), lined with functional groups that reversibly but selectively interact with the target (e.g. charged groups in ion channels, hydrogen bonding and hydrophobic groups in porins).^{14, 16, 137} Their superior selectivity and permeability arises from the synergistic effect of nanoconfinement of permeation with chemical functionality. The small pore diameter forces all solutes to closely interact with functional groups on the pore walls. The interactions between the solute and the functional groups in the pore control the partitioning and transport of the solutes in the pores. Thus, creating a simplified membrane that mimic their behavior can create a new generation of membranes with superior selectivity with a range of applications that span water treatment¹³⁸ to the separation of small organic and biomolecules in chemical and pharmaceutical manufacturing.

For example, membranes that can separate small organic molecules of similar size but differing charges have several applications, especially in the extraction and purification of small pharmaceutical molecules such as amino acids¹³⁹⁻¹⁴¹ and antibiotics.¹⁴²⁻¹⁴³ Membranes with pore walls that feature charged groups can accomplish this by favoring the passage of solutes that are uncharged or of opposite charge, but hindering the passage of co-ions.

Designing such selective membranes requires the creation of very small, <3 nm nanopores, and the integration of chemical functionality into the nanopores to tailor their surface chemistry to induce desired chemical interaction with the target

molecule. To date, most attempts to create membranes with charge-based selectivity have focused on narrowing and modifying the pores of track-etched (TE) or anodized alumina membranes including: electroless deposition of gold onto pore walls followed by chemisorption of an end-functionalized thiol onto the gold surface²¹⁻²⁸ or using chemical vapor deposition (CVD)³⁵⁻³⁷. Vertically aligned arrays of carbon nanotubes (CNT) can also act as membranes with functional cylindrical nanopores.^{52-53, 144} When the pore entrances are functionalized with carboxylic acid groups, these membranes show ion exclusion.¹⁴⁴⁻¹⁴⁵ All these approaches, however, require multi-step and complicated synthesis procedures. They also result in very low porosities (<1%, compared with 70-90% bulk porosity for typical membranes¹⁴⁶) that lead to membrane fluxes that are too low for most filtration applications. Because of these concerns, the materials prepared using these methods are used in microelectronics,¹⁴⁷ energy storage devices,¹⁴⁸ drug delivery¹⁴⁹ and sensors¹⁵⁰ rather than as filtration membranes.

Self-assembly is a promising tool for generating membranes with functional nanostructures using scalable, easier to implement methods.^{88, 151-157} The self-assembly of well-designed copolymer-based precursors can lead to formation of pores that can be chemically modified for desired selectivity through scalable manufacturing processes. Although amphiphilic block copolymers can microphase separate and form well-defined structures, reaching pore size smaller than 10 nm is very difficult. This limits their application to ultrafiltration and protein separations.¹⁵² Random and comb-shaped copolymers can form smaller and bi-

continuous domains down to 1 nm,^{63-64, 66, 158-159} and have shown size-selective screening of small molecules.

As an alternative to microphase separation, the assembly of spherical nano-assemblies such as micelles or colloidal nanoparticles into packed arrays can create porous systems that act as membrane selective layers. For instance, BCP micelles have been deposited onto a silicon wafer by spin coating to form a porous film of packed micelles that can perform size-based separation.¹⁶⁰⁻¹⁶² The compressibility of these micelles cause them to deform upon the application of pressure, causing changes in pore size.¹⁶² Alternatively, colloidal silica nanoparticles can be assembled into packed arrays that can be functionalized with polymers and modulate transport.¹⁶³⁻¹⁶⁸ These membranes can also be presumably used as membrane selective layers, though the brittleness and thickness of these layers may be of concern in pressure-driven processes. However, the large size of both BCP micelles and silica particles (45-200 nm) accessible in these studies lead to pore sizes between 7.5-100 nm, too large to address small molecule separations. Furthermore, these approaches have not been explored for imparting chemical structure-based selectivity in filtration applications.

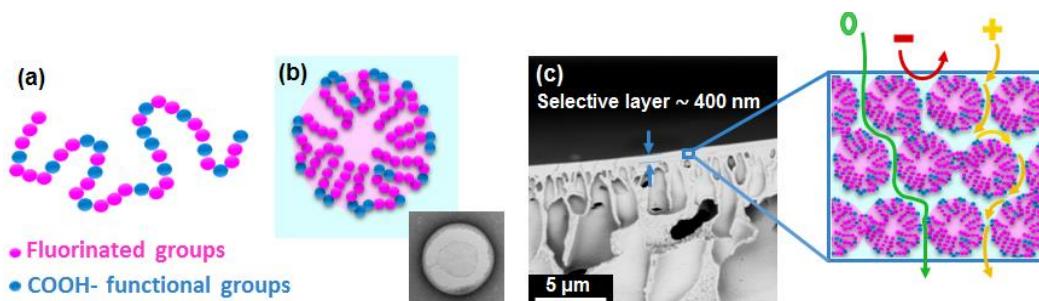
Almost all the methods mentioned above require post-modification steps that can increase the risk of undesired side reactions or damage to the membrane structure. The added manufacturing steps may also limit scalability. It is highly desirable to develop a single-step, scalable approach to generate membrane selective layers with a high density of <3 nm nanopores lined with tailored, well-defined functional groups, to yield membranes with high permeability and good

selectivity between solutes of similar size, but different chemical features (e.g. charge). There is also a knowledge gap in better understanding the mechanisms of transport and selectivity in such membranes.

In this chapter, we demonstrate the formation of novel membranes that feature a network of carboxylate functionalized nanochannels in their selective layer by depositing random copolymer micelles in alcohol onto a porous support using a single-step coating process (Scheme 2.1). These micelles are formed by the self-assembly of a random amphiphilic copolymer, poly(trifluoroethyl methacrylate-random-methacrylic acid) P(TFEMA-*r*-MAA),¹⁶⁹ and are stable in water. The resultant membranes feature a selective layer of a packed array of micelles with carboxylate functional surfaces. The interstices between these micelles, calculated to be approximately 1-3 nm at their narrowest point, serve as charged nanochannels through which water and solutes can pass. The negatively charged carboxylate groups lead to high separation selectivities between organic solutes of similar size but different charge, as demonstrated by diffusion and filtration experiments. These membranes effectively retain negatively charged solutes while allowing the passage of positively charged and neutral solutes of similar size, and exhibit water fluxes comparable with commercial membranes of similar pore size. Their permeation selectivity is enhanced further in competitive diffusion experiments as the neutral solutes prevent the entrance of anionic solutes into the nanopores. In addition to promising applications in charge-based separations in the industry, these membranes represent a novel approach to creating

membranes with carboxyl functional nanopores that can be further modified to enable a broad range of selectivities.

Scheme 2. 1. Formation mechanism of the membrane selective layer featuring charged nanochannels. Reprinted from¹⁷⁰. Copyright © 2017 American Chemical Society.



*(a) The random copolymer with fluorinated and carboxylated repeat units (b) Formation of micelles in methanol, (c) Coated micelles onto a porous support, where they form a packed array of spherical micelles with carboxylic acid functional surfaces. The interstices between the micelles act as effective nanopores through which permeation occurs. Ionized carboxylate groups impart charge-based selectivity through electrostatic interactions.

2.2. Materials and Methods

2.2.1. Materials

Methacrylic acid (MAA), azobisisobutyronitrile (AIBN), 4-methoxy phenol (MEHQ), small organic molecules including Brilliant Blue R (BBR), calcein sodium salt (CAL), Acid Blue 45 (AB45), Methyl Orange (MO), Rhodamine 6G (Rho6G), Basic Blue 3 (BB3), Vitamin B12 (B12), Riboflavin (RIB), and Rutin hydrate (RTH), pyrenetetrasulfonic acid tetrasodium salt (Na_4PTS) were purchased from Sigma Aldrich (St. Louis, MO). 2,2,2-Trifluoroethyl methacrylate (TFEMA) was purchased from Scientific Polymer Products Inc (Ontario, NY). Solvents (methanol, ethanol, dimethyl sulfoxide (DMSO), tetrahydrofuran (THF), hexane) and salts (NaCl , Na_2SO_4 , CaCl_2 , CaSO_4) were purchased from VWR (West Chester,

PA). Deuterated dimethyl sulfoxide (DMSO-d₆) was obtained from Cambridge Isotope Laboratory (Tewksbury, MA). Ultrapure deionized water generated by Biolab 3300 RO, a building wide RO/DI water purification unit by Mar Cor Purification was used for all experiments. All chemicals and solvents were reagent grade and used as received except for MAA and TFEMA, which were purified by passing through neutral and basic activated alumina columns, respectively (Sigma-Aldrich, MO). PAN-400 ultrafiltration membranes purchased from Nanostone Water, Inc. (Oceanside, CA) was used as the support membrane to provide mechanical support.

2.2.2. Polymer Synthesis and Characterization

P(TFEMA-*r*-MAA) was synthesized using a free radical polymerization mechanism. A total of 40 g of MAA and TFEMA and AIBN (0.02 g) were dissolved in 100 ml DMSO in a round bottom flask. The flask was sealed and purged with nitrogen for 30 min. Polymerization reaction occurred as the solution was heated under stirring at 55 °C for about 4 h. Then, 2 g of MEHQ was added to terminate the reaction. Copolymers were recovered by precipitation in a mixture of ethanol and hexane (1:3 v/v), re-dissolved in ethanol and washed three times in hexane to remove all monomer residues. The final product was then air dried overnight and dried in vacuum oven at 50 °C for 24 h. The yield was approximately 40%.

The synthesized copolymers were characterized using ¹H nuclear magnetic resonance (¹H NMR) spectroscopy. After dissolving the copolymers in DMSO-d₆, NMR spectra were acquired on a Bruker Avance III 500 spectrometer. Molecular

weight distribution measurements of the copolymers were acquired using a Shimadzu Gel Permeation Chromatography (GPC) System equipped with a TOSOH TSK gel GMHh-M mixed-bed column and guard column, equipped with both UV and refractive index detectors. THF was used as the mobile phase at 0.75 ml min⁻¹ elution rate and calibrated with low polydispersity poly(styrene) standards (TOSOH, PSt Quick Kit).

To measure water uptake, dry samples were weighed (W_{dry}) and then equilibrated in deionized water for two days at room temperature. The excess water was removed gently by dabbing with a filter paper and the sample was weighed immediately (W_{wet}). The water uptake was then calculated from the weight difference of the polymer in its hydrated and dry state using Eq. (2.1):

$$\text{Water uptake (\%)} = \frac{W_{wet} - W_{dry}}{W_{dry}} \times 100 \quad \text{Eq (2.1)}$$

2.2.3. Characterization of Micelles

Micellar solutions were prepared by directly dissolving the copolymer by stirring and heating at 40 °C overnight in methanol or THF directly. Dynamic Light Scattering (DLS) was performed using Nano Brook 90Plus PALS particle sizer (Brookhaven Instruments, Holtsville, NY) equipped with a He-Ne laser operated at 659 nm and with a 1 mm entrance aperture. Scattering measurements were performed at 25 °C and 90° angle. The copolymer was dissolved in methanol or THF at a concentration of 0.5 wt% for all experiments except for the determination of the critical micelle concentration, where a broad range of concentrations were tested. Solutions containing metal ions were prepared by first dissolving the metal

salts in methanol, and then dissolving the copolymer in this solution at a final concentration of 0.5 wt%. The concentration of metal ions in solution was quantified by the ratio r , defined as the number of moles of MAA repeat units per mole of metal ion. All samples were passed through a 0.45 μm syringe filter with Teflon membrane before analysis. Average hydrodynamic diameter of micelles was calculated using Non-Negative Least Squares (NNLS).

Atomic Force Microscopy (AFM) samples were made by spin coating the micellar solution on a freshly cleaved mica surface using two steps including a short spin at a slower rotation rate (5 s at 500 rpm) followed by a longer and much faster spin (2 min, 2500 rpm). This ensures the formation of a homogenous layer on the mica surface.

The nano-scale morphologies of micelles and films were studied by Transmission Electron Imaging (TEM, FEI Technai Spirit) operated at 80.0 kV. TEM samples were prepared by submerging a copper grid with carbon film into a 0.3 wt% copolymer solution in methanol, methanol/ $\text{Cu}(\text{OAc})_2$, or THF, followed by floating the grid on a droplet of DI water to freeze the structure. The solution prepared in methanol/ $\text{Cu}(\text{OAc})_2$ contained 20 moles of MAA repeat units per Cu^{2+} ion. Samples were then stained using 0.5 wt% $\text{Cu}(\text{OAc})_2$ aqueous solution by floating the TEM grid on the copper acetate solution for 5 minutes, followed by rinsing with DI water.

To study the effect of evaporation time, on micelle self-assembly, we prepared samples using conditions that closely mimics the membrane preparation

procedure. Copper grids were first submerged into a 0.3 wt% copolymer solution in methanol, followed by evaporating the solution for various times (0-20 s) and finally floating the grid on a droplet of DI water. The samples were stained afterward using 0.5 wt% Cu (OAc)₂ aqueous solution.

Fourier Transform Infrared (ATR-FTIR) spectroscopy was used to investigate the interactions of the copolymer with different metal ions. ATR-FTIR spectra of solutions in different solvents were acquired using a FT/IR-6200 spectrophotometer (JASCO Corp, Tokyo, Japan). The ATR-FTIR spectra were recorded over the range of 4000-600 cm⁻¹ at a 4 cm⁻¹ resolution. The copolymer solutions were prepared by first dissolving the metal salt (if any) in methanol, and then dissolving the copolymer in the solution at a final concentration of 5 wt%. The solution was placed on a ZnSe crystal using liquid chamber accessory and the spectra were collected in attenuated total reflection (ATR) mode using pure methanol as background.

Coordination of the copolymer with different metal ions was studied using UV-vis spectroscopy. The UV-Vis absorption spectra were recorded on a Thermo Scientific Genesys10S Spectrometer (Waltham, MA) for solution of metal ions as well as in presence of copolymer in the solution.

2.2.4. Membrane Fabrication and Characterization

The copolymer solutions for membrane preparation were prepared by dissolving 5 wt% of the copolymer in methanol by stirring at 40 °C for 24 h. Afterward, the solutions were filtered through 1 μm glass fiber syringe filter

(Whatman) and kept in an oven at 50 °C to eliminate the bubbles. Bubble/dust-free solutions were cast onto a PAN400 ultrafiltration membrane taped on a glass plate with an adjustable doctor blade (Gardco, Pompano Beach, FL) set to a gap size of 20 μm . The glass plate was immersed into a water bath after 20 s of solvent evaporation at room temperature.

The microstructure of the membrane was characterized by Supra 55 FESEM at 4 kV and 10 mm working distance. Dried membranes were frozen in liquid nitrogen and cut with a razor blade for cross-sectional imaging. To avoid charging, the samples were sputter coated (Cressington 108 manual, Ted Pella Inc., CA) with Au/Pd (60/40) for 120 s at 30 mA current in an argon atmosphere.

Atomic force microscopy (AFM) measurements were performed with a Dimension 3100 (Veeco, Plainview, NY) on a tapping mode. AFM cantilevers were purchased from Bruker with a $f_0=50\text{-}100$ kHz and $k=1\text{-}5$ N m^{-1} . Samples were dried and taped on a glass slide. A 10 $\mu\text{m} \times 10 \mu\text{m}$ area was scanned. The fast Fourier transform (FFT) analysis was obtained using Gwyddion software. Membrane hydrophilicity was measured with a Ramé-Hart contact angle goniometer (Succasunna, NJ) on dried membranes cut and taped onto glass plates.

2.2.5. Characterization of Membrane Performance

Diffusion experiments were performed using a side-by-side glass diffusion cell (PermeGear) with a cell volume of 7.0 ml and an effective permeation area of 1.8 cm^2 . A circular membrane swatch 1 inch in diameter was mounted between the two halves of the diffusion cell: feed and sink. A 0.1 mM solution of the desired

solute was placed in the feed half-cell, whereas the sink compartment was filled with DI water. Both solutions were continuously stirred to minimize concentration polarization. For measuring the diffusion rate of organic solutes, 1 ml of the solution in the sink was periodically taken and replaced with DI water. Solute concentration was measured by UV-visible spectroscopy (Thermo Scientific Genesys10S Spectrometer, Waltham, MA).

Filtration experiments were carried out using a 10 ml Amicon 8010 stirred, dead-end cell (Millipore) with filtration area of 4.1 cm² and a trans-membrane pressure of 40 psi. Cells were stirred at approximately 500 rpm to minimize concentration polarization. Transmembrane fluxes were measured by collecting each permeate in a container placed on top of a scale (Ohaus Scout Pro) connected to a computer and observing the total weight increase over time. The membrane permeance (L_p), defined as the flux (J) normalized by applied trans-membrane pressure (ΔP), was calculated according to:

$$L_p = \frac{J}{\Delta P} = \frac{1}{R_{\text{total}}} \quad \text{Eq. (2.2)}$$

R_{total} accounts for the resistance toward the flow of the coating and the support membrane itself. Resistances-in-series model was used to account for the hydraulic resistance posed by support membrane and the selective coating layer.

$$R_{\text{total}} = R_{\text{selective layer}} + R_{\text{support membrane}} \quad \text{Eq. (2.3)}$$

The support membrane resistance against the flow is negligible due to its high flux in comparison to the TFC membrane (820 L m⁻² h⁻¹ bar⁻¹) according to manufacturer specifications, confirmed in our filtration system). Selective layer

permeability (P_m) was thus calculated by normalizing the permeance with the selective layer thickness using:

$$P_m = \frac{\delta}{R_{\text{selective layer}}} \quad \text{Eq. (2.4)}$$

where δ is the selective layer thickness (μm) obtained from SEM images using ImageJ software, averaged over measurements on least 5 different membrane samples.

Membrane selectivity was determined by filtering a series of organic solutes (cationic, anionic and neutral) at the concentration of 0.1 mM. The first ml of filtrate was discarded, and the subsequent 1 ml was collected and used for measuring rejection.

$$R\% = \left(1 - \frac{C_P}{C_F}\right) \times 100 \quad \text{Eq. (2.5)}$$

where R is the solute rejection, C_F and C_P are the concentration of feed (0.1 mM) and permeate, respectively. The concentration of organic solutes was measured by UV-Visible spectroscopy. Two-solute separation experiments were performed using a similar procedure, but the total solute concentration in the feed was kept at 0.1 mM.

Salt retention experiments were carried out by dissolving different concentrations of salt (1, 5, and 10 mM) in DI water. The first ml was discarded, and the subsequent 2 ml was collected. The conductivity of the solution was measured using a conductivity meter (Cole-Parmer, Vernon Hills, IL). Rejections were calculated using Equation 2.5, given that in this concentration range,

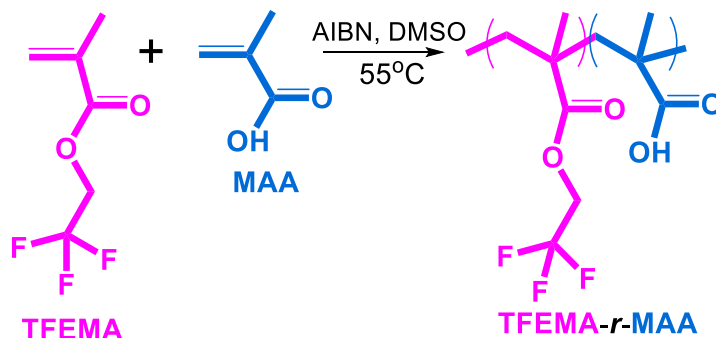
conductivity is linearly related with salt concentration. Membranes were soaked in DI water at least overnight between diffusion or filtration experiments to remove any organic solute or salt residues. DI water was filtered through the membranes before subsequent filtration experiments.

2.3. Results and Discussion

2.3.1. Copolymer Synthesis and Characterization

P(TFEMA-*r*-MAA) copolymer was synthesized using free radical polymerization as shown in Scheme 2.2. This method is simple and scalable, which is important for future commercial impact of related technologies.

Scheme 2. 2. Synthesis scheme for P(TFEMA-*r*-MAA). Reprinted with permission from¹⁷¹. Copyright © 2017, John Wiley and Sons.



Two batches of copolymer were synthesized using this method, with different TFEMA/MAA ratios (Table 2.1). The resultant copolymer compositions were calculated using the characteristic peaks of each monomer from ¹H NMR spectra (Figure 2.1). In both cases, the resultant copolymer compositions, obtained at about 40% conversion, were slightly higher in TFEMA content compared with the reaction mixture composition. These results are in agreement with additional

studies¹⁶⁹ that indicate the monomer sequence is close to random, with few, if any, PTFEMA blocks. While the resultant copolymers cannot be described as completely random, their segmental order is likely close. It should be noted that while these copolymers are truly statistical copolymers with the given caveats, we use the term “random copolymer” throughout this dissertation for the sake of simplicity, to clearly distinguish from block copolymers commonly investigated in current literature, and to use consistent terminology with past publications in the field where this effect was not often considered.

Table 2. 1. Compositions, molecular weights, water uptake values of synthesized copolymers, membrane pore size, membrane pore density, membrane permeance, selective layer permeability and water contact angle values. Reprinted from¹⁷⁰. Copyright © 2017 American Chemical Society.

Properties	CP40	CP50
MAA wt% in reaction mixture	50	70
MAA wt% in copolymer	45	55
Copolymer weight-average molar mass (kg mol ⁻¹)	1064	39 ^{a)}
Copolymer dispersity	1.75	1.72
Copolymer water uptake%	26±3	51±7
Membrane pore size (nm) ^{b)}	1-3	1-4
Pore density (×10 ¹⁴ pores m ⁻²)	2.3	4.1
Membrane permeance, L_p (L m ⁻² h ⁻¹ bar ⁻¹)	4.2±1.0	7.3±1.3
Selective layer permeability, P_m (L μm m ⁻² h ⁻¹ bar ⁻¹)	1.7±0.4	3.7±0.7
Contact Angle	82±3	69±4

^{a)} Likely underestimated due to limited solubility of CP50 in THF.

^{b)} Measured in dry state.

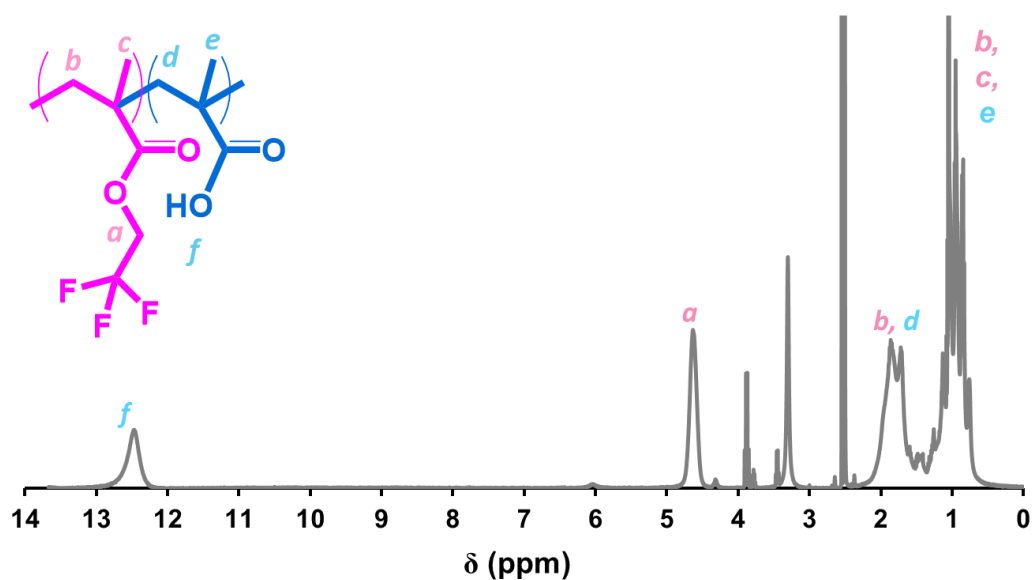


Figure 2. 1. ¹H NMR spectrum of CP40 deuterated DMSO showing the characteristic peaks and corresponding protons. a, and d peaks are used to calculate copolymer composition. Reprinted with permission from¹⁷¹. Copyright © 2017, John Wiley and Sons.

GPC analysis in tetrahydrofuran (THF) showed the successful synthesis of high molecular weight copolymers with polydispersities in agreement with typical values for free radical polymerization method (Table 2.1). We suspect, however, that these measurements were at least somewhat affected by the formation of micelles in THF¹⁶⁹ and the limited solubility of CP50 in this solvent, leading to the measurement of very different molecular weights for the CP40 and CP50 even though based on the similar synthesis conditions, similar molar masses were expected. Water uptake measurements indicate that copolymers with higher MAA content show higher water uptake, as expected from the hydrophilicity of this monomer.

2.3.2. Micelle Formation³

As mentioned in the introduction, block copolymers (BCPs) are able to create ordered structures and the wide variety of morphologies that can be achieved by manipulating block lengths and chemistries.¹⁷²⁻¹⁷⁸ Random copolymers (RCPs) can also form micelles¹⁷⁹⁻¹⁸¹ and microphase separated domains,^{158, 182} but this requires a much higher degree of incompatibility between segments and/or degree of solvent selectivity due to the close proximity and short clusters of the incompatible repeat units. When this criterion is achieved, RCPs can form an even wider range of micelle morphologies (spheres, rods, honeycombs, vesicles, etc.)¹⁷⁹ compared with BCPs. For example, BCPs with a charged block are typically limited to forming spherical micelles due to the high charge density in their corona. However, RCPs of similar repeat units can form a broader range of morphologies due to the lower charge density.^{179, 183-185}

From a practical point of view, RCPs are much easier to synthesize than BCPs, which require multi-step living polymerization procedures. Easier synthesis and morphological versatility make the RCPs great candidates for many applications, from drug encapsulation¹⁸⁶⁻¹⁸⁷ to optical materials and micro-electronics.¹⁸⁸⁻¹⁸⁹

To date, a large fraction of studies on micellar systems focus on solutions in water, a highly selective media that strongly favors the formation of micelles.¹⁹⁰⁻¹⁹² Supramolecular organization is possible but comparatively more unusual in non-

³ Reproduced in part with permission from reference 169. Copyright © 2017, John Wiley and Sons.

aqueous solvents, because achieving sufficiently selective solvation is difficult. While, BCPs with long corona chains (i.e. star micelles) can form micelles by direct dissolution in a single organic solvent,^{178, 193-197} RCP micelles in organic solvents have not, to our knowledge, been reported. Thus, we first explored the spontaneous self-assembly of the random copolymer synthesized in this study in two organic solvents, methanol and THF, that are selective for either the fluorinated or the hydrophilic segments. Additionally, we studied the effect of the addition of metal ions on micelle size and morphology.

2.3.2.1. Micelles in methanol

The MAA repeat units in the P(TFEMA-*r*-MAA) contain carboxylate functional groups and are highly incompatible with the TFEMA repeat units. PMAA homopolymer is a weak poly-acid, and highly soluble in methanol, which it interacts strongly with through hydrogen bonding. In contrast, PTFEMA homopolymer is a fluorinated, very hydrophobic polymer that is insoluble in methanol. Our results indicate that this incompatibility leads the RCP of these two monomers to form micelles and vesicles spontaneously in methanol. TEM analysis shows spherical micelles and some larger vesicles formed in methanol (Figure 2.2 a and b). To identify which segment forms the micelle corona, TEM samples were stained by copper acetate (Cu(OAc)₂), which complexes with carboxylate groups in MAA repeat units.¹⁹⁸ A dark outline in the TEM images (Figure 2.2 a), illustrating the staining of the outer surface of the micelle, indicates that MAA groups are located in the corona. TFEMA-rich sections of the polymer chain form the micelle core. PTFEMA homopolymer has a high T_g (80°C)¹⁹⁹ that imparts

stability to the micelle structure by limiting polymer mobility within the core.²⁰⁰⁻²⁰¹ Hydrogen bonding of MAA units with methanol also stabilizes the supramolecular assemblies.^{185, 202}

TEM analysis shows some large vesicles (100-200 nm) and some much smaller micelles (10-20 nm). However, sample preparation for TEM imaging may lead to artefacts due to drying, interactions between the micelles and the solvents used, and the formation of a thin layer on the grid. To confirm the presence of micelles and vesicles in solution and to better analyze the size distribution of these structures, we performed DLS. This analysis confirmed the presence of small micelles (7-15 nm) and larger vesicles (40-70 nm) with an average hydrodynamic diameter of 17 nm (Figure 2.3a) for CP40 copolymer. The bimodal distribution likely implies the formation of large compound micelles^{172, 202} and vesicles^{179, 203-204} in solution upon the fusion of smaller micelles. The two segments in RCPs are dispersed in close vicinity of each other along the polymer chain. This prevents the formation of clear boundaries that can be described as a core/shell structure,²⁰⁵ which leads to a thinner corona with weaker interactions with the solvent in comparison to BCPs.²⁰² This may lead to the clustering of smaller micelles and the formation of large vesicles, frequently observed in both random and block copolymers.^{187, 206} The larger size of the bigger aggregates in TEM image can be attributed to the flattening of micelles on TEM grid while drying or fusion of smaller particles induced by solvent evaporation and desolvation of micelle corona.¹⁸⁶⁻¹⁸⁷ A bimodal size distribution was also obtained for CP50 copolymer with average diameter of about 8 nm (Figure 2.3a). The smaller micelle size for

CP50 relative to CP40 can be attributed to the lower TFEMA content leading to shorter TFEMA segments, and thus smaller micelle cores.

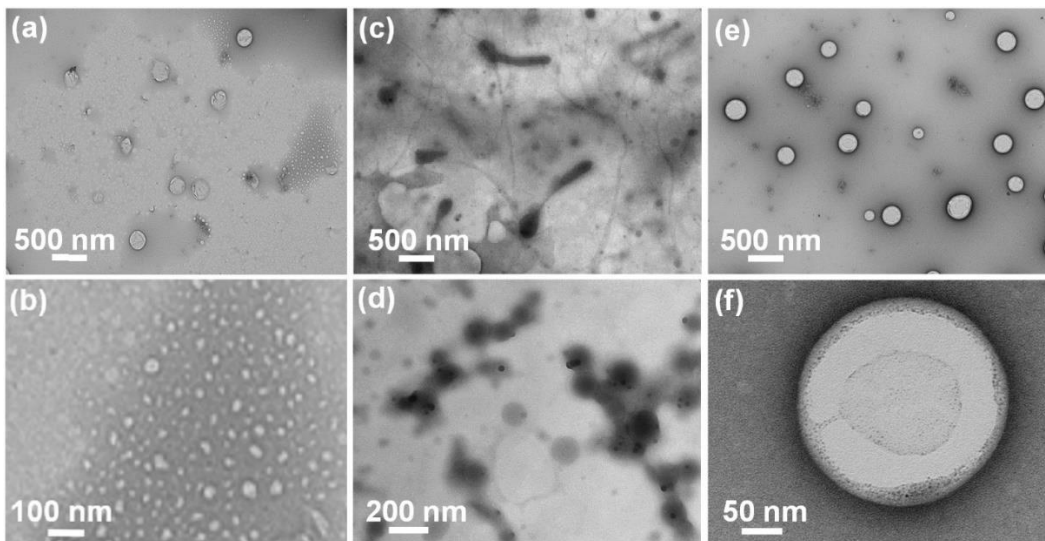


Figure 2. 2. TEM micrographs of supramolecular structures formed by P(TFEMA-*r*-MAA) prepared with 0.3 wt% copolymer in solution. (a, b) Micelles and vesicles formed in methanol; (c, d) Reverse micelles in THF, exhibiting the onset of morphological transition from sphere to rods; (e, f) Micelles and vesicles formed in methanol in the presence of Cu(OAc)₂ in polymer solution. All samples were stained by immersion in 0.5 wt% of Cu(OAc)₂ in water after preparation to identify carboxylic acid groups. Reprinted with permission from¹⁷¹. Copyright © 2017, John Wiley and Sons.

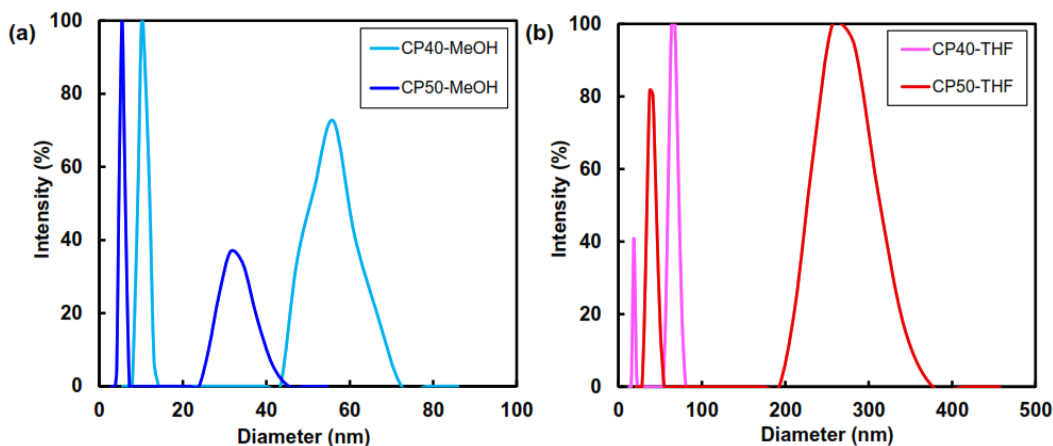


Figure 2. 3. DLS micelle size distribution for CP40 and CP50 in (a) Methanol, and (b) THF. Reprinted in part with permission from¹⁷¹. Copyright © 2017, John Wiley and Sons.

2.3.2.2. *Micelles in THF*

In non-polar solvents, BCPs may form reverse micelles whose cores are composed of the more hydrophilic component.^{196, 207} We documented the formation of reverse micelles with MAA-rich cores from P(TFEMA-*r*-MAA) in THF. TEM analysis showed micelles with various morphologies in THF, including spherical, rod-like and worm-like structures with MAA cores, stained with Cu(OAc)₂ (Figure 2.2c, d). The bulk/core regions of these micelles were stained with copper and appeared dark, confirming the segregation of MAA groups into these regions. Rods appeared to be bent rather than straight, with hemispherical caps at the rods ends. Higher magnification images (Figure 2.2d) suggest at least some of the rod-like structures could have been formed by the merger of spherical micelles. Due to the TEM sample preparation method, these rod-like assemblies may be present in solution and/or may have formed due to drying during TEM sample preparation. In either case, their formation is also likely enabled by the lower degree of ionization of MAA in THF, which has a lower dielectric constant than methanol.²⁰⁸ Electrostatic repulsion between MAA segments on the micelle corona in methanol favors spherical micelles. In contrast, weaker repulsive forces in the PTFEMA-rich corona in THF enable the coexistence of and transitions between multiple morphologies with similar free energies, including those with lower curvature such as cylinders and rods.²⁰⁹⁻²¹⁰ The micelle morphology is also affected by the fact that MAA is partially swollen by THF, creating a softer core that is capable of morphological transitions. Multiple morphologies may also arise from copolymer molecular weight dispersity.²¹⁰

As mentioned above, the TEM sample preparation process may introduce artefacts to the size of the observed assemblies. It also does not generate data that can statistically represent the size distribution of the formed structures. We used DLS to analyze the properties and sizes of these assemblies in solution. DLS analysis showed a bimodal size distribution (Figure 2.3b) with an average micelle diameter of ~ 45 nm for CP40, larger than in methanol. In case of CP50, also a bimodal size distribution was observed. This distribution included much larger micelles with average diameter of ~ 90 nm, twice the size observed in CP40. This could be attributed to larger micelle cores in CP50.

The lowest copolymer concentration at which micelles are formed is termed the critical micelle concentration (CMC). To determine this value for our copolymer in methanol, we performed DLS on copolymer solutions at a broad range of concentrations, from 0.01 mg/mL to 1 mg mL⁻¹ (Figure 2.4). A sudden shift in measured hydrodynamic radius is correlated with the formation of micelles.²¹¹⁻²¹² The CMC of the copolymer was found to be 0.066 mg/ml (1.09×10^{-7} M) in methanol (Figure 3a). This CMC value is similar to the range reported for block copolymers in water (typically in the order of 10^{-6} to 10^{-7} M), but much lower than typical values for small molecules surfactants (10^{-3} to 10^{-4} M).²¹³ The micelle size in methanol was relatively stable above the CMC, with only a minor increase in micelle size with increasing concentration. The CMC in THF was found to be around 0.026 mg/ml (4.15×10^{-8} M) using DLS (Figure 2.4b). THF preferentially solvates TFEMA segments over MAA segments, though it still

shows weak solvency for PMAA.¹⁹³ This can swell and plasticize micelles' core, resulting in larger micelles.

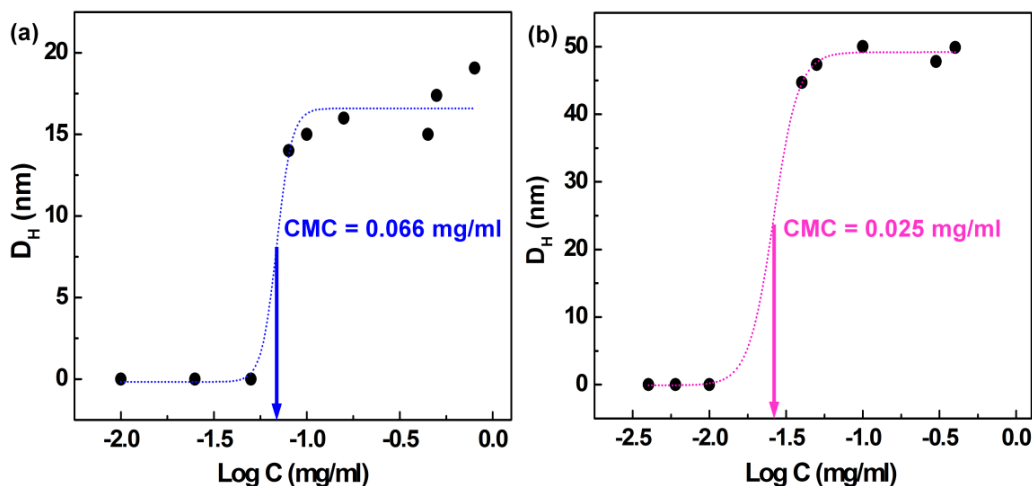


Figure 2. 4. Determination of CMC by DLS in (a) Methanol and (b) THF. Reprinted with permission from¹⁷¹. Copyright © 2017, John Wiley and Sons.

2.3.2.3. *Micelles morphology in a thin film*

We also examined the micelle morphology using AFM (Figure 2.5). A film of the copolymer micelles was deposited on mica by spin coating. A bumpy film of spherical micelles fused together formed upon spin coating a 0.3 wt% copolymer solution in methanol (Figure 2.5a). Spin casting a 0.1 wt% solution in methanol led to well-dispersed individual micelles with a height of ~5-10 nm (Figure 2.5b). This measured height is lower than that calculated through DLS, likely because micelles flattened on the substrate upon spin-casting and drying.²¹⁴ When deposited from THF, the copolymer formed rod like aggregates. This is likely a result of the drying process on the mica surface, where micelles merge into cylindrical morphologies with lower surface energy (Figure 2.5c). This phenomenon is prevented in methanol due to electrostatic repulsions between the partially ionized MAA coronas, and by

the high rigidity of the TFEMA-rich core. In THF, however, the TFEMA-rich corona is not charged, so micelles can easily contact each other. The MAA-rich core is plasticized by the solvent, which further enables the merger of micelles during the spin coating process.

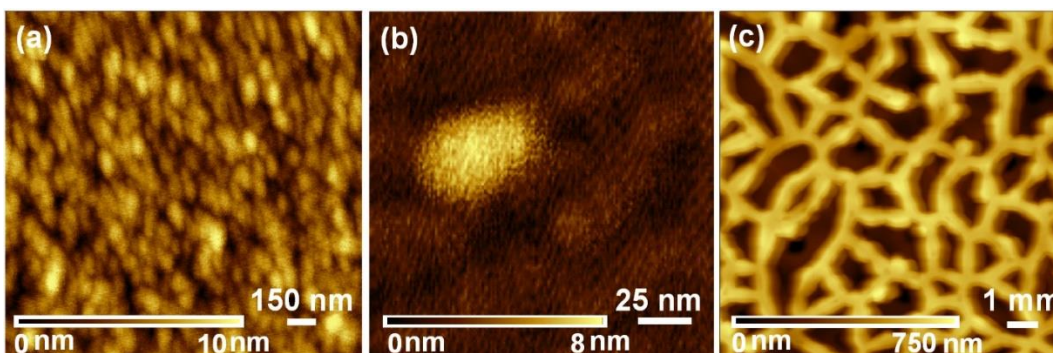


Figure 2. 5. Micelles cast from copolymer solution of (a) 0.3 wt% in methanol, (b) 0.1 wt% in methanol, and (c) 0.3 wt% in THF on mica. Reprinted with permission from¹⁷¹. Copyright © 2017, John Wiley and Sons.

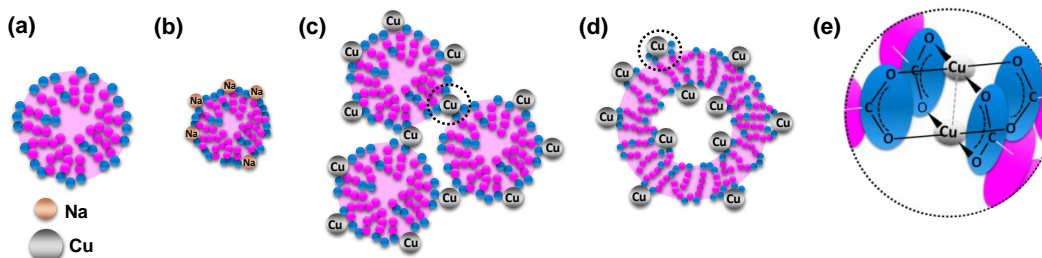
2.3.2.4. Interaction of dissolved metal ions with micelles

Coordination of metal ions with surfactants²¹⁵ or BCPs^{58, 216} during the formation of supramolecular structures can lead to new materials with tunable properties and impart additional features. Metal ions can interact with carboxylate groups through ionic/Coulombic interactions or through complexation. These interactions have been leveraged to fabricate functional nanostructured materials for isoporous membranes,²¹⁷⁻²¹⁸ catalysis,²¹⁹ biomedicine²²⁰ and precursors for inorganic or hybrid structures.²²¹

These metal ion-carboxylate interactions can also alter the size and morphology of micelles formed by small molecule surfactants²¹⁵ and BCPs^{203, 222-227} in water, depending on the chemistry and relative size of each block. For

example, although BCPs, especially those with ionizable blocks, have a tendency to form spherical micelles, it is possible to access other morphologies (e.g. rods, vesicles) by the addition of metal ions in aqueous solution.²²⁸⁻²²⁹ The change in micelle size and morphology upon addition of metal ions can arise from decreased electrostatic repulsion among charged groups in the micelle corona or from the complexation of functional groups in the copolymer with metal ions.²²⁹ These interactions can either draw the functional groups together to make larger micelles, or push them apart and increase curvature.²¹⁵ These effects have been extensively studied in BCP systems, but to our knowledge, the effect of added ions on micelle size and morphology has not been reported in micellar solutions formed by RCPs. Furthermore, in non-aqueous media (e.g., methanol), carboxylic acid groups exhibit a lower degree of dissociation than in water. This alters both the electrostatic interactions between functional groups in the corona and the interactions between the salt ions and the carboxylic acid groups in the micelles,²²⁹ likely leading to morphological changes in the micelles. Therefore, we would expect the size and morphology of the RCP micelles in methanol to change upon the addition of metal ions to solution. This implies that the supramolecular assembly of P(TFEMA-*r*-MAA) can be tuned by the addition of metal ions that interact with the COOH groups in MAA units.¹⁹⁸

Scheme 2. 3. The effect of metal ions on micelle size and morphology; (a) Micelle morphology in MeOH, (b) in presence of Na(OAc), (c) Formation of micelle clusters in presence of Cu(OAc)₂, (d) Transition from micelle to vesicle by addition of Cu(OAc)₂, and (e) Inter-micellar bridging by Cu²⁺. Reprinted with permission from¹⁷¹. Copyright © 2017, John Wiley and Sons.



We studied the effect of adding monovalent, divalent, and trivalent metal ions on micelle morphology and size in methanol. As shown in Figure 2.6a, the addition of sodium acetate (NaOAc) at a MAA: NaOAc molar ratio of 20 (termed $r = 20$) causes the average micelle size to decrease to 12 nm. Both the smaller micelles and the larger vesicles become smaller on average.

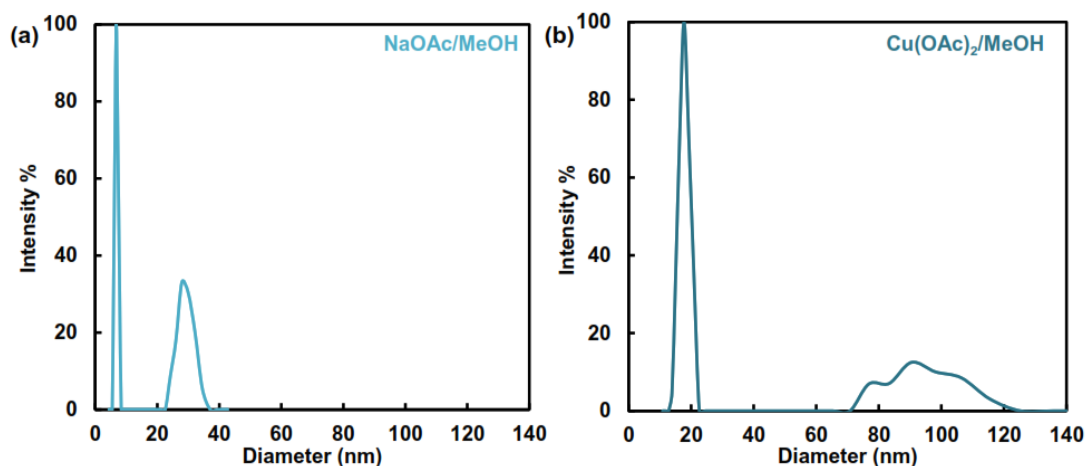


Figure 2. 6. DLS micelle size distribution for 0.5 w% micellar solutions in methanol (a) with Na⁺ added in methanol, $r=20$, and (b) with Cu²⁺ added, $r=20$; r is defined as the molar ratio of MAA groups to metal ions in solution. Reprinted with permission from¹⁷¹. Copyright © 2017, John Wiley and Sons.

To better understand the mechanism of this shift, we investigated the interaction of the metal ions with the copolymer in solution using FTIR (Figure

2.7). When the copolymer is dissolved in methanol in the absence of metal ions, the peak at 1700 cm^{-1} , characteristic of COOH groups, decreases while the band for deprotonated COO^- groups at 1390 cm^{-1} increases,²³⁰ showing partial deprotonation of acid groups. A triplet peak around 1730 cm^{-1} confirms hydrogen bonding with methanol (Appendix A1). When NaOAc is added at $r=20$, a broad absorption peak centered on 1575 cm^{-1} appears, arising from ionic interactions of Na^+ ions with carboxylate groups.^{198, 231} This peak grows when the NaOAc concentration is increased ($r=10$). This implies that the Na^+ and COO^- groups interact through electrostatic interactions. The decrease in micelle diameter likely arises from the insertion of Na^+ ions between the carboxylate groups, shielding electrostatic repulsions and pushing them apart to increase the curvature of the corona²³² (Scheme 2.2b).

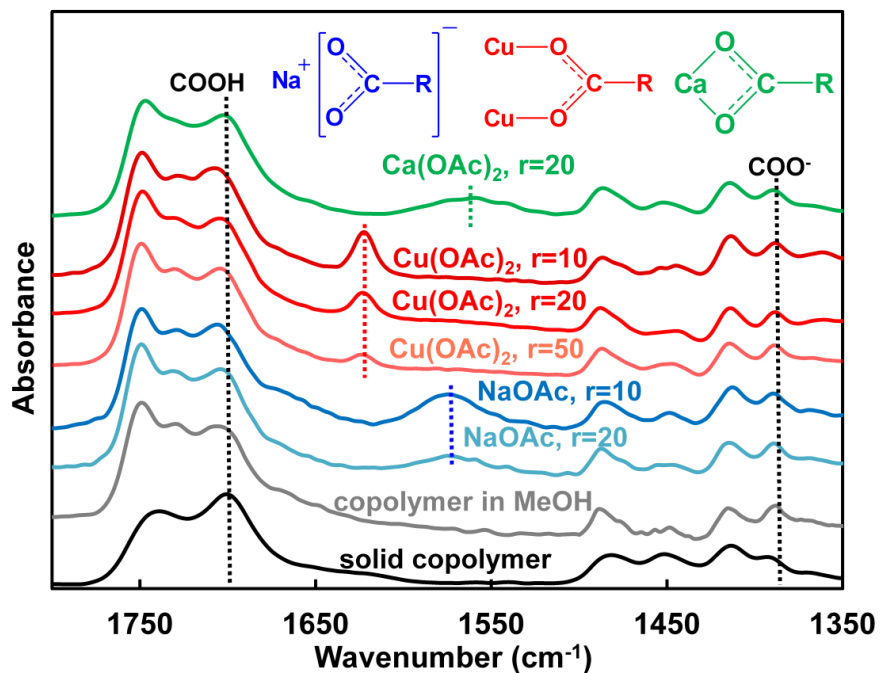


Figure 2. 7. FTIR spectra for the copolymer and its solutions in methanol with the addition of different metal ions at increasing concentrations. Reprinted with permission from¹⁷¹. Copyright © 2017, John Wiley and Sons.

Unlike monovalent ions (e.g. Na^+), divalent and trivalent cations can form complexes with multiple carboxylate groups. These complexes may take on different geometries, such as the bridging bidentate and chelating bidentate conformations (Figure 2.7)^{198, 233-236}. In the bridging bidentate configuration, a binuclear complex is formed through the association of two metal ions with two pairs of adjacent carboxylate groups. In the chelating bidentate configuration, both oxygen atoms of the carboxylate are bound to one metal ion. These interactions can affect the supramolecular assembly of carboxylate containing polymers, including P(TFEMA-*r*-MAA). Indeed, when $\text{Cu}(\text{OAc})_2$ was added to P(TFEMA-*r*-MAA) in methanol ($r = 20$), the size of both the smaller micelles and the larger vesicles increased (Figure 2.6b). The average micelle diameter increased to 20 nm. TEM images of supramolecular assembly in the presence of $\text{Cu}(\text{OAc})_2$ in methanol (Figure 2.2e, f) also showed large vesicles. This increase in size may arise from the complexation of the metal ions with multiple MAA units, pulling these groups together and flattening the interface. Cu^{2+} can also link multiple micelles together into clusters.²³⁷ The bridging of multiple carboxylate groups creates long chains of interlinked MAA groups and screens electrostatic repulsion between them. This allows them to pack closely and form vesicles^{232, 238} observed in the TEM images (Scheme 2.2c, d and e). To better understand the mechanism of interaction between Cu^{2+} ions and the MAA units, FTIR analysis was performed (Figure 2.7). The addition of $\text{Cu}(\text{OAc})_2$ to the copolymer dissolved in methanol led to a new peak at 1620 cm^{-1} that grows with increasing copper acetate concentration, corresponding to bridging bidentate complexation of the MAA groups with Cu^{2+} ions.^{230, 239} No

peaks associated with ionic (1575 cm^{-1}) or chelating bidentate interactions (1560 cm^{-1})²³⁹ were observed. The bridging bidentate conformation was further confirmed using UV-visible spectroscopy (Figure 2.8). The solution of $\text{Cu}(\text{OAc})_2$ in methanol had two absorption peaks at 310 nm and 703 nm in the absence of the copolymer. When the copolymer was added to the solution, the intensity of the peak at 703 nm increased with a slight shift to lower wavelengths. These changes in the UV spectrum indicate the complexation of Cu^{2+} ions with carboxylate groups.²⁴⁰ Both the shift and intensity enhancement were more pronounced with increasing Cu^{2+} ion concentration. The spectrum also depicts the type of complexation. The only absorption peak for copolymer solutions in methanol was in the UV region, at ~ 250 nm. However, when, the copolymer was dissolved in the presence of $\text{Cu}(\text{OAc})_2$, a shoulder peak at 370 nm appeared. This corresponds to the binuclear complex between Cu^{2+} ions and COOH groups.²³⁶ This indicates that, independent of the metal ion concentration, most or even all Cu^{2+} -MAA interactions are in the bridging bidentate conformation, likely favored due to short segmental distance between the carboxylate groups along a statistical polymer chain.²³⁵

Unlike copper, calcium and aluminum typically complex with carboxylate groups in the chelating bidentate configuration.^{230, 241} This is evident by the newly introduced peak at about 1560 cm^{-1} (Figure 2.7) attributed to the chelating bidentate complex of Ca^{2+} with carboxylic groups.^{230, 241} Unlike the bridging bidentate geometry that links adjacent carboxylate groups on the same polymer chain, chelating bidentate complexes often link carboxylate groups on separate polymer

chains. This induces gelation upon adding even very small amounts of $\text{Ca}(\text{OAc})_2$ ($r=50$).²⁴² Al^{3+} ions from AlCl_3 created a gel at an even lower concentration of $r=100$.

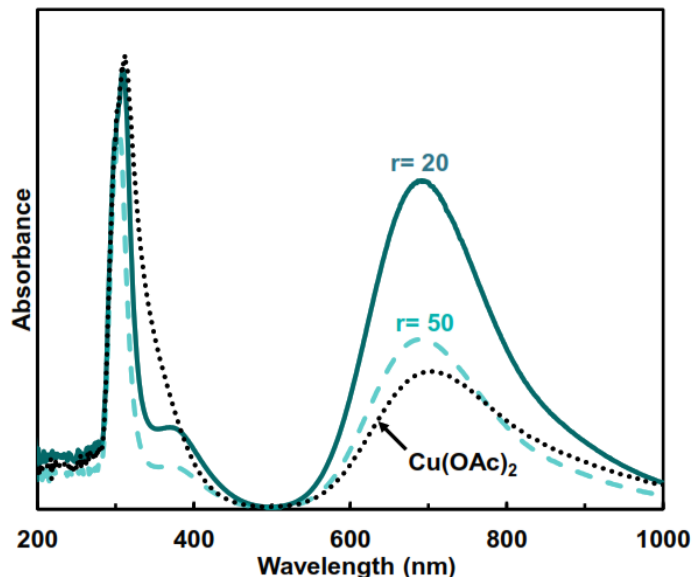


Figure 2. 8. UV-visible spectra showing the complexation of carboxylate with Cu^{2+} ions; $\text{Cu}(\text{OAc})_2$ in methanol is shown by dotted line, dash line corresponds to the copolymer solution with $\text{Cu}(\text{OAc})_2$ in methanol at $r=50$, and solid line shows the copolymer solution with $\text{Cu}(\text{OAc})_2$ at $r=20$. Reprinted with permission from¹⁷¹. Copyright © 2017, John Wiley and Sons.

The counter-ion to the complexing metal ions also plays a significant role. Chloride salts of Ca^{2+} and Cu^{2+} led to larger micelles compared with the corresponding acetate salts (Appendix A1). Furthermore, these salts did not form complexes with MAA groups according to FTIR and UV spectra, even at higher concentrations up to $r=1$ (Appendix A1). The formation of complexes may be curtailed by the fact that when $\text{Ca}^{2+}/\text{Cu}^{2+}$ ions interact with carboxylate groups, protons are released. In aqueous solution, these protons are accommodated through interactions with water molecules. Methanol, however, does not easily get protonated. When acetate salts are used, protons produced can bond with acetate ions and form acetic acid, a weak acid. This removes protons from the organic

solution, enabling further ionization of carboxylic acid groups on the micelles. In contrast, when CaCl_2 or CuCl_2 is used, the protons are not removed from the solution. This can suppress the ionization of the carboxylic acid groups, preventing the formation of adjacent COO^- groups that can form bidentate complexes,²¹⁰ and lead to an increase in micelle size due to weaker electrostatic repulsions in the corona.

Based on the results obtained in this section, we selected methanol as the solvent for membrane casting solution mainly due to formation micelles with more uniform size and presence of MAA groups on the corona. We expect that this morphology will benefit the final membrane structure as it may lead to increase in the carboxylate functional groups on the membrane pores as the micelles self-assemble and form the selective layer. In addition, as shown above, membranes have the potential for complexation with metal ions and subsequently metal ion removal from wastewater.

2.3.3. Formation of packed micelle arrays

We utilized the assembly of the micelles described above to form membrane selective layers that feature nanometer-scale channels with carboxylate functional walls, arising from the interstices between micelles packed together. To form such membrane selective layers, this micellar solution is coated onto a porous support (a commercial membrane with large pore size). Methanol is allowed to evaporate briefly to increase the local micelle concentration, forming a tightly packed micelle array triggered by capillary forces between the micelles.²⁴³⁻²⁴⁶ During evaporation,

particles on the topmost layer arrange themselves into the most favorable ordered structure. The coated membrane is then immersed into water. P(TFEMA-*r*-MAA) copolymers with ≤ 55 wt% MAA are insoluble in water, so this step causes the micelles to precipitate out quickly, their morphology preserved due to their rigid and hydrophobic TFEMA-rich core.

The water immersion step is crucial, because the packed micelle structure is not an equilibrium morphology. In general, micelles and vesicles formed in solution (here, in methanol) are very dynamic. Micelles formed by random copolymers are even more dynamic due to their thinner corona.¹⁸⁷ Their morphology changes upon solvent evaporation and during the formation of the selective layer. With a long enough evaporation time, the capillary pressure can reach a critical value above which particles are stressed above their limit of deformation. Micelles merge and forms a continuous, dense polymer layer. Other researchers have also observed that upon solvent evaporation, random copolymer micelles often merge.¹⁸¹ This means that controlling and stabilizing the micellar morphology far from equilibrium is important in this approach to bottom-up nanostructure fabrication.

To characterize the effect of drying time on how micelles assemble into packed arrays, we performed TEM on thin film samples prepared on TEM grids using a process that simulated the membrane formation process (Figure 2.9). We dipped TEM grids into 0.3 wt% CP40 copolymer micelle solutions in methanol to form a thin film. After varying evaporation times in air, the grids were dipped into water to fix the structure. When the polymer film was immediately submerged in DI water with no evaporation time, isolated ~ 20 nm micelles and some large

micelles or vesicles (~200 nm) were observed (Figure 2.9a). It is likely that smaller micelles were also present in solution that either merged to form these large structures or dispersed into the water due to lack of cohesion. Obviously, this structure is not suitable to serve as a membrane selective layer. When the solvent is allowed to evaporate for 10 s before immersion into water, clusters of smaller micelles were observed in the deposited film in addition to a small number of large vesicles (Figure 2.9b). When the film was dried for 20 s and then dipped in DI water, a closely packed array of micelles and vesicles of varying sizes spanning a large area was observed (Figure 2.9c). The dark stained regions, gaps between these micelles, can now act as effective nanochannels that would enable permeation through the membrane selective layer. Longer evaporation times led to merged micelles and continuous thin films (Appendix A1).

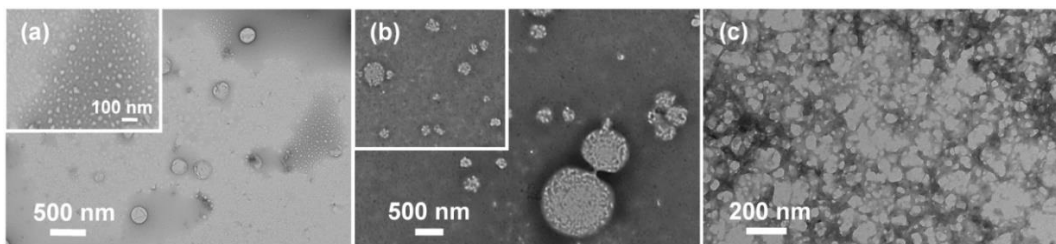


Figure 2. 9. TEM images of the P(TFEMA-*r*-MAA) micelle assemblies cast from a solution in methanol by immersion into water after (a) No evaporation time (b) 10 s evaporation and (c) 20 s evaporation. The insets in (a) and (b) show higher magnification images (scale bar: 100 nm) of the smaller ~ 20 nm micelles, in isolation or in clusters. Large vesicles and small isolated micelles cluster form packed assemblies upon solvent evaporation. Reprinted from¹⁷⁰. Copyright © 2017 American Chemical Society.

2.3.4. Membrane Formation and Morphology

These experiments showed that closely packed micelle arrays can be formed and stabilized by spreading the micelle-containing solution as a thin film, evaporating the solvent briefly, and then immersing the film into water to freeze the packed array before the micelles merge. As the next step, we aimed to apply this method to make micelle arrays on porous supports, to serve as membrane selective layers. During the use of these membranes, the carboxylate groups on the micelles become negatively charged in water due to their low pK_a (between 3-5.5 for PMAA homopolymer²⁴⁷⁻²⁴⁹). This enables the membrane to exhibit charge-based selectivity through Coulombic interactions between these pore walls and solutes. Furthermore, the carboxylic acid groups provide a great platform for further functionalization of the membrane.²⁵⁰

Membranes were fabricated from both copolymer compositions by depositing the copolymer micelles onto a commercial support membrane by a coating process, designed to enable the micelles to pack together on top of the membrane, but prevent their merging into a non-porous film. For this purpose, a solution of 5 wt% copolymer in methanol was spread onto a porous UF membrane (Polyacrylonitrile, PAN 400, Nanostone) using a doctor blade to form a thin layer. The solvent was allowed to evaporate for 20 s to direct the self-assembly of the copolymer into the desired nano-structured selective layer. Shorter evaporation times typically led to poor rejection, indicating incomplete coverage of the surface with the micelle arrays. Extended evaporation times lead to the merger of micelles to form a uniform, dense coating layer (Appendix A1). It is likely that when optimal

evaporation times are used, the resultant layer features the partial fusion of micelles at points of contact, perhaps through copolymer chains that bridge two micelles. Subsequently, the film was submerged into a water bath, which quickly precipitated the micelles, whose morphology is preserved due to the hydrophobicity and high T_g of PTFEMA core. The self-assembled random copolymer micelles are kinetically trapped in a packed array of spheres. Hydrogen bonding between MAA groups on the micelle surfaces also likely reinforces the integrity of this layer. The interconnected interstices between them provide permeation pathways, lined with carboxylic acid groups (Scheme 2.1).

The resultant membrane selective layer with packed micelles can be observed by high resolution scanning electron microscopy (SEM) imaging of membrane cross-sections and surfaces. SEM images for the support membrane and membranes made from both copolymers are shown in Figure 2.10. The surface morphology of the support membrane (Figure 2.10a) is distinctly different than that of the CP40 and CP50 coated membranes (Figure 2.10b and c), confirming the presence of a continuous selective layer. The surfaces of both CP40 and CP50 coated membranes feature closely packed small spherical micelles. Cross-sectional images of both copolymer coated membranes (Figures 2.10e and f) exhibit a ~400 nm thick selective layer well adhered onto the support membrane, shown in Figures 2.10d and g. At higher magnification (Figures 2.10h and i), a nicely packed array of spheres on top of the support can be seen for both copolymers. In case of the membrane prepared with the CP40 copolymer (Figure 2h), the micelle size distributions obtained from the cross-section and surface images are consistent with

both DLS and TEM (Appendix A1). However, the SEM image of the CP50 coated membrane (Figure 2.10i) shows larger micelles (20-25 nm) in comparison to DLS (8 nm). This can be attributed to bigger clusters forming during solvent evaporation in case of CP50 due to its lower hydrophobic repeat unit content, providing it with less rigidity and stability during the membrane formation process.

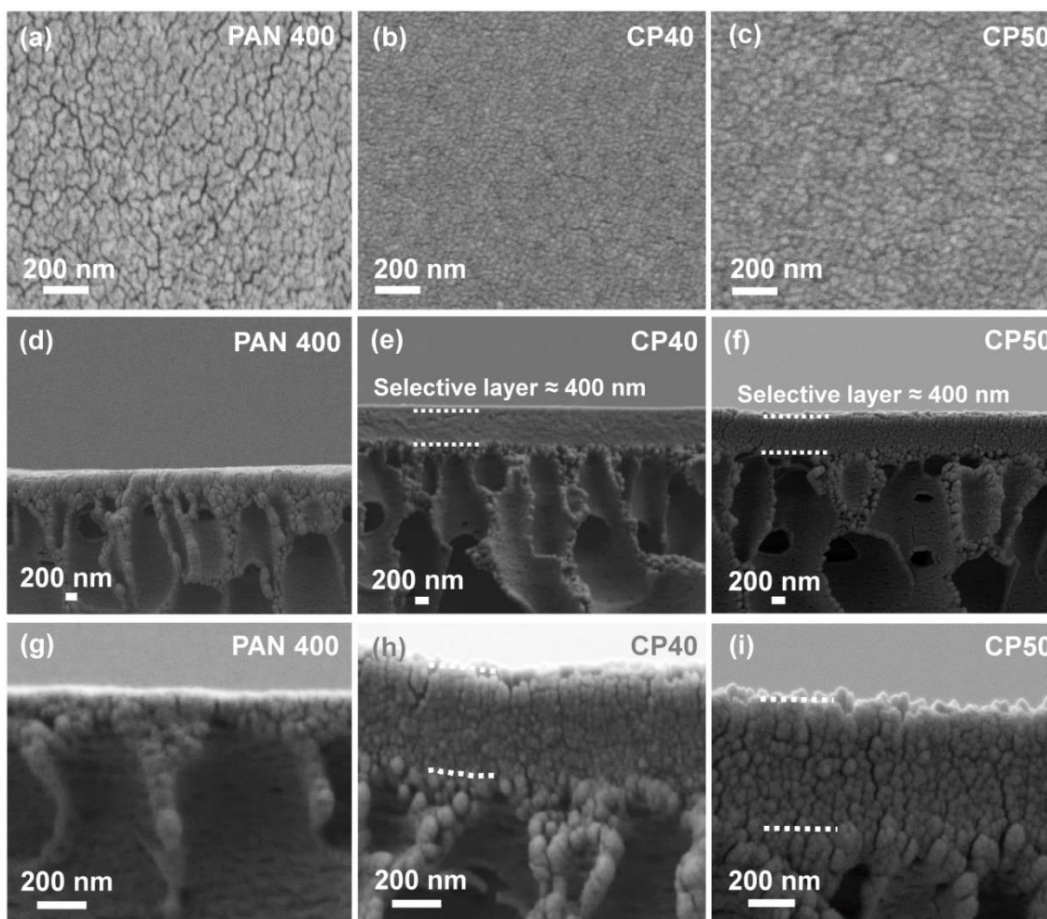


Figure 2. 10. SEM micrographs of (a) PAN 400 support membrane surface morphology, (b) CP40 membrane surface morphology, (c) CP50 membrane surface morphology, (d,g) PAN 400 cross section, (e, h) CP40 cross section, (f, i) CP50 cross section. Both CP40 and CP50 coated membranes exhibit packed arrays of micelles, interstices between which act as permeation pathways. Reprinted from¹⁷⁰. Copyright © 2017 American Chemical Society.

The micelles maintain their discrete structure throughout the layer in both copolymer coated membranes. The inter-micellar spaces provide the path for the

transport of solute through the selective layer. In some regions, especially in the topmost layer, the micelles arrange themselves into semi-regular arrays and provide a continuous path throughout the selective layer, similar to what has been reported for block copolymer micelle assembly.²¹⁷ The solute pathway is more tortuous in the layers below. The tight packing of the micelles in the top layer was also documented by atomic force microscopy (AFM) (Figure 2.11a). This image was analyzed to determine if the packed micelles showed significant ordering. Two-dimensional fast Fourier transform (2D-FFT) pattern of the AFM height image was radially integrated for a more quantitative evaluation using ImageJ software (Figure 2.11b). This plot shows peak positions (1: $\sqrt{3}$: 1.9) that suggest a high density of uniform micelles with a hexagonal close-packed (HCP) structure. The packing, however, is imperfect, with other irregular structures (pentagons, polygons) dispersed among the HCP array (Figure 2.11a). As a general rule, micelles of monodisperse size prefer to arrange in hexagonal patterns that lead to the densest possible packing.²⁵¹ The wide size distribution of the micelles observed in this case likely leads to the defects and heptagonal and pentagonal structures.²⁵² The position of q^* peak can further be used to calculate the lattice parameter of HCP structure to be $a=14$ nm (Appendix A1). Note that a corresponds to the distance between micelles' centers and thus larger than the micelle size. Thus, this value is overall consistent with the micelle size obtained by microscopy imaging and DLS experiments. The minor disparities between exact values can be attributed to the tip broadening effect in AFM, resolution of the tip, and potential fusion of the micelles on the surface during selective layer formation.

It is worth noting that the TEM image in Figure 2.9c is obtained in a condition that mimics the membrane fabrication process. The Figure shows closely packed, but not well-organized micelles. This could arise from the fact that TEM was acquired from a very thin layer formed on the TEM grid using a very dilute solution. Therefore, various forces that may be at play in creating the ordered structure in the multi-layered structure on the membrane may not be as significant in this system.

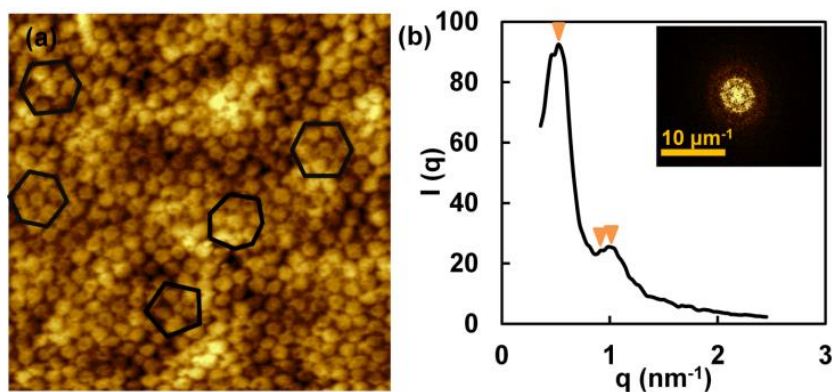


Figure 2. 11. (a) AFM height image of CP40 membrane ($10\ \mu\text{m} \times 10\ \mu\text{m}$ with z-range of 200 nm), showing spherical micelles packed in a hexagonal close packed (HCP) array with few irregular polygons (b) 2D FFT pattern corresponding to AFM height image (c) FFT analysis; dash markings correspond to $(q/q^*)^2 = 1, 3, 3.7$ showing almost 2D HCP structure. Reprinted from¹⁷⁰. Copyright © 2017 American Chemical Society.

Based on the packing geometry and the average micelle size determined from SEM micrographs (both surface and cross-section morphologies), we estimated the average membrane pore size¹⁶⁴⁻¹⁶⁵ to be around 3 nm for the CP40 membrane and slightly larger (4 nm) for the CP50 membrane (Appendix A1). It should be noted that this estimation relies exclusively on the geometry of the packed layer and does not account for the alignment or polydispersity of the micelles. It also utilizes the micelle size from SEM micrographs, which were obtained in the dry state. The

effective pore size in water is likely to be smaller due to the hydration of the copolymer.

This multilayered assembly of micelles creating an interconnected network of nanochannels offers significant advantages. The structure confines flow into nanometer-scale channels lined with a high density of functional groups.^{38, 253} The HCP structure, one of two densest packing structures for spheres, provides the narrowest pore size and hence a high density of functional groups lining the pores. This leads to more solute-pore-wall interactions during permeation. Unlike cylindrical nanochannels, this structure does not need to be aligned perpendicular to the membrane surface. While the high tortuosity may lead to slightly lower permeance,¹⁴⁶ it also increases solute-wall contacts during permeation. This can lead to enhanced separation selectivity.²⁵⁴ The presence of multiple permeation paths also minimizes the negative effects of potential pore clogging during operation. Therefore, these interconnected nanochannels provide superior permeation properties and selectivity.²⁵⁵ Finally, since the rigid and hydrophobic micelle core remains impervious to water and provides a rigid structure, the self-assembled nanostructure is resistant to swelling. This permits high and more stable permeability and selectivity in comparison with selective layers where the functional groups are spread throughout the layer.

The polymer concentration in the coating solution affects the final performance of the membrane. High polymer concentrations in the coating solution (>10 wt%) with the same evaporation times resulted in low membrane permeability ($0.15 \text{ L m}^{-2} \text{ h}^{-1} \text{ bar}^{-1}$). While this is at least partially due to the deposition of a larger

quantity of micelles on the membrane surface, it may also arise from the micelles merging into a non-porous film more quickly. The porous membrane support also had a significant impact on coating morphology and membrane performance. The multilayered micelle structure was not seen when support membranes with larger surface pore sizes were used (PVDF400R, Nanostone), Appendix A1. The large surface pore size most likely allowed the intrusion of micelles into the membrane, instead of forming a layer on top. The penetration of micelles inside the pores resulted in clogging the membrane pores, leading to very low permeability ($<0.1 \text{ L m}^{-2} \text{ h}^{-1} \text{ bar}^{-1}$). These results demonstrate that while the proposed approach is simple to execute overall, manufacturing parameters must be selected carefully to enable the formation of a stable layer of packed micelles, arrested on the membrane surface.

2.3.5. Membrane Performance

The permeation properties and selectivity of membranes prepared as above were studied using two types of experiments: Diffusion, and filtration. Diffusion tests are simple. Permeation under these conditions is well understood and modeled, and selectivity results can be linked to parameters such as solute diffusivity and solute-membrane affinity. Furthermore, most literature in the field of chemical selectivity in membranes reports diffusion test results.^{33, 37-38, 40, 256} However, membranes rarely operate under conditions used in these experiments. In realistic applications, pressure-driven flow through the membrane is used. Convective flow through the membrane during such operation may influence how the membrane behaves. Under pressure, some polymers may change their conformation or

solubility, leading to changes in rejection.⁶⁴ Transport limitations and boundary layer features can be significantly different in the two modes of operation, affecting performance. Thus, pressure-driven filtration experiments were also performed to characterize the performance of our membranes.

2.3.5.1. Effect of copolymer composition on membrane permeability

The permeance (L_p) of membranes prepared from both copolymers were measured by pressure-driven filtration experiments and are listed in Table 2.1. CP50 membranes showed higher permeance due to higher MAA content and thus higher hydrophilicity, confirmed by their lower contact angle. Both CP40 and CP50 coated membranes maintained high permeances ($4.2\text{--}7.3\text{ L m}^{-2}\text{ h}^{-1}\text{ bar}^{-1}$) comparable to commercially available nanofiltration membranes ($2.1\text{--}13.4\text{ L m}^{-2}\text{ h}^{-1}\text{ bar}^{-1}$) and some tight UF membranes with molecular weight cut-off (MWCO) values between 1000–3000 Da ($1.1\text{--}5.7\text{ L m}^{-2}\text{ h}^{-1}\text{ bar}^{-1}$) based on industrial specification sheets.²⁵⁷ We further calculated the selective layer permeability (P_m), defined as membrane permeance normalized by selective layer thickness, using the resistances in series model (see Supporting Information). Selective layer permeabilities were between $1.7\text{--}3.7\text{ L }\mu\text{m m}^{-2}\text{ h}^{-1}\text{ bar}^{-1}$, higher than that of commercial TFC nanofiltration membranes ($0.2\text{--}1.4\text{ L }\mu\text{m m}^{-2}\text{ h}^{-1}\text{ bar}^{-1}$),²⁵⁷ calculated assuming a selective layer thickness of $0.1\text{ }\mu\text{m}$.²⁵⁸⁻²⁵⁹ While the selectivity properties of commercial NF and UF membranes are by definition distinct from the proposed membranes, this serves as a broad comparison regarding their potential industrial use.

2.3.5.2. Effect of pH on membrane permeance

The membrane permeance did not change with pH when tested between pH 3-9 (Figure 2.12). This is in contrast to the pH responsive behavior shown in block copolymer membranes,^{155, 260} in which the pores can reversibly close or open and act as a pH-sensitive gate when the hydrophilic block contains weak acids or bases such as acrylic acid²⁶¹⁻²⁶² or pyridine.^{217, 243, 263} The difference arises due to the fact that PMAA segments in the PTFEMA-*r*-MAA random copolymer are very short, and cannot undergo the conformational transformations feasible for longer blocks found in BCPs.

The rejection properties of the CP40 membrane was also studied at different pH values. For this test, we prepared a 0.1 mM solution of pyrenetetrasulfonic acid tetrasodium salt (Na₄PTS, 8.8 Å). The PTS⁴⁻ ion remains ionized over a wide range of solution pH values. Na₄PTS was filtered through membrane at different pH values (pH= 4, 6, 7, 8). Similar rejections of about (90-98%) were obtained over the pH range tested (repeated on at least three membrane swatches).

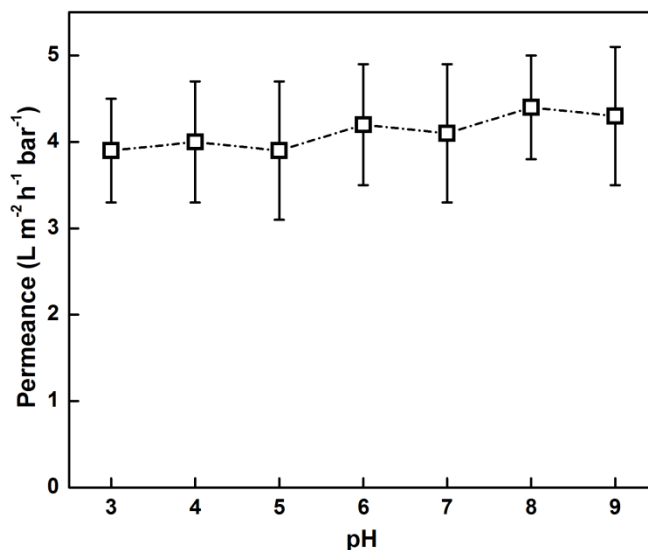


Figure 2. 12. Effect of pH on permeance of CP40 coated membrane, pH was adjusted by HCl or NaOH. Reprinted from¹⁷⁰. Copyright © 2017 American Chemical Society.

2.3.5.3. Diffusion experiments: charge-based selectivity between organic solutes

2.3.5.3.1. Single-solute diffusion experiments

Diffusion experiments with small organic molecules can provide insight into the relative effects of different transport mechanisms involved during permeation. In these membranes, electrostatic interactions between the solutes and the negatively charged carboxylate groups on the pore walls are expected to play the most dominant role on solute permeation. Thus, solute diffusion rate is expected to strongly depend on solute charge, leading to charge-based separation capabilities. In addition to the electrostatic interactions, steric effects can also contribute to permeation selectivity given the very small, 1–3 nm pores involved. Hydrophobic interactions and the adsorption of the solutes into the membrane pores can also play a role.

For these experiments, we selected a set of organic small molecules varying electrostatic charges: Basic blue 3 (BB3, cationic), Acid Blue 45 (AB45, anionic), and Riboflavin (RIB, neutral). All three solutes were selected to have similar calculated sizes (8.3–8.6 Å, calculated using Molecular Modeling Pro¹⁵⁸⁻¹⁵⁹) (Figure 2.13). The pH of the solutions used in diffusion and filtration experiments varied between 5.4 and 7.5 (Figure 2.13). The pK_a of carboxylic acid groups in the PMAA homopolymer is reported to be between 3- 5.5,²⁴⁷⁻²⁴⁹ below the pH of all used solutions. Therefore, the membrane is negatively charged in all reported experiments. This is further supported by the fact that anionic solute rejection remains unchanged with pH between pH 4- 8.

For each membrane, we used a side-by-side diffusion cell to quantify permeation rates under a concentration gradient driving force. We measured the total solute transferred through the membrane ($n_{\text{transferred}}$) and normalized it by the driving force for diffusion, the feed concentration (ΔC) to obtain the normalized moles of solute transferred, N , defined as:

$$N = \frac{n_{\text{transferred}}}{\Delta C}$$

To quantify differences in the flux of different molecules through the same membrane, we calculated selectivity coefficients (α), defined as the ratio of the permeation rates of two species whose charges are noted in the subscript (Table 2.2).

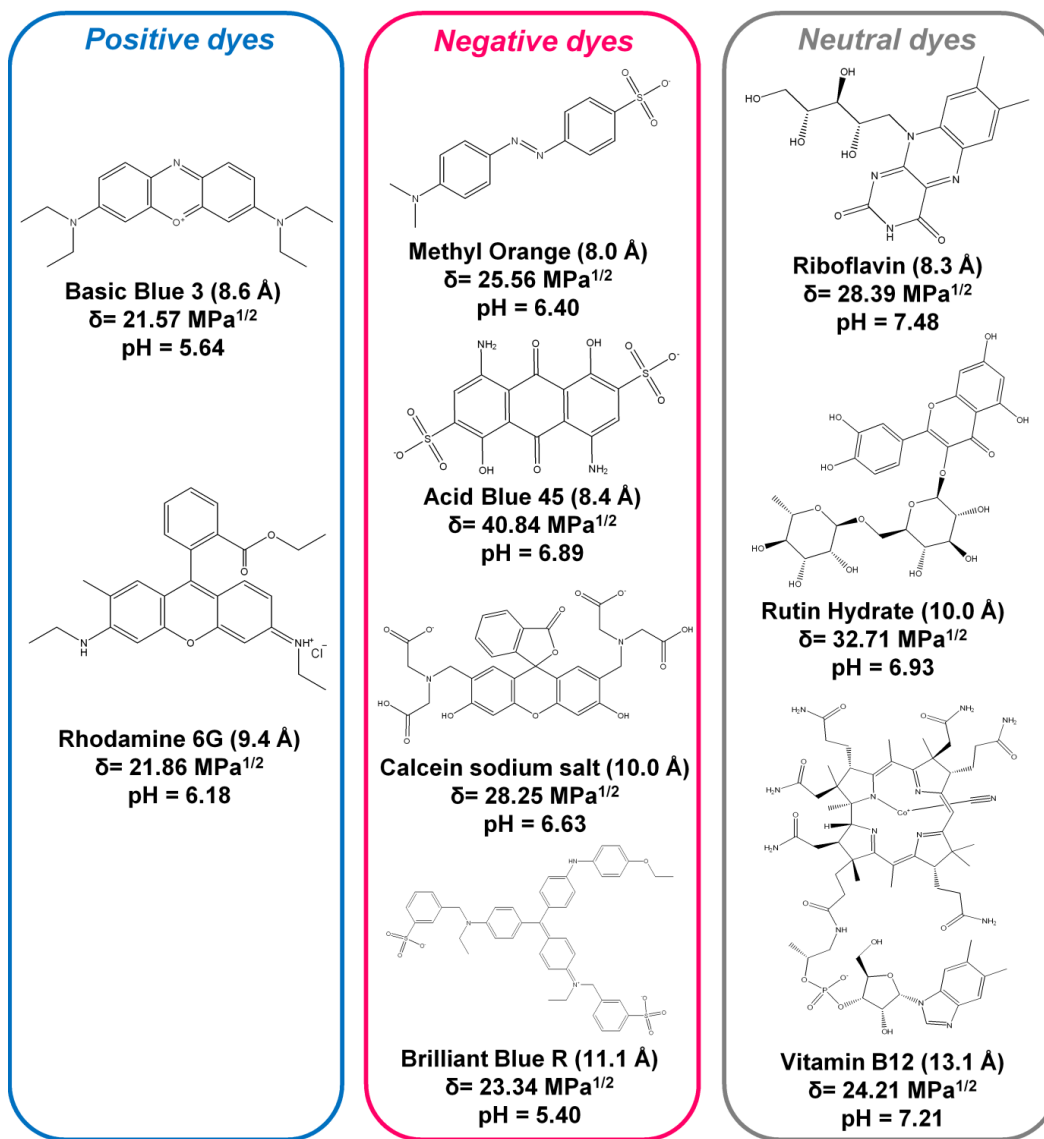


Figure 2. 13. Structure and solubility parameters of organic molecules; molecule size is calculated using Molecular Modeling Pro. Reprinted from¹⁷⁰. Copyright © 2017 American Chemical Society.

Table 2.2. Solute transfer rates and separation coefficients (α) for PAN400, CP40 and CP50 membranes in single-solute and competitive diffusion experiments. Reprinted from¹⁷⁰. Copyright © 2017 American Chemical Society.

Membrane code	Solute transfer rate ($\times 10^{-9}$ m s ⁻¹)					Separation factor for single-solute		Separation factor, $\alpha_{0/-}$ in mixture
	Single-solute			Mixture				
	BB3 (+)	AB45 (-)	RIB (0)	AB45 (-)	RIB (0)	(+) and (-), $\alpha_{+/-}$	(0) and (-), $\alpha_{0/-}$	
PAN400	338	276	359	245	264	1.2	1.3	1.1
CP40	21 \pm 3	0.75 \pm 0.05	197 \pm 9	- ^{a)}	238 \pm 8	28.1	263	>300 ^{b)}
CP50	107 \pm 7	21.5 \pm 1.5	203 \pm 4	- ^{a)}	265 \pm 6	5.0	9.4	>400 ^{b)}

^{a)} No detectable amount of AB45 was transferred; ^{b)} The α value is calculated by considering the detection limit at the end of the experiment.

To ensure all differences observed are attributable to the selective layer of packed micelles, we first tested the permeation of these solutes through the porous support membrane. All three solutes had similar permeation rates (Figure 2.14a). The similar permeation rates also confirm that all three solutes have about the same size and diffusivity. Support membrane showed a delay in permeation of positively charge molecules due to adsorption, likely due to the presence of negatively charged groups on the membrane incorporated by the manufacturer to prevent fouling. Nonetheless, the pseudo-steady-state fluxes of all three molecules are very similar. Hence, we expect that in this system, differences in ion permeation rates will be dominated by electrostatic interactions within the nanopores.

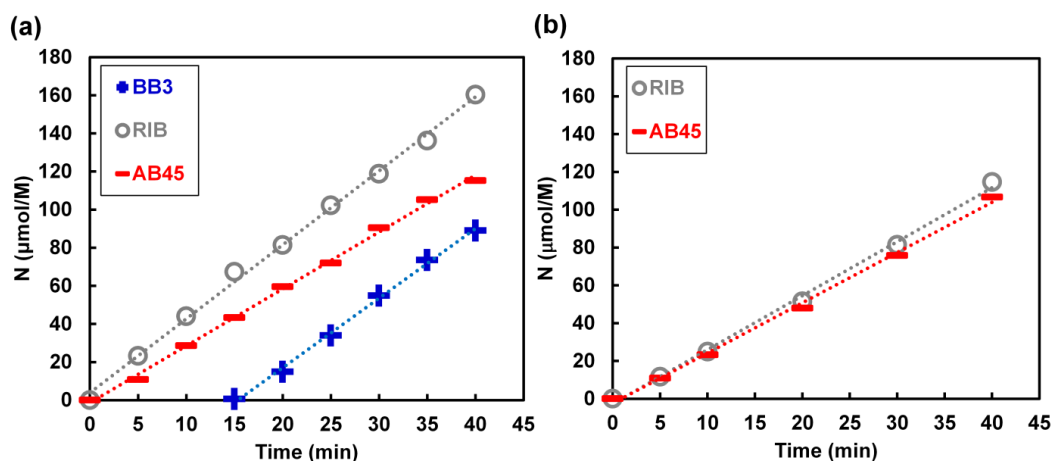


Figure 2. 14. Diffusion of organic molecules through support membrane in (a) Single-solute, and (b) Competitive diffusion experiment. Reprinted from¹⁷⁰. Copyright © 2017 American Chemical Society.

Figure 2.15 shows the permeation of these three solutes through the CP40 coated membrane. The neutral solute permeated through the membrane 263 times faster than the negatively charged solute of similar size due to the exclusion of negatively charged solutes from the pores as a result of repulsive forces. The $\alpha_{0/-}$ value of 263 is an order of magnitude higher than the highest value reported in the literature for functional nanopore membranes formed by bottom-up methods.⁴⁰ The positively charged solute started permeating through the membrane after a delay, associated with the adsorption of these solute ions onto the membrane pores due to Coulombic interactions. After sites are saturated, however, the positively charged solute starts to diffuse at a faster rate than the anionic molecules leading to $\alpha_{+/-}$ value of 28. The lower separation factor for the cationic molecule in comparison to the neutral one is likely due to several factors that slow down the permeation of cationic groups through the membrane. First, maintaining electroneutrality during the passage of cationic solutes across the membrane also requires the passage of

counter-ions, which are repelled by the negatively charged membrane. This slows down the passage of cationic solutes. We also observed significant adsorption of cationic solutes onto the membrane, leading to delayed penetration of the solute into the permeate (Table 2.3). This results in significant pore narrowing, given the similarity between the size of the pores and the solutes. Indeed, when diffusion rate of a neutral solute was measured again after exposing the membrane to the cationic solute, a slower diffusion rate was recorded, indicating that some of the pore blockage due to adsorption is not easily reversible. Extensive washing is required to obtain the original diffusion rate. Thus, experiments with cationic solutes were only run after all other experiments were complete.

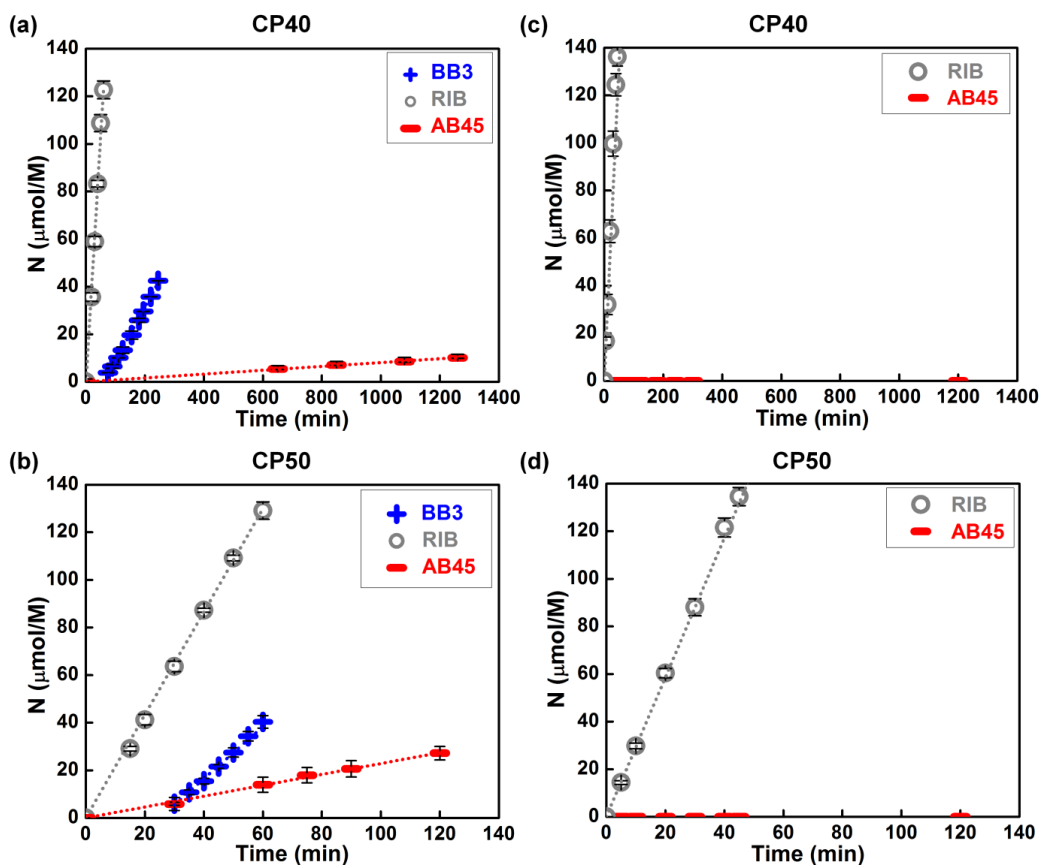


Figure 2. 15. The permeation of organic molecules through (a,c) CP40- and (b,d) CP50-coated membranes in (a,b) Single-solute and (c,d) Competitive diffusion

experiments for a mixture of negative and neutral solutes. Selectivity between neutral RIB and anionic AB45 is enhanced in competitive diffusion experiments, as the permeation rate of AB45 through both CP40- and CP50-coated membranes is shifted below the detection limit. N is defined as the total number of moles of solute transferred divided by feed concentration. Reprinted from¹⁷⁰. Copyright © 2017 American Chemical Society.

Effect of copolymer composition on membrane selectivity. Membrane selective layers prepared from CP40 and CP50 have different effective pore sizes and charge densities. The higher MAA content of CP50 can lead to higher charge density on the micelles. This is confirmed by static adsorption tests for the positively charged solute. Membranes with known areas prepared from CP40 and CP50 polymers, as well as the support membrane, were soaked in 10 ml solution of 0.005 mM BB3 overnight. The adsorption of this positively charged dye was calculated by measuring the dye concentration before and after the immersion using UV-Vis spectrophotometry and performing a mass balance. The support membrane exhibited significant adsorption of this dye (Table 2.3), likely due to the surface treatment of this commercial membrane during manufacture to improve wetting and fouling resistance. Both coated membranes showed significantly higher dye adsorption, however. The CP50 coated membrane adsorbed more BB3 than the CP40 coated membrane, as expected due to the higher MAA content in the copolymer. This confirms a higher BB3 binding capacity for CP50 than CP40.

Table 2. 3. Static adsorption experiments for support membrane, CP40 and CP50. Reprinted from¹⁷⁰. Copyright © 2017 American Chemical Society.

Membrane	moles adsorbed/cm² (×10⁶)
Support	6.4
CP40	7.3
CP50	10.0

On the other hand, CP50 coated membranes have slightly larger effective pore size and higher pure water permeability than their CP40 coated counterparts. The combination of these effects may influence membrane selectivity in different ways. Significantly higher permeation rates were observed for cationic and anionic solutes, whereas that of the riboflavin was comparable with the CP40-coated membrane (Table 2.2). Selectivities between solutes were lower, with $\alpha_{+/-}$ around 5 and $\alpha_{0/-}$ around 9 (Figure 2.15b). This implies that the increase in the pore size enabled easier passage of the anionic solutes despite the increase in the charge density along the walls. The relatively slower diffusion rate of the positively charged dye likely arises from the partial clogging of pores caused by more prominent adsorption of this solute, curtailing its flux more significantly than observed in the CP40-coated membrane.

2.3.5.3.2. *Competitive diffusion experiments*

The presence of multiple solutes can affect permeation selectivity during operation. For example, one solute may plasticize the membrane selective layer and

decrease the rejection of all others.²⁶⁴ Alternatively, the adsorption of solutes into the pores can lead to constant variation of the rejection of both species. In contrast, in biological pores, permeation selectivity is enhanced in multi-component systems as the solute with favorable interactions prevents other species from entering the pores.²⁵⁴ To better understand the selectivity mechanism of these membranes, we conducted diffusion experiments for a mixture of two solutes with very similar size but differing charge, anionic AB45 and neutral RIB, through both CP40 and CP50 coated membranes (Figure 2.15c and d).

The support membrane showed no selectivity between the two similarly sized solutes (Figure 2.14b). This is expected behavior for most porous materials. Interestingly, permeation selectivity through the CP40 coated membrane was significantly higher in competitive permeation experiments (Figure 2.15c). The normalized permeation rate of neutral Riboflavin was slightly enhanced in comparison with single solute diffusion experiments (Table 2.2). Even more strikingly, the passage of anionic solute was even more strongly inhibited. Similar behavior was observed for the CP50-coated membrane. The transport of the anionic solute was inhibited, whereas the permeation rate of the neutral molecule was enhanced (Figure 2.15d). No detectable amount of AB45 was transferred through either membrane even after 24 h. This meant that permeation selectivity could not be accurately measured; estimates in Table 2.2 indicate the minimum value based on the detection limits of our experiments.

This significantly enhanced selectivity, previously only recorded in membranes with functional nanopores prepared using complicated top-down

methods,²² is believed to arise from the two solutes competing for entrance into the very narrow nanochannels.²⁵⁴ When the “preferred” (in this case, neutral) solute enters the pore, it blocks the channel and prevents the entrance of the “unpreferred” (i.e. anionic) solute. Thus, it is not only more difficult for the anionic solute to enter the channel, but also less probable for it to translocate through the channel due to competition for space with neutral molecules. This results in much stronger inhibition of the permeation of the unfavorable solute compared with when it is present alone. The ability of only one solute to fit into the pore diameter has also been reported to lead to the enhancement of the transport of the “preferred” solute. Although the anionic solute molecules are mostly retained, they may still accumulate near pore entrances, hampering the back-diffusion of the neutral solute molecules, thereby increasing their forward flux.²⁵⁴ These results indicate that the presence of the very narrow channels in these membranes significantly alters some of the key transport mechanisms that dominate selectivity.

2.3.5.4. Rejection of organic solutes in filtration experiments

2.3.5.4.1. Single-solute filtration experiments

To get a better insight into the performance of these membranes under realistic conditions, we studied the membrane separation in pressure-driven filtration. Initially, we filtered a series of solutions each containing one organic solute. We surveyed cationic, anionic, and neutral solutes with various sizes and chemical structures (Figure 2.13).

The rejections of these solutes by the CP40 coated membrane are shown in Figure 2.16a, classified based on solute electrostatic charge. Similar results were also obtained for CP50 (Figure 2.16b). The rejections of anionic solutes were significantly higher than those of neutral and cationic solutes of comparable size. Positively charged solutes are also retained to a greater extent than the neutral ones. This is consistent with the diffusion experiments given the fact that cationic solutes rejected both by their size and electrostatic interaction. The passage of positively charged solutes through the membrane requires the passage of counter-ions bound to it to preserve electroneutrality. The passage of these counter-ions is strongly inhibited by the negatively charged membrane. In contrast, neutral solutes do not experience similar electrostatic interactions and their passage is solely controlled by steric hindrance. This leads to higher rejection of positively charged molecules in comparison to the neutral ones. Furthermore, significant adsorption of cationic solutes observed on the membrane, results in delayed penetration of the solute into the permeate. Rejection increases with increasing solute size, indicating some size sieving effects are also in play. However, the significant differences in rejections of solutes of similar size but different charge indicates that electrostatic interactions dominate the selectivity of these membranes, at least for small molecule solutes. This demonstrates that the proposed membranes are capable of charge-based separation of organic molecules of similar size.

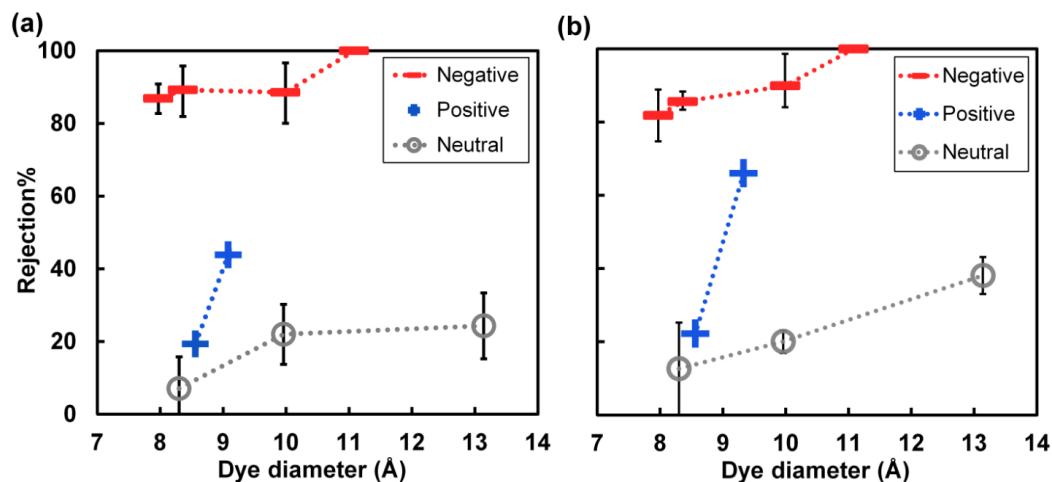


Figure 2.16. Rejections of organic molecules by the (a) CP40, and (b) CP50 coated membranes. Negatively charged solutes (from left to right: MO, AB45, CAL, BBR) are rejected by $>85\%$, whereas low rejections are observed for neutral (from left to right: RIB, RTH, B12) and cationic solutes (from left to right: BB3, Rho6G) of similar size. Reprinted from¹⁷⁰. Copyright © 2017 American Chemical Society.

2.3.5.4.2. Separation of two-solute mixtures based on solute charge

To study the separation behavior of these membranes under more realistic conditions, we filtered the same mixture as in the diffusion experiment (anionic AB45 and neutral RIB), through the CP40-coated membrane. The membrane retained the anionic solute by 96% while allowing the passage of the neutral dye to a large extent, with a rejection of only 23% (Figure 2.17a). Even better separation was achieved between solutes of larger size. The negatively charged solute Brilliant Blue R was retained by 98%, whereas neutral vitamin B12 was rejected by only 25% (Figure 2.17b). Similar results, exhibiting good separation capability between negatively charged and neutral solutes, were also obtained for CP50 coated membranes (Figure 2.17c and d). Similar to diffusion experiments, the rejection values for the anionic dyes in two-solute experiments with the CP40 coated membrane were slightly higher than those measured in single-solute experiments.

For example, the rejection of negatively charged Acid Blue 45 increased from 89% to 96%. All rejection values were comparable with those measured in single-solute tests for the CP50 coated membrane, possibly due to the slightly larger nanochannels.

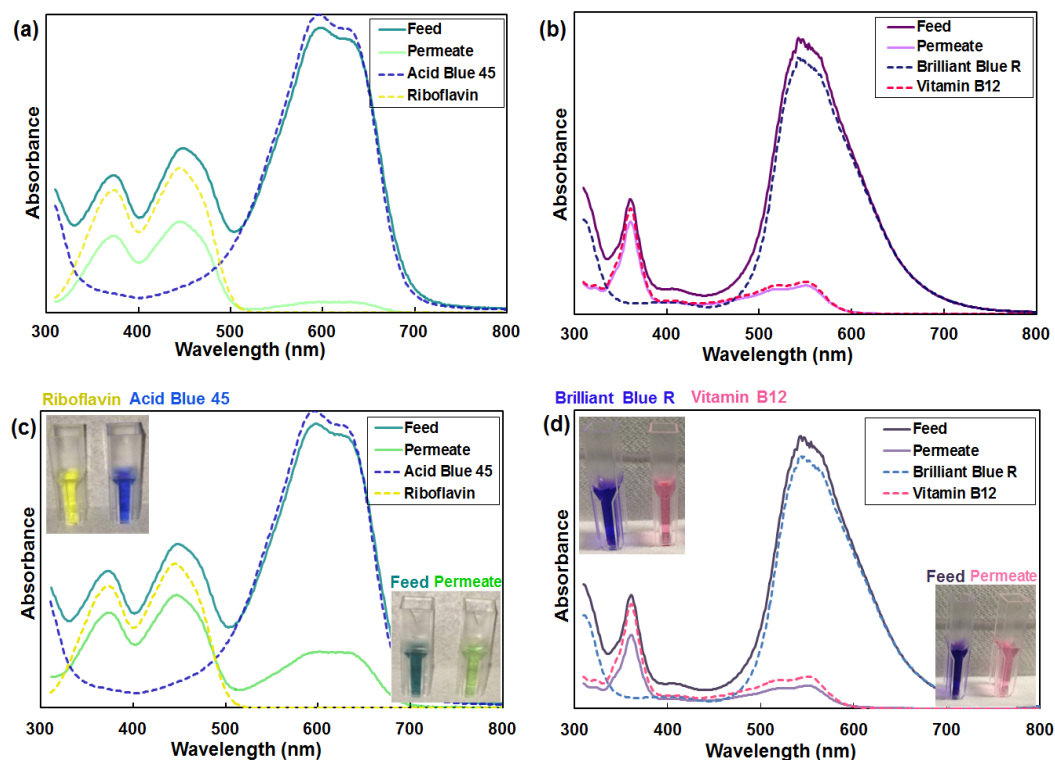


Figure 2.17. Separation of mixture of negative and neutral molecules (a) RIB and AB45 for CP40, (b) BBR and Vitamin B12 for CP40, (c) RIB and AB45 for CP50, (d) BBR and Vitamin B12 for CP50. Reprinted from¹⁷⁰. Copyright © 2017 American Chemical Society.

2.3.5.5. Effect of Ionic Strength on Organic Solute Rejection

In all the experiments described above, we assumed that the separation mechanism is primarily dominated by electrostatics. Charged groups lead to the formation of an electrical double layer (EDL) where co-ions are excluded and counter-ions are enriched inside the nanopores.²⁶⁵ Ionic selectivity for a charged

membrane depends strongly on channel size and the thickness of EDL, typically quantified by the Debye length (λ_D) and calculated according to Gouy-Chapman theory:²⁶⁵

$$\lambda_D = \left[\frac{1000 N_A e^2}{\epsilon_0 \epsilon_r k_B T} \sum_i z_i^2 M_i \right]^{-1/2} \quad Eq. (2.6)$$

where ϵ_0 and ϵ_r are the vacuum and relative permittivity, respectively; k_B is the Boltzmann constant, T is the absolute temperature, e is the elementary charge, N_A is the Avogadro number, z is the valence and M is molar concentration. If the EDL extends through the channel, the passage of co-ions would be strongly inhibited due to electrostatic repulsion. However, if the EDL thickness is smaller than the pore radius, co-ions can pass through the region far enough from the pore walls without being repelled. The Debye length, and hence the effect of Coulombic repulsions, diminishes as the ionic strength of the feed increases. The effective pore size through which anions can pass unimpeded is increased, resulting in lower rejection. Therefore, if separation is dominated by electrostatic interactions, higher feed ionic strength should lead to lower rejection of charged solutes.

To test this hypothesis, solutions of several solutes were prepared in 10 and 100 mM NaCl solutions (Figure 2.18). The Debye length for 10 mM and 100 mM NaCl solutions are calculated to be 3.0 nm and 0.96 nm, respectively. All negatively charged solutes were rejected more effectively in lower ionic strength solutions than at higher ionic strengths. The rejection of neutral solutes was low at all three ionic strengths, and within error margin of each other, as expected. These results

support our hypothesis that the key separation mechanism is in fact electrostatic repulsion, and the effects of solute size and hydrodynamic effects are much less pronounced.

It should be noted that in the 100 mM NaCl solution, the EDL thickness is lower than the calculated pore radius of ~ 1.5 nm. Nonetheless, anionic dyes are still rejected to a high degree. The obtained rejection could be due to the fact that membrane pore size in wet condition is in fact much smaller than the estimated pore size in dry state due to hydration of MAA segments. Alternatively, high tortuosity of the nanopores network may also contribute to its high rejection. The long tortuous path length could likely force the solute to interact with a larger functionalized surface area during permeation even when the EDL does not completely fill the pores.¹⁶⁶

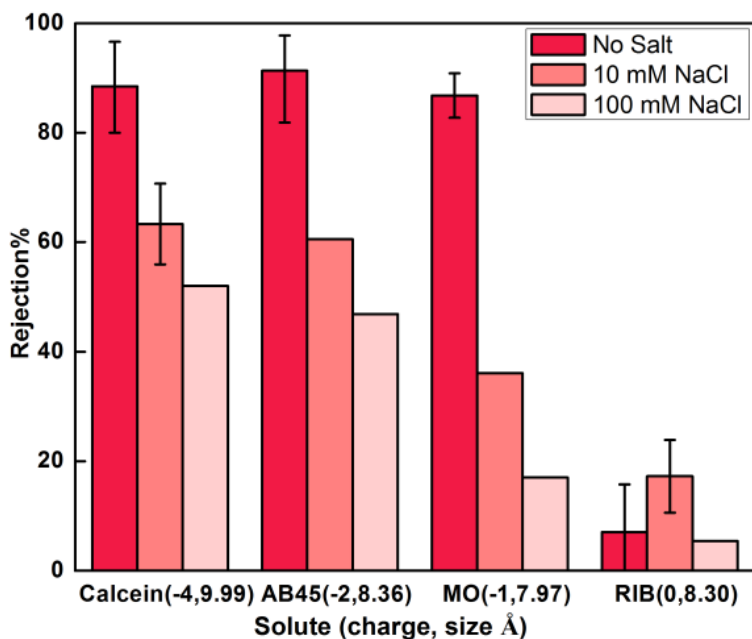


Figure 2.18. Effect of ionic strength on dye rejection of the CP40 membrane, consistent with selectivity driven by electrostatic interactions. Reprinted from¹⁷⁰. Copyright © 2017 American Chemical Society.

2.3.5.6. Salt rejection and rejection mechanism

To better understand the electrostatic interactions that dominate the selectivity of these membranes, we tested the rejection of salts by the CP40 membrane and compared the results to those obtained by Donnan equilibrium model. We measured the rejection of four salts with different anionic and cationic valences, Na_2SO_4 , NaCl , CaSO_4 , CaCl_2 , at different concentrations (1, 5, 10 mM). The CP40 membrane showed 87% rejection for Na_2SO_4 at 1 mM salt concentration (Figure 2.19), comparable to rejection values reported for some commercial nanofiltration (NF) membranes,²⁶⁶ even though this membrane is not designed or optimized for typical applications of NF such as water softening or salt removal. Other salts are rejected to a lower degree. Salts with higher anionic charge (i.e. SO_4^{2-} as opposed to Cl^-) and lower cationic charge (i.e. Na^+ as opposed to Ca^{2+}) are rejected better, as predicted for a negatively charged membrane. As ionic strength increases, the rejections of all salts decrease as electrostatic interactions are shielded.

The Donnan exclusion model describes electrochemical equilibria involved when a charged layer, such as a membrane selective layer, is in contact with an electrolyte solution. The presence of fixed charges on the membrane disfavors the passage of co-ions and favors the passage of counter-ions.²⁶⁷ During filtration, electroneutrality requires the exclusion of not only co-ions but also counter-ions. This leads to salt rejection (R), which can be predicted for a negatively charged membrane according to:²⁶⁸

$$R = 1 - \frac{C_m^-}{C_B^-} = 1 - \left(\frac{|z^-|C_B^-}{|z^-|C_m^- + C_m^x} \right)^{|z^-|/|z^+|} \quad \text{Eq. (2.7)}$$

where z^+ and z^- are the charges on the cation and anion of the salt, respectively, C_B^- and C_m^- are the concentration of co-ions in the solution and in the membrane phase, respectively, and C_m^x is the concentration of fixed charges in the membrane selective layer. Higher counter-ion valency and lower fixed charge density in the membrane leads to lower rejection. The co-ion concentration in the membrane phase C_m^- can be set equal to the permeate concentration.²⁶⁹ To determine if the selectivity of the proposed membrane can be modeled by this theory, we fit the salt rejection data to this equation using only the membrane charge density C_m^x as the fitting parameter. The values acquired from the model (Figure 2.19) mirror the experimental data perfectly, and strongly support the claim that electrostatic interaction is the major separation mechanism in our membrane.

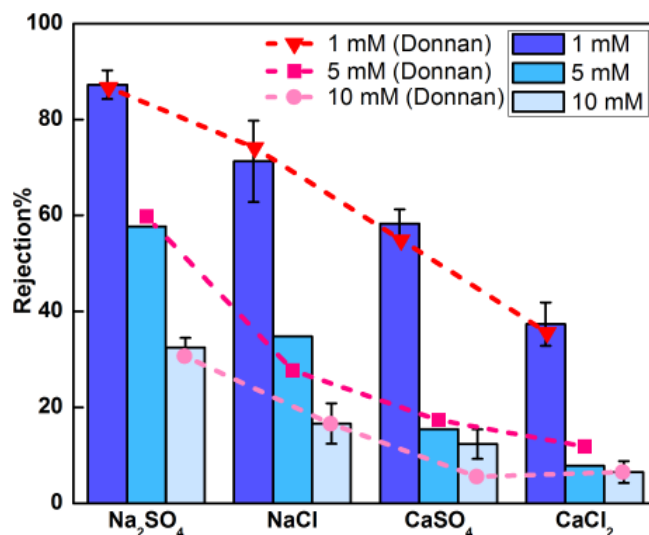


Figure 2. 19. Rejection of four salts at different concentrations by the CP40 coated membrane. Bars denote experimental data, and filled symbols show values calculated by fitting the Donnan model using a single parameter, C_m^x , obtained 3.65 mM. Reprinted from¹⁷⁰. Copyright © 2017 American Chemical Society.

Donnan exclusion model was specifically developed for selective layers with a homogeneous charge distribution, not porous media with charged surfaces. Thus, it is interesting that this model describes salt rejections in this membrane with a nanostructured selective layer. The calculated value of C_m^x , was 3.65 mM, a much lower value than the actual density of carboxylic groups in the selective layer if all COOH functional groups were assumed to be homogeneously distributed through the selective layer and ionized, as calculated below:

moles of MAA units per copolymer volume

$$= \frac{1 \text{ g copolymer} \times 0.45 \text{ wt\% MAA} \times 10^3}{86 \text{ g mol}^{-1}} = 5.2 \text{ mol MAA L}^{-1}$$

Packing density for HCP structure is 74%, further decreasing the charge density:

$$5.2 \text{ mol MAA L}^{-1} \times 0.74 = 3.85 \text{ mol MAA L}^{-1}$$

This mismatch likely arises partially from the trapping of some of the carboxylic groups inside the micelles, and from the incomplete dissociation of weakly acidic carboxylic acid groups in water. Furthermore, due to the nanostructure, the carboxyl groups are concentrated on the edges of the channels as opposed to evenly dispersed throughout, leading to lower charge densities in the middle sections of the pores. Overall, while this model describes salt rejection well, better models need to be developed to describe the selectivity of these membranes for organic molecules whose sizes would be more comparable with the nanopores.

2.4. Conclusions

We have demonstrated a novel approach to manufacturing membranes whose selective layers are formed of packed nanometer scale spherical polymer particles with carboxylate functional groups and showed they can be used for separating small molecule solutes based on their electrostatic charge. We have found that micelles formed by random copolymers of fluorinated TFEMA and carboxyl functional MAA in methanol can be deposited onto porous supports in a densely packed array if the support and the manufacturing methods are selected carefully. The interstices between these micelles act as carboxyl-functional nanopores, 1-3 nm in diameter at their narrowest point, through which water and other solutes can pass. Due to electrostatic interactions between solutes and deprotonated carboxylate groups, these membranes can separate organic molecules based on charge, allowing the passage of neutral and positively charged solutes while retaining negatively charged solutes of similar size. These membranes exhibited significantly high permeation selectivity (up to 263, between neutral and anionic solutes). Furthermore, this selectivity is enhanced in competitive diffusion experiments performed with a mixture of neutral and anionic solutes. The passage of anionic solutes is completely blocked within the 24-hour time frame of this experiment while the permeation rate of the neutral solute is enhanced. Due to the very small effective pore size of the membrane, the entry of favored neutral solutes into the nanochannels prevents the entry of the unfavored anionic solute molecules. Charge-based selectivity is also observed in filtration experiments as anionic solutes are highly retained, neutral solutes are easily permeated, and cationic solutes

heavily adsorb on the membrane. The rejection of charged organic compounds decreases with increasing ionic strength whereas that of neutral solutes remains the same, consistent with a separation mechanism dominated by electrostatic interactions. Salt retention properties of these membranes can be described by the Donnan exclusion model, though further studies are needed to better understand the implications of the presence of the nanoscale structures described. These membranes are promising for applications where charged and uncharged small molecule solutes are separated, such as the manufacture of pharmaceuticals or purification of naturally occurring compounds. Furthermore, the interesting nanostructured selective layer morphology obtained by this method can serve as a platform for the preparation of a wide range of membranes whose selective layers feature networks of functionalized nanochannels, promising for an even wider array of separations.

3 CHEMOSELECTIVE NANOPOROUS MEMBRANES FOR AROMATICITY-BASED SEPARATION OF SMALL MOLECULES

3.1. Introduction

Chemical separations account for approximately 10% of the world's energy consumption.²⁷⁰ Separation of small molecules is even more energy-intensive, often conducted by distillation, extraction or chromatography.¹⁰ In contrast, membrane filtration is energy-efficient, simple, and requires no additional chemicals.¹¹ However, the applicability of membranes today is often limited to size-based separation of molecules. Developing new membranes with high specificity and selectivity that can discriminate between molecules of similar size on the basis of their structure would transform chemical and pharmaceutical manufacturing, significantly cutting the energy use and carbon emissions associated with separations.²⁷¹ Membranes with such capability would also impact technologies for drug delivery, sensors, and barrier materials.²⁷²⁻²⁷⁴

Most attempts to construct membranes that perform chemical structure-based separations derive their inspiration from biological pores like porins and ion channels, which exhibit exceptional selectivity combined with efficient and fast permeation. These features arise from confining flow into constricted pores lined

with functional groups.^{16, 137, 275} The small pore size, on the order of the target solute (~1 nm for small molecules), forces all solutes to closely interact with the pore walls. Solutes that favorably but reversibly interact with the nanochannels are preferentially partitioned into the nanopores and prevent the entry of other solutes. This implies that synthetic membranes that feature very small pores (<3 nm for small molecule separations) lined with properly selected functional groups that selectively but reversibly interact with specific solutes can potentially separate organic molecules of similar size but different chemical features.

Most approaches to prepare such membranes involve modifying membranes with cylindrical through-pores by narrowing down and functionalizing their pores. These modification methods include electroless gold deposition,^{21, 25, 33, 276} atomic layer deposition,^{35, 277} and initiated chemical vapor deposition.³⁷ These approaches have shown that separations based on size, charge, hydrophobicity, and chirality can be achieved. However, broader use of these methods is limited due to complexity of the fabrication process and the very low porosity of the resultant membranes.

In contrast, generating functional nanopores by self-assembly can offer simpler, more scalable manufacture along with higher pore density and permeability. Block copolymers (BCPs) can form membranes with ordered structures and can be functionalized,¹⁵⁵ but due to their inherent size scale of microphase separation, it is extremely difficult to create < 5 nm pores needed for enhancing the separation of small molecules.²⁷⁸ Smaller nanopores can be formed by the self-assembly of other organic materials such as small molecule amphiphiles

with crown moieties,²⁷⁹ macrocyclic peptides,²⁸⁰ nanoparticle/dendrimer mixtures,⁴⁰ cross-linkable lyotropic liquid crystals,²⁸¹ and carbon nanotubes.⁵³ However, these approaches require custom synthesis of reagents (polymerizable surfactants, peptide rings). Many result in cylindrical nanopores that need to be aligned vertically to the surface, challenging to achieve in large scale manufacturing.^{43, 282-284} Thus, it is highly desired to develop functional membranes that offer more scalable manufacture, higher flexibility and porosity.

Furthermore, many of these systems show limited chemical functionalizability due to limited stability and/or poor accessibility of functional groups during post-modification steps.^{49, 285} This means most of these systems are limited in the types of separations they can perform. Indeed, only size- and charge-based selectivity has been demonstrated in membranes formed by self-assembly. For most applications, separations on more complex criteria are needed. Controlled selectivity requires membrane systems with tunable, customizable pore surface chemistry.

A potentially important application is the separation of solutes based on aromaticity or based on the electron density in an aromatic ring, which lead to π - π interactions with other aromatic groups. These interactions are ubiquitous in biological processes such as protein-ligand complexation, protein folding and stacking in duplex DNA,²⁸⁶⁻²⁸⁷ and in chemical processes that govern self-assembly, catalysis and transport.²⁸⁸ However, the possible role of π - π interactions in chemical selectivity of small molecules has not been explored in the context of membrane-based separations. Developing membranes that separate compounds

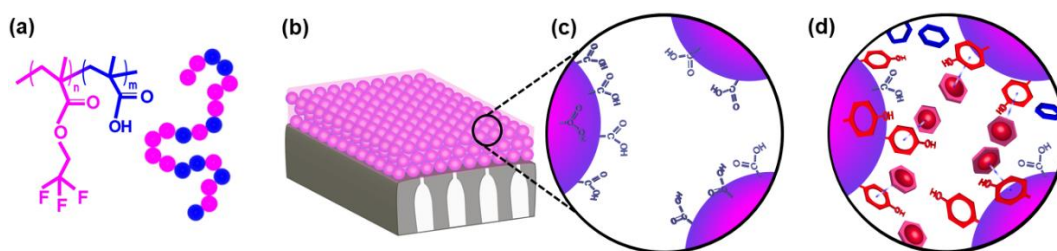
based on the presence and electron density of aromatic rings is of great interest for a wide range of applications from separation of aromatic amino acids for nutritional applications to cosmetics, pharmaceutical and drug delivery²⁸⁹⁻²⁹⁰. It also has the potential to influence one of the highest volume separations in petrochemical industry, dewaxing of aromatic compounds.

In this chapter, we demonstrate the first membranes that can separate two organic molecules of similar size and charge based on their chemistry, specifically the presence of an aromatic group. These membranes are manufactured using simple methods that are easily translatable to roll-to-roll manufacturing, by functionalizing the walls of 1-3 nm membrane pores formed by the self-assembly of a random copolymer during coating. This chapter builds on the membrane fabrication process described in chapter 2, which can be used to manufacture membranes whose selective layers consist of a packed array of micelles with carboxylic acid functional surfaces. This nanostructure is spontaneously formed during the coating of a porous support with a random copolymer solution.¹⁷⁰ The interstices between the micelles serve as permeation pathways ~1-3 nm in diameter, lined with carboxylate functional groups that were used to perform charge-based separations (Scheme 3.1).

Here, we demonstrate that these pore walls can be functionalized using straightforward, mild and highly efficient conjugation chemistry to control solute-wall interactions and customize the selectivity of the membrane for desired separations while maintaining high surface pore density and water permeability. We then describe the manufacture of membranes that can effectively separate an

aromatic compound, specifically an estrogen derivative, from a non-aromatic compound of similar size and charge (a cholesterol metabolite), mediated through π - π interactions that provide strong but reversible interactions between solute and pore walls, by functionalizing these membranes with tyrosinol (TYR). We study the effect of the functional groups lining the pore walls through diffusion experiments, and link this with quantitative information on wall-solute interactions measured by quartz crystal microbalance with dissipation (QCM-D). We also analyze transport in single-solute and competitive diffusion experiments to gain deeper insight into transport mechanisms occurring in this system. This study introduces a novel method with the potential for custom-designing functional membranes for membrane-based separation of organic compounds and demonstrates new transport phenomena that enhance chemical-structure-based selectivity upon the confinement of solute diffusion to nanoscale functional pores.

Scheme 3. 1. (a) Polymer chemistry, (b) Membrane structure, (c) Membrane nanopores lined with COOH groups (unfunctionalized membrane); and (d) Functionalized membrane selectivity mechanism in a competitive diffusion experiment.



3.2. Materials and Methods

3.2.1. Materials

Methacrylic acid (MAA), azobisisobutyronitrile (AIBN), 4-methoxy phenol (MEHQ), hormones including estrone sulfate sodium salt (ESTR) and Pregnenolone sulfate sodium salt (PREG), L-Tyrosinol hydrochloride (TYR), 2-Amino-3-cyclohexyl-1-propanol hydrochloride (ACP), N-Hydroxysuccinimide (NHS), 2-(N-Morpholino)ethanesulfonic acid (MES), Ammonium hydroxide solution (28% NH₃ in H₂O), Saline-sodium citrate (SSC) buffer (20× concentrate) and sodium hydroxide (NaOH) were purchased from Sigma Aldrich (St. Louis, MO). 2,2,2-Trifluoroethyl methacrylate (TFEMA) was purchased from Scientific Polymer Products Inc. (Ontario, NY). 1-ethyl-3-(3-dimethylaminopropyl)carbodiimide hydrochloride (EDC), HPLC-grade Acetonitrile (ACN), hydrogen peroxide (H₂O₂) and ultrapure distilled water were purchased from Thermo Fisher Scientific (Waltham, MA). Solvents (methanol, ethanol, dimethyl sulfoxide (DMSO), tetrahydrofuran (THF), hexane) and sodium chloride (NaCl) were purchased from VWR (West Chester, PA). Deuterated dimethyl sulfoxide (DMSO-d₆) was obtained from Cambridge Isotope Laboratory (Tewksbury, MA). All chemicals and solvents were reagent grade and used as received except for MAA and TFEMA, which were purified by passing through neutral and basic activated alumina columns, respectively (Sigma-Aldrich, MO). PAN-400 ultrafiltration membranes purchased from Nanostone Water, Inc. (Oceanside, CA) was used as the support membrane to provide mechanical support.

3.2.2. Polymer Synthesis and Characterization

P(TFEMA-*r*-MAA) was synthesized using a free radical polymerization method. 20 g each of TFEMA and MAA, and 0.02 g AIBN, were dissolved in 100 mL DMSO in a round bottom flask. The flask was sealed and purged with nitrogen for 30 min, and then placed in an oil bath set to 55 °C. Polymerization reaction occurred under stirring at 55 °C for about 4 h. To stop the reaction, the flask was removed from the oil bath and unsealed, and 2 g of MEHQ was added. Copolymer was recovered by precipitation in a mixture of ethanol and hexane (1:3 v/v), redissolved in ethanol and washed three times in hexane to remove all monomer residues. The final product was then air dried overnight and dried in vacuum oven at 50 °C for 24 h. The yield was about 40%.

The synthesized copolymer was characterized using ¹H nuclear magnetic resonance (¹H NMR) spectroscopy following peak assignments in Figure 2.1. After dissolving the copolymers in DMSO-d₆, NMR spectra were acquired on a Bruker Avance III 500 spectrometer. Molecular weight distribution measurement of the copolymer was acquired using a Shimadzu Gel Permeation Chromatography (GPC) System equipped with a TOSOH TSK gel GMHh-M mixed-bed column and guard column, equipped with both UV and refractive index detectors. THF was used as the mobile phase at 0.75 ml min⁻¹ elution rate and calibrated with low polydispersity poly(styrene) standards (TOSOH, PSt Quick Kit).

3.2.3. Membrane Fabrication and Characterization

The copolymer solutions for membrane preparation were prepared by dissolving 5 wt% of the copolymer in methanol by stirring at 40 °C for an overnight. Afterward, the solutions were filtered through 1 µm glass fiber syringe filter (Whatman) and kept in an oven at 50 °C to eliminate the bubbles. Bubble/dust-free solutions were cast onto a PAN400 ultrafiltration membrane taped on a glass plate with an adjustable doctor blade (Gardco, Pompano Beach, FL) set to a gap size of 20 µm. The glass plate was immersed into a water bath after 20 s of solvent evaporation at room temperature.

The microstructure of the membrane was characterized by Supra 55 FESEM at 3 kV and 7 mm working distance. Dried membranes were frozen in liquid nitrogen and cut with a razor blade for cross-sectional imaging. To avoid charging, the samples were sputter coated (Cressington 108 manual, Ted Pella Inc., CA) with Au/Pd (60/40) for 120 s at 30 mA current in an argon atmosphere. Attenuated total internal reflectance-Fourier transform infrared (ATR-FTIR) spectroscopy was used to identify the chemical composition of the membranes using a FT/IR-6200 spectrophotometer (JASCO Corp, Tokyo, Japan) over the range of 4000-600 cm⁻¹ at a 4 cm⁻¹ resolution. Prior to analysis, membranes were air-dried overnight.

3.2.4. Membrane Functionalization

Membranes were first immersed in 50 mM MES buffer at pH 6 for 1 h to deprotonate carboxylic acid groups. Next, to convert the carboxylate ions on the membrane to reactive intermediates, the membranes were immersed in EDC/NHS

solution with selected concentrations and molar ratios in MES buffer at room temperature on a nutating mixer for varying times. Unreacted EDC and NHS were removed by rinsing the membrane with 50 mM MES buffer (pH 6) for three times. For amine conjugation, the membrane was immersed in a solution containing the selected concentration of desired amino compound in 5× SSC buffer (adjusted pH to 8 with 0.1 M NaOH) on a nutating mixer at varying time. Unreacted amines were removed by rinsing the membrane with 2× SSC buffer twice and final rinsing with DI water. Samples were taken out at different time intervals during each step for infrared measurements.

3.2.5. Characterization of Membrane Performance

3.2.5.1. Filtration experiments

Water permeability was measured using a 10 ml Amicon 8010 dead-end stirred cell (Millipore) with a filtration area of 4.1 cm², stirred at 500 rpm, at a trans-membrane pressure of 40 psi. Flux were calculated by monitoring the mass of permeate, collected on a scale (Ohaus Scout Pro) connected to a computer. The membrane permeance (L_p), defined as the water flux (J) normalized by applied trans-membrane pressure (ΔP), was calculated as:

$$L_p = \frac{J}{\Delta P} = \frac{1}{R_{\text{total}}} \quad \text{Eq. (3.1)}$$

R_{total} accounts for the resistance toward the flow of the coating and the support membrane itself. Resistances-in-series model was used to account for the hydraulic resistance posed by support membrane and the selective coating layer.

$$R_{\text{total}} = R_{\text{selective layer}} + R_{\text{support membrane}} \quad \text{Eq. (3.2)}$$

The resistance against flow due to the support membrane, $R_{\text{support membrane}}$, is negligible due to its high flux in comparison to the TFC membrane ($820 \text{ L m}^{-2} \text{ h}^{-1} \text{ bar}^{-1}$) according to manufacturer specifications, confirmed in our filtration system). Selective layer permeability (P_m) was thus calculated by normalizing the permeance with the selective layer thickness using:

$$P_m = \frac{\delta}{R_{\text{selective layer}}} \quad \text{Eq. (3.3)}$$

where δ is the selective layer thickness (μm) obtained from SEM images using ImageJ software, averaged over measurements on at least 5 different membrane samples.

3.2.5.2. Diffusion experiments

Permeation studies were performed in a U-shaped two compartment cell (PermeGear) with a cell volume of 7.0 ml and an effective permeation area of 1.8 cm^2 . A circular membrane swatch 1 inch in diameter was mounted between the two halves of the diffusion cell, one acting as the feed compartment and the other as the permeate compartment.

The feed compartment contained 100 ppm solution of desired solute (ESTR, PREG) and permeate half-cell was filled with DI water. The flux of the permeating solute through the membrane and into the permeate compartment was monitored by periodically by removing an aliquot (1 ml) of the permeate solution, replacing it with 1 ml DI water, and assaying the aliquot using high-pressure liquid

chromatography coupled with mass spectroscopy (LC-MS, Finnigan Surveyer LC system and Finnigan LTQ, Thermo Scientific, Waltham, MA). 20 μl of samples or standards were injected into a C18 Analytical Column (BetaSil™ C18 Column, 3 μm particle size, 100 mm length, 2.1 mm internal diameter, Thermo Scientific™, Waltham, MA) equilibrated with 95:5 water:ACN containing 0.02 v/v% ammonium hydroxide. A gradient was started to 60:40 water:ACN over 5 min, then ramped up to 95:5 water:ACN, followed by a 2 min equilibration step.

The quantification was performed by tracking m/z values of 349.16 and 395.24 for ESTR and PREG, respectively. Xcalibur™ Software (Thermo Scientific) was used for data acquisition and quantification of the area under the curve for both ESTR and PREG peaks. A standard curve for each solute was generated to convert the area values to concentrations.

Membranes were soaked in DI water at least overnight between diffusion experiments to remove any organic solute or salt residues.

3.2.6. Quartz Crystal Microbalance with Dissipation (QCM-D) Studies

3.2.6.1. Preparation and coating of the quartz crystal sensor

To study the interaction between each solute and selective layer, we used Quartz Crystal Microbalance with Dissipation (QCM-D, Q-Sense, Frölunda, Sweden). 0.3-mm-thick AT-quartz crystals coated with a 100-nm-thick gold layer (Qsx 301) with a fundamental frequency of $f_0 = 4.95 \pm 0.05$ MHz were used as substrates. Prior to use, Au-coated crystals were cleaned by UV/ozone treatment for 10 min. They were then heated in a 5:1:1 mixture of ultrapure water, 25 v/v% Ammonia and 30

v/v% H₂O₂ to 75 °C for 5 min. They were rinsed with ultrapure water afterward, dried with nitrogen, and placed under UV/ozone treatment for another 10 min.

To obtain a thin and uniform film on the crystal sensor, a solution containing 1 wt% copolymer in methanol was spin-coated at 2000 rpm for 1 min. The samples were then dried in a vacuum oven at 70 °C for 30 min to remove the solvent residue.

3.2.6.2. Measuring coating layer thickness

The areal mass (ng cm⁻²) of the selective layer was also measured using QCM-D through analysis of the frequency shift. First, the frequency shift of the bare sensor was monitored until a stable baseline was obtained (± 1 Hz) upon gas injection. The sensor was then taken out and spin-coated as described above. The quartz crystal was again placed into the measurement chamber and frequency change upon coating was recorded. The mass of the solute adsorbed on the quartz crystal surface over time was estimated by Sauerbrey's Equation ²⁹¹:

$$\Delta m = -C \frac{\Delta f}{n} \quad \text{Eq. (3.4)}$$

where C is the sensitivity constant $C = 17.7 \text{ ng m}^{-2} \text{ Hz}^{-1}$, n is the overtone, and Δf is frequency change.

Thickness can be obtained by dividing the mass change to the copolymer density ρ (1.1 g cm⁻³):

$$\delta = \frac{\Delta m}{\rho} \quad \text{Eq. (3.5)}$$

3.2.6.2. Adsorption/Desorption of solute on the selective layer

For tracking the adsorption and desorption of the solute, frequency change at different harmonics ($n= 1, 3, 5, 7, \dots, 13$) was recorded upon injection of different solutes. The sensor was first equilibrated with ultrapure water until a stable baseline was established. Next, a solution containing 50 ppm of desired solute (e.g., PREG) was introduced to measurement cell using a peristaltic pump (Ismatec IPC-N 4) at a flow rate of $50 \mu\text{l min}^{-1}$ at room temperature. When the adsorption reached saturation, as evidenced by a plateau in the signal, the solution was again substituted with ultrapure water to track desorption of the solute and hence the reversibility of the interactions. The next solute (e.g., ESTR) was injected afterward and its adsorption/desorption was compared. QSoft 401 and QTools Software were used for data acquisition and data analysis, respectively.

3.3. Results and Discussion

3.3.1. Copolymer Synthesis and Unfunctionalized Membrane Formation

In the previous chapter, we described a novel, scalable approach for creating membranes whose selective layers contain a network of carboxylic acid functionalized nanochannels by self-assembly of the random copolymer as it is coated onto a porous support.¹⁷⁰ This copolymer, poly(trifluoroethyl methacrylate-*random*-methacrylic acid), P(TFEMA-*r*-MAA), is synthesized by free radical copolymerization. The extreme incompatibility between the highly hydrophilic MAA units and very hydrophobic, fluorinated TFEMA segments leads to the formation of micelles in methanol.¹⁶⁹ When a solution of these micelles is coated

onto a porous support under preferred conditions, they create a selective layer of closely packed micelles on top of the support, with pore size of about 1-3 nm. In this chapter, we leverage the versatility of the carboxylic acid groups that line these pores, and their easy conversion to numerous functionalities using conventional conjugation techniques. This includes the formation of reactive intermediates that are then coupled to an amine to form an amide, often termed EDC/NHS chemistry.²⁹²

P(TFEMA-*r*-MAA) was synthesized as described in the previous chapter, following previously reported procedures.¹⁶⁹⁻¹⁷⁰ The copolymer used in this study was found to have a number-average molecular weight of 606 kg mol⁻¹ and dispersity of 1.75 by GPC based on polystyrene standards. Using ¹H NMR, the MAA content of the resultant copolymer was measured to be 45 ± 3 wt% at 40% conversion. A 5 wt% solution of the copolymer in methanol was spread onto a porous UF membrane (polyacrylonitrile, PAN 200 kDa, Nanostone) by a doctor blade to form a thin and uniform film. After a brief solvent evaporation time of 20 s to direct the self-assembly of the micelles, the film was immersed in DI water to freeze the structure. As a result, the self-assembled random copolymer micelles were kinetically trapped in a nicely packed array of spheres. The interconnected interstices between the micelles act as nanochannels that are all lined with carboxylic acid functional groups, accessible for further functionalization. This membrane, essentially identical to the one used for charge-based separations (previous chapter),¹⁷⁰ is described as the “unfunctionalized” membrane.

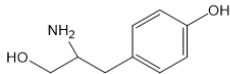
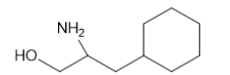
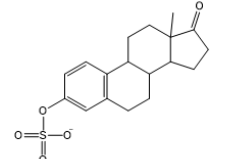
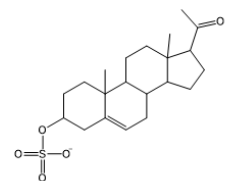
3.3.3. Selection of Surface Functionality and Membrane Functionalization

In this study, we aimed to demonstrate that this membrane can serve as a platform for separations based on more complex chemical criteria by converting the carboxylic acid groups to other functionalities selected to preferentially interact with one molecule over another. This feature makes them ideal for addressing a broad range of separation challenges. As an initial demonstration of this approach for designing chemoselective membranes, we chose to focus on leveraging π - π interactions between the preferred solute and pore walls. π - π interactions are highly reversible with fast time constants.²⁹³ Their strength can be predictably tuned by selecting substituents on aromatic rings.²⁹⁴⁻²⁹⁶ The most favorable π - π interactions occur between an electron-rich aromatic ring and an electron-poor aromatic ring.^{294,}

297

Efficient separation and purification of hormones from others with similar chemical structures is essential for drug manufacture and in analytical applications for clinical diagnosis.²⁹⁸⁻²⁹⁹ Therefore, we selected two steroid hormones as an example of a pair of solutes with similar size and charge but different aromaticity. Estrone sulfate (ESTR), the most abundant estrogen precursor in the blood stream, has an aromatic ring. Pregnenolone sulfate (PREG), a relative of progesterone derived from cholesterol, does not have any aromatic rings (Table 3.1). Besides this, ESTR and PREG are very similar in size (8.4, 8.9 Å, respectively), charge (-1), and functional groups. This means that variations in their diffusion rates would likely be due to solute-pore wall interactions.

Table 3. 1. Structure, size and van Krevelen solubility parameters of organic molecules used in this study.

Name	Abbreviation	Chemical structure	size (Å)	δ_d (MPa ^{1/2})	δ_p (MPa ^{1/2})	δ_H (MPa ^{1/2})
Tyrosinol	TYR		6.7	24.4	7.6	31.3
2-Amino-3-cyclohexyl-1-propanol	ACP		6.8	16.8	4.5	21.6
Estrone Sulfate	ESTR		8.4	22.9	7.8	25.3
Pregnenolone Sulfate	PREG		8.9	18.2	6.2	19.8

We hypothesized that if there are aromatic groups lining the pores, only ESTR can interact with them through π - π interactions. The strength and direction (attractive vs. repulsive) of π - π interactions correlate closely with the electron densities in the aromatic ring. Rings that have electron donating groups as substituents have a partial negative charge on the aromatic ring and tend to interact more strongly with solutes containing electron withdrawing substituents. This is typically quantified by Hammett substituent constants measured at the para position, σ_p .^{297, 300-302} The OSO_3^- group on ESTR is electron withdrawing, with $\sigma_p = 0.42$ (calculated by Molecular Modeling Pro Software). The $-\text{OH}$ substituent on phenol groups is electron donating, with $\sigma_p = -0.37$.³⁰³ Thus, if the pore walls are functionalized with a phenol containing group, we would expect attractive π - π interactions between them and ESTR molecules.

To test this hypothesis, we functionalized the membrane pores with phenol-containing groups using EDC/NHS chemistry to covalently attach the phenol-containing molecule tyrosinol (TYR) to the pore walls (Table 3.1). As a control, we functionalized another membrane with a non-aromatic molecule with similar functional groups, 2-Amino-3-cyclohexyl-1-propanol (ACP) (Table 3.1). TYR-functionalized surfaces are expected to preferentially interact with ESTR over PREG, whereas unfunctionalized or ACP-functionalized surfaces would not exhibit as prominent a difference in interactions.

The functionalization reaction is conducted in aqueous solution under very mild conditions. It involves the activation of the carboxyl groups to form reactive intermediates (Figure 3.1) that then react with a primary amine group to form a covalent amide bond. To achieve high degrees of functionalization, we screened different parameters by performing attenuated total reflection – Fourier transform infrared spectroscopy (ATR-FTIR) and tracking relevant peaks after activation and amidation steps. Infrared spectrum for unfunctionalized membrane (bottom spectrum) is shown in Figure 3.1a. The two interconnected peaks at about 1738 and 1705 cm^{-1} are assigned to the $-\text{C}=\text{O}$ stretching vibration of ester carbonyl (i.e., TFEMA unit) and carboxylic acid (i.e. MAA unit), respectively. The smaller peak at 1565 cm^{-1} is attributed to the fraction of acid groups that are deprotonated $-\text{COO}^-$. Membranes were then activated using EDC/NHS chemistry that leads to formation of reactive intermediates (Figure 3.1a, top spectrum) that can react with amino compound in the next step. The peaks from these intermediates containing carbonyl groups overlaps in the range of 1700-1800 cm^{-1} and obscures some smaller peaks.

For a clearer observation and assignment of the peaks, we deconvoluted the carbonyl peak coming from these intermediate species: NHS-ester, and anhydride using Fityk software (Figure 3.1b). The formation of the succinimidyl ester is evidenced by prominent triplet bands of 1745, 1775 and 1810 cm^{-1} attributed to the antisymmetric and symmetric vibration of the carbonyl groups of the succinimide cycle and $\nu_{\text{C=O stretching}}$ vibration of the ester unit, respectively. Although the NHS-ester peak dominates over the anhydride, a large amount of anhydride was also formed with characteristic doublet bands at 1760 and 1800 cm^{-1} , associated with antisymmetric and symmetric $\nu_{\text{C=O stretching}}$ vibration. Both NHS-ester and anhydride can directly react with primary amine containing molecules and form covalent amide bond, with NHS-ester being a more reactive species.

Another product that can potentially form as a result of EDC/NHS activation is N-acylurea. The formation of N-acylurea is undesirable, since it is a stable product and will not react with amino compounds. The minimal intensity of doublet peaks at 1550 and 1650 cm^{-1} signature of amide bond of N-acylurea confirms minor formation of side products at the conditions enlisted here.

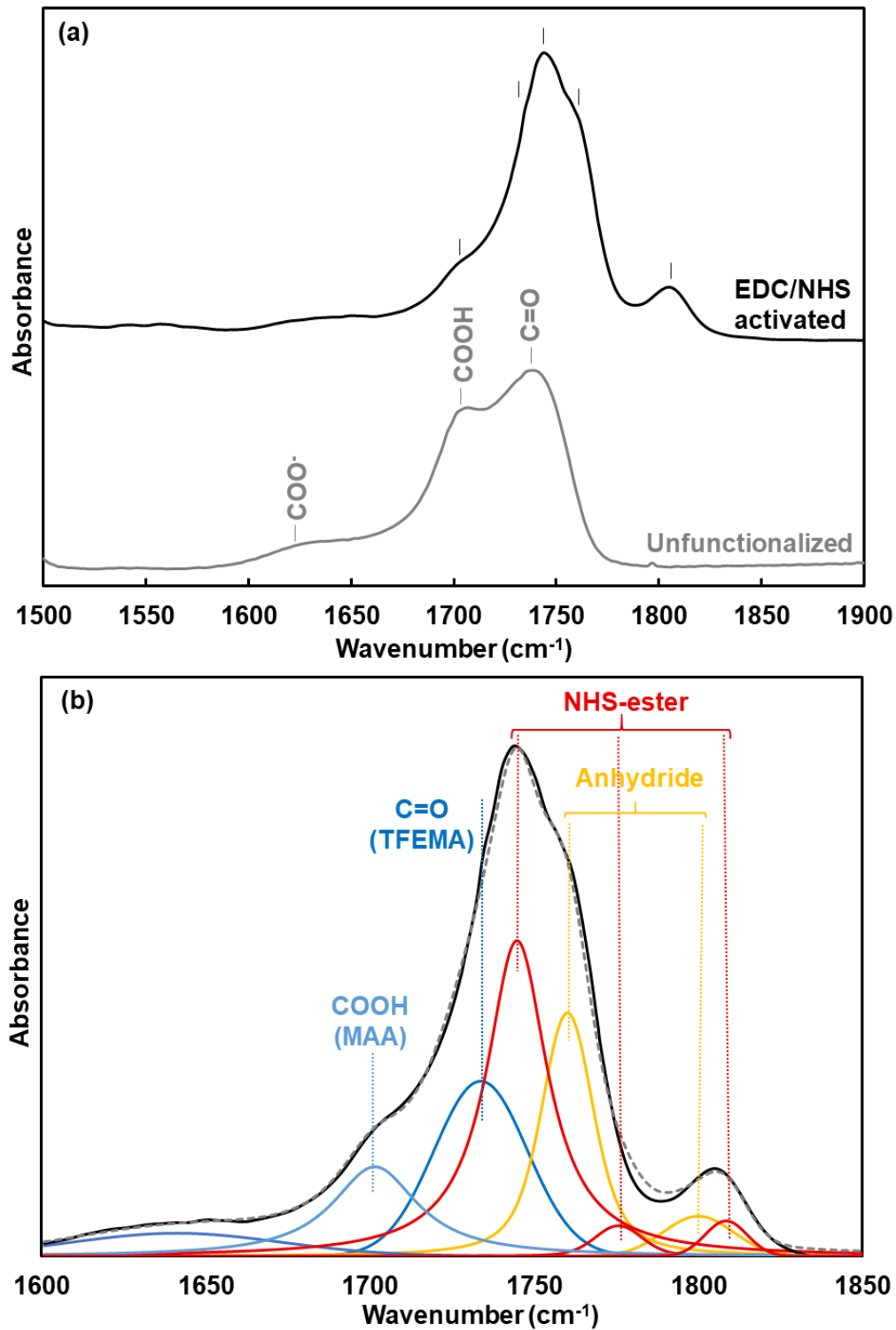


Figure 3. 1. FTIR spectra of (a) membrane before and after EDC/NHS activation; (b) deconvolution of the carbonyl stretching region of the activated membrane; NHS-ester and anhydride intermediates were formed.

The ATR-FTIR spectra was also collected after amidation. Figure 3.2a depicts the spectra for unfunctionalized and TYR-functionalized membranes prepared using the optimal procedures (Figure 3.2a, bottom and middle spectrum). The figure shows almost complete conversion of the carboxylic acid groups, and the formation of new aromatic and amide bonds. This demonstrates successful attachment of TYR molecules. The spectrum of the membrane functionalized with ACP also showed evidence of functionalization, as indicated by peaks corresponding to amide groups (Figure 3.2a, top spectrum). Field Emission Scanning Electron Microscopy (FESEM) imaging showed that the closely packed micelles forming the membrane selective layer remain intact after functionalization with TYR (Figure 3.2b, c). This confirms that this simple, straightforward approach allows functionalization without damage to the membrane structure.

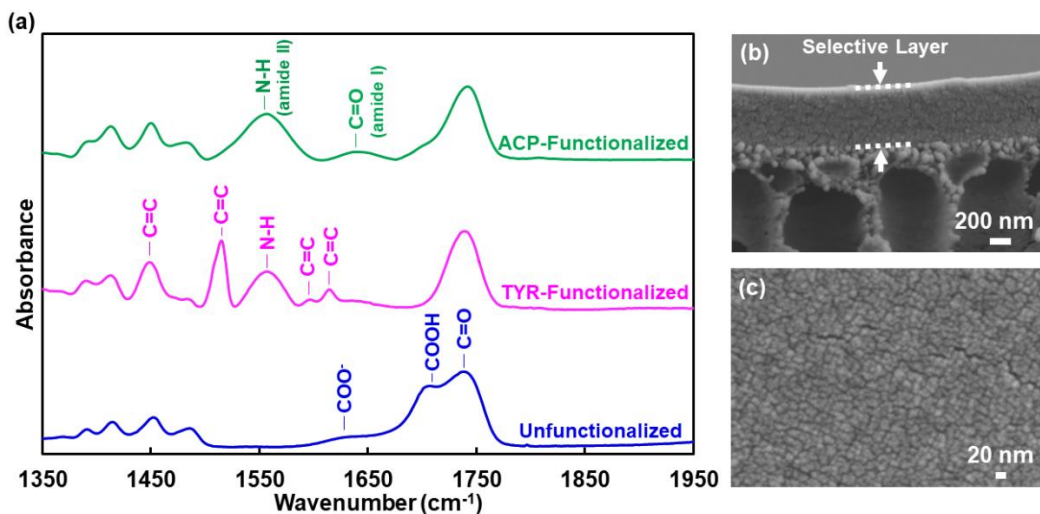


Figure 3. 2. (a) Infrared spectra of unfunctionalized and functionalized membranes. Formation of new amide bonds upon functionalization confirms covalent attachment of amino compounds. SEM micrographs of (b) Membrane cross section, and (c) Membrane surface; showing the packed micelle structure is intact upon membrane functionalization.

3.3.4. Solute/Pore Wall Interactions that Control Permeation

To confirm our predictions regarding the selectivity of pore-solute interactions and to obtain quantitative evidence of adsorption/desorption equilibria, we used quartz crystal microbalance with dissipation, QCM-D. For this purpose, a quartz crystal resonator was coated with a thin film of the copolymer (~70 nm, Appendix A2) to mimic the surface chemistry of the pore walls. The surface was functionalized with TYR or ACP using the same procedure used for membranes. Frequency change, which is directly proportional to the mass of solute adsorbed on the surface,³⁰⁴ was recorded upon exposing the crystal to a solution of either PREG or ESTR.

Figure 3.3 displays the frequency shifts for unfunctionalized, TYR-functionalized and ACP-functionalized films upon exposure to each solute, followed by its desorption. For all membranes, a larger frequency shift was observed for ESTR in comparison to PREG solution, corresponding to higher adsorbed mass of ESTR. To evaluate the QCM results more quantitatively, we defined a heuristic parameter, “adsorption selectivity”, β :

$$\beta = \frac{\Delta n_{ESTR}}{\Delta n_{PREG}}$$

where Δn is the moles of solute whose name is noted in the subscript adsorbed on the surface measured by frequency shift (f) of the gold sensor.

For the unfunctionalized membrane, an adsorption selectivity β of 2.9 was obtained. While no π - π interactions are present, the phenol groups in ESTR can

interact more strongly with the –COOH groups on the surface through hydrogen bonding than PREG molecules, as evidenced by the hydrogen bonding solubility parameters of these solutes (Table 3.1).

When the surface was functionalized with TYR, a much larger frequency change was observed upon the injection of ESTR. This clearly illustrates ESTR has higher affinity to the TYR-functionalized surface through π - π interactions. In contrast, the adsorption of PREG decreased in comparison to the unfunctionalized surface. The TYR-functionalized surface was much more selective for ESTR, with a β value of 11.7.

The ACP-functionalized surface did not include any aromatic rings, but –OH groups similar to the TYR groups. Frequency shift due to ESTR adsorption was lower than that observed on the unfunctionalized and TYR-functionalized films. The ACP-functionalized surface has lower hydrogen bonding potential and no aromatic groups to enhance this interaction. The amount of PREG adsorbed on this surface was comparable to the unfunctionalized film. This resulted in a β value of 1.7, indicating that ACP-functionalized membranes have limited preference for ESTR.

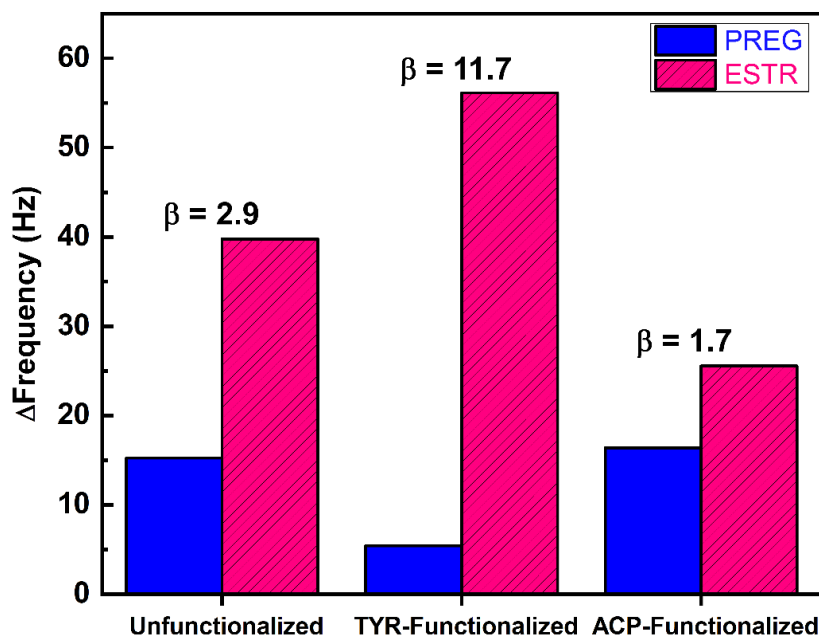


Figure 3. 3. Frequency shift upon injection of hormones for unfunctionalized and functionalized films.

For all the membranes, rinsing with DI water lead to immediate and complete desorption of bound solutes, indicated by an increase in frequency to its initial value (Appendix A2). This shows that the interactions of solutes with functional groups on all the membranes are fully reversible.

3.3.5. Membrane Permeance

3.3.5.1. Water permeance: pressure-driven filtration

Most membranes are utilized in pressure-driven filtration applications. Water permeance, defined as the flux of pure water normalized by applied trans-membrane pressure, is a crucial performance criterion for membrane use. Yet, this value is rarely reported for membranes designed for chemical structure-based selectivity. The very low porosity of membranes prepared by top-down methods

often results in very low flux. The membranes reported here are expected to have much higher pore density, leading to measurable water permeance. To document this, I measured the water permeance of the membranes using a dead-end filtration cell at trans-membrane pressure of 40 psi. The water permeance of unfunctionalized membranes was $4.5 \pm 0.8 \text{ L m}^{-2} \text{ h}^{-1} \text{ bar}^{-1}$. This is significantly lower than that of support membrane, $820 \text{ L m}^{-2} \text{ h}^{-1} \text{ bar}^{-1}$, confirming the presence of a coating layer. Upon TYR functionalization, we expect a slight decrease in the membrane permeance as the TYR molecule (6.7 \AA) partially fills the 1-3 nm nanopores. Indeed, a decline on membrane permeance to $3.1 \pm 0.6 \text{ L m}^{-2} \text{ h}^{-1} \text{ bar}^{-1}$ was observed.

Membrane permeance is strongly dependent on selective layer thickness, which can be further optimized by adjusting manufacturing parameters upon scale-up. Selective layer permeability is defined as membrane permeance normalized by the selective layer thickness. We calculated the selective layer permeability to be 1.8 ± 0.3 and $1.3 \pm 0.2 \text{ L } \mu\text{m m}^{-2} \text{ h}^{-1} \text{ bar}^{-1}$ for unfunctionalized and functionalized membranes, respectively, using the resistances-in-series model (Eq. 3.3). These values are comparable to that of commercial TFC nanofiltration membranes ($0.2\text{--}1.4 \text{ L } \mu\text{m m}^{-2} \text{ h}^{-1} \text{ bar}^{-1}$),²⁵⁷ calculated assuming a selective layer thickness of $0.1 \mu\text{m}$.²⁵⁸⁻²⁵⁹ While the selectivity properties of commercial NF membranes are by definition distinct from the proposed membranes, this serves as a broad comparison regarding their potential industrial use. This data implies that if these membranes were manufactured at large-scale with thin selective layers, modules that operate at industrially relevant fluxes can be built and utilized in manufacturing.

3.3.5.2. Permeation of Aromatic and Non-Aromatic Organic Molecules

3.3.5.2.1. Single-solute diffusion experiments

We initially studied the transport of organic molecules through these membranes using diffusion experiments with a feed containing only one type of solute at a time, in aqueous solution. We hypothesized that given the small pore size of these membranes, molecular interactions between the solutes and pore walls would control the relative permeation rates of solutes of similar size.^{12, 159}

To determine how these differences in solute-pore interactions affect permeation, we conducted diffusion experiments in a two-compartment cell. The feed half-cell was filled with 100 ppm solution of desired solute, one at a time. Samples were taken periodically from permeate half-cell and solute concentration was assayed using high-pressure liquid chromatography coupled with mass spectroscopy (LC-MS). Figure 3.4a shows nanomoles of the permeating solute through the support membrane versus time (i.e. permeation rate) for both hormones, ESTR (pink) and PREG (blue), through the support membranes. To quantify the ratio between diffusion rates of the two solutes, we defined theoretical permeation selectivity α_T as the ratio of the permeation rate of ESTR to that of PREG. Both solutes showed very similar diffusion rates through the support membrane ($\alpha_T = 1$) as expected given its large pore size. This confirms that these solutes have similar diffusivity and indicates any selectivity in the coated membranes results from selective layer.

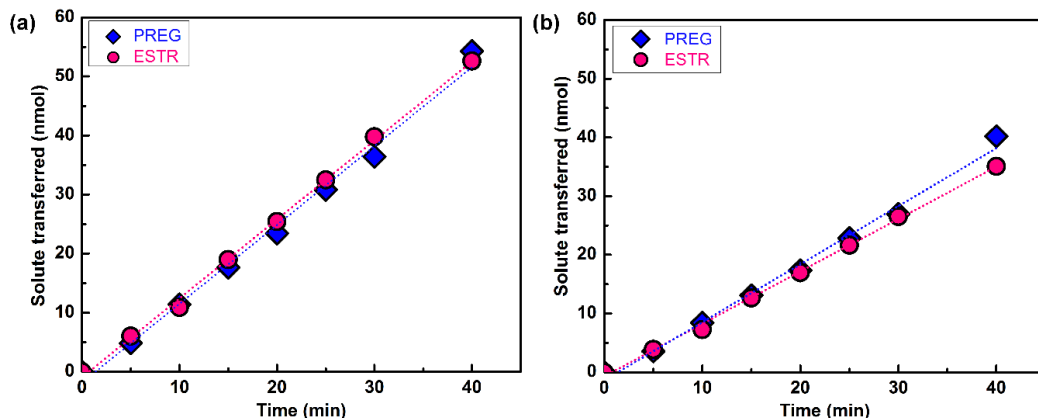


Figure 3. 4. Diffusion of steroid hormones through support membrane (PAN400) in (a) Single-solute, and (b) Competitive diffusion experiment.

Figure 3.5 depicts the nanomoles of each solute transferred through the unfunctionalized, TYR-functionalized and ACP functionalized membranes. The diffusion rate of PREG, the non-aromatic molecule, through the unfunctionalized membrane was ~ 1.9 times higher than that of aromatic ESTR ($\alpha_T=0.53$) (Figure 3.5a). ESTR interacts slightly more strongly with the $-\text{COOH}$ groups on the unfunctionalized membrane than PREG, as indicated by the QCM-D data. These interactions appear to slow down the passage of this molecule as it hops between neighboring binding sites, while PREG molecules can pass through the membrane unhindered.³⁰⁵⁻³⁰⁶

Upon functionalization with TYR (Figure 3.5b), the transport rate of PREG was significantly enhanced despite the slightly smaller pore size relative to the unfunctionalized membrane. This is consistent with the lower degree of adsorption measured in QCM-D experiments. The overall negative charge of the membrane is also reduced upon the conversion of most of the acid groups to phenol. This results in less repulsion between the pore wall and PREG molecules and thus easier

passage through the membrane. The transport rate of ESTR increased only slightly in comparison to the unfunctionalized membrane. Although the electrostatic repulsion was significantly reduced, favorable π - π interactions between the phenol groups in TYR and ESTR appears to slow down the permeation of ESTR. These results are consistent with hopping transport mechanism, where adsorption/desorption equilibria dominate the time a solute takes to reach the permeate side.¹² In single solute experiments, the least interactive solute transfers most quickly. Transient trapping of the preferred solute as it hops through the binding sites inside the pores retards its permeation.³⁰⁷ As a result, PREG diffused 11.2 times faster than ESTR through this membrane ($\alpha_T=0.089$).

To confirm that π - π interactions and favorable binding of ESTR to phenol groups of the pores cause this change in transport rates, we performed an analogous experiment with the ACP-functionalized membrane (Figure 3.5c). The diffusion rate of both PREG and ESTR were increased compared with the unfunctionalized membrane upon the decrease in membrane surface charge. ESTR diffused slightly more slowly than PREG ($\alpha_T=0.63$), in agreement with previous results and QCM-D data. This confirms that the significant changes in membrane selectivity observed in the TYR-functionalized membrane arise from π - π interactions, and not from simple changes in surface charge. Flux of both solutes and theoretical selectivities (α_T) for all membranes are summarized in Fig. 3.5d.

3.3.5.2.1. *Competitive diffusion experiments*

Single-solute diffusion experiments are often used to estimate the ability of a new membrane material to separate a mixture. Researchers typically calculate a theoretical selectivity α_T as above, by dividing the permeation rates of the two solutes measured in isolation and hypothesize this ratio will be maintained when a mixture is fed to the membrane. However, in real applications, the target molecule will be present in the feed with at least one other molecule. This might affect the permeation selectivity of the membrane in different ways depending on how the solutes interact with the membrane material. In most cases, selectivity either remains similar or decreases (e.g. due to plasticization). In contrast, when the membrane pores are small and comparable to the size of molecules being separated, the solute with higher affinity to the pore walls (i.e., preferred solute) can prevent the entry of others into the pore. This results in higher transport selectivity for the preferred solute in comparison with the theoretical selectivity α_T calculated from single solute experiments. Therefore, in addition to more accurately simulating realistic operation conditions, comparing data from single-solute and competitive diffusion experiments can illuminate transport mechanisms in these membranes.

To explore this point, we performed competitive diffusion experiments with feed solutions containing 100 ppm of each solute, ESTR and PREG. Competitive selectivity α_C is defined as the ratio of the fluxes of ESTR to PREG, analogous to α_T from single solute experiments. The support membrane showed no selectivity between the two hormones ($\alpha_C = 1.1$; Figure 3.4b). Figures 3.5e-g depict the diffusion of the two solutes in these competitive diffusion experiments through the

three membranes studied. Interestingly, all three membranes preferentially permeated ESTR, reversing the selectivity observed in single solute experiments.

For the unfunctionalized membrane (Figure 3.5e), the diffusion rate of both solutes decreased in the competitive experiment in comparison to single solute experiments as expected since the two solutes are competing over the narrow space of the pores. This decrease was much more pronounced for PREG, making its permeation slightly slower than EST and leading to $\alpha_C = 1.5$. This implies that the ESTR molecules, which interact more with the pore walls in comparison to PREG, permeate through the membrane similar to before, but also inhibit the permeation of the unpreferred PREG molecules. The ACP-functionalized membrane also shows a slow-down of PREG permeation rate and a reversal of selectivity (Figure 3.5g), but to a lesser extent ($\alpha_C = 1.2$). This is in agreement with the QCM-D data, which shows the ACP-functionalized membrane is less selective towards ESTR than the unfunctionalized membrane.

The most prominent change in selectivity was observed for the TYR-functionalized membrane, which interacts most selectively with ESTR through π - π interactions as indicated by QCM-D experiments. In competitive permeations with this membrane (Figure 3.5f), the diffusion rate of PREG dropped dramatically in comparison to single-solute experiments. The permeation rate of ESTR was slightly enhanced. Overall, ESTR permeated through this membrane 7.1 times faster than PREG (Fig. 3.5h). At the end of the 30 h long experiment, the sink compartment contained about 8 times as much ESTR as PREG, demonstrating the enrichment of the preferred solute in the permeate side. This is a successful separation of a mixture

of two very similar molecules, based on a relatively minor chemical structure difference.

The enhanced permeation of the preferred solute (in this case ESTR) and inhibition of unpreferred solute (i.e., PREG) in competitive permeation experiments is in close analogy to biological pores. I hypothesize that this effect arises from competition between the two solutes for narrow space inside the nanochannels, whose diameter (~1-3 nm) is comparable to the size of the solutes (~1 nm). The confined space limits the entry of other solute molecules once a channel is occupied. ESTR which the pore walls preferentially interact with, has a higher probability of partitioning into the pores. ESTR molecules also spend a longer time in the pores, as indicated by their slower permeation in single solute experiments. This excludes the unpreferred solute, PREG, from entering the pores and slows down its permeation drastically. As a result, ESTR permeates through the membrane faster than PREG when they are both present. Furthermore, it is possible that the PREG molecules that are excluded from the pores accumulate near pore entrance, circumventing the back-diffusion of ESTR molecules and increase their forward flux relative to single-solute experiments.²⁵⁴

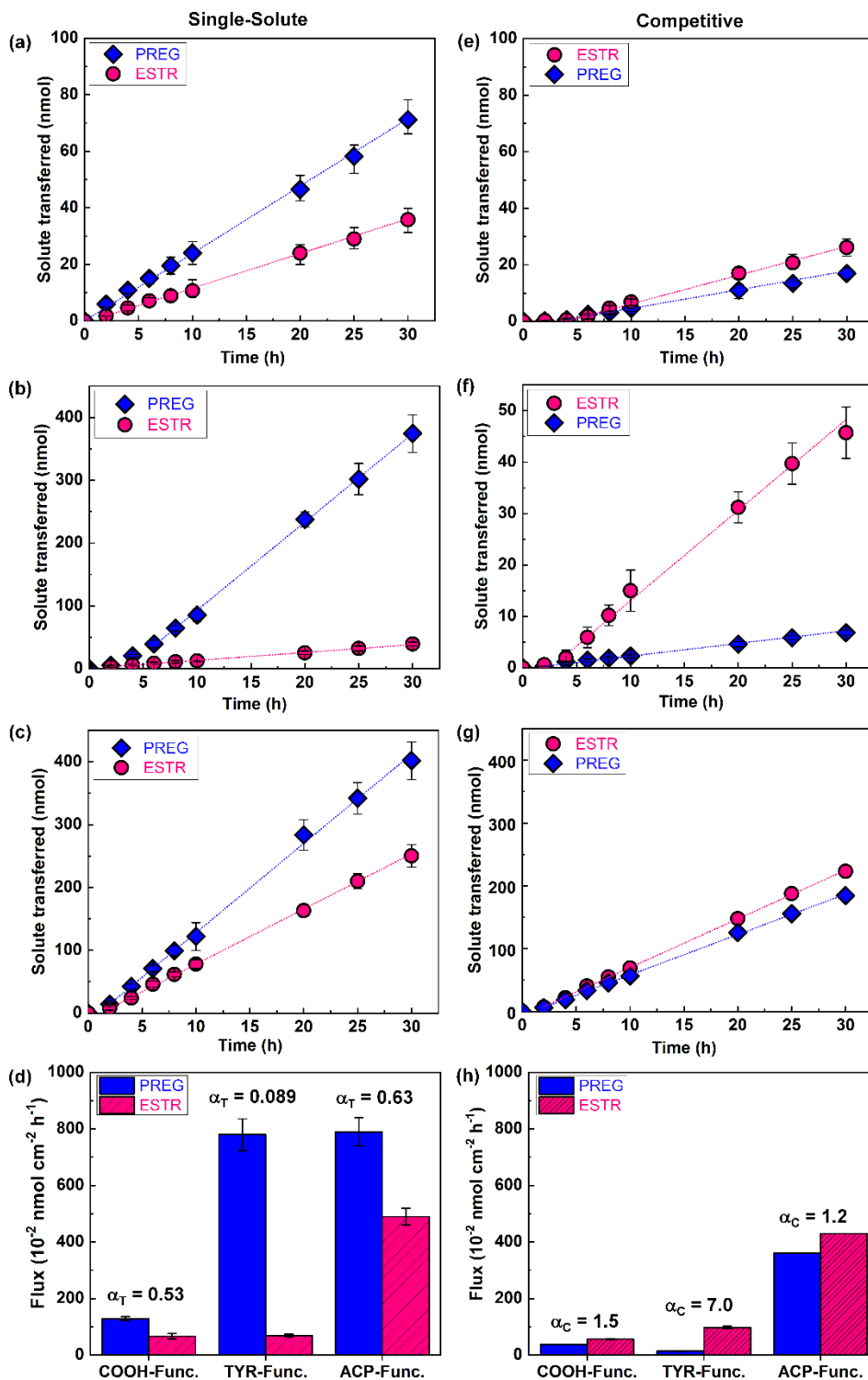


Figure 3.5. Permeation of steroid hormones through (a,e) Unfunctionalized and (b,f) TYR-functionalized and (c,g) ACP-functionalized membrane in (a-c) single-solute and (e-g) Competitive diffusion experiments. Permeation flux and selectivity in (d) Single-solute, and (h) Flux in competitive diffusion experiments. All experiments demonstrate aromaticity-driven selectivity. The selectivity pattern is switched in competitive experiments.

3.4. Conclusions

These results demonstrate that in a membrane whose pores are ~1-3 nm in diameter, comparable in size with small organic molecules, solute-pore wall interactions can dominate solute transport selectivity. The unusual transport phenomena arising from the confinement of permeation into nanoscale pores leads to a large mismatch in single-solute and competitive transport selectivities. Furthermore, this membrane manufacturing method enables the customization of pore chemistry through an easy conjugation reaction, enabling us to screen a variety of solute-wall interactions in addition to the π - π interactions that is the focus of this study. We also demonstrated that QCM-D is an effective method to screen these surface/solute pairs in terms of preferential interactions to guide these studies. As such, this initial work opens up the way to many investigations focused on studying the effect of nanoconfinement and solute/wall interactions on permeation.

The results confirm that incorporation of phenol groups on the walls of the nanopores created in this membrane system leads to membranes with unprecedented transport selectivity, up to ~7 times, between two steroid hormones with similar size and charge based on their aromaticity. This is a very high diffusion selectivity for small molecules with similar size and charge using a clean, and energy efficient membrane separation process. In fact, this is, to our knowledge, the first demonstration of membrane-based separation for small molecules based on their aromaticity. The functional groups were introduced on the membrane pore walls using a straightforward conjugation chemistry. It is not hard to imagine designing membranes for each targeted separation by identifying desired functional

groups on pore walls, screening them by QCM-D, and easily functionalizing these membranes through EDC/NHS chemistry. Furthermore, the membranes used in this study are manufactured through simple and scalable methods that can be adapted to roll-to-roll manufacturing, taking advantage of the self-assembly of random copolymer micelles. They exhibit industrially relevant water permeances. As such, this new membrane technology has the promise to become a platform for designing custom membrane filters for complex separations that cannot be addressed by today's membranes.

4 A NOVEL METHOD FOR FABRICATION OF ULTRATHIN SELECTIVE LAYERS: INTERFACIALLY INITIATED FREE RADICAL POLYMERIZATION (IIFRP)⁴

4.1. Introduction

Protein purification is of great importance in a wide range of applications including the pharmaceutical, biotechnology, cosmetics and food industries as well as in enzymatic catalysis.³⁰⁸⁻³⁰⁹ Membrane separation processes are attractive for these applications due to their high throughput, ease of implementation and cost effectiveness.³¹⁰⁻³¹¹ However, critical challenges remain in the use of membranes for protein purification. First, protein separations require membranes with well-controlled selectivity.³¹²⁻³¹⁵ Second, fouling due to the adsorption of the proteins and other biomolecules in the feed leads to substantial decline in membrane permeance and lifetime,³¹⁶⁻³¹⁷ and can cause shifts in membrane pore size.^{316, 318-319} Addressing these concerns can broaden the use of membrane processes in the manufacture and purification of biopharmaceuticals.

⁴ Reproduced with permission from reference 333. Copyright © 2018, American Chemical Society.

Hydrogels are especially promising materials for membranes targeted at protein purification, because they are effective, versatile, tunable, functionalizable, and inherently fouling resistant.⁹⁹ Selectivity can be controlled by the mesh size of the cross-linked polymer, with effective pore sizes typically in the ultrafiltration (UF) range (1-5 nm), suitable for protein purification.³²⁰ Functional groups can be easily integrated into these selective layers, enabling more targeted control of membrane selectivity and broadening their potential applications to protein separations. Moreover, hydrogels are inherently hydrophilic, which makes them very fouling resistant.^{94, 100, 321-322} Despite these promising features, if the hydrogel will serve as the selective layer of a membrane, it has to be as thin as possible, because membrane flux is inversely proportional to the layer thickness. However, the fabrication of hydrogels as thin, defect-free membrane selective layers remains a major challenge.

Existing literature on hydrogel membranes focus mainly on free-standing films.^{100, 320, 323-324} These hydrogel films are prepared by dissolving the monomer and initiator in an aqueous solution, spreading this mixture into a thin layer, and initiating polymerization, typically by UV illumination. This results in the formation of a very thick hydrogel layer (100-900 μm), and the resultant membranes have very low flux. To decrease film thickness while maintaining mechanical integrity, 1-10 μm hydrogel layers can be formed on porous supports by carefully designed coating methods.^{99, 325} However, this approach requires a high viscosity monomer solution and specific wetting properties to achieve a good coating that remains on top of the membrane. The viscosity can be increased with

additives (e.g. high molecular weight inert polymers)⁹⁴, but this can simultaneously change coating properties such as pore size.^{94, 103-104} Another surface modification approach, grafting^{99, 102} from the membrane surface, creates a polymer brush lining the membrane pores and surface rather than a continuous selective layer.^{102, 124} To form a selective layer by grafting, the pore diameter has to be spanned by growing polymer chains from a limited number of initiating sites on pores followed by cross-linking. This can require long reaction times and is prone to defects due to pore size polydispersity in the support membrane. Thus, there is a critical need for a simple and reproducible fabrication method that enables the formation of a very thin, defect-free hydrogel selective layer using processes that can be easily integrated into large scale manufacturing schemes. Such a method would enable the development of a wide range of membrane materials not only for protein purification, but also for wastewater treatment^{94, 106} and gas separation applications.³²⁶⁻³²⁷

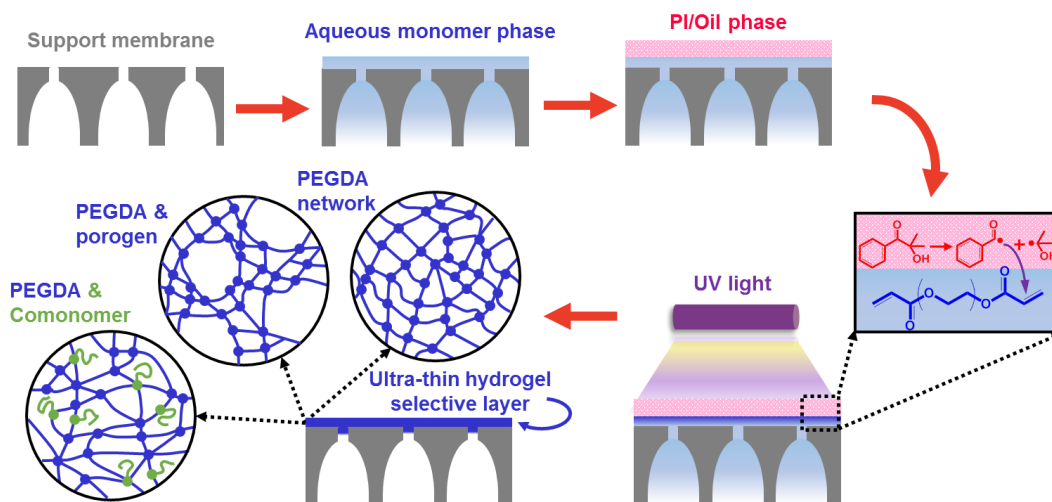
The most common method for the large-scale fabrication of membranes with ultra-thin selective layers is interfacial polymerization (IP).³²⁸⁻³²⁹ Thin film composite (TFC) membranes fabricated using this method feature a very thin selective layer (typically <100 nm) on a porous support that provides mechanical integrity.³³⁰⁻³³² IP involves the polymerization of two highly reactive monomers segregated in two immiscible phases (i.e. a diamine in aqueous solution and a diacyl chloride in an organic phase). The polymer forms as a thin film at the interface of the two phases covering the surface of the porous support. Although this method is established, simple, and scalable to a roll-to-roll process, it is limited to a narrow

range of polymer chemistries that are formed by condensation polymerization. IP cannot be applied to polymers prepared by free radical polymerization (FRP) such as hydrogels. It also cannot be used to fabricate inherently hydrophilic layers, because one of the monomers has to be oil-soluble. Furthermore, IP also generates a highly cross-linked and dense layer that limits the application of this method to desalination and reverse osmosis (RO). Larger pore sizes suitable for protein purification are typically not easily accessible.

Our approach to addressing these challenges centers on a novel, scalable and robust fabrication method inspired by IP, called Interfacially Initiated Free Radical Polymerization (IIFRP). The novelty of this approach arises from its ability to create ultra-thin, fully hydrophilic selective layers from a wide range of water-soluble monomers that propagate by free radical polymerization (e.g. acrylates, methacrylates, acrylamides). In IIFRP, as illustrated in Scheme 4.1, the monomer(s) and initiator are segregated into two immiscible phases: an aqueous monomer, and an organic/oil phase containing photoinitiator. The support membrane is first immersed in the aqueous monomer solution, which fills its pores and leaves a thin layer on its surface. The organic/oil layer containing an oil-soluble photoinitiator is then added to cover the top of the membrane. Upon irradiation with a UV lamp, a uniform and thin hydrogel layer is formed at the oil-water interface spanning the surface of the support membrane. Limited solubility of the initiator in the monomer layer, and the interfacial tension between the aqueous and oil layers creates a uniform, continuous, defect-free selective layer at the interface.

This is the first demonstration of a new, simple, scalable, reliable and robust technique for manufacturing membranes with ultra-thin, defect-free hydrogel selective layers. In this chapter, we first show that IIFRP can be used to create layers as thin as <100 nm on commercially available porous supports. Then, we depict that the permeance and pore size of selective layers formed by IIFRP can be readily altered through simple parameters (e.g. monomer concentration, UV exposure time) or through the addition of comonomers or inert polymers in the monomer solution. Finally, we demonstrate the stability and extremely high fouling resistance of the hydrogel layer in filtering protein solutions. This new technique, IIFRP, could serve as a platform for manufacturing membranes with a broad range of properties (e.g. selectivity, affinity) for several applications beyond protein purification, such as wastewater treatment, natural gas upgrading, and water purification.

Scheme 4. 1. Schematic showing fabrication of membranes with ultra-thin hydrogel selective layers by interfacially initiated free radical polymerization (IIFRP).^{*} Reproduced with permission from³³³. Copyright © 2018, American Chemical Society.



*A porous support membrane is immersed in an aqueous monomer solution, which fills its pores and leaves a thin layer on its surface. The membrane is then covered with an oil phase containing a photoinitiator (PI) and irradiated with UV light. The hydrophobic photoinitiator dissociates and reacts with the aqueous monomer at the interface, forming a thin hydrogel layer covering the support. The monomer solution can contain PEGDA with or without porogens or comonomers, which can alter layer permeability and control selectivity.

4.2. Materials and Methods

4.2.1. Materials

Poly(ethylene glycol) diacrylate (PEGDA, average Mn 700 Da), poly(ethylene glycol) methyl ether acrylate (PEGMEA, average Mn 480 Da), poly(ethylene glycol) (PEG, average Mn 200, 600), 2-hydroxy-2-methylpropiophenone also known as Darocur® 1173 (photoinitiator, PI), and bovine serum albumin (BSA) were purchased from Sigma-Aldrich (St. Louis, MO). N-hexadecane (99%), were purchased from ACROS Organics™. Cytochrome C, equine heart, +90%, and Aprotinin, from bovine lung were purchased from Alfa Aesar (Ward Hill, MA). Phosphate buffered saline (PBS) packs (0.1 M sodium phosphate, 0.15 M sodium chloride, pH 7.2) was purchased from Thermo Scientific (Rockford, IL). Reagent alcohol was obtained from VWR (West Chester, PA). Ultrapure deionized water generated by Biolab 3300 RO, a building wide RO/DI water purification unit by Mar Cor Purification was used for all experiments. All the chemicals were analytical grade and used without further purification. Polysulfone (PS35, 20 kDa) ultrafiltration membranes purchased from Nanostone Water, Inc. (Oceanside, CA) were used as the support membrane to provide mechanical stability.

4.2.2. Fabrication of Ultrathin Hydrogel Layer

The support membrane (Polysulfone, PS, Nanostone) was first washed with ethanol, dried, and then taped along all edges onto a glass plate. An aqueous solution containing 5-20 v/v% PEGDA (700 g mol^{-1}), with or without additives (PEG200, 600, or PEGMEA), was poured on the support membrane. The support membrane was equilibrated with this aqueous monomer solution for 3 min to provide enough time for monomers, comonomers and porogens to diffuse into the pores. The aqueous solution was then poured out and the membrane surface was gently dabbed using a filter paper to remove any residual droplets. A solution of 0.1 v/v% of oil-soluble PI (Darocur®) in n-hexadecane was poured on the membrane surface. The membrane surface was covered with a glass plate to prevent initiation from PS support membrane.³³⁴⁻³³⁵ Subsequently, the membrane was exposed to 365 nm UV light with an 8 W hand-held UV lamp (Spectronics Corp., Westbury, NY) for varying times (1-20 min). The excess solution covering the membrane was then poured out and the membrane surface was washed with a 1:1 water:ethanol mixture several times and kept in DI water overnight to ensure the complete removal of unreacted monomer, additives, initiator, and hexadecane.

4.2.3. Membrane Characterization

The microstructure of the membrane was characterized Field-Emission Scanning Electron Microscopy (FESEM, Supra 55) at 4 kV and 7 mm working distance. Dried membranes were frozen in liquid nitrogen and cut with a razor blade

for cross-sectional imaging. Samples were sputter coated (Cressington 108 manual, Ted Pella Inc., CA) with Au/Pd (60/40) in an argon atmosphere.

Attenuated Total Internal Reflectance-Fourier Transform Infrared (ATR-FTIR) spectra of membranes were collected using a FT/IR-6200 spectrophotometer (JASCO Corp, Tokyo, Japan) over the range of 4000-600 cm^{-1} at a 2 cm^{-1} resolution. Prior to analysis, membranes were air-dried for 24 hours.

4.2.4. Membrane Performance.

Filtration experiments were performed using an Amicon 8010 dead-end stirred cell (Millipore) with a cell volume of 10 mL and an effective filtration area of 4.1 cm^2 attached to a 1-gallon reservoir. The cell was stirred at 500 rpm. Tests were conducted at an applied trans-membrane pressure (TMP) of 40 psi. Water flow rate through the membranes was measured by collecting the permeate in a container placed on a scale (Ohaus Scout Pro) connected to a computer and recording the increase in permeate weight over time. The membrane permeance (L_p) was calculated by normalizing flux (J), defined as the water flow rate divided by active membrane area, with applied trans-membrane pressure (ΔP):

$$L_p = \frac{J}{\Delta P} \quad \text{Eq. (4.1)}$$

Membrane performance in protein filtration was studied by filtering solutions of a series of proteins with different sizes at a concentration of 100 ppm in PBS buffer one at a time. The first 1 mL of filtrate was discarded, and the subsequent 1 mL was collected. The concentration of protein in this filtrate was measured using

UV-Visible spectroscopy (Thermo Scientific Genesys 10S Spectrometer, Waltham, MA) at 285 nm for BSA and Aprotinin and 410 for Cytochrome C. Protein rejection was calculated according to:

$$R\% = \left(1 - \frac{C_P}{C_F}\right) \times 100 \quad \text{Eq. (4.2)}$$

where R is the solute rejection, and C_F and C_P are the concentration of feed (100 ppm) and permeate, respectively. Membranes were washed (soaked in DI water and DI water was filtered through overnight) before subsequent protein filtration experiments. No significant shift in water permeance was noted between protein filtration experiments.

The fouling properties of the membrane was investigated in a cross-flow system with a flat-frame membrane module (Sterlitech CF016A, Kent, WA) integrated with a KrosFlo® Research II TFF System (Spectrum Laboratories, Inc., Compton, CA). The CF016 cell, with an as-manufactured effective membrane area of 20.6 cm² and a channel depth of 2.3 mm, was fitted with an impermeable plastic mask that allowed the installation of round membrane swatches with an effective filtration area of 4.1 cm². Experiments were performed at trans-membrane pressure (TMP) of 40 psi and feed flow rate of 135 ml min⁻¹, corresponding to a shear rate of 9.4 s⁻¹ and a Reynolds number of 120, indicating laminar flow. This value was selected based on literature that reports more severe irreversible fouling occurring at low Re numbers.³³⁶⁻³³⁸

4.3. Results and Discussion

4.3.1. Hydrogel Layer Morphology

As the first demonstration of the IIFRP method to manufacture membranes with hydrogel selective layers, we first immersed a commercial UF membrane (PS35, Nanostone), which will act as the porous support, into an aqueous solution containing the poly(ethylene glycol) diacrylate (PEGDA) monomer. In most cases, we added an inert hydrophilic polymer, poly(ethylene glycol) with an average molar mass of 200 g mol^{-1} , PEG200, as an additive. The selection was based on the previous literature stating that inert short chain PEG can create a porous network,³³⁹⁻³⁴¹ which in turn would be expected to lead to an increase in membrane permeance. The effect of additives on membrane permeance and selectivity is further discussed in the following section. Next, we removed the support from the aqueous solution, dabbed off the excess, and covered it with the oil solution, n-hexadecane containing 0.1 v/v% of the hydrophobic photoinitiator (PI), Darocur® 1173. We then exposed it to UV light, which caused the initiator to form free radicals in the oil phase that then diffused to the aqueous phase and started the polymerization of PEGDA (Scheme 4.1). The membrane surface was covered by a glass plate during UV exposure to prevent initiation from PS support membrane upon exposing to UV light, as reported in previous studies.³³⁴⁻³³⁵ A control experiment performed without the addition of PI into the oil phase did not lead to a significant change in permeance.

Our approach, IIFRP, is in direct contrast to the established photo-initiated free radical polymerization (FRP) methods for preparing hydrogel layers, where monomers and PI are both in the aqueous phase. Using this method, a solution containing only the monomer and the PI cannot typically be coated onto a porous support. The solution is instantly absorbed into the membrane pores through capillary action and the whole support is filled with hydrogel. Indeed, when the above procedure was performed using a monomer solution containing a water-soluble initiator, this was the result (Figure 4.1). The viscosity of the solution can sometimes be increased by increasing the concentration of the solution or adding high molecular weight polymers,⁹⁴ but this often results in the formation of a very thick layer and changes the resultant membrane properties. Furthermore, the uneven exposure to UV light and polymerization-induced phase separation (PIPS) can lead to macro-scale porosity in the film.^{323, 342}

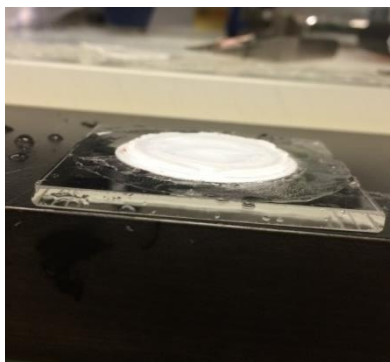


Figure 4. 1. Membrane prepared using single phase aqueous solution containing 40 v/v% PEGDA and 1 wt% water-soluble PI (Irgacure 2959) showing formation of a very thick and non-uniform hydrogel layer on the PS support. Reproduced with permission from³³³. Copyright © 2018, American Chemical Society.

In contrast, IIFRP segregates the reactants (i.e. monomers and PI) into two separate phases. Free radicals formed by PI upon UV exposure diffuse to the

oil/water interface and react with the monomers in the aqueous monomer solution to initiate polymerization. Since the PI is insoluble in water, the polymer layer starts forming at and growing from the oil/water interface. When UV irradiation is stopped, the polymerization process also ends, arresting the growth of the selective layer. Thus, longer UV irradiation times are expected to result in thicker selective layers. This would not necessarily be the case for homogeneous FRP, where longer exposure would likely increase the degree of cross-linking but not necessarily the coating thickness once the gel point is reached. It is also in contrast to traditional IP, where the formation of the highly cross-linked selective layer at the interface hinders the diffusion of the monomers, leading to a self-limiting reaction. The mesh size of the hydrogel layer that forms in IIFRP is much larger in comparison to the monomer size. This means monomers easily diffuse to the interface and react with the initiating radicals, enabling the hydrogel layer to build as long as radicals are generated through UV irradiation.

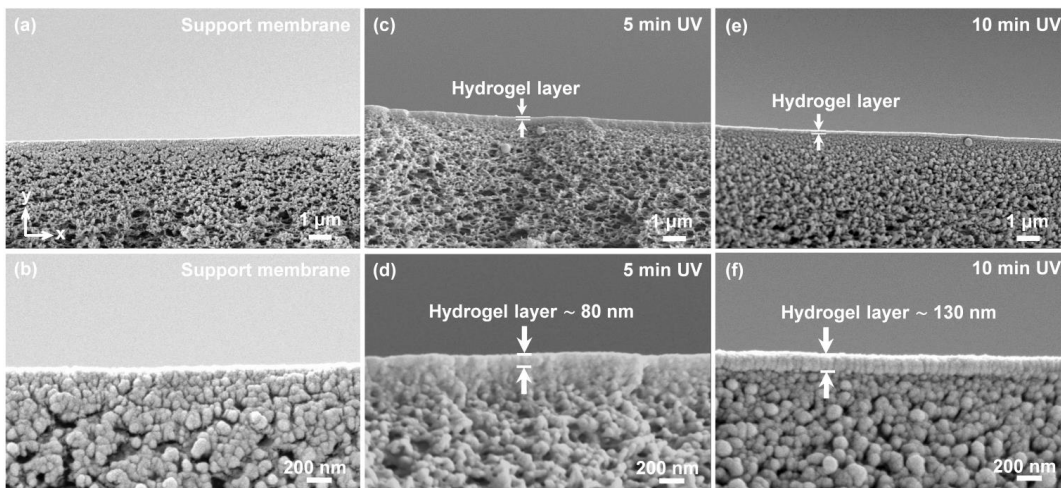


Figure 4. 2. Morphology of (a) Support membrane, PS, (b) Higher magnification of PS support, (c) Hydrogel layer at 5 min UV exposure time (d) Higher magnification of hydrogel at 5 min UV exposure time, (e) Hydrogel layer after 10

min UV exposure time, (f) Hydrogel layer at 10 min UV exposure time at higher magnification. Continuous and uniform hydrogel layers are formed on the support membrane upon exposure to UV at varying times. Longer UV exposure time leads to formation of a thicker layer. Reproduced with permission from³³³. Copyright © 2018, American Chemical Society.

To test this hypothesis, we prepared membranes with varying UV irradiation times and analyzed the resultant membrane morphology by Field Emission Scanning Electron Microscopy (FESEM). Figures 4.2a and 4.2b show the commercial polysulfone (PS) membrane with nominal molecular weight cut-off (MWCO) of 20 kDa that we utilized as the porous support throughout the study. Typical of asymmetric ultrafiltration membranes, the membrane has smaller pores on top and larger macrovoids in the sublayers. When IIFRP was applied to this support membrane using 5 v/v% PEGDA as the monomer solution and a UV exposure time of 5 min, a very thin hydrogel coating layer was formed (Figure 4.2c, d). The higher magnification image of this membrane (Figure 4.2d) shows the presence of the layer more clearly. The layer is well-integrated into the support, penetrating slightly below the top surface pores and anchoring into the support as envisioned. This morphology prevents the delamination of the layer, but also makes it difficult to clearly identify the boundaries of this layer and determine the thickness. To further confirm the evenness and uniformity of the hydrogel layer formed on the support membrane, we dissolved the support layer in dichloromethane and transferred the hydrogel layer to a wire lasso (Figure 4.3). Although, the layer is very thin, it formed an integral surface across the whole 1-cm diameter of the lasso, providing solid evidence of the uniform and continuous nature of the hydrogel layer.



Figure 4. 3. Photograph of a smooth hydrogel (5 v/v% PEGDA-5 min UV exposure) transferred to a wire lasso. Reproduced with permission from³³³. Copyright © 2018, American Chemical Society.

When IIFRP was performed using 10 min UV exposure under identical conditions, a more distinct layer is formed compared with the shorter irradiation time of 5 min (Figure 4.2e). Notably, the layer appears to be uniform throughout the membrane imaged along the x-direction labeled in the figure. This uniform layer is maintained throughout the entire membrane sample, imaged in different frames sampling the length of the sample (data not shown), clearly indicating the consistent nature of this simple method. A higher magnification image of this membrane (Figure 4.2f) shows that the layer is also uniform across the layer thickness (y-direction). The coating is thicker and more distinct in this sample compared to 5 min UV exposure time, allowing a rough estimation of the thickness to be around 130 nm. Longer UV exposure appears to increase the dry thickness of the hydrogel layer. For example, an even longer exposure time of 20 min led to the formation of a hydrogel layer with thickness of 260 nm, about twice the one formed at 10 min UV exposure time (Figure 4.4). Accounting for the uniform thickness of the

aqueous prepolymer layer during the polymerization and the status of the membrane sample during SEM imaging (i.e. dried), the observed difference in the thickness is likely due to the polymerization process penetrating into the membrane to different extents. Importantly, this result suggests that simple fabrication parameters such as UV irradiation time can be used to impart various membrane properties (e.g. layer thickness and penetration).

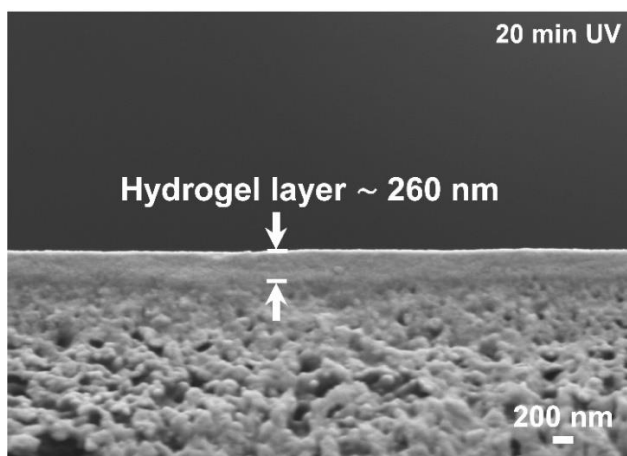


Figure 4. 4. FESEM image of a membrane formed with 20 min UV exposure time, with a thicker hydrogel layer. Reproduced with permission from³³³. Copyright © 2018, American Chemical Society.

4.3.2. Chemical Structure of the Hydrogel Layer

In order to further confirm the formation of the ultra-thin hydrogel layers, we performed attenuated total reflection – Fourier transform infrared spectroscopy (ATR-FTIR) on membranes prepared by IIFRP using a monomer solution containing 5 v/v% PEGDA, 2.5 v/v% PEG200 and a UV exposure of 5 min (Figure 4.5). PEGDA (Figure 4.5a) forms a cross-linked network upon photo-induced free radical polymerization on the membrane surface. This leads to an increase in the

density of C-H bonds (blue) in comparison with the support membrane material PS, and also introduces ester groups (pink).

Indeed, upon the deposition of the cross-linked PEGDA selective layer by IIFRP, the broad absorbance peak around 2800-3000 cm^{-1} (top spectrum) corresponding to the C-H stretching vibration increases in intensity.³⁴³⁻³⁴⁴ This peak is very weak in the support membrane (bottom spectrum), which does not contain as high a concentration of C-H groups (labeled blue in Figure 4.5a). This clearly confirms the presence of the PEG hydrogel layer. The presence and chemical structure of the coating layer is also confirmed by the appearance of the C=O stretching peak at 1723 cm^{-1} arising from the ester bond at each end of the PEGDA (labeled pink),³⁴³ while the IR spectrum of the support membrane (bottom) shows no such peak.

In addition, the coating shows no significant absorbance at 1620 – 1640 cm^{-1} . This wavelength range corresponds to the vinyl groups in PEGDA that are converted to single bonds upon polymerization.³⁴³ The lack of a peak in this range in the spectrum of the coated membrane suggests that the formed hydrogel layer is mostly or fully polymerized, mostly free of unpolymerized or partially polymerized PEGDA monomer.

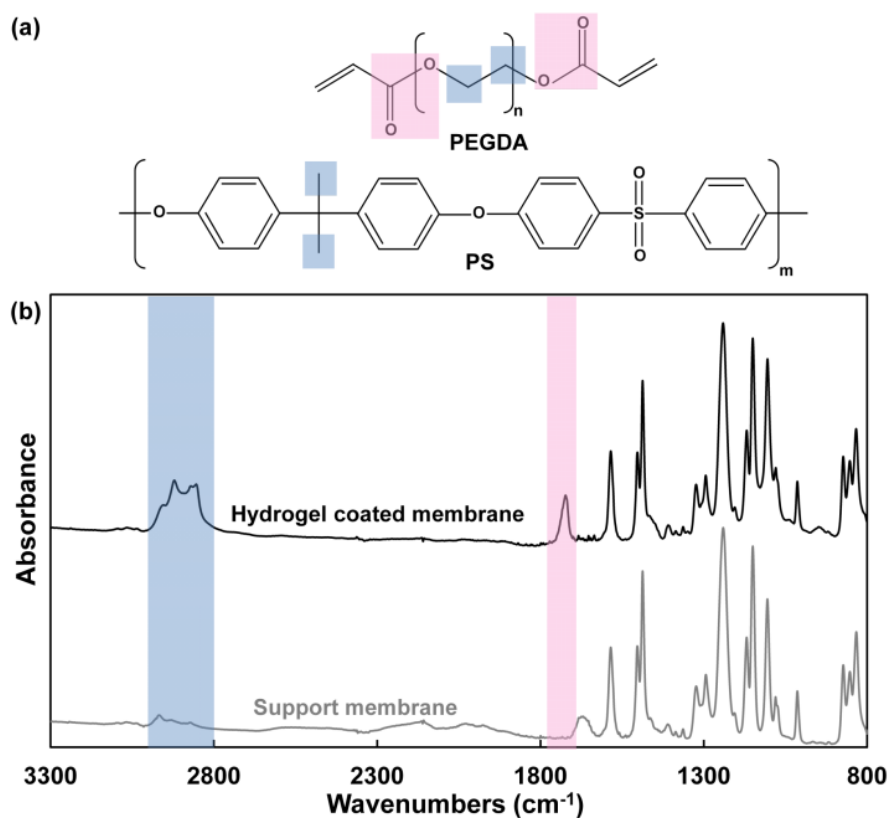


Figure 4. 5. (a) Chemical structure of PEGDA and PS, (b) ATR-FTIR spectra of PS support membrane (bottom) and coated with an ultra-thin hydrogel layer (top) with 5 min UV exposure. Absorption bands corresponding to CH (blue) and ester (pink) groups are marked to demonstrate the formation of a cross-linked PEGDA hydrogel selective layer in the PS support. Reproduced with permission from³³³. Copyright © 2018, American Chemical Society.

Given the chemical structure and low thickness of these selective layers, the resultant membranes are expected to be highly permeable. However, this needs to be verified by filtration experiments that demonstrate their performance in more realistic situations. Thus, next the permeation properties of the hydrogel-coated membranes were examined.

4.3.3. Membrane Permeation Properties

To characterize how membranes prepared by IIFRP perform in aqueous filtration applications, we performed filtration experiments using a dead-end system. First, we aimed to understand the effect of IIFRP process parameters such as the UV exposure time on membrane permeance. For this, monomer solution containing 5 v/v% PEGDA and 2.5 v/v% PEG200 was used to form hydrogel layers by IIFRP at different UV exposure times (4-20 min) on identical support membranes. Deionized water was filtered through the membrane until the flow rate stabilized. Pure water permeance, defined as the water flux through the membrane normalized by the applied pressure difference of 40 psi, was calculated. As Figure 4.6 shows permeance was stable over a wide range of transmembrane pressures, up to 60 psi. This indicates and no irreversible collapse of pores upon exposure to high trans-membrane pressure.³²⁴

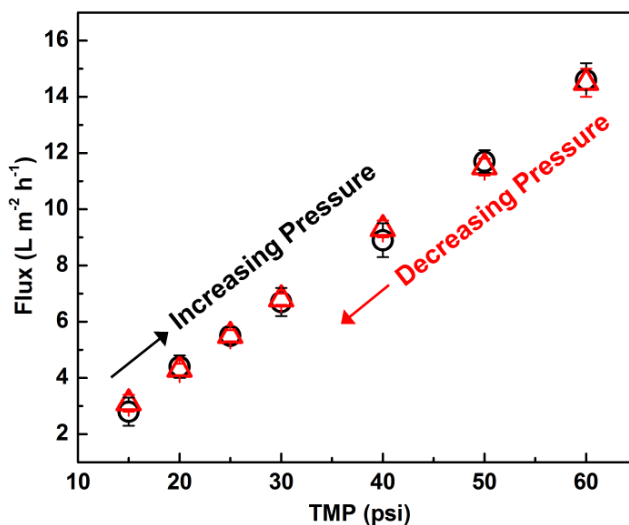


Figure 4. 6. Effect of transmembrane difference on flux for hydrogel membrane prepared with monomer solution containing 5 v/v% PEGDA, 2.5 v/v% PEG200. Reproduced with permission from³³³. Copyright © 2018, American Chemical Society.

The support membrane was measured to have a water permeance of $1250 \pm 60 \text{ L h}^{-1} \text{ m}^{-2} \text{ bar}^{-1}$. Figure 4.7 shows the water permeances of these hydrogel-coated membranes. Even the membrane prepared with the shortest UV exposure time of 4 minutes had a substantially lower permeance than the support membrane, $6.2 \text{ L h}^{-1} \text{ m}^{-2} \text{ bar}^{-1}$. This indicates the formation of the hydrogel layer. Membranes prepared with 5 to 20 min UV exposure times also showed substantially lower permeances compared with the support membrane. Longer UV exposure initially lead to lower permeance, but the values reached a plateau after 10 minutes, indicated by the dotted line (B-Spline fitting). A minimum UV exposure time of 4 min was needed for the formation of a uniform hydrogel layer with permeation properties that are distinctly different from the support membrane. Shorter exposure times (1-3 min) lead to membranes with permeances comparable with the support membrane, indicating that a complete hydrogel layer integrated into the support had not yet formed at this time. These results correlate well with and further confirm the morphological results acquired via FESEM. The membrane featuring a thinner hydrogel layer (5 min) exhibits 1.4 times higher permeance than the ones with thicker layers (20 min). The error bars shown in Figure 3 represent the maximum and minimum permeance values measured during the test of at least 5 samples for each condition. The narrow range of resultant permeances, indicated by the small error bars, clearly depicts the reproducible, consistent, robust and reliable nature of our simple IIFRP method.

The permeance range we have achieved in this study is comparable to commercial thin film composite (TFC) membranes with crosslinked selective

layers prepared by IP with the largest available pore size. These membranes are tight ultrafiltration (UF) membranes, typically designed for nominal molecular weight cut-off (MWCO) values between 1000 - 3000 Da. For example, according to industrial specification sheets, UF membranes manufactured by GE with nominal MWCOs between 1000 - 3000 Da have permeances between 1.12- 5.65 L m⁻² h⁻¹ bar⁻¹.³⁴⁵ It is also significantly higher than free-standing hydrogel membranes reported in the literature, 0.002 to 0.3 l m⁻² h⁻¹ bar⁻¹.

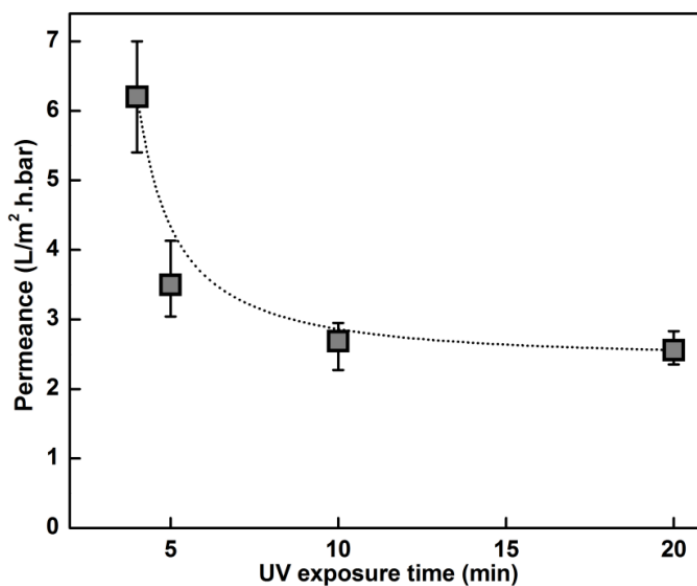


Figure 4. 7. Effect of UV exposure time on membrane permeance; all membranes are prepared with monomer solution containing 5% PEGDA and 2.5% PEG200. Significant difference between the permeance of the support membrane and hydrogel-coated membranes indicates the formation of the hydrogel layer, with permeances depending on UV exposure time. Reproduced with permission from³³³. Copyright © 2018, American Chemical Society.

At this stage, the water permeance of our membrane is lower than values listed for commercial membranes commonly used for bioseparations such as regenerated cellulose UF membranes.³⁴⁶ However, as discussed below, the fouling behavior of hydrogel membranes are significantly different from most commercial

membranes, which are prone to severe fouling upon exposure to solutions containing organic macromolecules (e.g. proteins, polysaccharides) and oil.^{2-3, 347} The IIFRP method presented here enables the preparation of membranes with highly hydrophilic hydrogel selective layers with excellent anti-fouling properties. These membranes retain their initial permeance fully even when filtering protein solutions, as demonstrated in the data below. In contrast, commercial membranes, including those made of the relatively hydrophilic regenerated cellulose, often exhibit severe declines in permeance during the filtration of protein solutions due to fouling. For example, even though the Ultracel PLCGC membrane manufactured by EMD Millipore with MWCO of 10 kDa has a higher permeance when tested with pure water, its permeance declines severely during the filtration of protein solutions. Some reported permeances during the filtration of representative protein solutions (bovine skim colostrum whey or surfactin) range between $1.7 \text{ L m}^{-2} \text{ h}^{-1} \text{ bar}^{-1}$ and $7 \text{ L m}^{-2} \text{ h}^{-1} \text{ bar}^{-1}$,³⁴⁸⁻³⁴⁹ comparable with the permeances documented for membranes reported here. Similarly high flux decline has also been reported for larger MWCO Ultracel membranes.³⁵⁰⁻³⁵² Thus, the exceptional fouling resistance of membranes prepared by IIFRP can enable comparable and more stable membrane permeance during the filtration of protein solutions encountered in bioseparations.

Furthermore, we believe that the IIFRP process has the potential to be tuned and optimized by changing other parameters (e.g. photoinitiator concentration, monomer concentration, additives) to further improve the permeance of resultant membranes. Improved flux can also be achieved by identifying the optimal support

membrane for each application. The literature shows that the selection of the support membrane can change the permeance of the TFC membranes by up to an order of magnitude.³⁵³ Therefore, highly competitive and stable permeances can be achieved upon the optimization of the IIFRP process for each targeted bioseparation.

4.3.4. Membrane Selectivity and Protein Rejection

Next, the performance of hydrogel-coated membranes prepared by IIFRP was examined for the filtration of protein solutions in a dead-end filtration setup (Figure 4.8). For this, different protein solutions were filtered through the hydrogel-coated membranes prepared with a monomer solution of 5 v/v% PEGDA and 2.5 v/v% PEG200 at different UV exposure times (5-20 min). The membranes were first compacted by filtering deionized water for at least 3 hours. Three proteins with different molecular weights and hydrodynamic radii (R_H) were tested: Aprotinin (6.5 kDa, $R_H \sim 1.3$ nm), Cytochrome C (12 kDa, $R_H \sim 1.7$ nm), and bovine serum albumin (BSA, 66 kDa, $R_H \sim 3.5$ nm).³⁵⁴ Each protein was dissolved in phosphate buffered saline (PBS) at a concentration of 100 ppm and filtered through the membrane one at a time. Rejection (R) was calculated by measuring the UV absorbances of feed and permeate at 280 nm for BSA and Aprotinin and 410 nm for Cytochrome C according to Eq. (4.2).

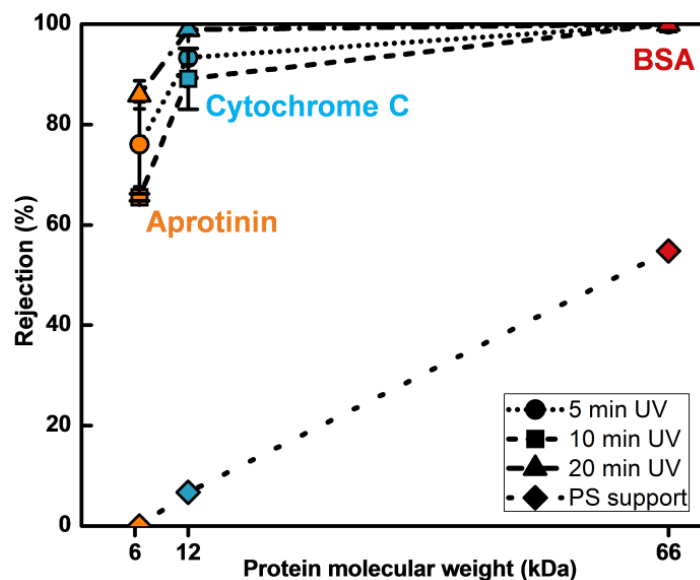


Figure 4. 8. Rejection properties of hydrogel-coated membranes. The PS support membrane shows limited rejection for all three proteins, whereas cross-linked PEGDA coated membranes prepared by IIFRP reject Cytochrome C and BSA by >90%, indicating a MWCO around 8-10 kDa. Reproduced with permission from³³³. Copyright © 2018, American Chemical Society.

Figure 4.8 shows the rejection of these three proteins by the support membrane and three hydrogel-coated membranes prepared by IIFRP using different UV irradiation times. All hydrogel-coated membranes exhibit similar rejection properties, with an effective pore size significantly smaller than the support membrane. For the smallest protein Aprotinin (6.5 kDa), all the membranes prepared by IIFRP show moderate rejection (65 – 85%). In contrast, Aprotinin passes through the support membrane with no measurable rejection. All three hydrogel-coated membranes show higher rejection (90 – 99.9%) for the slightly larger Cytochrome C (12 kDa) than the support membrane, which shows only 6% rejection. Finally, for the largest protein, BSA (66 kDa), complete rejection within the detection limit (>99%) was obtained for all the three hydrogel-coated membranes, whereas 55% rejection was observed for the support membrane. This

is consistent with a MWCO of about 8-10 kDa for the hydrogel-coated membranes, clearly illustrating the formation of a selective layer that controls membrane selectivity and protein rejection.

All three hydrogel coated membranes had similar rejections, within error margins of each other. This suggests that UV exposure time mainly affects hydrogel layer thickness and not the hydrogel mesh size. Importantly, all the consistent protein rejection results with small error bars (indicating the rejection range from minimum 3 membrane samples per condition) confirm minimal defects throughout the membrane area (4.1 cm²), providing evidence of the reliable and robust nature of IIFRP for preparing membrane selective layers. Furthermore, the hydrogel selective layer shows a much sharper sized-based cut-off in comparison to the support membrane.

4.3.5. Effect of Drying on Membrane Performance

Since membranes are usually delivered in dry state, we investigated the effect of drying and rehydration on membrane permeance and rejection properties. For this, membrane composition of 5 v/v% PEGDA and 2.5 v/v% PE200 was selected as an example. The membrane was air-dried overnight and soaked in water afterward. Then, membrane permeance and rejection were measured. Both permeance and cytochrome C rejection of the membranes remained unchanged after two drying and rehydration cycles. This confirms the absence of any cracks, pore collapse or defects upon loss of water.

4.3.6. Effect of Monomer Solution Composition on Membrane Selectivity and Permeance

Membrane selectivity and permeance is affected by various parameters that can be adjusted in the IIFRP process, including the composition of the aqueous monomer solution. These parameters can be used to tune membrane pore size, optimize the process to achieve high permeance while maintaining desired selectivity, and to incorporate desired functional groups in the selective layer for various purposes. For example, the PEGDA concentration in this solution can be changed. Alternatively, other components can be added to this solution. Inert polymers such as low molecular weight poly(ethylene glycol) (PEG) can act as porogens by altering the cross-link density and hence mesh size, or create larger scale voids through PIPS. Comonomers can also alter the mesh size by increasing the distance between cross-links, but also incorporate functional groups in the selective layer. The IIFRP process allows a wide selection of such components; as long as these components are water-soluble, they can be used.

To demonstrate this, we prepared PEGDA hydrogel-coated membranes by IIFRP using different PEGDA concentrations (5-20 v/v%) in the monomer solution, and also using PEG200 as an additive at a volume ratio of 2:1 PEGDA:PEG200. The pure water permeance of these membranes, prepared with 5 min UV exposure, was measured in a dead-end filtration system at a trans-membrane pressure (TMP) of 40 psi.

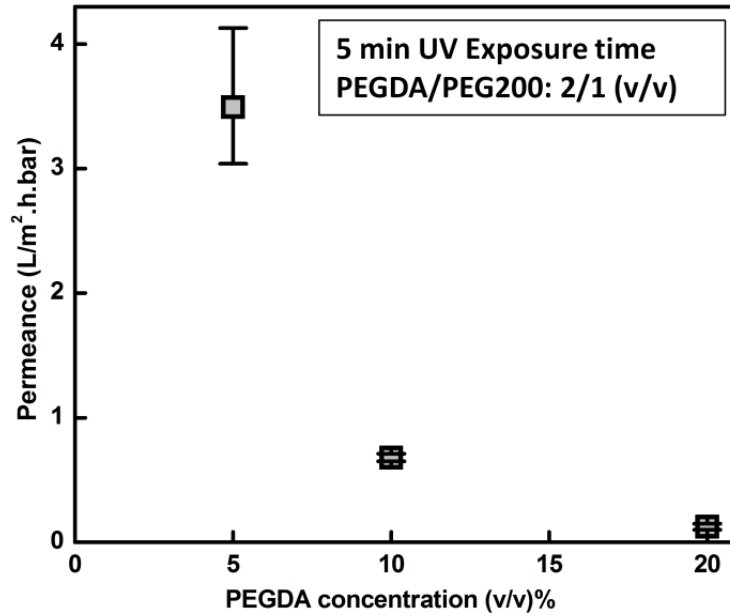


Figure 4. 9. Effect of PEGDA concentration on membrane permeance. Error bars indicate the range of permeances obtained for a minimum of three samples.

Figure 4.9 shows the change in membrane pure water permeance with varying PEGDA concentration in the monomer solution. When the PEGDA concentration increased from 5 v/v% to 10 v/v%, membrane permeance decreased by 5 times. The permeance decreased further upon increasing PEGDA content to 20 v/v%. This trend could be attributed to the formation of a selective layer with higher polymer content and cross-link density, and therefore a smaller effective pore size of the hydrogel network. These results are consistent with the literature on free-standing PEG hydrogels in that monomer content directly controls the hydrogel layer cross-link density, which would in turn determine the effective mesh size and MWCO.³⁵⁵⁻³⁵⁶ The IIFRP hydrogel-coated membranes also show thicker dry thickness upon increased PEGDA concentration due to faster polymerization achieved at higher monomer concentrations, and to higher polymer content in the

resultant hydrogel layer leading to a thicker film when dried for SEM imaging (Figure 4.10).

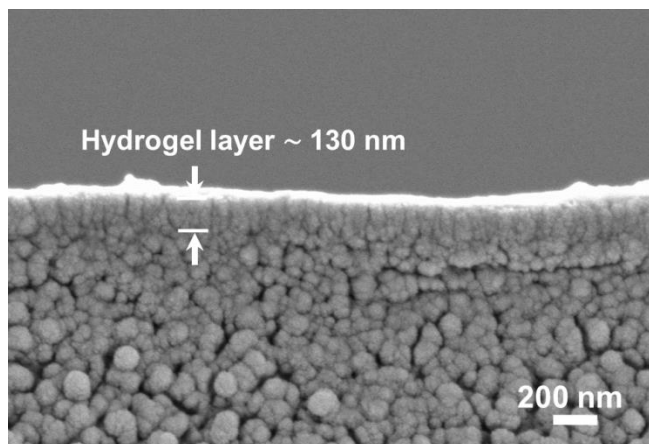


Figure 4. 10. Membrane prepared with monomer solution containing 10 v/v% PEGDA and 5 min UV exposure time; a thicker layer is formed compared to monomer solution with 5 v/v% PEGDA at same UV exposure time. Reproduced with permission from³³³. Copyright © 2018, American Chemical Society.

We next examined the effect of different inert additives such as low molecular weight PEG (PEG200 and PEG600, with average molar masses of 200 Da and 600 Da, respectively) on the permeation and rejection properties of membranes prepared by IIFRP of PEGDA (Table 4.1). For this, we added the PEG oligomers at varying concentrations (0 – 30 v/v%) to the monomer solution and performed IIFRP using a 5 min UV exposure time. The presence of PEG oligomers during the gelation of PEGDA in water is reported to cause phase separation between PEG and PEGDA during photopolymerization, termed polymerization induced phase separation (PIPS).³⁵⁵ PEG oligomers are inert porogens that do not polymerize with PEGDA, and are washed away upon rinsing.³⁵⁷ This leads to the formation of pores or voids.^{355, 358-359} The presence of voids within the selective layer leads to an increase in the permeance and/or pore size of the resultant

membranes, enabling us to tune their separation properties to the desired application.

Table 4.1 shows the pure water permeances of these membranes, and the rejections of two proteins, BSA and Cytochrome C, as an indicator of their effective pore size. The two top rows of Table 4.1 show that a small amount of PEG200 (2.5 v/v%) increases the permeance by 1.8 times over the hydrogel-coated membrane without the PEG200 while maintaining similar protein rejection properties. Increasing PEG200 content further to 10 v/v% increases the membrane permeance to about 3 times the value for the membrane prepared without PEG200 but causes no significant change in rejection. Our hypothesis is that PIPS during this process does not create interconnected large pores, but discrete voids, or cells, similar to those observed in closed-cell foams. The voids are enclosed with continuous hydrogel “walls” within the selective layer, so membrane selectivity is unchanged. However, the enclosed voids do not pose resistance to flow. Hence, the “effective film thickness”, or the net thickness that will pose resistance to flow, is lower than the depth polymerization progresses to. This can improve the permeance subsequently, without changing the mesh size of the PEGDA network.³⁶⁰ As an interesting parallel, recent studies have reported the presence of interspersed voids within the thin polyamide selective layers of RO membranes manufactured by IP method.^{330, 361} These voids are filled with water during filtration and result in the creation of a shorter diffusion path and thus higher permeance. Our results indicate that a similar mechanism of increased permeance may be at play when PEG200 is used as an additive at low to moderate concentrations, though these results warrant

further morphological characterization as a future study. In addition, PIPS may lead to an increase in the fractional free volume of the selective layer by creating voids smaller than the size of the protein within the layer, again leading to a higher permeance without a change in selectivity.

Table 4. 1. Effect of comonomer/porogens as additives in monomer solution on hydrogel-coated membranes' permeance and rejection properties. Reproduced with permission from³³³. Copyright © 2018, American Chemical Society.

Membrane Samples	Permeance (L m ⁻² h ⁻¹ bar ⁻¹)	BSA Rejection%	Cytochrome C Rejection%
5% PEGDA	1.9 ± 0.3	>99*	92.5 ± 1.1
5% PEGDA/ 2.5% PEG200	3.5 ± 0.5	>99	93.4 ± 2.0
5% PEGDA/ 10% PEG200	5.9 ± 0.4	>99	96.7 ± 1.3
5% PEGDA/ 20% PEG200	3.8 ± 1.2	>99	94.9 ± 0.9
5% PEGDA/ 30% PEG200	6.3 ± 1.6	85 ± 2	71 ± 7
5% PEGDA/ 30% PEG600	8.1 ± 1.5	70 ± 7	65 ± 9
5% PEGDA/ 2.5% PEGMEA	2.6 ± 0.7	>99	95.0 ± 0.6
7.5% PEGDA	1.1 ± 0.3	>99	99.5 ± 0.3

* Detection limit

Error margins indicate standard deviation from at least three samples.

Upon further addition of PEG200 (20 v/v%), the permeance decreases, yet similar rejection properties are obtained. This decrease in permeance could be explained by the fact that high amount of PEG200 ($\delta = 19.1 \text{ MPa}^{1/2}$)³⁶² can increase the solubility of the PI ($\delta = 24.3 \text{ MPa}^{1/2}$, calculated using Molecular Modeling Pro Software) in the water phase ($\delta = 47.9 \text{ MPa}^{1/2}$).³⁶³ This may cause some of the PI to partition into the monomer solution before UV exposure, leading the polymerization reaction to no longer occur just at the interface, allowing the hydrogel layer to penetrate into the membrane pores. However, when 30 v/v%

PEG200 was used in the monomer solution, the resultant permeance was about three times the value for the membrane prepared without any PEG200. This was accompanied with a decrease in the rejection of both BSA and Cytochrome C. This is likely due to the formation of interconnected pores by PIPS at this high concentration of PEG200. Inert additives such as PEG oligomers can also interfere with the polymerization reaction when present at high concentrations.³⁶⁴ This could also have resulted in the observed decrease in protein rejection.

PEG600 has been documented to create larger pores in cross-linked PEG gels than PEG200 due to PIPS occurring more significantly than with PEG200.³⁴⁰ Yet, our results indicate that addition of 10-20 v/v% PEG600 leads to similar results as those obtained with similar amounts of PEG200. Similar to PEG200, higher permeance (more than four times in comparison to the one without porogen) and lower protein rejections were obtained at 30 v/v% PEG600. These changes, however, were more significant than those observed for PEG200. The formation of larger pores by PEG600 can be attributed to either PIPS occurring to a larger extent in comparison to the PEG200 porogen,³⁴⁰ or to PEG600 inhibiting polymerization to a greater extent than PEG200.³⁶⁰ This shows that the hydrogel network can be easily tuned using different porogens.

Cross-link density and PIPS can also be influenced by the presence of a mono-functional comonomer such as poly(ethylene glycol) methyl ether acrylate (PEGMEA) mixed with PEGDA in the monomer solution.³⁴² The results in the two bottom rows of Table 4.1 show that copolymerization of PEGMEA with PEGDA leads to a higher membrane permeance in comparison with a membrane made with

PEGDA only (7.5 v/v%). BSA is fully retained by both membranes, whereas the rejection of smaller Cytochrome C decreases somewhat, indicating a slight increase in the effective pore size of the membrane. The replacement of some PEGDA with PEGMEA would decrease the cross-link density in comparison with the membrane containing only PEGDA, leading to this higher mesh size that controls protein selectivity.^{323, 342} Long pendant chains introduced by the addition of PEGMEA to the hydrogel network can disrupt polymer chain packing and thus decrease crosslink density.³⁶⁵ Also, PEGMEA with free methoxy chain end-groups decrease the cross-link density by decreasing the fraction of poly-functional monomers that create cross-links and providing more fractional free volume in the network.^{323, 342} Unlike PEG porogens, PEGMEA also participates in the polymerization reaction. This increases the effective monomer concentration in solution (compared with, for example, the membrane prepared from 5% PEGDA and 2.5% PEG200) and hence leads to a higher polymer content and lower permeance in comparison with membranes prepared with inert porogens from 5% PEGDA.

Finally, consistently small deviations (i.e. permeance range shown by error bars in Figure 4.9 and standard deviations in Table 4.1) were obtained for each condition tested using these additives. This indicates the robustness and reliability of our simple process for forming hydrogel membrane selective layers. Combined, the results in Figure 4.9 and Table 4.1 demonstrate that the IIFRP technique yields readily tunable membrane parameters widening the scope for various protein separation applications. Also, while not fully explored in this study, the selective layer can be modified to include any other water-soluble components (e.g.

comonomers, porogens, nanomaterials). By carefully tuning the parameters, hydrogel selective layer can be designed for targeted separations (e.g. charged- or affinity-based separations).

4.3.7. Fouling Resistance

Fouling resistance is crucial for the successful use of membranes.³⁶⁶ Fouling is a particularly prominent challenge in protein separation applications, because proteins are especially prone to adsorb on the membrane surface and inside the pores.³¹⁶⁻³¹⁷ This can cause substantial flux decline and cause changes in membrane selectivity due to pore narrowing.^{316, 318-319} Therefore, it is crucial for newly developed membrane materials to resist fouling to ensure reliable, long term operation, especially for such high-fouling applications. We thus examined the fouling of hydrogel-coated membranes prepared by IIFRP during the filtration of a protein solution over an extended period of time. For this, we performed a cyclic filtration experiment with 100 ppm BSA solution as a model protein in a cross-flow set up at a TMP of 40 psi, feed flow rate of 135 ml min⁻¹, corresponding to a shear rate of 9.4 s⁻¹ over two 6-hour periods of protein filtration, between which deionized water was filtered through the membrane for two hours (Figure 4.11). Experiments were performed using a round membrane swatch with an effective filtration area of 4.1 cm². For the fouling experiment, we chose the membrane prepared with 5 v/v% PEGDA and 2.5 v/v% PEG200 at UV exposure time of 5 min as an example. This membrane showed high permeance and high rejection for BSA (>99%), so no internal pore fouling was expected, emphasizing the fouling resistance of the hydrogel layer covering the surface.

The membrane was first equilibrated and compacted by filtering DI water for 5 hours. The initial water flux at the end of this period, termed J_0 , was measured to be $12.5 \text{ L m}^{-2} \text{ h}^{-1}$, corresponding to a permeance of $4.6 \text{ L m}^{-2} \text{ h}^{-1} \text{ bar}^{-1}$. Next, BSA solution was filtered through the membrane for 6 hours. The membrane initially showed <2% reduction in flux during the filtration of this solution, and no further noticeable decline in flux throughout the six-hour period. It is worth noting that the 2% drop in the flux of protein solution could arise from the osmotic pressure difference caused by the presence of retained solutes in the feed and from concentration polarization rather than an indication of any fouling.³⁶⁷⁻³⁶⁸ The lack of further flux decline during operation implies no build-up of foulants occurs on the membrane surface, due to the adsorption of proteins or due to cake formation.³⁶⁹⁻³⁷⁰ Next, to test the reversibility of this minor decline in flux and confirm its cause, the feed was switched to DI water for two hours. The membrane immediately returned to its initial flux without the need for backwashing or chemical cleaning, clearly indicating excellent resistance to fouling by this protein. Comparable results were achieved during the second protein filtration cycle. No fouling was observed in this second protein filtration cycle either. BSA molecules were retained by >99%. The membrane immediately returned to its initial water flux upon water filtration. This result clearly illustrates the excellent anti-fouling property and robustness of our hydrogel-coated membrane over extended exposure to protein solutions. In contrast, commercial UF membranes used in protein separations (e.g. made of PS) are known to foul extensively and immediately upon exposure to protein solutions, often leading to severe flux decline during the

filtration of the solution, as well as flux declines of more than 50% that cannot be reversed even by more complex physical cleaning procedures compared with those used in this experiment.^{94, 319, 371} The excellent fouling resistance demonstrated in this experiment illustrates the potential of IIFRP to prepare highly fouling resistant membranes for protein separation.

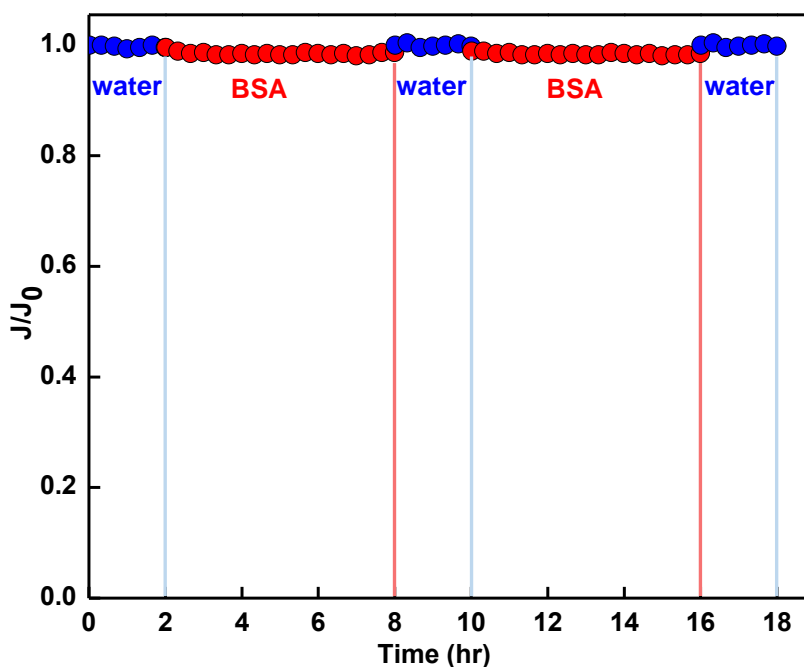


Figure 4. 11. Long-term fouling resistance of hydrogel-coated membrane upon exposure to a model protein (BSA) solution. Tests performed in a cross-flow set up at a TMP of 40 psi; flux is normalized by average initial water flux. Hydrogel-coated is extremely fouling resistant suitable for protein purification. Reproduced with permission from³³³. Copyright © 2018, American Chemical Society.

4.4. Conclusions

This report is the first demonstration of a new, robust interfacial polymerization-based technique, IIFRP, to manufacture membranes with ultra-thin hydrogel selective layers, their key performance parameters in relevant to protein purification and separation applications. As an initial demonstration of this

technique, this study focused on membranes with cross-linked PEGDA selective layers, prepared using varying UV irradiation times and with comonomers or inert additives. The formation of uniform hydrogel layers as thin as <100 nm was documented at different UV exposure times using FESEM and confirmed via FTIR. Water filtration experiments showed that membranes prepared by IIFRP exhibited reliable and consistent performance. Uniform selective layers with complete coverage were formed at a UV irradiation time of 4-5 minutes, with longer exposures leading to thicker selective layers and lower permeance without any significant shift in selectivity. The filtration of proteins with different molecular weights revealed the formation of defect-free and uniform selective layers, indicated by complete rejection of higher molecular weight solutes. Initial membranes prepared with solutions containing 5 v/v% PEGDA and 2.5 v/v% PEG200 had a MWCO of around 8-10 kDa. The permeance can be further improved, and MWCO can be adjusted, by adjusting simple fabrication parameters such as the monomer concentration or by the incorporation of comonomers or inert additives that act as porogens in the monomer solution. Lastly, extended protein filtration experiments showed that the membranes exhibit excellent anti-fouling properties and stability for protein purification.

Taken together, these results indicate that the newly described IIFRP is a facile and robust fabrication strategy to manufacture membranes with uniform and defect-free hydrogel selective layers with tunable protein filtration properties. Unlike common single-phase polymerization methods used to prepare membranes with hydrogel selective layers, IIFRP allows for the formation of ultra-thin

hydrogel layers. Furthermore, IIFRP leads to uniform selective layers due to the formation of the hydrogel layer at an interface spanning the surface of the support, minimizing defects. We envision that this novel fabrication method can open up promising routes for industrial scale fabrication of ultra-thin hydrogel selective layers. Furthermore, IIFRP can be readily extended to the fabrication of hydrogels with additional functionalities via incorporation of different comonomers (e.g. charged monomers, zwitterions, etc.) in a reliable and reproducible manner for a variety of applications.

5 CONCLUSIONS AND FUTURE PROSPECTS

The main theme of this thesis was the development of new fabrication methods that would address two key challenges of membrane systems today: limited selectivity, and restricted membrane chemistries. My work used tools of polymer chemistry and self-assembly to propose novel solutions to these problems and has led to the development of new platforms for preparing functional membranes.

In chapter 2, Fabrication of charged nanochannels membranes by self-assembly of random copolymer micelles was shown. An amphiphilic copolymer was synthesized using free radical polymerization, a simple and scalable method which is important for future scale up of these membranes. The high incompatibility between the two segments of the copolymer led to spontaneous formation of micelles in alcohol. The membrane is then fabricated using the self-assembly of these micelles by a simple and scalable coating process on a commercial porous support. The interstices between these packed array of micelles serves as charged nanochannels (1-3 nm) through which water and solutes can pass. The high density of negatively charged carboxylate groups along the pores led to unprecedented separation selectivities between sub-nanometer organic solutes of similar size but different charge. Similar to biological pores (e.g., ion channels), the selectivity was

further enhanced in competitive diffusion experiment as a result of nanoconfinement. At high ionic strength, the rejection of negatively charged solutes decreased suggesting Donnan exclusion mechanism is effective. This further confirmed by filtration of salt solutions with different concentrations and valences. Importantly, the membranes showed high permeability, comparable to industrial membranes. Overall, the results in chapter 2 present a promising approach for scalable fabrication of membranes that can separate solutes based on their charge. The applications for such selective separations include purifying pharmaceutical ingredients, such as amino acids and antibiotics, and also biofuels-manufacturing processes that use emerging solvents, such as ionic liquids.

Table 5.1 summarizes different methods described in the literature for this purpose, including the approach described in this dissertation. Compared with other approaches described in the literature, the membranes developed here had much higher permeance and selectivity and were manufactured using an easier and scalable approach.

Carboxylic acid groups are well-known to form complexes with metal ions.¹⁷¹ Presence of heavy metals is a major environmental concern³⁷³ as they are released into the environment by various industries such as battery manufacturing, non-ferrous metallurgical manufacturing, and electrical, paper and mining industries.³⁷⁴ They are also at times present as natural components of water, as they are found naturally in the earth's crust and thus can be released to the environment by soil erosion and mining.³⁷⁵

Table 5. 1. Comparison of the work described here with other membranes for charge-based separation of small organic molecules reported in literature.

Method	Smallest pore size (nm)	Range of available functional groups	Ease of manufacture and scalability	Porosity/ Permeability	Highest reported selectivity for a charge-based separation of small molecules
Gold nanotube membranes ²²	0.9	Very high	Very low	Very Low	13.3
Polymer self-assembly inside the PCTE ³⁷²	4.5	Very limited	Very high	Very Low	3.5
NP-Den assembly ⁴⁰	7	High	Medium	Medium	11
Micelle self-assembly (this work)	1-3	Very high	Very high	Very high	263

The high density of carboxylate groups lining the pores of the membranes presented here, make them very promising for the capture of heavy metal ions. Given the small size of metal ions, reverse osmosis (RO) which makes use of a size-selective membrane can be used to efficiently remove metal ions from water. However, RO membranes require high operational pressure. They are also unable to separate metal ions from one another, as they operate solely based on size sieving. Carboxylic groups lining the pores can capture the metal ions by selectively binding to them, while it operates at much lower pressure.

Our preliminary results showed high adsorption capacity for several metal ions (e.g., Cu, Al, Fe, etc.). This can be widely expanded for various metal ions (i.e., membrane functionalization) within future studies.

In chapter 3, the versatility of these membranes for aromaticity-based separation was demonstrated. The carboxylic acid groups on the pore walls can be readily converted into phenol groups using a straightforward conjugation chemistry (EDC/NHS), which can in turn, separate molecules with similar size and charge based on their aromaticity. The functional group is selected to have favorable interactions with the solute. These membranes showed excellent transport selectivity (up to 7 times) between two steroid hormones of similar size and charge following the hopping mechanism. The interactions between solute and functional groups on the membranes were studied using QCM-D. This report is the first demonstration of membrane-based separation for small molecules based on their aromaticity.

This proof of concept shows that we can design membranes for each targeted separation by identifying desired functional groups on pore walls, screening them by QCM-D, and easily functionalizing these membranes through EDC/NHS chemistry. Thus, the membrane functionality can be easily leveraged for a variety of separations. This indicates a promising future project direction for even more complex separations such as chirality-based separation.

Because the selectivity of these membranes is a result of sequential binding and unbinding between solute and functional groups, feed concentration might play a role in membrane selectivity. According to facilitated transport theory, which we believe is in effect for these chemoselective membranes, flux of preferred solute initially increases linearly with feed concentration and the plot of flux versus feed concentration should then flatten at higher concentration. Future studies are needed

to study if the facilitated transport mechanism is in effect for membranes developed here.

To further improve membrane selectivity the copolymer compositions and molecular weight can be altered. In addition, selectivity of these membranes will likely increase with grafting from the carboxylic acid groups. This is because grafting from COOH groups that line the pores will decrease pore size while the functional group density increases in the pores, both of which are expected to enhance membrane selectivity. Grafting methods such as Activators ReGenerated by Electron Transfer Atom Transfer Radical Polymerization (ARGET ATRP) can be utilized to initiate polymerization from the functional groups on the membrane pore surfaces and graft polymer chains of various functionalities into the membrane pores. Initial experiments confirmed successful grafting, while the selectivity of these membranes warrant further studies.

Stimuli-responsive membranes respond to changes in feed conditions (e.g., temperature, pH, ionic strength, presence of specific analytes) or external fields or stimuli (e.g., electric or magnetic fields, light exposure) and exhibit a change in performance parameters such as permeability and/or selectivity.³⁷⁶ Such membranes can act as smart valves that increase or constrict flow without the need for external control, enabling the user to control and tune parameters such as pore size to suit specific application it is used for. This capability may enable automated regulation of specific compounds or reactants upstream from the membrane without external intervention. This can be of great use in water and wastewater treatment or biomanufacturing. In addition, changes may be used in controlling the binding and

release of a target compound, opening up opportunities for the design of membrane adsorbers, most commonly used in removing trace compounds for water treatment and for the downstream processing of biopharmaceuticals. As previous studies show, also partly studied in chapter 2, random copolymers do not possess responsive behavior due to their structural feature. Grafting from the pores can also impart responsive behavior to the membrane.

In chapter 4, a novel method for the fabrication of ultrathin hydrogel layer was presented, IIFRP. The layer performance was studied in relevant to protein purification. By altering simple experimental parameters (e.g., UV exposure time, monomer concentration, porogen, comonomer) the hydrogel layer properties can be tuned. The membranes showed superior fouling resistant property upon long term exposure to protein solution.

Table 5.2 compares the approach presented in this dissertation with other available approaches. The IIFRP technique enables ultrathin coatings from a wide range of monomer solution viscosities, is fast and easily scalable to roll-to-roll processing and can incorporate functional nanomaterials.

This new, robust and consistent method can open up a whole new direction for the fabrication of ultrathin membranes for various applications. In chapter 4, we used porogens to increase membrane permeance.

Table 5. 2. Comparison of our approach with alternative TFC membrane preparation techniques

Feature	Interfacial step growth polymerization (IP)	Coating (e.g. doctor blade, spray)	Grafting from membrane		Our approach (IIFRP)
			Plasma	Surface-initiated polymerization	
Ultrathin coating possible (<200 nm)	✓	✗	✓	✓	✓
Hydrogel layers possible	✗	✓	✓	✓	✓
Uniform, defect-free layer	✓	✗	✗	✗	✓
Wide range of MWCO	✗	✓	✓	✓	✓
Well-controlled chemistry	Somewhat	✓	✗	✓	✓
Easy incorporation of nanomaterials	✗	✓	✗	✗	✓
No damage to support layer	✓	✓	✗	✗	✓
Time for continuous layer	Short	Short	Varies	Long	Short
Works with low-viscosity solution	✓	✗	✓	✓	✓

The membrane permeance can be enhanced by different approaches. One of the most important factors that can play a major role in interfacial polymerization and subsequently the membrane permeance is the type of support membrane and its MWCO. Literature shows a significant impact (up to an order of magnitude) of the support membrane on the permeance of the TFC membranes.³⁵³ My initial experiments showed different results for various support membranes (PAN, PVDF, PS with different MWCOs). Thus, optimizing the support membrane would be beneficial for future projects.

The hydrogel mesh size can be further tuned using different PEGDA molecular weights. Different comonomers with different functionalities can be readily added to the hydrogel selective layer to impart new functionalities such as:

- *Sulfopropyl methacrylate (SPMA)* to impart negative charge into the selective layer for charge-based selectivity, increase charged solute rejection, and prevent fouling by negatively charged foulants.
- *Sulfobetaine methacrylate (SBMA)* to impart zwitterionic groups into the selective layer to improve hydrophilicity, permeability and fouling resistance,^{89, 377-379} change selectivity,^{377, 379} and create membranes that respond to feed ionic strength.^{121, 314, 378-384}
- *Poly(ethylene glycol) acrylate (PEGA)* to increase mesh size^{323, 385}

Furthermore, literature shows amorphous cross-linked hydrogel networks are very promising for removal of CO₂ and H₂S from mixture of light gases such as H₂, N₂, CH₄. Because polar ether groups in PEGDA have high affinity for CO₂ or other polar gases such as H₂S, which results in high permeation selectivity.^{326-327, 386} However, the current method for manufacturing hydrogel layers result in a very thick layer with very low permeance. Our new method, IIFRP enables formation of very thin layer. My preliminary results confirmed orders of magnitude higher permeation of CO₂ with very high selectivity for CO₂/N₂. This could potentially be a step forward toward processing this large quantity of emitted CO₂. According to the EPA, approximately 6.87 billion metric tons of CO₂ are released in the U.S, accounting for 81% of all greenhouse gas emission.³⁸⁷ Furthermore, incorporation

of functional groups with higher affinity to CO₂ (e.g., amines, ionic liquids) within the hydrogel selective layer, may enables even higher permeation selectivity.³⁸⁶

This new method is not limited to hydrogels. In fact, it can be extended to new emerging applications such as organic solvent separations. This is possible by appropriate selection of a polyfunctional monomer that does not swell in organic solvents such as alcohol. Also, the same method could be applied for fabrication of hydrophobic layer on a porous support by using an oil soluble monomer and water-soluble initiator. In essence, the method presented in this dissertation is very versatile for all various applications and can opens up a whole new direction.

APPENDICES

A1 SELECTIVE TRANSPORT THROUGH MEMBRANES WITH CHARGED NANOCANNELS FORMED BY SELF-ASSEMBLY OF RANDOM COPOLYMER MICELLES

A1.1. Documentation of Hydrogen Bonding in Methanol Using FTIR Spectroscopy

To document micelle stabilization through hydrogen bonding between MAA groups and methanol, FTIR experiments were performed on micellar solutions in methanol and copolymer powder (Figure A1.1). The hydrogen bonding is evident by carboxylic acid peak broadening at $\sim 1730\text{ cm}^{-1}$ that is visible only in the methanol solution. A broad peak in the absorbance range of $3200\text{-}3400\text{ cm}^{-1}$ is also an indication of hydrogen bond formation between hydroxyl groups.²⁰² These peaks, highlighted in yellow, are not present in polymer in solid powder form.

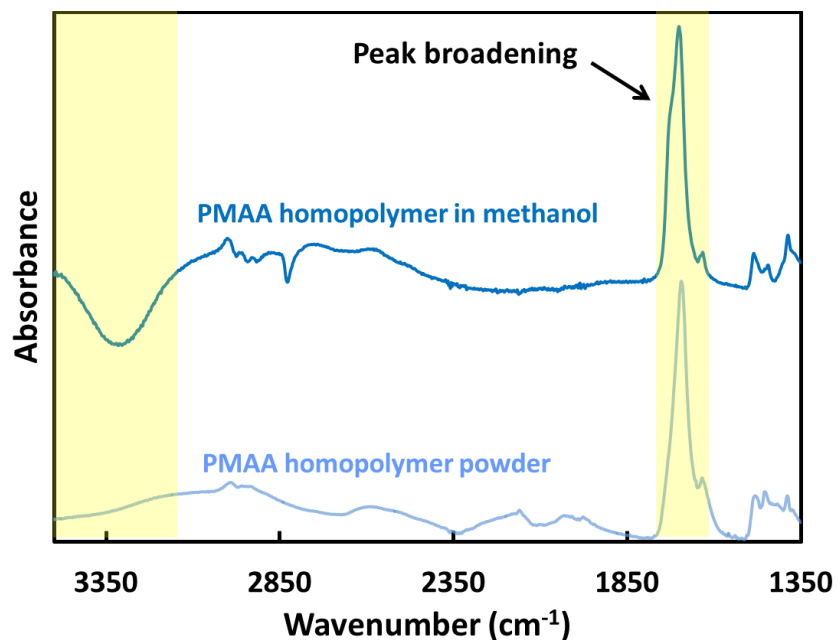


Figure A1. 1. FTIR spectra of the copolymer solution in methanol and solid copolymer powder. Yellow highlighted regions correspond to hydrogen bonding between copolymer and methanol.

A1.2. Effect of Metal Ions on Micelle Size Quantified by DLS

DLS analysis was used to measure the average effective hydrodynamic diameter of micelles in solution (Table A1.1). All measurements were performed in solutions containing 0.5 wt% copolymer in methanol, with various salts added to the solution. Here, r is the molar ratio between COOH groups in the copolymer to metal ions.

Table A1. 1. Effective hydrodynamic diameters measured in P(TFEMA-*r*-MAA) solutions in methanol in the presence of different metal salts.

Metal salt	r	Average micelle size (nm)
-	-	17.1
NaOAc	20	12.4
NaOAc	10	11.4
Cu(OAc) ₂	20	20.3
Cu(OAc) ₂	10	20.6
CuCl ₂	20	28.7
CuCl ₂	1	34.01
CaCl ₂	20	32.0
CaCl ₂	1	35.79

A1.3. Characterization of Complexation Geometries Using UV-vis and FTIR Spectroscopy

The coordination geometries upon addition of metal ions were further confirmed using UV-visible spectroscopy. A solution of 5 wt% copolymer with CuCl₂ at a molar ratio MAA:CuCl₂ of 20 (i.e. r=20) was prepared in methanol. The control sample prepared was with same CuCl₂ concentration in methanol but without the copolymer.

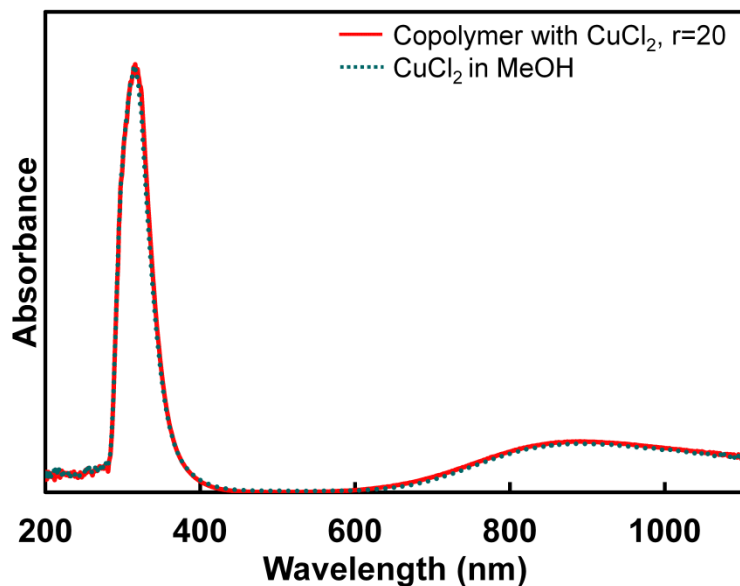


Figure A1. 2. UV-visible spectra of the copolymer solution with CuCl₂.

Solutions of 5 wt% copolymer with CuCl₂ and CaCl₂ (r=20) in methanol were used for FTIR analysis. They showed no peaks at about 1620 cm⁻¹ or 1550 cm⁻¹ corresponding to bridging and chelating bidentate complexation, respectively.²³⁹ This further confirms that counterions bound to metal ions can affect the complexation of metal ions with carboxylates.

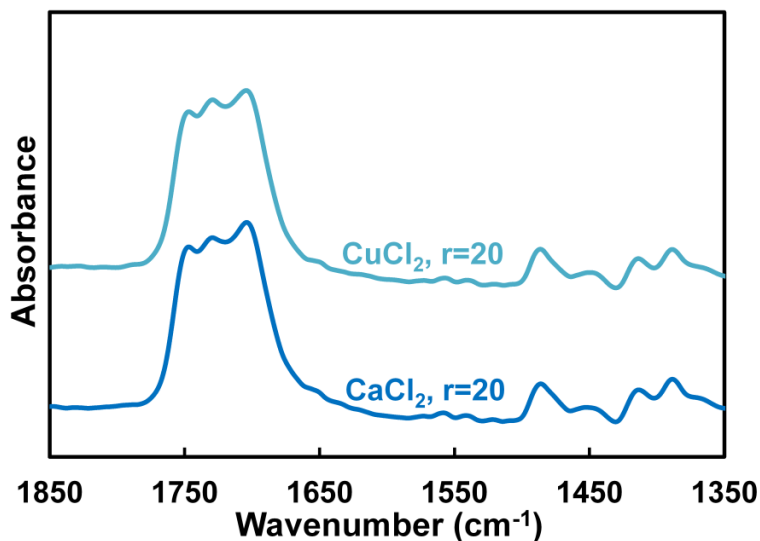


Figure A1. 3. FTIR spectra of copolymer solution in methanol in presence of CuCl₂ and CaCl₂.

A1.4. Effect of Solvent Evaporation Time on Membrane Morphology

We examined the effect of solvent evaporation time before submerging in water for membrane by imaging a membrane coated with a solution of CP50 and immersed in water after a 2 minute evaporation time. As can be seen from Figure A1.4, the coating layer is dense and uniform, with no distinct micelles visible.

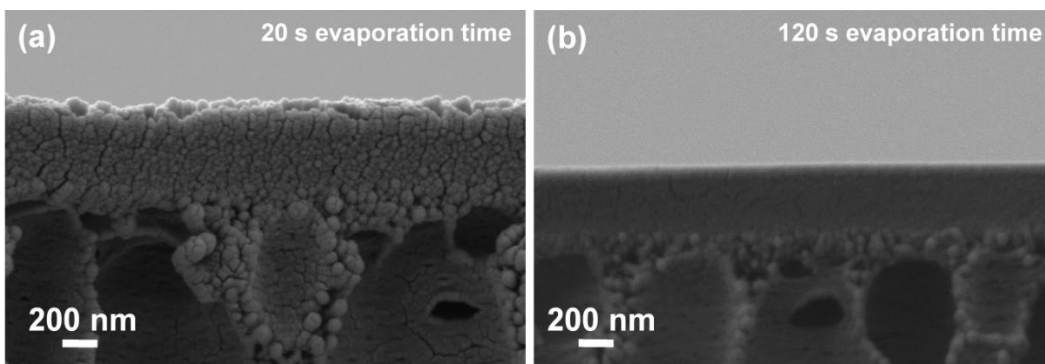


Figure A1. 4. Effect of solvent evaporation time on selective layer structure of CP50-coated membrane (a) 20 s and (b) 120 s evaporation time.

A1.5 Effect of Support Membrane Surface Morphology

Figure A1.5a and b shows two commercial membrane surface morphologies. As the Figure illustrates, PDVF membrane has much bigger pores on the membrane surface resulting in the penetration of micelles into the pores and clogging the membrane instead of forming a uniform coating layer on top as the case of PAN 400. Thus, the multilayered micelle structure was not seen when support membranes with larger surface pore sizes were used (PVDF400R, Nanostone). The penetration of micelles inside the pores result in clogging the membrane pores, leading to very low permeability ($<0.1 \text{ L m}^{-2} \text{ h}^{-1} \text{ bar}^{-1}$).

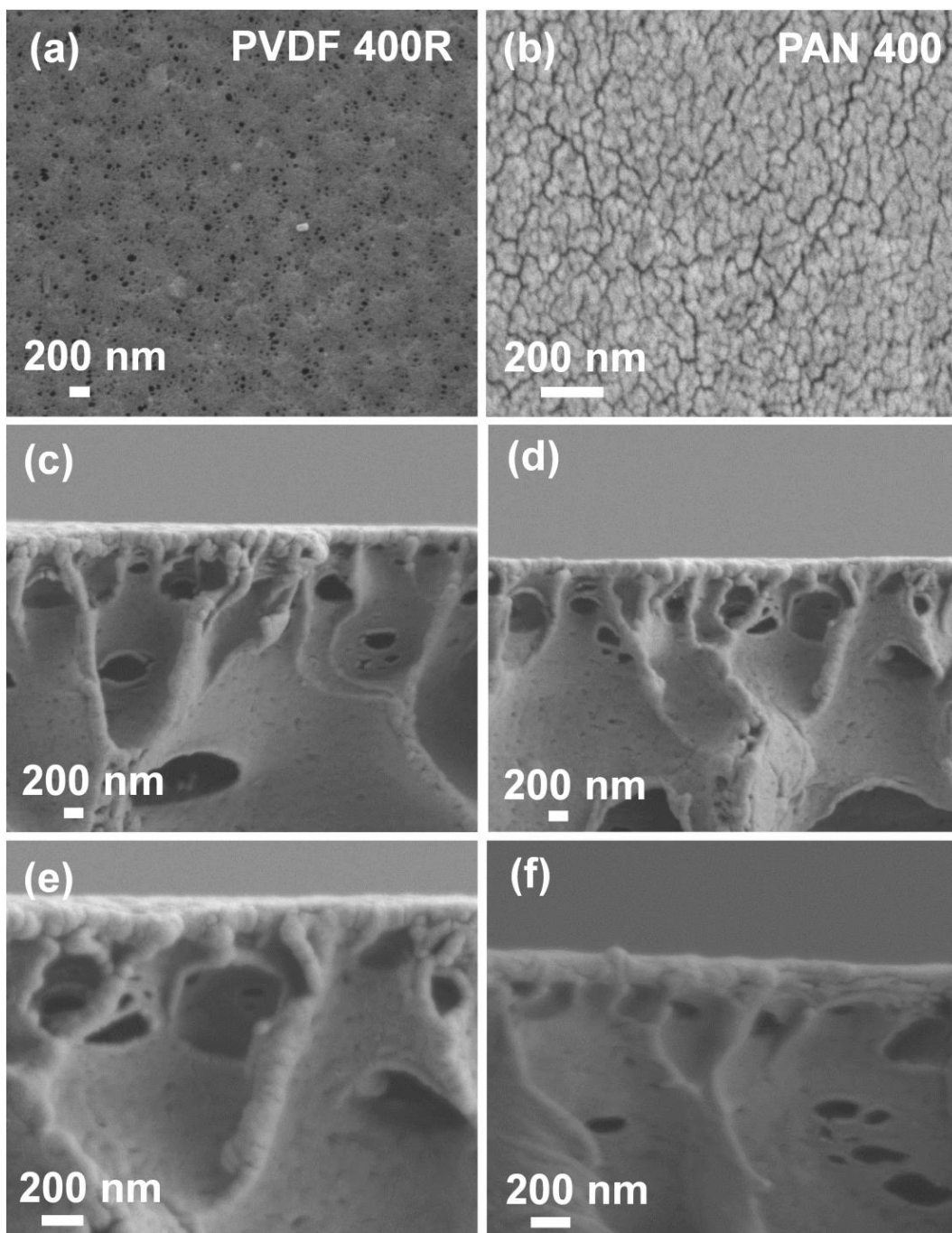


Figure A1. 5. Surface morphology of (a) PVDF 400R (MWCO: 250K), (b) PAN 400 (MWCO: 200K), (c,e) cross-section of PVDF 400R support membrane, (d,f) Cross-section of PVDF 400R membrane coated with CP40 polymer. No coating is visible when PVDF 400R was used as the support membrane.

A1.6. Determination of the Micelle Size Distribution from FESEM Images

To estimate the effective size of the nanopores present in the membranes described here, we first analyzed the high resolution FESEM images to estimate the average size of micelles forming each selective layer. Micelle size distribution was calculated using ImageJ software.

Using Cross-Section Images for Micelle Size Distribution

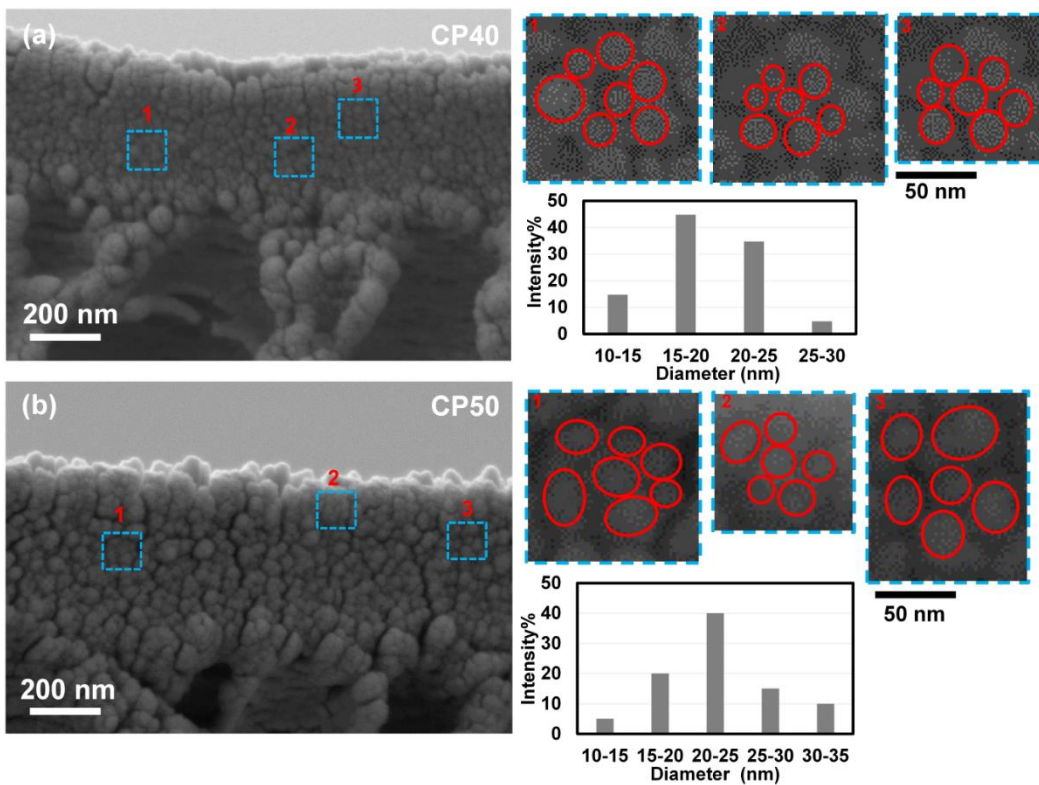


Figure A1.6.1. Micelle size distributions for (a) CP40 and (b) CP50 membranes; calculated using Image J software.

Image analysis indicated an average micelle size of 19 nm for CP40, consistent with the DLS estimate of 17 nm. The CP50 membrane had an average micelle size of 23 nm in the selective layer.

Using Surface Images for Micelle Size Distribution

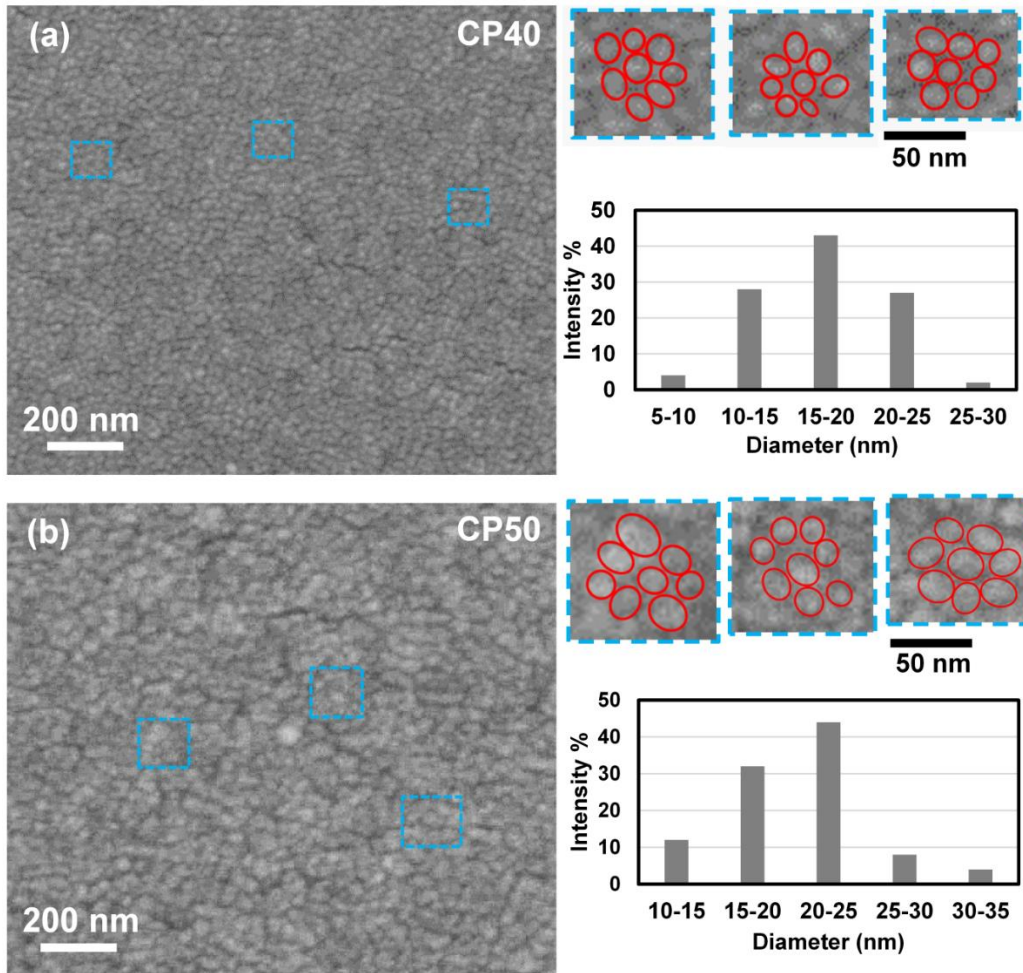


Figure A1. 6. 2. Micelle size distributions for (a) CP40 and (b) CP50 coated membranes.

Average micelle size was found to be 17.8 nm and 20.5 nm for CP40 and CP50 respectively. The value obtained using surface images are very close to those obtained from the cross-section images above.

A1.7. Membrane Pore Size Estimation

To estimate the effective size of the nanopores present in the membranes described here, the average micelle size obtained from the image analysis of cross-sectional FESEM images was used. These values were a close match to those obtained from surface images. AFM data indicated that the micelles were arranged in a hexagonal close packed array, at least on the surface. Using this packing geometry and the micelle sizes calculated above, we estimated the effective size of the pores in the interstices of the micelles using two geometric models.

Method 1: Fitting sphere in the void

In this model, we neglected the edges around the sphere fitting into the triangular-shape void.¹⁶⁵ r_p is considered the distance from nanopores center to the nearest sphere and calculated as follows:

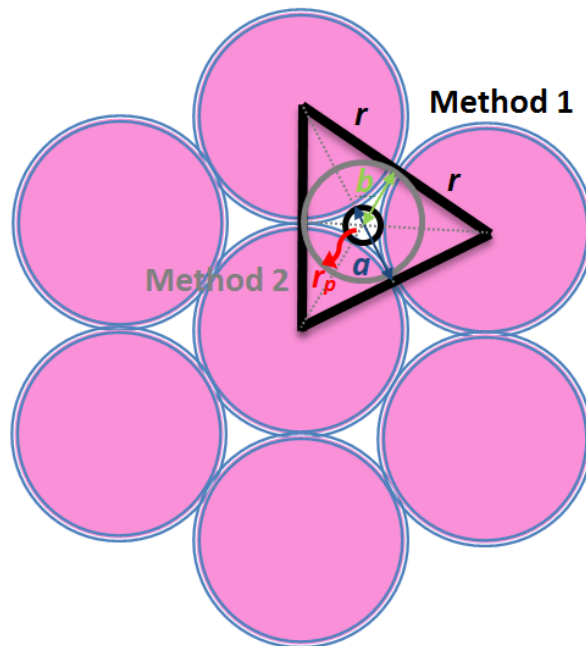


Figure A1. 7. HCP structure and pore geometry.

$$r_p = a - b$$

$$r + a = \sqrt{(2r)^2 - r^2} = r\sqrt{3} \rightarrow$$

$$a = r(\sqrt{3} - 1)$$

$$b = r \tan\left(\frac{\pi}{6}\right)$$

$$r_p = r(\sqrt{3} - 1) - r \tan\left(\frac{\pi}{6}\right) = 0.155r$$

CP40: SEM image give average micelle diameter of 19.0 nm:

$$r_p = 0.155 \times 9.53 = 1.47 \text{ nm}$$

CP50: SEM image give average micelle diameter of 23.3 nm:

$$r_p = 0.155 \times 11.65 = 1.81 \text{ nm}$$

Using this approach, r_p was calculated to be 1.5 and 1.8 nm for CP40 and CP50, respectively. This corresponds to pore diameters of 3.0 and 3.6 nm, respectively.

Method 2: Considering the whole void volume

In this method, we fit a sphere considering the whole triangle-shape void and calculated the pore size as follows:

$$r + a = \sqrt{(2r)^2 + r^2} = r\sqrt{3}$$

$$a = r(\sqrt{3} - 1)$$

$$b = r \tan\left(\frac{\pi}{6}\right)$$

$$S_{tri} = (a + r) * 2r / 2 = (r(\sqrt{3} - 1) + r) * r = \sqrt{3}r^2$$

$$S_{curv.} = 3 * \left(\frac{1}{6}\pi r^2\right) = \frac{1}{2}\pi r^2$$

$$\pi r_p^2 = S_{tri} - S_{curve} = \sqrt{3}r^2 - \frac{1}{2}\pi r^2$$

$$r_p = \sqrt{\frac{\sqrt{3}r^2 - \frac{1}{2}\pi r^2}{\pi}} = 0.226r$$

CP40: $r_p = 0.226 \times 9.525 = 2.15$ nm

CP50: $r_p = 0.226 \times 11.65 = 2.63$ nm

Using this method, slightly larger r_p was obtained. r_p values are 2.1 and 2.6 nm for CP40 and CP50, respectively. This corresponds to pore diameters of 4.2 and 5.2 nm, respectively.

A1.8. Calculating the Lattice Parameters (a, d)

The position of q^* peak obtained by FFT analysis can be used to calculate lattice parameter for HCP structure.

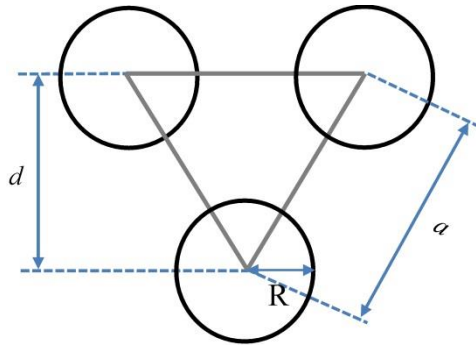


Figure A1. 8. Lattice parameters for HCP structure.

$$d = \frac{2\pi}{q^*} = \frac{\sqrt{3}}{2} a \rightarrow a = 14 \text{ nm}$$

The value obtained using this analysis is consistent with micelle size obtained by both FESEM and DLS. Note that a is the distance between micelles centers and thus larger than the micelle size.

A2 CHEMOSELECTIVE NANOPOROUS MEMBRANES FOR AROMATICITY-BASED SEPARATION OF SMALL MOLECULES

A2.1. Selective layer thickness measurement with QCM-D

The thickness of the coated layer onto quartz crystal sensor can be calculated using QCM³³¹. This estimate is based on the measurement of the areal mass of the selective layer. Figure A2.1 represents the frequency shift of the sensor both before and after coating with the copolymer solution at 3rd overtone. Quartz crystal has the best energy trapping at the 3rd overtone³⁹⁵. Higher harmonics also had a consistent and overlapped frequency shifts. The left side shows the frequency of the bare sensor, before coating with selective layer, and the right side shows the vibration frequency of the coated sensor. The areal mass of the selective layer (ng cm^{-2}) is directly correlated with frequency change and can be calculated using Sauerbrey Eq. The thickness of the selective layer can then be obtained, by dividing areal mass to the density of the selective layer (1.1 g cm^{-3}). The selective layer thickness value of $\sim 70 \text{ nm}$ was obtained using QCM analysis.

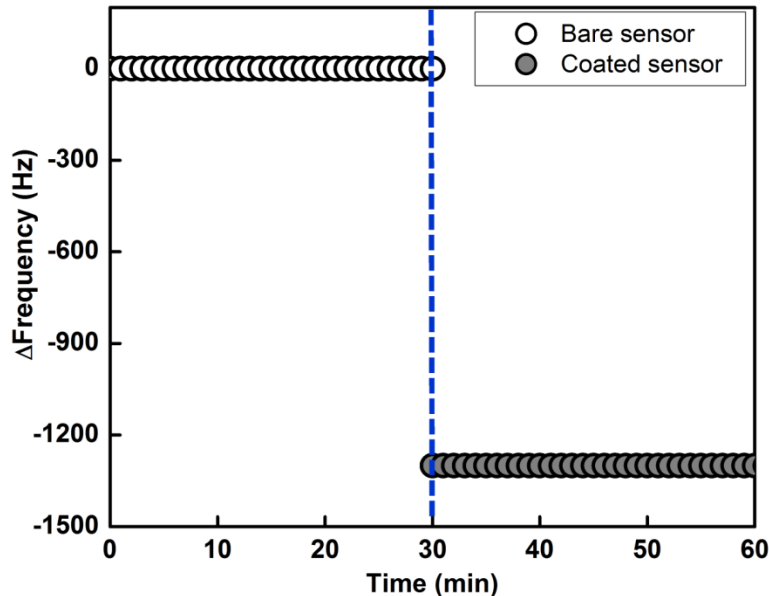


Figure A2. 1. Representative vibration frequency of the bare sensor (open symbols), and coated sensor (solid symbols) at $n=3$. The change in frequency is directly correlated with the mass of selective layer.

A2.2. Adsorption/Desorption of Hormones on the Selective Layer

To track the adsorption and desorption of solutes on the selective layer, we used QCM-D. Frequency shift of a coated quartz crystal was recorded upon injection of different solutions at different overtones ($n=1, 3, 5, \dots, 13$). Figure A2.2 displays the frequency shifts for both unfunctionalized and functionalized layers as a function of time upon exposure to hormones. As shown in Figure A2.2a for unfunctionalized membrane, first a stable baseline was measured by passing ultrapure water through the crystal surface (region I). After 2 h, solution of 50 ppm PREG was injected into the measurement chamber of the QCM-D (region II). A rapid decrease in resonating frequency was observed initially, followed by an immediate increase. The frequency value shortly tends toward a steady state and stays constant upon further exposure to PREG implying saturation of adsorption

quantity. Adsorption of PREG molecules is most likely due to counterions' binding to the negatively charge surface (i.e. electrostatic attraction). This is evident by overshooting in frequency observed initially upon injecting PREG. In fact, overshooting is likely due to the fact that a fraction of solute, which initially adsorb onto the surface most likely through counterion binding, desorb immediately as a result of repulsion between the negatively charged ions bound to these counterions (to maintain electroneutrality) with negatively charged layer (COO^-)³⁹⁶. In any case, this effect is transient, and equilibrium is reached shortly. The decrease in the frequency value (shown by dotted line) in comparison to the baseline corresponds to adsorbed amount of PREG molecules onto the polymer surface as a result of counterion attraction and some hydrogen bonding.

Next, to track desorption of this solute, the surface was rinsed with DI water (region III). The frequency reached its initial value instantaneously, reflecting that the adsorption is reversible. Subsequently, a solution of 50 ppm ESTR was injected into the measurement chamber (region IV). As the ESTR molecules are being adsorbed onto the surface, the frequency decreases until reaches a plateau. A larger frequency shift was observed for ESTR in comparison to PREG solution, corresponding to higher adsorbed amount of ESTR. The result is consistent with the diffusion experiment, confirming preferential adsorption of ESTR due to more hydrogen bonding potential with carboxylate groups that slows down its permeation through the membrane. The final rinsing step was conducted (region V) leading to fully desorption of bound solutes accompanied (i.e. fully reversible binding) by an increase in frequency to its initial value.

An analogous experiment was conducted after functionalizing the membrane with TYR, Figure A2.2a. Similarly, a baseline was first established by passing ultrapure water through the chamber for 2 h (region I). Subsequently, PREG solution was introduced into the measurement cell for 2 h (region II). Similarly, an overshoot in frequency was observed, which reached steady state indicating completion of adsorption process. The amount of PREG adsorbed on the functionalized membrane is much lower than that of unfunctionalized membrane, suggesting less favorable interaction. This could be due to less counterion bridging effect in case of phenol which is only partially negative as a result of electron donating group substituent. This explain higher diffusion rate of PREG for functionalized membrane. Next, DI water was injected in order to track desorption of PREG molecules bound to the surface (region III). Frequency ascended to its initial baseline, confirming the reversibility of the interaction. Next, ESTR solution was passed through the surface (region IV). An immediate and steep drop in the resonance frequency was observed corresponding to the binding and adsorption of the ESTR molecules to the surface of the crystal. This change in frequency is considerably larger in functionalized membrane, illustrating more affinity of ESTR to functional group on the layer. Finally, the surface was washed by flushing DI water through the chamber (region V). The reversibility of the interaction is reflected again in fully desorption of ESTR and frequency value reverting quickly to its initial value.

Thus, from QCM-D monitoring, it is apparent that the selective permeation of ESTR is a result of stronger interactions with phenol groups. Additional evidence

for this conclusion was obtained from a similar QCM study of a layer functionalized with ACP, Figure A2.2b. The overshooting was not observed in ACP-Functionalized sample, confirming our hypothesis on the effect of counterion binding for charged/partially charged surface. In the absence/significant reduction of the negative charge on the surface (and hence no overshooting in frequency for this membrane, Supporting Information), the adsorbed amount of PREG could be the result of hydrogen bonding between the solute and both alcohol (OH group) and amide groups (N-H bond) on the selective layer. In comparison to unfunctionalized membrane, much lower ESTR was detected on the sensor. This is due to absence of π -stacking interaction and much lower hydrogen bonding, if any (with remaining COOH groups). Thus, a β value of 1.6 was achieved. This undoubtedly confirms the effect of π -stacking interaction on selective adsorption of ESTR molecules.

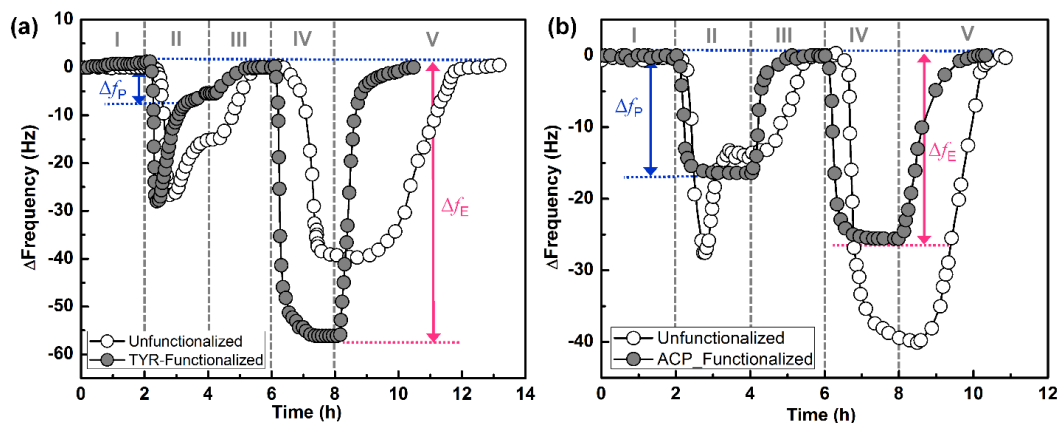


Figure A2. 2. Frequency shift vs. time upon injection of hormones for unfunctionalized and (A) TYR-Functionalized, (B) ACP-Functionalized membranes at $n = 3$. The change in frequency for PREG and ESTR is shown with blue and pink arrows, respectively for both functionalized membranes.

REFERENCES

1. Geise, G. M.; Lee, H. S.; Miller, D. J.; Freeman, B. D.; Mcgrath, J. E.; Paul, D. R., Water Purification by Membranes: The Role of Polymer Science. *J. Polym. Sci. Part B Polym. Phys.* **2010**, *48* (15), 1685-1718.
2. Sadeghi, I.; Aroujalian, A.; Raisi, A.; Dabir, B.; Fathizadeh, M., Surface modification of polyethersulfone ultrafiltration membranes by corona air plasma for separation of oil/water emulsions. *J. Membr. Sci.* **2013**, *430*, 24-36.
3. Sadeghi, I.; Aroujalian, A.; Raisi, A.; Fathizadeh, M.; Dabir, B., Effect of solvent, hydrophilic additives and corona treatment on performance of polyethersulfone UF membranes for oil/water separation. *Procedia Engineer* **2012**, *44*, 1539-1541.
4. Bernardo, P.; Drioli, E.; Golemme, G., Membrane Gas Separation: A Review/State of the Art. *Ind Eng Chem Res* **2009**, *48* (10), 4638-4663.
5. Rathore, A. S.; Shirke, A., Recent Developments in Membrane-Based Separations in Biotechnology Processes: Review. *Prep Biochem Biotech* **2011**, *41* (4), 398-421.
6. Daufin, G.; Escudier, J. P.; Carrere, H.; Berot, S.; Fillaudeau, L.; Decloux, M., Recent and emerging applications of membrane processes in the food and dairy industry. *Food Bioprod Process* **2001**, *79* (C2), 89-102.
7. Petersen, R. J., Composite Reverse Osmosis and Nanofiltration Membranes. *Journal of Membrane Science* **1993**, *83* (1), 81-150.
8. Mohammad, A. W.; Teow, Y. H.; Ang, W. L.; Chung, Y. T.; Oatley-Radcliffe, D. L.; Hilal, N., Nanofiltration membranes review: Recent advances and future prospects. *Desalination* **2015**, *356*, 226-254.
9. U.S., D. O. E., Technical topic descriptions FY 2012 SBIR and STTR programs. In *Technical topic descriptions FY 2012 Small business innovation research (SBIR) and small business technology transfer (STTR) programs*, 2012.
10. Seader, J. D.; Henley, E. J.; Roper, D. K., *Separation process principles : chemical and biochemical operations*. 3rd ed.; Wiley: Hoboken, NJ, 2011; p xxvi, 821 p.
11. Baker, R. W., *Membrane technology and applications*. 2nd ed.; J. Wiley: Chichester ; New York, 2004; p x, 538 p.
12. Zilman, A.; Di Talia, S.; Jovanovic-Talisman, T.; Chait, B. T.; Rout, M. P.; Magnasco, M. O., Enhancement of transport selectivity through nano-channels by non-specific competition. *Plos Comput Biol* **2010**, *6* (6), e1000804.
13. Baker, R. W., Future directions of membrane gas separation technology. *Ind Eng Chem Res* **2002**, *41* (6), 1393-1411.
14. Koebnik, R.; Locher, K. P.; Van Gelder, P., Structure and function of bacterial outer membrane proteins: barrels in a nutshell. *Mol. Microbiol.* **2000**, *37* (2), 239-253.
15. Zeth, K.; Thein, M., Porins in prokaryotes and eukaryotes: common themes and variations. *Biochem J* **2010**, *431*, 13-22.
16. Schirmer, T., General and specific porins from bacterial outer membranes. *J. Struct. Biol.* **1998**, *121* (2), 101-109.
17. Lim, R. Y. H.; Fahrenkrog, B.; Koser, J.; Schwarz-Herion, K.; Deng, J.; Aebi, U., Nanomechanical basis of selective gating by the nuclear pore complex. *Science* **2007**, *318* (5850), 640-643.
18. Yang, R.; Asatekin, A.; Gleason, K. K., Design of conformal, substrate-independent surface modification for controlled protein adsorption by chemical vapor deposition (CVD). *Soft Matter* **2012**, *8* (1), 31-43.

19. Ostuni, E.; Chapman, R. G.; Holmlin, R. E.; Takayama, S.; Whitesides, G. M., A survey of structure-property relationships of surfaces that resist the adsorption of protein. *Langmuir* **2001**, *17* (18), 5605-5620.
20. Galaev, I. Y., New methods of protein purification: Affinity ultrafiltration. *Biochemistry-Moscow* **1999**, *64* (8), 849-856.
21. Nishizawa, M.; Menon, V. P.; Martin, C. R., Metal Nanotubule Membranes with Electrochemically Switchable Ion-Transport Selectivity. *Science* **1995**, *268* (5211), 700-702.
22. Lee, S. B.; Martin, C. R., pH-switchable, ion-permselective gold nanotubule membrane based on chemisorbed cysteine. *Anal. Chem.* **2001**, *73* (4), 768-775.
23. Martin, C. R.; Nishizawa, M.; Jirage, K.; Kang, M. S.; Lee, S. B., Controlling ion-transport selectivity in gold nanotubule membranes. *Adv. Mater.* **2001**, *13* (18), 1351-1362.
24. Hou, Z. Z.; Abbott, N. L.; Stroeve, P., Self-assembled monolayers on electroless gold impart pH-responsive transport of ions in porous membranes. *Langmuir* **2000**, *16* (5), 2401-2404.
25. Hulteen, J. C.; Jirage, K. B.; Martin, C. R., Introducing chemical transport selectivity into gold nanotubule membranes. *J. Am. Chem. Soc.* **1998**, *120* (26), 6603-6604.
26. Velleman, L.; Shapter, J. G.; Losic, D., Gold nanotube membranes functionalised with fluorinated thiols for selective molecular transport. *J. Membr. Sci.* **2009**, *328* (1-2), 121-126.
27. Lee, S. B.; Mitchell, D. T.; Trofin, L.; Nevanen, T. K.; Soderlund, H.; Martin, C. R., Antibody-based bio-nanotube membranes for enantiomeric drug separations. *Science* **2002**, *296* (5576), 2198-2200.
28. Lakshmi, B. B.; Martin, C. R., Enantioseparation using apoenzymes immobilized in a porous polymeric membrane. *Nature* **1997**, *388* (6644), 758-760.
29. Wirtz, M.; Parker, M.; Kobayashi, Y.; Martin, C. R., Template-synthesized nanotubes for chemical separations and analysis. *Chem-Eur J* **2002**, *8* (16), 3573-3578.
30. Wirtz, M.; Parker, M.; Kobayashi, Y.; Martin, C. R., Molecular sieving and sensing with gold nanotube membranes. *Chem Rec* **2002**, *2* (4), 259-267.
31. Steinle, E. D.; Mitchell, D. T.; Wirtz, M.; Lee, S. B.; Young, V. Y.; Martin, C. R., Ion channel mimetic micropore and nanotube membrane sensors. *Anal. Chem.* **2002**, *74* (10), 2416-2422.
32. Gyurcsanyi, R. E., Chemically-modified nanopores for sensing. *Trac-Trend Anal Chem* **2008**, *27* (7), 627-639.
33. Martin, C. R.; Nishizawa, M.; Jirage, K.; Kang, M., Investigations of the transport properties of gold nanotubule membranes. *J. Phys. Chem. B* **2001**, *105* (10), 1925-1934.
34. Chun, K. Y.; Stroeve, P., Protein transport in nanoporous membranes modified with self-assembled monolayers of functionalized thiols. *Langmuir* **2002**, *18* (12), 4653-4658.
35. Velleman, L.; Triani, G.; Evans, P. J.; Shapter, J. G.; Losic, D., Structural and chemical modification of porous alumina membranes. *Micropor Mesopor Mat* **2009**, *126* (1-2), 87-94.
36. Li, F. B.; Li, L.; Liao, X. Z.; Wang, Y., Precise pore size tuning and surface modifications of polymeric membranes using the atomic layer deposition technique. *J. Membr. Sci.* **2011**, *385* (1-2), 1-9.
37. Asatekin, A.; Gleason, K. K., Polymeric Nanopore Membranes for Hydrophobicity-Based Separations by Conformal Initiated Chemical Vapor Deposition. *Nano Lett.* **2011**, *11* (2), 677-686.
38. Savariar, E. N.; Krishnamoorthy, K.; Thayumanavan, S., Molecular discrimination inside polymer nanotubules. *Nat. Nanotechnol.* **2008**, *3*, 112-117.

39. Suh, H. S.; Kim, D. H.; Moni, P.; Xiong, S. S.; Ocola, L. E.; Zaluzec, N. J.; Gleason, K. K.; Nealey, P. F., Sub-10-nm patterning via directed self-assembly of block copolymer films with a vapour-phase deposited topcoat. *Nat. Nanotechnol.* **2017**, *12* (6), 575-+.
40. Park, M.; Subramani, C.; Rana, S.; Rotello, V. M., Chemoselective nanoporous membranes via chemically directed assembly of nanoparticles and dendrimers. *Adv. Mater.* **2012**, *24*, 5862-5866.
41. Carter, B. M.; Wiesenauer, B. R.; Hatakeyama, E. S.; Barton, J. L.; Noble, R. D.; Gin, D. L., Glycerol-based bicontinuous cubic lyotropic liquid crystal monomer system for the fabrication of thin-film membranes with uniform nanopores. *Chem. Mater.* **2012**, *24*, 4005-4007.
42. Hatakeyama, E. S.; Gabriel, C. J.; Wiesenauer, B. R.; Lohr, J. L.; Zhou, M. J.; Noble, R. D.; Gin, D. L., Water filtration performance of a lyotropic liquid crystal polymer membrane with uniform, sub-1-nm pores. *Journal of Membrane Science* **2011**, *366* (1-2), 62-72.
43. Gin, D. L.; Noble, R. D., Designing the Next Generation of Chemical Separation Membranes. *Science* **2011**, *332* (6030), 674-676.
44. Gin, D. L.; Bara, J. E.; Noble, R. D.; Elliott, B. J., Polymerized lyotropic liquid crystal assemblies for membrane applications. *Macromolecular Rapid Communications* **2008**, *29* (5), 367-389.
45. Zhou, M. J.; Nemade, P. R.; Lu, X. Y.; Zeng, X. H.; Hatakeyama, E. S.; Noble, R. D.; Gin, D. L., New type of membrane material for water desalination based on a cross-linked bicontinuous cubic lyotropic liquid crystal assembly. *Journal of the American Chemical Society* **2007**, *129* (31), 9574-9575.
46. Lu, X. Y.; Nguyen, V.; Zeng, X. H.; Elliott, B. J.; Gin, D. L., Selective rejection of a water-soluble nerve agent stimulant using a nanoporous lyotropic liquid crystal-butyl rubber vapor barrier material: Evidence for a molecular size-discrimination mechanism. *Journal of Membrane Science* **2008**, *318* (1-2), 397-404.
47. Clark, T. D.; Buehler, L. K.; Ghadiri, M. R., Self-assembling cyclic beta(3)-peptide nanotubes as artificial transmembrane ion channels. *Journal of the American Chemical Society* **1998**, *120* (4), 651-656.
48. Ghadiri, M. R.; Granja, J. R.; Buehler, L. K., Artificial Transmembrane Ion Channels from Self-Assembling Peptide Nanotubes. *Nature* **1994**, *369* (6478), 301-304.
49. Xu, T.; Zhao, N. N.; Ren, F.; Hourani, R.; Lee, M. T.; Shu, J. Y.; Mao, S.; Helms, B. A., Subnanometer Porous Thin Films by the Co-assembly of Nanotube Subunits and Block Copolymers. *Acs Nano* **2011**, *5* (2), 1376-1384.
50. Lopez-Lorente, A. I.; Simonet, B. M.; Valcarcel, M., The Potential of Carbon Nanotube Membranes for Analytical Separations. *Analytical Chemistry* **2010**, *82* (13), 5399-5407.
51. Mi, W. L.; Lin, Y. S.; Li, Y. D., Vertically aligned carbon nanotube membranes on macroporous alumina supports. *Journal of Membrane Science* **2007**, *304* (1-2), 1-7.
52. Holt, J. K.; Noy, A.; Huser, T.; Eaglesham, D.; Bakajin, O., Fabrication of a carbon nanotube-embedded silicon nitride membrane for studies of nanometer-scale mass transport. *Nano Lett.* **2004**, *4* (11), 2245-2250.
53. Hinds, B. J.; Chopra, N.; Rantell, T.; Andrews, R.; Gavalas, V.; Bachas, L. G., Aligned multiwalled carbon nanotube membranes. *Science* **2004**, *303* (5654), 62-65.
54. Carter, B. M.; Wiesenauer, B. R.; Hatakeyama, E. S.; Barton, J. L.; Noble, R. D.; Gin, D. L., Glycerol-Based Bicontinuous Cubic Lyotropic Liquid Crystal Monomer System for the Fabrication of Thin-Film Membranes with Uniform Nanopores. *Chem. Mater.* **2012**, *24* (21), 4005-4007.

55. Beginn, U.; Zipp, G.; Mourran, A.; Walther, P.; Moller, M., Membranes containing oriented supramolecular transport channels. *Adv. Mater.* **2000**, *12* (7), 513-+.
56. Matyjaszewski, K.; Tsarevsky, N. V., Nanostructured functional materials prepared by atom transfer radical polymerization. *Nat Chem* **2009**, *1* (4), 276-288.
57. Park, C.; Yoon, J.; Thomas, E. L., Enabling nanotechnology with self assembled block copolymer patterns. *Polymer* **2003**, *44* (22), 6725-6760.
58. Schacher, F. H.; Rugar, P. A.; Manners, I., Functional Block Copolymers: Nanostructured Materials with Emerging Applications. *Angewandte Chemie-International Edition* **2012**, *51* (32), 7898-7921.
59. Yang, S. Y.; Ryu, I.; Kim, H. Y.; Kim, J. K.; Jang, S. K.; Russell, T. P., Nanoporous membranes with ultrahigh selectivity and flux for the filtration of viruses. *Advanced Materials* **2006**, *18* (6), 709-712.
60. Jeong, U. Y.; Ryu, D. Y.; Kim, J. K.; Kim, D. H.; Wu, X. D.; Russell, T. P., Precise control of nanopore size in thin film using mixtures of asymmetric block copolymer and homopolymer. *Macromolecules* **2003**, *36* (26), 10126-10129.
61. Qiu, X.; Yu, H.; Karunakaran, M.; Pradeep, N.; Nunes, S. P.; Peinemann, K., Selective Separation of Similarly Sized Proteins with Tunable Nanoporous Block Copolymer Membranes. *ACS Nano* **2013**, *7*, 768-776.
62. Jones, R. L.; Kumar, S. K.; Ho, D. L.; Briber, R. M.; Russell, T. P., Chain conformation in ultrathin polymer films. *Nature* **1999**, *400* (6740), 146-149.
63. Akthakul, A.; Salinaro, R. F.; Mayes, A. M., Antifouling polymer membranes with subnanometer size selectivity. *Macromolecules* **2004**, *37* (20), 7663-7668.
64. Asatekin, A.; Mayes, A. M., Responsive Pore Size Properties of Composite NF Membranes Based on PVDF Graft Copolymers. *Sep. Sci. Technol.* **2009**, *44* (14), 3330-3345.
65. Asatekin, A.; Mennitti, A.; Kang, S.; Elimelech, M.; Morgenroth, E.; Mayes, A. M., Antifouling nanofiltration membranes for membrane bioreactors from self-assembling graft copolymers. *Journal of Membrane Science* **2006**, *285*, 81-89.
66. Asatekin, A.; Olivetti, E. A.; Mayes, A. M., Fouling resistant, high flux nanofiltration membranes from polyacrylonitrile-graft-poly(ethylene oxide). *J. Membr. Sci.* **2009**, *332* (1-2), 6-12.
67. Foster, D. P.; Jasnow, D.; Balazs, A. C., Macrophase and Microphase Separation in Random Comb Copolymers. *Macromolecules* **1995**, *28* (9), 3450-3462.
68. Hester, J. F.; Olugebefola, S. C.; Mayes, A. M., Preparation of pH-responsive polymer membranes by self-organization. *Journal of Membrane Science* **2002**, *208* (1-2), 375-388.
69. Modestino, M. A.; Paul, D. K.; Dishari, S.; Petrina, S. A.; Allen, F. I.; Hickner, M. A.; Karan, K.; Segalman, R. A.; Weber, A. Z., Self-Assembly and Transport Limitations in Confined Nafion Films. *Macromolecules* **2013**, *46* (3), 867-873.
70. Shinozaki, A.; Jasnow, D.; Balazs, A. C., Microphase Separation in Comb Copolymers. *Macromolecules* **1994**, *27* (9), 2496-2502.
71. Ahn, S. H.; Koh, J. H.; Seo, J. A.; Kim, J. H., Structure control of organized mesoporous TiO₂ films templated by graft copolymers for dye-sensitized solar cells. *Chem Commun* **2010**, *46* (11), 1935-1937.
72. Kim, Y. W.; Lee, D. K.; Lee, K. J.; Kim, J. H., Single-step synthesis of proton conducting poly(vinylidene fluoride) (PVDF) graft copolymer electrolytes. *European Polymer Journal* **2008**, *44* (3), 932-939.
73. Ahn, S. H.; Chi, W. S.; Park, J. T.; Koh, J. K.; Roh, D. K.; Kim, J. H., Direct Assembly of Preformed Nanoparticles and Graft Copolymer for the Fabrication of Micrometer-thick, Organized TiO₂ Films: High Efficiency Solid-state Dye-sensitized Solar Cells. *Advanced Materials* **2012**, *24* (4), 519-522.

74. Ahn, S. H.; Jeon, H.; Son, K. J.; Ahn, H.; Koh, W.-G.; Ryu, D. Y.; Kim, J. H., Efficiency improvement of dye-sensitized solar cells using graft copolymer-templated mesoporous TiO₂ films as an interfacial layer. *Journal of Materials Chemistry* **2011**, *21* (6), 1772-1779.
75. Kim, Y. W.; Choi, J. K.; Park, J. T.; Kim, J. H., Proton conducting poly(vinylidene fluoride-co-chlorotrifluoroethylene) graft copolymer electrolyte membranes. *Journal of Membrane Science* **2008**, *313* (1-2), 315-322.
76. Roh, D. K.; Park, J. T.; Ahn, S. H.; Ahn, H.; Ryu, D. Y.; Kim, J. H., Amphiphilic poly(vinyl chloride)-g-poly(oxyethylene methacrylate) graft polymer electrolytes: Interactions, nanostructures and applications to dye-sensitized solar cells. *Electrochim Acta* **2010**, *55* (17), 4976-4981.
77. Asatekin, A.; Mayes, A. M., Responsive pore size properties of composite NF membranes based on PVDF graft copolymers. *Separ. Sci. Technol.* **2009**, *44* (14), 3330-3345.
78. Qu, S.; Dilenschneider, T.; Phillip, W. A., Preparation of chemically-tailored copolymer membranes with tunable ion transport properties. *ACS. Appl. Mater. Interfaces* **2015**, *7*, 19746-19754.
79. Loeb, S.; Sourirajan, S., *Sea water demineralization by means of an osmotic membrane*. ACS: Washington DC, 1963; Vol. 38.
80. Cadotte, J. E. Reverse osmosis membrane. 4,039,440, 1977.
81. Petersen, R. J.; Cadotte, J. E., Thin film composite reverse osmosis membranes. In *Handbook of industrial membrane technology*, Porter, M. C., Ed. Noyes Publications: Park Ridge, N.J., 1990; pp 307-348.
82. An, Q. F.; Sun, W. D.; Zhao, Q.; Ji, Y. L.; Gao, C. J., Study on a novel nanofiltration membrane prepared by interfacial polymerization with zwitterionic amine monomers. *Journal of Membrane Science* **2013**, *431*, 171-179.
83. Lind, M. L.; Suk, D. E.; Nguyen, T. V.; Hoek, E. M. V., Tailoring the Structure of Thin Film Nanocomposite Membranes to Achieve Seawater RO Membrane Performance. *Environmental Science & Technology* **2010**, *44* (21), 8230-8235.
84. Mo, Y. H.; Tiraferri, A.; Yip, N. Y.; Adout, A.; Huang, X.; Elimelech, M., Improved Antifouling Properties of Polyamide Nanofiltration Membranes by Reducing the Density of Surface Carboxyl Groups. *Environmental Science & Technology* **2012**, *46* (24), 13253-13261.
85. Miao, J.; Zhang, R.; Bai, R., Poly (vinyl alcohol)/carboxymethyl cellulose sodium blend composite nanofiltration membranes developed via interfacial polymerization. *Journal of Membrane Science* **2015**, *493*, 654-663.
86. Li, R. H.; Barbari, T. A., Performance of Poly(Vinyl Alcohol) Thin-Gel Composite Ultrafiltration Membranes. *Journal of Membrane Science* **1995**, *105* (1-2), 71-78.
87. Ju, H.; McCloskey, B. D.; Sagle, A. C.; Kusuma, V. A.; Freeman, B. D., Preparation and characterization of crosslinked poly(ethylene glycol) diacrylate hydrogels as fouling-resistant membrane coating materials. *Journal of Membrane Science* **2009**, *330* (1-2), 180-188.
88. Asatekin, A.; Vannucci, C., Self-Assembled Polymer Nanostructures for Liquid Filtration Membranes: A Review. *Nanosci. Nanotech. Let.* **2015**, *7* (1), 21-32.
89. Bengani, P.; Kou, Y.; Asatekin, A., Zwitterionic copolymer self-assembly for fouling resistant, high flux membranes with size-based small molecule selectivity. *Journal of Membrane Science* **2015**, *493*, 755-765.
90. Geise, G. M.; Doherty, C. M.; Hill, A. J.; Freeman, B. D.; Paul, D. R., Free volume characterization of sulfonated styrenic pentablock copolymers using positron annihilation lifetime spectroscopy. *Journal of Membrane Science* **2014**, *453* (0), 425-434.

91. Geise, G. M.; Freeman, B. D.; Paul, D. R., Sodium chloride diffusion in sulfonated polymers for membrane applications. *Journal of Membrane Science* **2013**, *427* (0), 186-196.
92. Nykanen, A.; Nuopponen, M.; Laukkanen, A.; Hirvonen, S. P.; Rytela, M.; Turunen, O.; Tenhu, H.; Mezzenga, R.; Ikkala, O.; Ruokolainen, J., Phase behavior and temperature-responsive molecular filters based on self-assembly of Polystyrene-block-poly(N-isopropylacrylamide)-block-polystyrene. *Macromolecules* **2007**, *40* (16), 5827-5834.
93. Henmi, M.; Nakatsuji, K.; Ichikawa, T.; Tomioka, H.; Sakamoto, T.; Yoshio, M.; Kato, T., Self-Organized Liquid-Crystalline Nanostructured Membranes for Water Treatment: Selective Permeation of Ions. *Adv. Mater.* **2012**, *24* (17), 2238-2241.
94. Ju, H.; McCloskey, B. D.; Sagle, A. C.; Wu, Y. H.; Kusuma, V. A.; Freeman, B. D., Crosslinked poly(ethylene oxide) fouling resistant coating materials for oil/water separation. *J. Membr. Sci.* **2008**, *307* (2), 260-267.
95. Borns, M. A.; Kalakkunnath, S.; Kalika, D. S.; Kusuma, V. A.; Freeman, B. D., Dynamic relaxation characteristics of crosslinked poly(ethylene oxide) copolymer networks: Influence of short chain pendant groups. *Polymer* **2007**, *48* (25), 7316-7328.
96. Freeman, B.; Pinnau, I., Separation of gases using solubility-selective polymers. *Trends Polym Sci* **1997**, *5* (5), 167-173.
97. Kalika, D. S.; Kalakkunnath, S.; Danquah, M. K.; Lin, H. Q.; Kusuma, V. A.; Freeman, B. D., Influence of network structural modifications on the properties of crosslinked poly(ethylene oxide) copolymer membranes for CO₂ separations. *Abstr Pap Am Chem S* **2009**, 237.
98. Lin, H. Q.; Freeman, B. D.; Kalakkunnath, S.; Kalika, D. S., Effect of copolymer composition, temperature, and carbon dioxide fugacity on pure- and mixed-gas permeability in poly(ethylene glycol)-based materials: Free volume interpretation. *Journal of Membrane Science* **2007**, *291* (1-2), 131-139.
99. Yang, Q.; Adrus, N.; Tomicki, F.; Ulbricht, M., Composites of functional polymeric hydrogels and porous membranes. *Journal of Materials Chemistry* **2011**, *21* (9), 2783-2811.
100. Kang, G. D.; Cao, Y. M.; Zhao, H. Y.; Yuan, Q., Preparation and characterization of crosslinked poly(ethylene glycol) diacrylate membranes with excellent antifouling and solvent-resistant properties. *J. Membr. Sci.* **2008**, *318* (1-2), 227-232.
101. van Rijn, P.; Tutus, M.; Kathrein, C.; Zhu, L.; Wessling, M.; Schwaneberg, U.; Boker, A., Challenges and advances in the field of self-assembled membranes. *Chemical Society Reviews* **2013**, *42* (16), 6578-6592.
102. Bhattacharya, A.; Misra, B. N., Grafting: a versatile means to modify polymers - Techniques, factors and applications. *Prog. Polym. Sci.* **2004**, *29* (8), 767-814.
103. Nam, K. T.; Kim, D. W.; Yoo, P. J.; Chiang, C. Y.; Meethong, N.; Hammond, P. T.; Chiang, Y. M.; Belcher, A. M., Virus-enabled synthesis and assembly of nanowires for lithium ion battery electrodes. *Science* **2006**, *312* (5775), 885-888.
104. Allen, M.; Willits, D.; Mosolf, J.; Young, M.; Douglas, T., Protein cage constrained synthesis of ferrimagnetic iron oxide nanoparticles. *Adv. Mater.* **2002**, *14* (21), 1562-1565.
105. Ji, Y. L.; An, Q. F.; Zhao, Q.; Sun, W. D.; Lee, K. R.; Chen, H. L.; Gao, C. J., Novel composite nanofiltration membranes containing zwitterions with high permeate flux and improved anti-fouling performance. *Journal of Membrane Science* **2012**, *390*, 243-253.
106. La, Y. H.; McCloskey, B. D.; Sooriyakumaran, R.; Vora, A.; Freeman, B.; Nassar, M.; Hedrick, J.; Nelson, A.; Allen, R., Bifunctional hydrogel coatings for water purification

- membranes: Improved fouling resistance and antimicrobial activity. *Journal of Membrane Science* **2011**, 372 (1-2), 285-291.
107. Lee, Y. M.; Shim, I. K., Plasma surface graft of acrylic acid onto a porous poly(vinylidene fluoride) membrane and its riboflavin permeation. *Journal of Applied Polymer Science* **1996**, 61 (8), 1245-1250.
108. Michel, V.; Marzin, C.; Tarrago, G.; Durand, J., New membranes bearing pyridinic ligands by plasma graft polymerization. *Journal of Applied Polymer Science* **1998**, 70 (2), 359-366.
109. Tran, T. D.; Mori, S.; Suzuki, M., Plasma modification of polyacrylonitrile ultrafiltration membrane. *Thin Solid Films* **2007**, 515 (9), 4148-4152.
110. Taniguchi, M.; Kilduff, J. E.; Belfort, G., Low fouling synthetic membranes by UV-assisted graft polymerization: monomer selection to mitigate fouling by natural organic matter. *Journal of Membrane Science* **2003**, 222 (1-2), 59-70.
111. Ulbricht, M.; Matuschewski, H.; Oechel, A.; Hicke, H. G., Photo-induced graft polymerization surface modifications for the preparation of hydrophilic and low-protein-adsorbing ultrafiltration membranes. *Journal of Membrane Science* **1996**, 115 (1), 31-47.
112. Ulbricht, M.; Oechel, A.; Lehmann, C.; Tomaszewski, G.; Hicke, H. G., Gas-Phase Photoinduced Graft-Polymerization of Acrylic-Acid onto Polyacrylonitrile Ultrafiltration Membranes. *Journal of Applied Polymer Science* **1995**, 55 (13), 1707-1723.
113. Yang, B.; Yang, W. T., Thermo-sensitive switching membranes regulated by pore-covering polymer brushes. *Journal of Membrane Science* **2003**, 218 (1-2), 247-255.
114. Yu, H. J.; Cao, Y. M.; Kang, G. D.; Liu, J. H.; Li, M.; Yuan, Q., Enhancing antifouling property of polysulfone ultrafiltration membrane by grafting zwitterionic copolymer via UV-initiated polymerization. *Journal of Membrane Science* **2009**, 342 (1-2), 6-13.
115. Mao, C. B.; Flynn, C. E.; Hayhurst, A.; Sweeney, R.; Qi, J. F.; Georgiou, G.; Iverson, B.; Belcher, A. M., Viral assembly of oriented quantum dot nanowires. *Proceedings of the National Academy of Sciences of the United States of America* **2003**, 100 (12), 6946-6951.
116. Culver, J. N.; Brown, A. D.; Zang, F.; Gnerlich, M.; Gerasopoulos, K.; Ghodssi, R., Plant virus directed fabrication of nanoscale materials and devices. *Virology* **2015**, 479-480, 200-212.
117. Culver, J. N., Tobacco mosaic virus assembly and disassembly: Determinants in pathogenicity and resistance. *Annual Review of Phytopathology* **2002**, 40, 287-308.
118. Balci, S.; Bittner, A. M.; Hahn, K.; Scheu, C.; Knez, M.; Kadri, A.; Wege, C.; Jeske, H.; Kern, K., Copper nanowires within the central channel of tobacco mosaic virus particles. *Electrochimica Acta* **2006**, 51 (28), 6251-6257.
119. Douglas, T.; Young, M., Virus particles as templates for materials synthesis. *Adv. Mater.* **1999**, 11 (8), 679-681.
120. Li, Q.; Zhou, B.; Bi, Q.-Y.; Wang, X.-L., Surface modification of PVDF membranes with sulfobetaine polymers for a stably anti-protein-fouling performance. *Journal of Applied Polymer Science* **2012**, 125 (5), 4015-4027.
121. Zhao, Y.-H.; Wee, K.-H.; Bai, R., A Novel Electrolyte-Responsive Membrane with Tunable Permeation Selectivity for Protein Purification. *Acs Appl Mater Inter* **2009**, 2 (1), 203-211.
122. Lilly, J. L.; Romero, G.; Xu, W.; Shin, H. Y.; Berron, B. J., Characterization of Molecular Transport in Ultrathin Hydrogel Coatings for Cellular Immunoprotection. *Biomacromolecules* **2015**, 16 (2), 541-549.
123. Kızılel, S.; Pérez-Luna, V. H.; Teymour, F., Photopolymerization of Poly(Ethylene Glycol) Diacrylate on Eosin-Functionalized Surfaces. *Langmuir* **2004**, 20 (20), 8652-8658.

124. Carroll, T.; Booker, N. A.; Meier-Haack, J., Polyelectrolyte-grafted microfiltration membranes to control fouling by natural organic matter in drinking water. *J. Membr. Sci.* **2002**, *203* (1-2), 3-13.
125. Mubarak, A.; Veronika, B.; Schiedt, B.; Neumann, R.; Ensinger, W., Fabrication and functionalization of single asymmetric nanochannels for electrostatic/hydrophobic association of protein molecules. *Nanotechnology* **2008**, *19*, 1-9.
126. Martin, C. R.; Siwy, Z., Learning nature's way: biosensing with synthetic nanopores. *Science* **2007**, *317*, 331-332.
127. Choi, Y.; Baker, L. A.; Hillebrenner, H.; Martin, C. R., Biosensing with conically shaped nanopores and nanotubes. *Phys. Chem. Chem. Phys.* **2006**, *8*, 4976-4988.
128. Han, A. P.; Schurmann, G.; Mondin, G.; Bitterli, R. A.; Hegelbach, N. G.; de Rooij, N. F.; Staufer, U., Sensing protein molecules using nanofabricated pores. *Appl. Phys. Lett.* **2006**, *88* (9).
129. Mara, A.; Siwy, Z.; Trautmann, C.; Wan, J.; Kamme, F., An asymmetric polymer nanopore for single molecule detection. *Nano Lett.* **2004**, *4*, 497-501.
130. Schiedt, B.; Healy, K.; Morrison, A. P.; Neumann, R.; Siwy, Z., Transport of ions and biomolecules through single asymmetric nanopores in polymer films. *Nucl. Instrum. Methods Phys. Res. B* **2005**, *236*, 109-116.
131. Li, J.; Stein, D.; McMullan, C.; Branton, D.; Aziz, M. J.; Golovchenko, J. A., Ion-beam sculpting at nanometre length scales. *Nature* **2001**, *412* (6843), 166-169.
132. Healy, K., Nanopore-based single molecule DNA analysis. *Nanomedicine* **2007**, *2*, 459-481.
133. Howorka, S.; Cheley, S.; Bayley, H., Sequence-specific detection of individual DNA strands using engineered nanopores. *Nat. Biotechnol.* **2001**, *19* (7), 636-639.
134. Plecis, A.; Schoch, R. B.; Renaud, P., Ionic transport phenomena in nanofluidics: Experimental and theoretical study of the exclusion-enrichment effect on a chip. *Nano Lett.* **2005**, *5* (6), 1147-1155.
135. Fan, R.; Yue, M.; Karnik, R.; Majumdar, A.; Yang, P. D., Polarity switching and transient responses in single nanotube nanofluidic transistors. *Phys. Rev. Lett.* **2005**, *95* (8).
136. Desai, T. A.; Hansford, D. J.; Kulinsky, L.; Nashat, A. H.; Rasi, G.; Tu, J.; Wang, Y.; Zhang, M.; Ferrari, M., Nanopore Technology for Biomedical Applications. *Biomed. Microdevices* **1999**, *2* (1), 11-40.
137. Mackinnon, R., Pore Loops - an Emerging Theme in Ion-Channel Structure. *Neuron* **1995**, *14* (5), 889-892.
138. Kim, S. J.; Ko, S. H.; Kang, K. H.; Han, J., Direct seawater desalination by ion concentration polarization. *Nat. Nanotechnol.* **2010**, *5* (4), 297-301.
139. Hong, S. U.; Bruening, M. L., Separation of amino acid mixtures using multilayer polyelectrolyte nanofiltration membranes. *J. Membr. Sci.* **2006**, *280* (1-2), 1-5.
140. Ku, J. R.; Lai, S. M.; Ileri, N.; Ramirez, P.; Mafe, S.; Stroeve, P., pH and ionic strength effects on amino acid transport through Au-nanotubule membranes charged with self-assembled monolayers. *J. Phys. Chem. C* **2007**, *111* (7), 2965-2973.
141. Shim, Y. K.; Chellam, S., Steric and electrostatic interactions govern nanofiltration of amino acids. *Biotechnol. Bioeng.* **2007**, *98* (2), 451-461.
142. Wang, K. Y.; Chung, T. S., The characterization of flat composite nanofiltration membranes and their applications in the separation of Cephalexin. *J. Membr. Sci.* **2005**, *247* (1-2), 37-50.
143. Wang, K. Y.; Xiao, Y. C.; Chung, T. S., Chemically modified polybenzimidazole nanofiltration membrane for the separation of electrolytes and cephalixin. *Chem. Eng. Sci.* **2006**, *61* (17), 5807-5817.

144. Fornasiero, F.; Park, H. G.; Holt, J. K.; Stadermann, M.; Grigoropoulos, C. P.; Noy, A.; Bakajin, O., Ion exclusion by sub-2-nm carbon nanotube pores. *PNAS* **2008**, *105*, 17250-17255.
145. Holt, J. K.; Park, H. G.; Wang, Y.; Stadermann, M.; Artykhin, A. B.; Grigoropoulos, C. P.; Noy, A.; Bakajin, O., Fast mass transport through sub-2-nanometer carbon nanotubes. *Science* **2006**, *312*, 1034-10367.
146. Baker, R. W., *Membrane technology and applications*. McGraw-Hill: New York, 2000.
147. De Volder, M. F. L.; Tawfick, S. H.; Baughman, R. H.; Hart, A. J., Carbon Nanotubes: Present and Future Commercial Applications. *Science* **2013**, *339* (6119), 535-539.
148. Baughman, R. H.; Zakhidov, A. A.; de Heer, W. A., Carbon nanotubes - the route toward applications. *Science* **2002**, *297* (5582), 787-792.
149. Strasinger, C.; Paudel, K. S.; Wu, J.; Hammell, D.; Pinninti, R. R.; Hinds, B. J.; Stinchcomb, A., Programmable Transdermal Clonidine Delivery Through Voltage-Gated Carbon Nanotube Membranes. *J. Pharm. Sci.* **2014**, *103* (6), 1829-1838.
150. Baker, L. A.; Choi, Y. S.; Martin, C. R., Nanopore membranes for biomaterials synthesis, biosensing and bioseparations. *Curr. Nanosci.* **2006**, *2* (3), 243-255.
151. Nunes, S. P., Block Copolymer Membranes for Aqueous Solution Applications. *Macromolecules* **2016**, *49* (8), 2905-2916.
152. Qiu, X. Y.; Yu, H. Z.; Karunakaran, M.; Pradeep, N.; Nunes, S. P.; Peinemann, K. V., Selective Separation of Similarly Sized Proteins with Tunable Nanoporous Block Copolymer Membranes. *Acs Nano* **2013**, *7* (1), 768-776.
153. Gu, Y.; Wiesner, U., Tailoring Pore Size of Graded Mesoporous Block Copolymer Membranes: Moving from Ultrafiltration toward Nanofiltration. *Macromolecules* **2015**, *48* (17), 6153-6159.
154. Dorin, R. M.; Phillip, W. A.; Sai, H.; Werner, J.; Elimelech, M.; Wiesner, U., Designing block copolymer architectures for targeted membrane performance. *Polymer* **2014**, *55* (1), 347-353.
155. Kaner, P.; Bengani-Lutz, P.; Sadeghi, I.; Asatekin, A., Responsive filtration membranes by polymer self-assembly. *Technology* **2016**, *4* (4), 217-228.
156. Nunes, S. P.; Behzad, A. R.; Peinemann, K. V., Self-assembled block copolymer membranes: From basic research to large-scale manufacturing. *J. Mater. Res.* **2013**, *28* (19), 2661-2665.
157. Zhang, Y. Z.; Sargent, J. L.; Boudouris, B. W.; Phillip, W. A., Nanoporous membranes generated from self-assembled block polymer precursors: Quo Vadis? *J. Appl. Polym. Sci.* **2015**, *132* (21).
158. Bengani, P.; Kou, Y.; Asatekin, A., Zwitterionic copolymer self-assembly for fouling resistant, high flux membranes with size-based small molecule selectivity. *J. Membr. Sci.* **2015**, *493*, 755-765.
159. Vannucci, C.; Taniguchi, I.; Asatekin, A., Nanoconfinement and Chemical Structure Effects on Permeation Selectivity of Self-Assembling Graft Copolymers. *Acs Macro Lett.* **2015**, *4* (9), 872-878.
160. Tyagi, P.; Raschip, I. E.; Deratani, A.; Quemener, D., Reversible 2D/3D Coatings from Zipper-Assembly of Block Copolymer Micelles. *Adv. Mater.* **2013**, *25* (27), 3739-3744.
161. Mouline, Z.; Semsarilar, M.; Deratani, A.; Quemener, D., Stimuli responsive nanostructured porous network from triblock copolymer self-assemblies. *Polym. Chem.* **2015**, *6* (11), 2023-2028.
162. Tyagi, P.; Deratani, A.; Bouyer, D.; Cot, D.; Gence, V.; Barboiu, M.; Phan, T. N. T.; Bertin, D.; Gimes, D.; Quemener, D., Dynamic Interactive Membranes with Pressure-

- Driven Tunable Porosity and Self-Healing Ability. *Angew. Chem. Int. Edit* **2012**, *51* (29), 7166-7170.
163. Abelow, A. E.; Zharov, I., Poly(l-alanine)-modified nanoporous colloidal films. *Soft Matter* **2009**, *5* (2), 457-462.
164. Khabibullin, A.; Zharov, I., Nanoporous membranes with tunable pore size by pressing/sintering silica colloidal spheres. *ACS Appl. Mater. Interfaces* **2014**, *6*, 7712-7718.
165. Schepelina, O.; Zharov, I., Polymer-modified opal nanopores. *Langmuir* **2006**, *22* (25), 10523-10527.
166. Zharov, I.; Khabibullin, A., Surface-modified silica colloidal crystals: nanoporous films and membranes with controlled ionic and molecular transport. *Acc. Chem. Res.* **2014**, *47* (2), 440-449.
167. Green, E.; Fullwood, E.; Selden, J.; Zharov, I., Functional membranes via nanoparticle self-assembly. *Chem. Commun.* **2015**, *51* (37), 7770-7780.
168. Zharov, I.; Khabibullin, A., Surface-Modified Silica Colloidal Crystals: Nanoporous Films and Membranes with Controlled Ionic and Molecular Transport. *Accounts Chem. Res.* **2014**, *47* (2), 440-449.
169. Sadeghi, I.; Asatekin, A., Spontaneous Self-Assembly and Micellization of Random Copolymers in Organic Solvents. *Macromol. Chem. Phys.* **2017**.
170. Sadeghi, I.; Kronenberg, J.; Asatekin, A., Selective Transport through Membranes with Charged Nanochannels Formed by Scalable Self-Assembly of Random Copolymer Micelles. *Acs Nano* **2018**, *12* (1), 95-108.
171. Sadeghi, I.; Asatekin, A., Spontaneous Self-Assembly and Micellization of Random Copolymers in Organic Solvents. *Macromol. Chem. Phys.* **2017**, *218* (20).
172. Zhang, L. F.; Eisenberg, A., Multiple morphologies and characteristics of "crew-cut" micelle-like aggregates of polystyrene-b-poly(acrylic acid) diblock copolymers in aqueous solutions. *J. Am. Chem. Soc.* **1996**, *118* (13), 3168-3181.
173. Geng, Y.; Ahmed, F.; Bhasin, N.; Discher, D. E., Visualizing worm micelle dynamics and phase transitions of a charged diblock copolymer in water. *J. Phys. Chem. B* **2005**, *109* (9), 3772-3779.
174. Yu, K.; Eisenberg, A., Bilayer morphologies of self-assembled crew-cut aggregates of amphiphilic PS-b-PEO diblock copolymers in solution. *Macromolecules* **1998**, *31* (11), 3509-3518.
175. Yu, K.; Zhang, L. F.; Eisenberg, A., Novel morphologies of "crew-cut" aggregates of amphiphilic diblock copolymers in dilute solution. *Langmuir* **1996**, *12* (25), 5980-5984.
176. Holder, S. J.; Sommerdijk, N. A. J. M., New micellar morphologies from amphiphilic block copolymers: disks, toroids and bicontinuous micelles. *Polym Chem-Uk* **2011**, *2* (5), 1018-1028.
177. Jiang, X.; Qu, W.; Pan, D.; Ren, Y.; Williford, J. M.; Cui, H. G.; Luijten, E.; Mao, H. Q., Plasmid-Templated Shape Control of Condensed DNA-Block Copolymer Nanoparticles. *Advanced Materials* **2013**, *25* (2), 227-232.
178. Zhulina, E. B.; Borisov, O. V., Theory of Block Polymer Micelles: Recent Advances and Current Challenges. *Macromolecules* **2012**, *45* (11), 4429-4440.
179. Zhu, X.; Liu, M., Self-assembly and morphology control of new L-glutamic acid-based amphiphilic random copolymers: giant vesicles, vesicles, Spheres, and honeycomb film. *Langmuir* **2011**, *27*, 12844-12850.
180. Cheng, R.; Tian, M.; Sun, S.; Liu, C.; Wang, Y.; Liu, Z. T.; Liu, Z. W.; Jiang, J., Light-triggered disruption of PAG-based amphiphilic random copolymer micelles. *Langmuir* **2015**, *31*, 7758-7763.
181. Li, L.; Raghupathi, K.; Song, C.; Prasad, P.; Thayumanavan, S., Self-assembly of random copolymers. *Chem. Commun.* **2014**, *50*, 13417-13432.

182. Bengani-Lutz, P.; Converse, E.; Cebe, P.; Asatekin, A., Self-Assembling Zwitterionic Copolymers as Membrane Selective Layers with Excellent Fouling Resistance: Effect of Zwitterion Chemistry. *ACS Applied Materials & Interfaces* **2017**, *9* (24), 20859-20872.
183. Tian, F.; Yu, Y. Y.; Wang, C. C.; Yang, S., Consecutive morphological transitions in nanoaggregates assembled from amphiphilic random copolymer via water-driven micellization and light-triggered dissociation. *Macromolecules* **2008**, *41* (10), 3385-3388.
184. Li, N.; Li, Y. B.; Wang, X. G., Fractal Structures from Amphiphilic Random Azo Copolymer. *Macromolecules* **2011**, *44* (21), 8598-8606.
185. Liu, X. Y.; Kim, J. S.; Wu, J.; Eisenberg, A., Bowl-shaped aggregates from the self-assembly of an amphiphilic random copolymer of poly(styrene-co-methacrylic acid). *Macromolecules* **2005**, *38* (16), 6749-6751.
186. Dan, K.; Bose, N.; Ghosh, S., Vesicular assembly and thermo-responsive vesicle-to-micelle transition from an amphiphilic random copolymer. *Chem Commun* **2011**, *47* (46), 12491-12493.
187. Shao, Y.; Jia, Y. G.; Shi, C. Y.; Luo, J. T.; Zhu, X. X., Block and Random Copolymers Bearing Cholic Acid and Oligo(ethylene glycol) Pendant Groups: Aggregation, Thermosensitivity, and Drug Loading. *Biomacromolecules* **2014**, *15* (5), 1837-1844.
188. Ikkala, O.; ten Brinke, G., Functional materials based on self-assembly of polymeric supramolecules. *Science* **2002**, *295* (5564), 2407-2409.
189. Aida, T.; Meijer, E. W.; Stupp, S. I., Functional Supramolecular Polymers. *Science* **2012**, *335* (6070), 813-817.
190. Hill, J. P.; Shrestha, L. K.; Ishihara, S.; Ji, Q. M.; Ariga, K., Self-Assembly: From Amphiphiles to Chromophores and Beyond. *Molecules* **2014**, *19* (6), 8589-8609.
191. Karayianni, M.; Pispas, S., Self-Assembly of Amphiphilic Block Copolymers in Selective Solvents. *Springer Ser Fluores* **2016**, *16*, 27-63.
192. Muller, F.; Delsanti, M.; Auvray, L.; Yang, J.; Chen, Y. J.; Mays, J. W.; Demé, B.; Tirrell, M.; Guenoun, P., Ordering of urchin-like charged copolymer micelles: Electrostatic, packing and polyelectrolyte correlations. *The European Physical Journal E* **2000**, *3* (1), 45-53.
193. Pitsikalis, M.; Woodward, J.; Mays, J. W.; Hadjichristidis, N., Micellization of model graft copolymers in dilute solution. *Macromolecules* **1997**, *30* (18), 5384-5389.
194. LaRue, I.; Adam, M.; Zhulina, E. B.; Rubinstein, M.; Pitsikalis, M.; Hadjichristidis, N.; Ivanov, D. A.; Gearba, R. I.; Anokhin, D. V.; Sheiko, S. S., Effect of the Soluble Block Size on Spherical Diblock Copolymer Micelles. *Macromolecules* **2008**, *41* (17), 6555-6563.
195. Zhulina, E. B.; Adam, M.; LaRue, I.; Sheiko, S. S.; Rubinstein, M., Diblock Copolymer Micelles in a Dilute Solution. *Macromolecules* **2005**, *38* (12), 5330-5351.
196. Ding, J. F.; Liu, G. J.; Yang, M. L., Multiple morphologies of polyisoprene-block-poly(2-cinnamoyl ethyl methacrylate) and polystyrene-block-poly(2-cinnamoyl ethyl methacrylate) micelles in organic solvents. *Polymer* **1997**, *38* (21), 5497-5501.
197. Tung, P. H.; Kuo, S. W.; Chen, S. C.; Lin, C. L.; Chang, F. C., Micellar morphologies of self-associated diblock copolymers in acetone solution. *Polymer* **2007**, *48* (11), 3192-3200.
198. Deacon, G. B.; Phillips, R. J., Relationships between the Carbon-Oxygen Stretching Frequencies of Carboxylate Complexes and the Type of Carboxylate Coordination. *Coordin. Chem. Rev.* **1980**, *33* (3), 227-250.
199. Kurata, S.; Yamazaki, N., Mechanical-Properties of Poly(Alkyl Alpha-Fluoroacrylate)S as Denture Base Materials. *J. Dent. Res.* **1989**, *68* (3), 481-483.

200. Vamvakaki, M.; Palioura, D.; Spyros, A.; Armes, S. P.; Anastasiadis, S. H., Dynamic light scattering vs H-1 NMR investigation of pH-responsive diblock copolymers in water. *Macromolecules* **2006**, *39* (15), 5106-5112.
201. Chen, Y. J.; Zhang, Y. Y.; Wang, Y. F.; Sun, C.; Zhang, C. C., Synthesis, characterization, and self-assembly of amphiphilic fluorinated gradient copolymer. *J Appl Polym Sci* **2013**, *127* (3), 1485-1492.
202. Zhou, J. F.; Wang, L.; Wang, C. L.; Chen, T.; Yu, H. J.; Yang, Q., Synthesis and self-assembly of amphiphilic maleic anhydride-stearyl methacrylate copolymer. *Polymer* **2005**, *46* (24), 11157-11164.
203. Zhang, L. F.; Yu, K.; Eisenberg, A., Ion-induced morphological changes in "crew-cut" aggregates of amphiphilic block copolymers. *Science* **1996**, *272* (5269), 1777-1779.
204. Discher, D. E.; Eisenberg, A., Polymer vesicles. *Science* **2002**, *297* (5583), 967-973.
205. Luo, Y. L.; Wang, Y.; Wang, X.; Xu, F.; Chen, Y. S., Thermosensitive tribranchia star-shaped s-P(NIPAM-co-DMAM) random copolymer micelle aggregates: Preparation, characterization, and drug release applications. *Journal of Biomaterials Applications* **2016**, *30* (6), 662-676.
206. Gao, Z. S.; Varshney, S. K.; Wong, S.; Eisenberg, A., Block-Copolymer Crew-Cut Micelles in Water. *Macromolecules* **1994**, *27* (26), 7923-7927.
207. Spatz, J. P.; Mossmer, S.; Moller, M., Metastable reverse globular micelles and giant micellar wires from block copolymers. *Angewandte Chemie International Edition in English* **1996**, *35* (13-14), 1510-1512.
208. Huheey, J. E., *Inorganic chemistry*. 3rd ed.; Harper and Row: London, 1983.
209. Choucair, A.; Eisenberg, A., Control of amphiphilic block copolymer morphologies using solution conditions. *Eur Phys J E* **2003**, *10* (1), 37-44.
210. Zhang, L. F.; Eisenberg, A., Formation of crew-cut aggregates of various morphologies from amphiphilic block copolymers in solution. *Polym Advan Technol* **1998**, *9* (10-11), 677-699.
211. Baloch, M. K.; Ahmad, F.; Rauf, A.; Durrani, G. F., Effect of polyethyleneoxide and sodium chloride over the micellization behavior of sodium dodecyl sulfate. *J Appl Polym Sci* **2009**, *114* (3), 1444-1448.
212. Giri, N.; James, S. L., A metal complex that imitates a micelle. *Chem. Commun.* **2011**, *47* (1), 245-247.
213. Adams, M. L.; Lavasanifar, A.; Kwon, G. S., Amphiphilic block copolymers for drug delivery. *J Pharm Sci-Us* **2003**, *92* (7), 1343-1355.
214. Miller, A. C.; Bershteyn, A.; Tan, W.; Hammond, P. T.; Cohen, R. E.; Irvine, D. J., Block Copolymer Micelles as Nanocontainers for Controlled Release of Proteins from Biocompatible Oil Phases. *Biomacromolecules* **2009**, *10* (4), 732-741.
215. Owen, T.; Butler, A., Metallosurfactants of Bioinorganic Interest: Coordinationinduced Self assembly. *Coordin. Chem. Rev.* **2011**, *225*, 678-687.
216. Fustin, C. A.; Guillet, P.; Schubert, U. S.; Gohy, J. F., Metallo-supramolecular block copolymers. *Advanced Materials* **2007**, *19* (13), 1665-1673.
217. Nunes, S. P.; Sougrat, R.; Hooghan, B.; Anjum, D. H.; Behzad, A. R.; Zhao, L.; Pradeep, N.; Pinnau, I.; Vainio, U.; Peinemann, K. V., Ultraporous Films with Uniform Nanochannels by Block Copolymer Micelles Assembly. *Macromolecules* **2010**, *43* (19), 8079-8085.
218. Nunes, S. P.; Behzad, A. R.; Hooghan, B.; Sougrat, R.; Karunakaran, M.; Pradeep, N.; Vainio, U.; Peinemann, K. V., Switchable pH-Responsive Polymeric Membranes Prepared via Block Copolymer Micelle Assembly. *Acs Nano* **2011**, *5* (5), 3516-3522.

219. Zarka, M. T.; Nuyken, O.; Weberskirch, R., Amphiphilic Polymer Supports for the Asymmetric Hydrogenation of Amino Acid Precursors in Water. *Chem. Eur. J.* **2003**, *9*, 3228-3234.
220. Li, Y. L.; Hindi, K.; Watts, K. M.; Taylor, J. B.; Zhang, K.; Li, Z. C.; Hunstad, D. A.; Cannon, C. L.; Youngs, W. J.; Wooley, K. L., Shell crosslinked nanoparticles carrying silver antimicrobials as therapeutics. *Chem Commun* **2010**, *46* (1), 121-123.
221. Chai, J.; Wang, D.; Fan, X. N.; Buriak, J. M., Assembly of aligned linear metallic patterns on silicon. *Nat Nanotechnol* **2007**, *2* (8), 500-506.
222. Krogstad, D. V.; Choi, S. H.; Lynd, N. A.; Audus, D. J.; Perry, S. L.; Gopez, J. D.; Hawker, C. J.; Kramer, E. J.; Tirrell, M. V., Small Angle Neutron Scattering Study of Complex Coacervate Micelles and Hydrogels Formed from Ionic Diblock and Triblock Copolymers. *J. Phys. Chem. B* **2014**, *118* (45), 13011-13018.
223. Krogstad, D. V.; Lynd, N. A.; Choi, S. H.; Spruell, J. M.; Hawker, C. J.; Kramer, E. J.; Tirrell, M. V., Effects of Polymer and Salt Concentration on the Structure and Properties of Triblock Copolymer Coacervate Hydrogels. *Macromolecules* **2013**, *46* (4), 1512-1518.
224. Krogstad, D. V.; Lynd, N. A.; Miyajima, D.; Gopez, J.; Hawker, C. J.; Kramer, E. J.; Tirrell, M. V., Structural Evolution of Polyelectrolyte Complex Core Micelles and Ordered-Phase Bulk Materials. *Macromolecules* **2014**, *47* (22), 8026-8032.
225. Laaser, J. E.; Jiang, Y. M.; Sprouse, D.; Reineke, T. M.; Lodge, T. P., pH- and Ionic-Strength-Induced Contraction of Polybasic Micelles in Buffered Aqueous Solutions. *Macromolecules* **2015**, *48* (8), 2677-2685.
226. Zhang, L. F.; Eisenberg, A., Thermodynamic vs kinetic aspects in the formation and morphological transitions of crew-cut aggregates produced by self-assembly of polystyrene-*b*-poly(acrylic acid) block copolymers in dilute solution. *Macromolecules* **1999**, *32* (7), 2239-2249.
227. Guenoun, P.; Davis, H. T.; Tirrell, M.; Mays, J. W., Aqueous Micellar Solutions of Hydrophobically Modified Polyelectrolytes. *Macromolecules* **1996**, *29* (11), 3965-3969.
228. Shen, H. W.; Zhang, L. F.; Eisenberg, A., Multiple pH-induced morphological changes in aggregates of polystyrene-block-poly(4-vinylpyridine) in DMF/H₂O mixtures. *Journal of the American Chemical Society* **1999**, *121* (12), 2728-2740.
229. Zhang, L. F.; Eisenberg, A., Morphogenic effect of added ions on crew-cut aggregates of polystyrene-*b*-poly(acrylic acid) block copolymers in solutions. *Macromolecules* **1996**, *29* (27), 8805-8815.
230. McCluskey, P. H.; Snyder, R. L.; Condrate, R. A., Infrared Spectral Studies of Various Metal Polyacrylates. *J Solid State Chem* **1989**, *83* (2), 332-339.
231. Nicholson, J. W.; Wasson, E. A.; Wilson, A. D., Thermal-Behavior of Films of Partially Neutralized Poly(Acrylic Acid) .3. Effect of Magnesium and Calcium-Ions. *Brit Polym J* **1988**, *20* (2), 97-101.
232. Owen, T.; Pynn, R.; Martinez, J. S.; Butler, A., Micelle-to-vesicle transition of an iron-chelating microbial surfactant, Marinobactin E. *Langmuir* **2005**, *21* (26), 12109-12114.
233. Mandel, M.; Leyte, J. C., Interaction of Poly(Methacrylic Acid) + Bivalent Counterions. I. *J Polym Sci Part A* **1964**, *2*, 2883-2899.
234. Mandel, M.; Leyte, J. C., Interaction of Polymethacrylic Acid + Bivalent Counterions. II. *J Polym Sci Part A* **1964**, *2*, 3771-3780.
235. Truong, N. D.; Medjahdi, G.; Sarazin, D.; Francois, J., Effect of the Carboxylate Group Distribution on Potentiometric Titration of Acrylamide-Acrylic Acid Copolymers. *Polym Bull* **1990**, *24* (1), 101-106.

236. Francois, J.; Heitz, C.; Mestdagh, M. M., Spectroscopic study (uv-visible and electron paramagnetic resonance) of the interactions between synthetic polycarboxylates and copper ions. *Polymer* **1997**, *38* (21), 5321-5332.
237. Zeng, B. R.; Wu, Y. G.; Kang, Q. L.; Chang, Y.; Yuan, C. H.; Xu, Y. T.; Chang, F. C.; Dai, L. Z., Metal-ions directed self-assembly of hybrid diblock copolymers. *J Mater Res* **2014**, *29* (22), 2694-2706.
238. Huang, X.; Cao, M. W.; Wang, J. B.; Wang, Y. L., Controllable organization of a carboxylic acid type gemini surfactant at different pH values by adding copper(II) ions. *J. Phys. Chem. B* **2006**, *110* (39), 19479-19486.
239. Nicholson, J. W., The effect of trivalent metal nitrates on the properties of dental cements made from poly(acrylic acid). *J Appl Polym Sci* **1998**, *70* (12), 2353-2359.
240. Oikonomou, E. K.; Bokias, G.; Kallitsis, J. K., Comparative study of electrostatic binding vs. complexation of Cu²⁺ ions with water-soluble polymers containing styrene sulphonic acid and/or maleic acid units or their sodium salt forms. *J Polym Sci Pol Phys* **2008**, *46* (12), 1149-1158.
241. Konradi, R.; Rhe, J., Interaction of Poly(methacrylic acid) Brushes with Metal Ions: An Infrared Investigation. *Macromolecules* **2004**, *37* (18), 6954-6961.
242. Yalpani, M., Polysaccharides: Synthesis Modifications and Structure/Property Relations. *Elsevier* **1989**, *Amsterdam*.
243. Min, Y. J.; Akbulut, M.; Kristiansen, K.; Golan, Y.; Israelachvili, J., The role of interparticle and external forces in nanoparticle assembly. *Nat. Mater.* **2008**, *7* (7), 527-538.
244. Kralchevsky, P. A.; Denkov, N. D.; Paunov, V. N.; Velev, O. D.; Ivanov, I. B.; Yoshimura, H.; Nagayama, K., Formation of 2-Dimensional Colloid Crystals in Liquid-Films under the Action of Capillary Forces. *J. Phys. Condens. Mat.* **1994**, *6*, A395-A402.
245. Nikoobakht, B.; Wang, Z. L.; El-Sayed, M. A., Self-assembly of gold nanorods. *J. Phys. Chem. B* **2000**, *104* (36), 8635-8640.
246. Bowden, N.; Oliver, S. R. J.; Whitesides, G. M., Mesoscale self-assembly: Capillary bonds and negative menisci. *J. Phys. Chem. B* **2000**, *104* (12), 2714-2724.
247. Diez-Pena, E.; Quijada-Garrido, I.; Frutos, P.; Barrales-Rienda, J. M., Analysis of the swelling dynamics of crosslinked P(N-iPAAm-co-MAA) copolymers, the corresponding homopolymers and their interpenetrating networks. Kinetics of water penetration into the gel above the pK(a) of MAA comonomeric units. *Polym. Int.* **2003**, *52* (6), 956-965.
248. Zhang, J.; Peppas, N. A., Synthesis and characterization of pH- and temperature-sensitive poly(methacrylic acid)/poly(N-isopropylacrylamide) interpenetrating polymeric networks. *Macromolecules* **2000**, *33* (1), 102-107.
249. De Ruiter, J., Carboxylic Acids. In: *Principles of drug action 1* **2005**.
250. Hermanson, G. T., *Bioconjugate Techniques* **2008**, *2nd Edition*, 1-1202.
251. Vogel, N.; Retsch, M.; Fustin, C. A.; del Campo, A.; Jonas, U., Advances in Colloidal Assembly: The Design of Structure and Hierarchy in Two and Three Dimensions. *Chem. Rev.* **2015**, *115* (13), 6265-6311.
252. Miao, W. K.; Yi, A.; Yan, Y. K.; Ren, L. J.; Chen, D.; Wang, C. H.; Wang, W., A poly(polyoxometalate)-b-poly(hexanoic acid) block copolymer: synthesis, self-assembled micelles and catalytic activity. *Polym. Chem.* **2015**, *6* (42), 7418-7426.
253. Savariar, E. N.; Sochat, M. M.; Klaikherd, A.; Thayumanavan, S., Functional group density and recognition in polymer nanotubes. *Angew. Chem. Int. Ed.* **2009**, *48*, 110-114.
254. Zilman, A.; Talia, S.; Jovanovic-Talisman, T.; Chait, B. T.; Rout, M. P.; Magnasco, M. O.; Magnasco, M. O., Enhancement of transport selectivity through nano-channels by non-specific competition. *PLoS Comput. Biol.* **2010**, *6* (6), 1-11.

255. Pindzola, B. A.; Jin, J. Z.; Gin, D. L., Cross-linked normal hexagonal and bicontinuous cubic assemblies via polymerizable gemini amphiphiles. *J. Am. Chem. Soc.* **2003**, *125* (10), 2940-2949.
256. Caspi, Y.; Zbaida, D.; Cohen, H.; Elbaum, M., Synthetic Mimic of Selective Transport Through the Nuclear Pore Complex. *Nano Lett.* **2008**, *8* (11), 3728-3734.
257. Pine, A. S.; Menyuk, N.; Dresselhaus, G., Laser-Emission Study of the Pressure-Dependence of the Energy-Gap in Tellurium. *Solid State Commun* **1979**, *31* (3), 187-191.
258. Fell, C. J. D., *In Membrane separations technology : principles and applications; Noble, R. D., Stern, A. S.* Elsevier, Chapter 4: Amsterdam 1995.
259. Ventoza, T. P.; Lloyd, D. R., Poly(Ether Sulfone) Membranes for Desalination - Membrane Preparation and Characterization. *Desalination* **1985**, *56* (Nov), 381-394.
260. Clodt, J. I.; Filiz, V.; Rangou, S.; Buhr, K.; Abetz, C.; Höche, D.; Hahn, J.; Jung, A.; Abetz, V., Double stimuli-responsive isoporous membranes via post-modification of pH-sensitive self-assembled diblock copolymer membranes. *Adv. Funct. Mater.* **2013**, *23*, 731-738.
261. Mulvenna, R. A.; Weidman, J. L.; Jing, B.; Pople, J. A.; Zhu, Y.; Boudouris, B. W.; Phillip, W. A., Tunable nanoporous membranes with chemically-tailored pore walls from triblock polymer templates. *J. Membr. Sci.* **2014**, *470*, 246-256.
262. Liu, G.; Ding, J., Diblock thin films with densely hexagonally packed nanochannels. *Adv. Mater.* **1998**, *10*, 69-71.
263. Phillip, W. A.; Dorin, R. M.; Werner, J.; Hoek, E. M. V.; Wiesner, U.; Elimelech, M., Tuning Structure and Properties of Graded Triblock Terpolymer-Based Mesoporous and Hybrid Films. *Nano Lett.* **2011**, *11* (7), 2892-2900.
264. Staudt-Bickel, C.; Koros, W. J., Improvement of CO₂/CH₄ separation characteristics of polyimides by chemical crosslinking. *J. Membr. Sci.* **1999**, *155* (1), 145-154.
265. Hiemenz, P. C.; Rajagopalan, R., Principles of colloid and surface chemistry. *CRC Press* **1997**, *third edition*.
266. Cadotte, J.; Foreaster, R.; Kim, M.; Peterson, R.; Stocker, T., Nanofiltration membranes broaden the use of membrane separation technology. *Desalination* **1988**, *70*, 77-88.
267. Ohki, S.; Ohshima, H., *In Electrical double layers in biology; Blank, M.* Plenum Press: New York, 1986.
268. Schaep, J.; Van der Bruggen, B.; Vandecasteele, C.; Wilms, D., Influence of ion size and charge in nanofiltration. *Sep. Purif. Technol.* **1998**, *14* (1-3), 155-162.
269. Yaroshchuk, A.; Staude, E., Charged Membranes for Low-Pressure Reverse-Osmosis Properties and Applications. *Desalination* **1992**, *86* (2), 115-134.
270. Sholl, D. S.; Lively, R. P., Seven chemical separations to change the world (vol 532, pg 435, 2016). *Nature* **2016**, *533* (7603), 316-316.
271. Sholl, D. S.; Lively, R. P., Seven chemical separations to change the world. *Nature* **2016**, *532*, 435-437.
272. Schacher, F. H.; Rupa, P. A.; Manners, I., Functional block copolymers: nanostructured materials with emerging applications. *Angew. Chem. Int. Ed.* **2012**, *51*, 7898-7921.
273. Hou, X.; Jiang, L., Learning from Nature: Building Bio-Inspired Smart Nanochannels. *Acs Nano* **2009**, *3* (11), 3339-3342.
274. Jackson, E. A.; Hillmyer, M. A., Nanoporous Membranes Derived from Block Copolymers: From Drug Delivery to Water Filtration. *Acs Nano* **2010**, *4* (7), 3548-3553.
275. Lim, R. Y. H.; Aebi, U.; Fahrenkrog, B., Towards reconciling structure and function in the nuclear pore complex. *Histochemistry and Cell Biology* **2008**, *129* (2), 105-116.

276. Jirage, K. B.; Hulteen, J. C.; Martin, C. R., Nanotubule-based molecular-filtration membranes. *Science* **1997**, *278* (5338), 655-658.
277. Escobar, C. A.; Zulkifli, A. R.; Faulkner, C. J.; Trzeciak, A.; Jennings, G. K., Composite Fluorocarbon Membranes by Surface-Initiated Polymerization from Nanoporous Gold-Coated Alumina. *ACS Appl. Mater. Interfaces* **2012**, *4* (2), 906-915.
278. Sinturel, C.; Bates, F. S.; Hillmyer, M. A., High chi-Low N Block Polymers: How Far Can We Go? *Acs Macro Lett.* **2015**, *4* (9), 1044-1050.
279. Beginn, U.; Zipp, G.; Moller, M., Functional membranes containing ion-selective matrix-fixed supramolecular channels. *Adv. Mater.* **2000**, *12* (7), 510-+.
280. Chapman, R.; Danial, M.; Koh, M. L.; Jolliffe, K. A.; Perrier, S., Design and properties of functional nanotubes from the self-assembly of cyclic peptide templates. *Chem Soc Rev* **2012**, *41* (18), 6023-6041.
281. Gin, D. L.; Lu, X. Y.; Nemade, P. R.; Pecinovsky, C. S.; Xu, Y. J.; Zhou, M. J., Recent advances in the design of polymerizable lyotropic liquid-crystal assemblies for heterogeneous catalysis and selective separations. *Adv Funct Mater* **2006**, *16* (7), 865-878.
282. Ghadiri, M. R.; Granja, J. R.; Milligan, R. A.; Mcree, D. E.; Khazanovich, N., Self-Assembling Organic Nanotubes Based on a Cyclic Peptide Architecture. *Nature* **1993**, *366* (6453), 324-327.
283. Zhang, C.; Xu, T., Co-assembly of cyclic peptide nanotubes and block copolymers in thin films: controlling the kinetic pathway. *Nanoscale* **2015**, *7* (37), 15117-15121.
284. Feng, X.; Tousley, M. E.; Cowan, M. G.; Wiesenauer, B. R.; Nejati, S.; Choo, Y.; Noble, R. D.; Elimelech, M.; Gin, D. L.; Osuji, C. O., Scalable Fabrication of Polymer Membranes with Vertically Aligned 1 nm Pores by Magnetic Field Directed Self-Assembly. *Acs Nano* **2014**, *8* (12), 11977-11986.
285. Hourani, R.; Zhang, C.; van der Weegen, R.; Ruiz, L.; Li, C. Y.; Ketten, S.; Helms, B. A.; Xu, T., Processable Cyclic Peptide Nanotubes with Tunable Interiors. *J. Am. Chem. Soc.* **2011**, *133* (39), 15296-15299.
286. Fasan, R.; Dias, R. L. A.; Moehle, K.; Zerbe, O.; Obrecht, D.; Mittl, P. R. E.; Grutter, M. G.; Robinson, J. A., Structure-activity studies in a family of beta-hairpin protein epitope mimetic inhibitors of the p53-HDM2 protein-protein interaction. *Chembiochem* **2006**, *7* (3), 515-526.
287. Malinovskii, V. L.; Samain, F.; Haner, R., Helical arrangement of interstrand stacked pyrenes in a DNA framework. *Angew. Chem. Int. Edit* **2007**, *46* (24), 4464-4467.
288. Meyer, E. A.; Castellano, R. K.; Diederich, F., Interactions with aromatic rings in chemical and biological recognition. *Angewandte Chemie-International Edition* **2003**, *42* (11), 1210-1250.
289. Leuchtenberger, W.; Huthmacher, K.; Drauz, K., Biotechnological production of amino acids and derivatives: current status and prospects. *Appl Microbiol Biot* **2005**, *69* (1), 1-8.
290. Capela, E. V.; Quental, M. V.; Domingues, P.; Coutinho, J. A. P.; Freire, M. G., Effective separation of aromatic and aliphatic amino acid mixtures using ionic-liquid-based aqueous biphasic systems. *Green Chem* **2017**, *19* (8), 1850-1854.
291. Marx, K. A., Quartz crystal microbalance: A useful tool for studying thin polymer films and complex biomolecular systems at the solution-surface interface. *Biomacromolecules* **2003**, *4* (5), 1099-1120.
292. Hermanson, G. T., *Bioconjugate Techniques*. 3RD ED. ed.; ELSEVIER ACADEMIC PRESS: London, 2013.
293. Lobert, M.; Bandmann, H.; Burkert, U.; Buchele, U. P.; Podsadlowski, V.; Klärner, F. G., Dynamics in host-guest complexes of molecular tweezers and clips. *Chem-Eur J* **2006**, *12* (6), 1629-1641.

294. Wheeler, S. E., Substituents Effect in π -Stacking Interactions. In *Noncovalent Forces, Challenges and Advances in Computational Chemistry and Physics*, Scheiner, S., Ed. Springer International Publishing: Switzerland, 2015; pp 421-442.
295. Hunter, C. A.; Lawson, K. R.; Perkins, J.; Urch, C. J., Aromatic interactions. *J Chem Soc Perk T 2* **2001**, (5), 651-669.
296. Cockroft, S. L.; Perkins, J.; Zonta, C.; Adams, H.; Spey, S. E.; Low, C. M. R.; Vinter, J. G.; Lawson, K. R.; Urch, C. J.; Hunter, C. A., Substituent effects on aromatic stacking interactions. *Org Biomol Chem* **2007**, 5 (7), 1062-1080.
297. Cockroft, S. L.; Hunter, C. A.; Lawson, K. R.; Perkins, J.; Urch, C. J., Electrostatic control of aromatic stacking interactions. *J. Am. Chem. Soc.* **2005**, 127 (24), 8594-8595.
298. Boggs, A. S. P.; Bowden, J. A.; Galligan, T. M.; Guillette, L. J.; Kucklick, J. R., Development of a multi-class steroid hormone screening method using Liquid Chromatography/Tandem Mass Spectrometry (LC-MS/MS). *Analytical and bioanalytical chemistry* **2016**, 408 (15), 4179-4190.
299. Nowakowska, J.; Pikul, P.; Ciura, K.; Piotrowicz, J., A simple TLC and HPTLC method for separation of selected steroid drugs. *Cent Eur J Chem* **2013**, 11 (8), 1297-1308.
300. Lewis, M.; Bagwill, C.; Hardebeck, L. K. E.; Wireduaah, S., The use of Hammett constants to understand the non-covalent binding of aromatics. *Computational and Structural Biotechnology Journal* **2012**, 1 (1), 1-9.
301. Yuan, X. G.; Wang, W. M.; Tian, Z. Q.; Bi, S. W.; Ma, J., Electron-donating groups and high ring strain promoted ring opening of methylenecyclopropanes catalyzed by rhodium and iridium complexes. *J Organomet Chem* **2016**, 811, 29-39.
302. Lewis, M.; Bagwill, C.; Hardebeck, L.; Wireduaah, S., The Use of Hammett Constants to Understand the Non-Covalent Binding of Aromatics. *Comput. Struct. Biotechnol. J.* **2012**, 1, 1-9.
303. Hansch, C.; Leo, A.; Taft, R. W., A Survey of Hammett Substituent Constants and Resonance and Field Parameters. *Chem. Rev.* **1991**, 91 (2), 165-195.
304. Marx, K. A., Quartz crystal microbalance: a useful tool for studying thin polymer films and complex biomolecular systems at the solution-surface interface. *Biomacromolecules* **2003**, 4 (5), 1099-1120.
305. Shen, M.; Keten, S.; Lueptow, R. M., Rejection mechanisms for contaminants in polyamide reverse osmosis membranes. *J. Membr. Sci.* **2016**, 509, 36-47.
306. Asatekin, A.; Gleason, K., Polymeric nanopore membranes for hydrophobicity-based separations by conformal initiated chemical vapor deposition. *Nano Lett.* **2011**, 11, 677-686.
307. Shen, M.; Keten, S.; Lueptow, R. M., Dynamics of water and solute transport in polymeric reverse osmosis membranes via molecular dynamics simulations. *Journal of Membrane Science* **2016**, 506, 95-108.
308. Labrou, N. E., Protein Purification: An Overview. *Methods Mol. Biol.* **2014**, 1129, 3-10.
309. Hettiarachchy, N.; Sato, K.; Marshall, M.; Kannan, A., *Food Proteins and Peptides: Chemistry, Functionality, Interactions, and Commercialization*. CRC Press: Taylor & Francis Group: FL, 2016.
310. van Reis, R.; Zydney, A., Membrane separations in biotechnology. *Curr. Opin. Biotech.* **2001**, 12 (2), 208-211.
311. Charcosset, C., Membrane processes in biotechnology: An overview. *Biotechnol. Adv.* **2006**, 24 (5), 482-492.
312. Zhao, Y. H.; Wee, K. H.; Bai, R. B., A Novel Electrolyte-Responsive Membrane with Tunable Permeation Selectivity for Protein Purification. *ACS Appl. Mater. Inter.* **2010**, 2 (1), 203-211.

313. Huang, R.; Kostanski, L. K.; Filipe, C. D. M.; Ghosh, R., Environment-responsive hydrogel-based ultrafiltration membranes for protein bioseparation. *Journal of Membrane Science* **2009**, *336* (1-2), 42-49.
314. Li, Q.; Bi, Q. Y.; Lin, H. H.; Bian, L. X.; Wang, X. L., A novel ultrafiltration (UF) membrane with controllable selectivity for protein separation. *J. Membr. Sci.* **2013**, *427*, 155-167.
315. Adrus, N.; Ulbricht, M., Novel hydrogel pore-filled composite membranes with tunable and temperature-responsive size-selectivity. *J. Mater. Chem.* **2012**, *22* (7), 3088-3098.
316. Nilsson, J. L., Protein Fouling of Uf Membranes - Causes and Consequences. *Journal of Membrane Science* **1990**, *52* (2), 121-142.
317. Tang, C. Y. Y.; Chong, T. H.; Fane, A. G., Colloidal interactions and fouling of NF and RO membranes: A review. *Adv Colloid Interfac* **2011**, *164* (1-2), 126-143.
318. Kang, S.; Asatekin, A.; Mayes, A. M.; Elimelech, M., Protein antifouling mechanisms of PAN UF membranes incorporating PAN-g-PEO additive. *J. Membr. Sci.* **2007**, *296* (1-2), 42-50.
319. Marshall, A. D.; Munro, P. A.; Tragardh, G., The Effect of Protein Fouling in Microfiltration and Ultrafiltration on Permeate Flux, Protein Retention and Selectivity - a Literature-Review. *Desalination* **1993**, *91* (1), 65-108.
320. Ju, H.; McCloskey, B. D.; Sagle, A. C.; Kusuma, V. A.; Freeman, B. D., Preparation and characterization of crosslinked poly(ethylene glycol) diacrylate hydrogels as fouling-resistant membrane coating materials. *J. Membr. Sci.* **2009**, *330* (1-2), 180-188.
321. Andrade, J. D.; Hlady, V.; Jeon, S. I., Poly(ethylene oxide) and protein resistance - Principles, problems, and possibilities. *Adv Chem Ser* **1996**, *248*, 51-59.
322. Sagle, A. C.; Van Wagner, E. M.; Ju, H.; McCloskey, B. D.; Freeman, B. D.; Sharma, M. M., PEG-coated reverse osmosis membranes: Desalination properties and fouling resistance. *J. Membr. Sci.* **2009**, *340* (1-2), 92-108.
323. Sagle, A. C.; Ju, H.; Freeman, B. D.; Sharma, M. M., PEG-based hydrogel membrane coatings. *Polymer* **2009**, *50* (3), 756-766.
324. Wu, Y. H.; Park, H. B.; Kai, T.; Freeman, B. D.; Kalika, D. S., Water uptake, transport and structure characterization in poly(ethylene glycol) diacrylate hydrogels. *J. Membr. Sci.* **2010**, *347* (1-2), 197-208.
325. van Rijn, P.; Tutus, M.; Kathrein, C.; Zhu, L. L.; Wessling, M.; Schwaneberg, U.; Boker, A., Challenges and advances in the field of self-assembled membranes. *Chem. Soc. Rev.* **2013**, *42* (16), 6578-6592.
326. Lin, H. Q.; Van Wagner, E.; Freeman, B. D.; Toy, L. G.; Gupta, R. P., Plasticization-enhanced hydrogen purification using polymeric membranes. *Science* **2006**, *311* (5761), 639-642.
327. Lin, H. Q.; Kai, T.; Freeman, B. D.; Kalakkunnath, S.; Kalika, D. S., The effect of cross-linking on gas permeability in cross-linked poly(ethylene glycol diacrylate). *Macromolecules* **2005**, *38* (20), 8381-8393.
328. Cadotte, J. E. Reverse osmosis membrane. 3,926,798, December 1975, 1975.
329. Cadotte, J. E. Interfacially synthesized reverse osmosis membrane. 4,277,344, July 1981, 1981.
330. Lin, L.; Lopez, R.; Ramon, G. Z.; Coronell, O., Investigating the void structure of the polyamide active layers of thin-film composite membranes. *Journal of Membrane Science* **2016**, *497*, 365-376.
331. Lin, L.; Feng, C. C.; Lopez, R.; Coronell, O., Identifying facile and accurate methods to measure the thickness of the active layers of thin-film composite membranes - A comparison of seven characterization techniques. *J. Membr. Sci.* **2016**, *498*, 167-179.

332. Soroush, A.; Barzin, J.; Barikani, M.; Fathizadeh, M., Interfacially polymerized polyamide thin film composite membranes: Preparation, characterization and performance evaluation. *Desalination* **2012**, *287*, 310-316.
333. Sadeghi, I.; Yi, H.; Asatekin, A., A Method for Manufacturing Membranes with Ultrathin Hydrogel Selective Layers for Protein Purification: Interfacially Initiated Free Radical Polymerization (IIFRP). *Chem. Mater.* **2018**, *30* (4), 1265-1276.
334. Yamagishi, H.; Crivello, J. V.; Belfort, G., Development of a Novel Photochemical Technique for Modifying Poly(Arylsulfone) Ultrafiltration Membranes. *J. Membr. Sci.* **1995**, *105* (3), 237-247.
335. Pieracci, J.; Crivello, J. V.; Belfort, G., Increasing membrane permeability of UV-modified poly(ether sulfone) ultrafiltration membranes. *J. Membr. Sci.* **2002**, *202* (1-2), 1-16.
336. Culfaz, P. Z.; Haddad, M.; Wessling, M.; Lammertink, R. G. H., Fouling behavior of microstructured hollow fibers in cross-flow filtrations: Critical flux determination and direct visual observation of particle deposition. *J. Membr. Sci.* **2011**, *372* (1-2), 210-218.
337. Razi, B.; Aroujalian, A.; Fathizadeh, M., Modeling of fouling layer deposition in cross-flow microfiltration during tomato juice clarification. *Food Bioprod Process* **2012**, *90* (C4), 841-848.
338. Rezaei, H.; Ashtiani, F. Z.; Fouladitajar, A., Fouling Behavior and Performance of Microfiltration Membranes for Whey Treatment in Steady and Unsteady-State Conditions. *Braz J Chem Eng* **2014**, *31* (2), 503-518.
339. Appleyard, D. C.; Chapin, S. C.; Doyle, P. S., Multiplexed Protein Quantification with Barcoded Hydrogel Microparticles. *Anal. Chem.* **2011**, *83* (1), 193-199.
340. Choi, N. W.; Kim, J.; Chapin, S. C.; Duong, T.; Donohue, E.; Pandey, P.; Broom, W.; Hill, W. A.; Doyle, P. S., Multiplexed Detection of mRNA Using Porosity-Tuned Hydrogel Microparticles. *Anal. Chem.* **2012**, *84* (21), 9370-9378.
341. Yang, C. X.; Choi, C. H.; Lee, C. S.; Yi, H. M., A Facile Synthesis-Fabrication Strategy for Integration of Catalytically Active Viral-Palladium Nanostructures into Polymeric Hydrogel Microparticles via Replica Molding. *Acs Nano* **2013**, *7* (6), 5032-5044.
342. Wu, Y. H.; Park, H. B.; Kai, T.; Freeman, B. D.; Kalika, D. S., Water uptake, transport and structure characterization in poly(ethylene glycol) diacrylate hydrogels. *J. Membr. Sci.* **2010**, *347* (1-2), 197-208.
343. Peter, M.; Tayalia, P., An alternative technique for patterning cells on poly(ethylene glycol) diacrylate hydrogels. *RSC Adv.* **2016**, *6* (47), 40878-40885.
344. Xiao, Y. H.; He, L.; Che, J. F., An effective approach for the fabrication of reinforced composite hydrogel engineered with SWNTs, polypyrrole and PEGDA hydrogel. *J. Mater. Chem.* **2012**, *22* (16), 8076-8082.
345. <https://www.sterlitech.com/flat-sheet-membranes-specifications.html>.
346. <https://www.lenntech.com/Data-sheets/Millipore-Ultrafiltration-Membranes-L.pdf>.
347. Van der Bruggen, B.; Vandecasteele, C.; Van Gestel, T.; Doyen, W.; Leysen, R., A review of pressure-driven membrane processes in wastewater treatment and drinking water production. *Environ. Prog.* **2003**, *22* (1), 46-56.
348. Lu, R. R.; Xu, S. Y.; Wang, Z.; Yang, R. J., Isolation of lactoferrin from bovine colostrum by ultrafiltration coupled with strong cation exchange chromatography on a production scale. *J. Membr. Sci.* **2007**, *297* (1-2), 152-161.
349. Isa, M. H. M.; Coraglia, D. E.; Frazier, R. A.; Jauregi, P., Recovery and purification of surfactin from fermentation broth by a two-step ultrafiltration process. *J. Membr. Sci.* **2007**, *296* (1-2), 51-57.

350. Kwon, B.; Molek, J.; Zydney, A. L., Ultrafiltration of PEGylated proteins: Fouling and concentration polarization effects. *J. Membr. Sci.* **2008**, *319* (1-2), 206-213.
351. Lim, Y. P.; Mohammad, A. W., Effect of solution chemistry on flux decline during high concentration protein ultrafiltration through a hydrophilic membrane. *Chem Eng J* **2010**, *159* (1-3), 91-97.
352. Jermann, D.; Pronk, W.; Boller, M.; Schafer, A. I., The role of NOM fouling for the retention of estradiol and ibuprofen during ultrafiltration. *J. Membr. Sci.* **2009**, *329* (1-2), 75-84.
353. Ghosh, A. K.; Hoek, E. M. V., Impacts of support membrane structure and chemistry on polyamide-polysulfone interfacial composite membranes. *J. Membr. Sci.* **2009**, *336* (1-2), 140-148.
354. Talmard, C.; Guilloureau, L.; Coppel, Y.; Mazarguil, H.; Faller, P., Amyloid-beta peptide forms monomeric complexes with Cu-II and Zn-II prior to aggregation. *Chembiochem.* **2007**, *8* (2), 163-165.
355. Jung, S.; Yi, H., Facile Micromolding-Based Fabrication of Biopolymeric-Synthetic Hydrogel Microspheres with Controlled Structures for Improved Protein Conjugation. *Chem. Mater.* **2015**, *27* (11), 3988-3998.
356. Jung, S.; Abel, J. H.; Starger, J. L.; Yi, H., Porosity-Tuned Chitosan-Polyacrylamide Hydrogel Microspheres for Improved Protein Conjugation. *Biomacromolecules* **2016**, *17* (7), 2427-2436.
357. Le Goff, G. C.; Srinivas, R. L.; Hill, W. A.; Doyle, P. S., Hydrogel microparticles for biosensing. *Eur. Polym. J.* **2015**, *72*, 386-412.
358. Dusek, K., Phase Separation in Ternary Systems Induced by Crosslinking. *Chem. Zvesti* **1971**, *25* (3), 184-189.
359. Boots, H. M. J.; Kloosterboer, J. G.; Serbutoviez, C.; Touwslager, F. J., Polymerization-induced phase separation .1. Conversion-phase diagrams. *Macromolecules* **1996**, *29* (24), 7683-7689.
360. Lee, A. G.; Arena, C. P.; Beebe, D. J.; Palecek, S. P., Development of Macroporous Poly(ethylene glycol) Hydrogel Arrays within Microfluidic Channels. *Biomacromolecules* **2010**, *11* (12), 3316-3324.
361. Wong, M. C. Y.; Lin, L.; Coronell, O.; Hoek, E. M. V.; Ramon, G. Z., Impact of liquid-filled voids within the active layer on transport through thin-film composite membranes. *J. Membr. Sci.* **2016**, *500*, 124-135.
362. Li, M. G.; Humayun, M.; Hughes, B.; Kozinski, J. A.; Hwang, D. K., A microfluidic approach for the synthesis and assembly of multi-scale porous membranes. *RSC Adv.* **2015**, *5* (121), 100024-100029.
363. Zeng, W.; Du, Y.; Xue, Y.; Frisch, H., Solubility Parameters. In *Physical Properties of Polymers Handbook*, Mark, J., Ed. Springer: NY, 2007; pp 289-303.
364. Pregibon, D. C.; Doyle, P. S., Optimization of Encoded Hydrogel Particles for Nucleic Acid Quantification. *Anal. Chem.* **2009**, *81* (12), 4873-4881.
365. Stevens, M. P., In *Polymer Chemistry: An Introduction*, Oxford University Press: New York, 1998; pp 70-74.
366. Guo, W. S.; Ngo, H. H.; Li, J. X., A mini-review on membrane fouling. *Bioresource Technol.* **2012**, *122*, 27-34.
367. Schafer, A. I., *Natural Organics Removal Using Membranes: Principles, Performance, and Cost*. CRC Press: Boca Raton, 2001.
368. Fathizadeh, M.; Tien, H. N.; Khivantsev, K.; Song, Z.; Zhou, F.; Yu, M., Polyamide/nitrogen-doped Graphene Oxide Quantum Dots (N-GOQD) Thin Film Nanocomposite Reverse Osmosis Membranes for High Flux Desalination. *Desalination* **2017**.

369. Vandenberg, G. B.; Smolders, C. A., Flux Decline in Ultrafiltration Processes. *Desalination* **1990**, *77* (1-3), 101-133.
370. Palacio, L.; Ho, C. C.; Zydney, A. L., Application of a pore-blockage - Cake-filtration model to protein fouling during microfiltration. *Biotechnol. Bioeng.* **2002**, *79* (3), 260-270.
371. Matthiasson, E., The Role of Macromolecular Adsorption in Fouling of Ultrafiltration Membranes. *J. Membr. Sci.* **1983**, *16* (Dec), 23-36.
372. Elaprakash, N.; Savariar, K.; Krishnamoorthy, K.; Thayumanavan, S., Molecular discrimination inside polymer nanotubules. *Nat. Nanotechnol.* **2008**, *3*, 112-117.
373. Lepp, N. W., *Effect of Heavy Metal Pollution on Plants*. Springer Netherlands: 1981.
374. Fu, F. L.; Wang, Q., Removal of heavy metal ions from wastewaters: A review. *J Environ Manage* **2011**, *92* (3), 407-418.
375. Morais, S.; G., C. F.; Pereira, M. L., Heavy Metals and Human Health. In *Environmental Health: Emerging issues and practice*, 2012; pp 227-246.
376. Wandera, D.; Wickramasinghe, S. R.; Husson, S. M., Stimuli-responsive membranes. *J. Membr. Sci.* **2010**, *357* (1-2), 6-35.
377. Kim, K. K.; Hsu, A.; Jia, X. T.; Kim, S. M.; Shi, Y. M.; Dresselhaus, M.; Palacios, T.; Kong, J., Synthesis and Characterization of Hexagonal Boron Nitride Film as a Dielectric Layer for Graphene Devices. *Acs Nano* **2012**, *6* (10), 8583-8590.
378. Li, Q.; Bi, Q. Y.; Zhou, B.; Wang, X. L., Zwitterionic sulfobetaine-grafted poly(vinylidene fluoride) membrane surface with stably anti-protein-fouling performance via a two-step surface polymerization. *Applied Surface Science* **2012**, *258* (10), 4707-4717.
379. Ni, L.; Meng, J.; Geise, G. M.; Zhang, Y.; Zhou, J., Water and salt transport properties of zwitterionic polymers film. *Journal of Membrane Science* **2015**, *491*, 73-81.
380. Georgiev, G. S.; Karnenska, E. B.; Vassileva, E. D.; Kamenova, I. P.; Georgieva, V. T.; Iliev, S. B.; Ivanov, I. A., Self-assembly, anti polyelectrolyte effect, and nonbiofouling properties of polyzwitterions. *Biomacromolecules* **2006**, *7* (4), 1329-1334.
381. Li, J.-H.; Li, M.-Z.; Miao, J.; Wang, J.-B.; Shao, X.-S.; Zhang, Q.-Q., Improved surface property of PVDF membrane with amphiphilic zwitterionic copolymer as membrane additive. *Applied Surface Science* **2012**, *258* (17), 6398-6405.
382. Rohani, M. M.; Zydney, A. L., Protein transport through zwitterionic ultrafiltration membranes. *Journal of Membrane Science* **2012**, *397*, 1-8.
383. Shao, Q.; Jiang, S., Molecular Understanding and Design of Zwitterionic Materials. *Advanced Materials* **2015**, *27* (1), 15-26.
384. Wu, J.; Lin, W. F.; Wang, Z.; Chen, S. F.; Chang, Y., Investigation of the Hydration of Nonfouling Material Poly(sulfobetaine methacrylate) by Low-Field Nuclear Magnetic Resonance. *Langmuir* **2012**, *28* (19), 7436-7441.
385. Wu, Y.-H.; Park, H. B.; Kai, T.; Freeman, B. D.; Kalika, D. S., Water uptake, transport and structure characterization in poly(ethylene glycol) diacrylate hydrogels. *Journal of Membrane Science* **2010**, *347* (1-2), 197-208.
386. Liu, J. Y.; Hou, X. D.; Park, H. B.; Lin, H. Q., High-Performance Polymers for Membrane CO₂/N₂ Separation. *Chem-Eur J* **2016**, *22* (45), 15980-15990.
387. <https://www3.epa.gov/climatechange/ghgemissions/inventoryexplorer/#allsectors/allgas/gas/current>.
388. Li, Q.; Xie, R.; Mintz, E. A.; Shang, J. K., Enhanced Visible-Light Photocatalytic Degradation of Humic Acid by Palladium-Modified Nitrogen-Doped Titanium Oxide. *Journal of the American Ceramic Society* **2007**, *90* (12), 3863-3868.
389. Doong, R.-A.; Lai, Y.-J., Dechlorination of tetrachloroethylene by palladized iron in the presence of humic acid. *Water Research* **2005**, *39* (11), 2309-2318.

390. Wunder, S.; Polzer, F.; Lu, Y.; Mei, Y.; Ballauff, M., Kinetic Analysis of Catalytic Reduction of 4-Nitrophenol by Metallic Nanoparticles Immobilized in Spherical Polyelectrolyte Brushes. *J. Phys. Chem. C* **2010**, *114* (19), 8814-8820.
391. Pradhan, N.; Pal, A.; Pal, T., Catalytic Reduction of Aromatic Nitro Compounds by Coinage Metal Nanoparticles. *Langmuir* **2001**, *17* (5), 1800-1802.
392. Pradhan, N.; Pal, A.; Pal, T., Silver nanoparticle catalyzed reduction of aromatic nitro compounds. *Colloids Surf., A* **2002**, *196* (2-3), 247-257.
393. Susanto, H.; Arafat, H.; Janssen, E. M. L.; Ulbricht, M., Ultrafiltration of polysaccharide-protein mixtures: Elucidation of fouling mechanisms and fouling control by membrane surface modification. *Separation and Purification Technology* **2008**, *63* (3), 558-565.
394. Yang, C.; Jung, S.; Yi, H., A biofabrication approach for controlled synthesis of silver nanoparticles with high catalytic and antibacterial activities. *Biochem Eng J* **2014**, *89*, 10-20.
395. Johannsmann, D., Viscoelastic, mechanical, and dielectric measurements on complex samples with the quartz crystal microbalance. *Phys Chem Chem Phys* **2008**, *10* (31), 4516-4534.
396. Yamada, M.; Shiratori, S. S., Smoke sensor using mass controlled layer-by-layer self-assembly of polyelectrolytes films. *Sensor Actuat B-Chem* **2000**, *64* (1-3), 124-127.